

High Performance Lithium Niobate Resonators for Passive Voltage Amplification in Radio Frequency Applications

Submitted in partial fulfillment of the requirements for
the degree of
Doctor of Philosophy

in

Electrical and Computer Engineering

Luca Colombo

B.S., Mechanical Engineering, Politecnico di Milano (2013)

M.S., Mechanical Engineering, Politecnico di Milano (2015)

Carnegie Mellon University
Pittsburgh, PA

September, 2019

Copyright © 2019, Luca Colombo

ABSTRACT

Internet of Things (IoT) applications are fostering the development of near-zero power consumption and event-driven Radio Frequency (RF) sensors that can outperform traditional networks based on scheduling algorithms. In case of infrequent events, asynchronous Wake-Up Radio Receivers (WuRx) are the desired solution to attain high sensitivity (<100 dBm) and ultra-low-power consumption (\sim tens of nW). The strict available power budget led to drastic reduction of active components in the WuRx, which relies more extensively on passive voltage amplification and filtering in the RF Front-End (RFFE).

High performance microelectromechanical (MEM) piezoelectric resonators are an ideal solution as Matching Network (MN) in the RFFE due to their compact footprint, high quality factor at resonance (Q_s) and range of operation (up to few GHz). Despite the availability of successful commercial products, such as Aluminum Nitride (AlN) Film Bulk Acoustic Resonators (FBARs), WuRx are driving the demand for devices which can simultaneously exhibit large quality factor and large k_t^2 or, overall, a large Figure of Merit (FoM, defined as $Q_s \cdot k_t^2$).

This dissertation focuses on the development of high performance X-cut Lithium Niobate (LN) MEMS Laterally Vibrating Resonators (LVRs) to be implemented as the matching network of novel WuRx architectures. The requirements of these devices in terms of operating frequency (f_{RF}), static capacitance (C_0), and Figure of Merit are investigated according to the sensitivity optimization of the Resonant Micromechanical Receiver (RMR) envisioned at Carnegie Mellon University. Different established and innovative piezoelectric MEMS technologies are compared to identify the solution that offers the highest FoM while satisfying the matching constraints provided by the RMR numerical optimization. Preliminary work on X-cut Lithium Niobate resonators operating in the S_0 mode exhibited incredibly high k_t^2 ($> 30\%$) combined with good Q_s ($\sim 1,500$), which translate to FoM greater than 400 (similar to commercial FBARs performance).

Since the operating frequency and the load condition of the matching network are usually fixed, the Figure of Merit, and in particular the quality factor, is the only lever available to increase the sensitivity of the RMR. The resonators geometry is thus thoroughly investigated through Finite Element Analysis (FEA) to maximize Q_s and consequently the achievable voltage amplification. Fabricated devices showed Q_s as high as 8,000 in vacuum at 100 MHz, with $k_t^2 = 28\%$ and FoM $> 2,500$, the highest ever reported to date for piezoelectric MEMS operating in the frequency range of interest for WuRx. Devices at higher frequencies showed improved performance compared to the state-of-the-art, with Q_s greater than 2,500 up to 550 MHz.

Damping mechanism in X-cut LN LVRs were investigated on fabricated devices. Air damping (Q_{air}) proven to be a significant source of quality factor degradation up to 200 MHz, with Q_s reduction in the order of 20 – 30%, while becomes negligible above 550 MHz. Anchor losses were investigated on devices with different plate length (L) over width (W) aspect ratios. Shorter resonators exhibit lower Q_s due to energy leakage through the substrate, over the entire frequency range of interest. As a consequence, the quality factor of devices with limited aperture ($L_e < 5 \lambda$) showcased a stronger dependency from the anchor dimensions. The electrical loading introduced by the Interdigitated Electrodes (IDE) and the interconnects were identified as the main damping mechanism in resonators with high L/W ratios. Cryogenic measurements highlighted Q_s as high as 26,000 at base temperature (10 K), hinting that anchor losses play a limited role in devices with a slender geometry. A tradeoff between electrical loading and anchor losses was also identified.

The limited static capacitance (C_0) achievable for the optimized resonator geometries required the investigation of alternative solutions to match those devices to the typical input capacitive load of an envelope detector (~ 1 pF). Arrays of identical, parallel resonators and alternative matching network configuration were investigated for this purpose. In the first case, arrays with C_0 of 1 pF and quality factor greater than 2,000, with $k_t^2 = 30\%$ and FoM = 600 were demonstrated at 50 MHz. Frequency mismatch between the elements was identified as the main damping mechanism for reduction in effective Q_s and was modeled through a statistical Monte Carlo approach. An alternative matching network based on a combination of series and parallel resonators (L-network)

with identical C_0 was also investigated, showcasing a gain 30% higher than a simple series configuration (46 V/V vs. 35 V/V for a capacitive load of 1 pF) and a higher robustness in regards to frequency variations.

ACKNOWLEDGEMENTS

First, I would like to thank my advisor, Professor Gianluca Piazza, for the priceless opportunity he offered me, and his constant guidance and support through the entire doctorate program. As a mentor, he taught me valuable lessons which go beyond the mere technical knowledge. I will always admire his passion about scientific research and his vision. It was an honor to be one of his students.

I would also like to thank Professor Tamal Mukherjee, Professor Sonbin Gong, and Professor Cristian Cassella for serving in my defense committee. Their suggestions and feedbacks have been fundamental in finalizing the present work. I am grateful to Professors Rick Carley, Matteo Rinaldi, Gary Fedder, Jeyanandh Paramesh, Jim Bain, Maysam Chamanzar, Jim Bain, and Larry Pileggi for their help during my PhD.

I am thankful to all the present and past members of the PMaNS lab, and all the colleagues I had the honor to work with: Zachary Schaffer, James Best, Ashraf Mahmoud, Mohamed Hakim, Jitendra Pal, Hoe Joon Kim, Emad Mehdizadeh, Enes Calayir, Changting Xu, Lutong Cai, Shafee Khan, Ayaz Masud, Yuyi Shen, Mary Beth Galanko, Mohammed Darwish, Flavius Pop, Mazen Soliman, Hoda Abdelsalam, Matts Forssell, Jay Reddy, and Isen Ozalp. I am particularly grateful to Abhay Kochhar and Gabriel Vidal-Álvarez for their advices and mentoring during my years at Carnegie Mellon University. A special thanks is due to my colleague Pietro Simeoni, who has been the best friend, roommate, and colleague anybody could ask for.

As a CMU Nanofab enthusiast, I am deeply grateful to Matthew Moneck, Mark Weiler, Norman Gottron, Mason Risley, James Rosvanis, and Dante Boni for their hard, meticulous work, their patience and the precious suggestions they always shared with me.

Among my Pittsburgh friends, I would especially like to thank Gabriele, Antonis, Emilio, Taylor, and Marina for their unconditional friendship and support who made me feel at home, even if I was 6,000 miles away from it. I would also like to thank Niccolò, Alessandro, Dimitrios, Brandon, Toygun, Alp, Stephen, Paula, Gwen, Husni, Alex, Jose, Simone, Francesca, Matteo,

Gabriel, the whole Jukestick soccer team, the International Student Union (ISU) members, and all my other friends for the time and the experiences shared together.

I am thankful to my parents, Mauro and Paola, my siblings, Alessandro, Stefano, Silvia and Pier, and my lifetime friends, in particular Alessio, Luca, Andrea, Gabriele, Valentina, Davide, and Marta, who supported me and encouraged me throughout this journey on the other side of the ocean.

Finally, I wish to thank Matilde. Her presence in the last few months, while performing the last experiment and writing my thesis, meant more than she thinks.

This work was fully funded in the framework of the N-ZERO Project by the Defense Advanced Research Projects Agency (DARPA) under contract No. HR0011-15-C-0137.

Tempora mutantur, nos et mutamur in illis.

To all the people who have supported me along this journey.

TABLE OF CONTENTS

ABSTRACT	iii
ACKNOWLEDGEMENTS	vi
TABLE OF CONTENTS	ix
LIST OF TABLES	xii
LIST OF FIGURES	xiii
CHAPTER 1: INTRODUCTION	1
1.1. The N-ZERO Project Challenge	2
1.2. Wake-Up Radio Receivers (WuRx)	4
1.3. MEMS Resonators as Matching Networks	6
1.4. Thesis Outline	8
CHAPTER 2: RESONANT MICROMECHANICAL RECEIVER (RMR)	10
2.1. Matching Network (MN)	11
2.1.1. Series Inductor (LC Tank)	13
2.1.2. Transformer with Parallel Inductor	14
2.1.3. 1-port MEMS Series Resonator	15
2.1.4. 2-port MEMS Resonator	19
2.1.5. Transformer with Parallel Resonator	21
2.1.6. Matching Networks Comparison	23
2.2. Electrostatic MEMS demodulator	25
2.3. CMOS TIA	27
2.4. RMR Numerical Optimization	28
CHAPTER 3: PIEZOELECTRIC MEMS RESONATORS TECHNOLOGIES	33
3.1. Laterally Vibrating Resonators (LVRs)	34
3.1.1. Static Capacitance (C_0) Modeling and Excitation Mode	37
3.1.2. Impact of FoM and C_0 on Voltage Amplification	40
3.2. Comparison between LVRs Technologies	42
3.2.1. Aluminum Nitride (AlN)	42
3.2.2. Scandium-doped Aluminum Nitride (ScAlN)	45
3.2.3. Y-cut Lithium Niobate (LN)	49
3.2.4. X-cut Lithium Niobate (LN)	55
3.3. Conclusions and Figure of Merit (FoM) Remarks	57
CHAPTER 4: X-CUT LITHIUM NIOBATE LVRs	59

4.1. Design and Fabrication of 50 MHz devices.....	61
4.1.1. COMSOL® Simulations	63
4.1.2. Experimental Plan and Fabrication.....	65
4.1.3. Device Characterization.....	68
4.1.4. Arrays Performance.....	74
4.2. Design and Fabrication of Higher Frequency Devices	76
4.2.1. Experimental Plan and Fabrication.....	76
4.2.2. Device Characterization.....	84
4.3. Characterization of Damping Mechanism.....	93
4.3.1. Air Damping.....	93
4.3.2. Series Resistance Modeling.....	94
4.3.3. Impact of Electrical Loading.....	97
4.3.4. Anchor Losses	98
4.3.5. Frequency Mismatch in Arrays of Resonators	101
4.3.6. Conclusions on Damping Mechanism.....	109
CHAPTER 5: X-cut LVRs as Matching Networks	110
5.1. 1-port LVRs Gain.....	110
5.1.1. 100 MHz LVRs Gain Simulation	112
5.1.2. Considerations on Arrays	115
5.2. Effects of Spurious Modes on Gain	116
5.2.1. Frequency Pulling Modeling	119
5.2.2. Impact of Spurious Modes Key Parameters on Gain.....	124
5.3. L-network Topology.....	128
5.3.1. Analytical Modeling	130
5.3.2. Numerical Optimization	132
5.3.3. System Demonstration	134
CHAPTER 6: CONCLUSIONS AND FUTURE WORK.....	136
6.1. Future Research Direction	137
APPENDIX A: FABRICATION PROCESSES.....	139
A.1. Aluminum Nitride (AlN).....	139
A.2. Scandium-doped Aluminum Nitride (Sc_{0.2}Al_{0.2}N)	140
A.3. Y-cut Lithium Niobate (LN).....	141
A.4. X-cut Lithium Niobate (LN).....	142
APPENDIX B: FREQUENCY PULLING	143
APPENDIX C: STRESS GRADIENT EXTRACTION	145
APPENDIX D: MATRIX ROTATIONS	148
APPENDIX E: OVERETCH MODELING	155

BIBLIOGRAPHY AND REFERENCES157

LIST OF TABLES

Table 2.1: List of RMR fixed parameters.	29
Table 3.1: Measured parameters, geometrical dimensions and estimated R_s , C_0 and C_f for the devices reported in Fig. 3.16. De-embedded k_t^2 and Q_s are also reported.	54
Table 3.2: Recap of the performance demonstrated by the most notable LVRs technologies. $Sc_{0.4}Al_{0.6}N$ and X-cut LN properties and performance are presented as reported in [57] and [66].	57
Table 4.1: Standard geometry parameters.	66
Table 4.2: Experimental parametric investigation.	66
Table 4.3: Identified modes exhibited by an optimized X-cut LVR and main extracted parameters. Modes at 33.72, 102.99, 115.99, 240.35, and 406.1 MHz showed noisy or split peaks, which prevented the extraction of Q_s	74
Table 4.4: Statistical distribution of f_s , Q_s , k_t^2 and C_0 measured on 8 identical standard resonators. Resonant frequency as a function of the position are also reported.	75
Table 4.5: Investigated frequencies and rounded wavelengths for S_0 mode resonators.	77
Table 4.6: Standard geometry constant parameters.	79
Table 4.7: Experimental plan for 50 MHz devices.	79
Table 4.8: Experimental plan for 100, 200, 550 and 800 MHz devices.	79
Table 4.9: Experimental plan for 400 MHz and 1 GHz devices.	80
Table 4.10: Lengths and widths of each element of the resistive network depicted in Fig. 4.39. For the estimation of the resistance of each component, the following geometry was investigated: $\lambda = 56 \mu\text{m}$, $L_{\text{route}} = 76 \mu\text{m}$, $L_{\text{pad}} = W_{\text{pad}} = 80 \mu\text{m}$, $L_a = W_a = g = L_b = 0.75\lambda$, $L_c = 13\lambda$, $N_p = 3$, $c = 0.3$, $t_m = 300 \text{ nm}$, and $\rho = 5.7e-8 \Omega \cdot \text{m}$	96
Table 4.11: Statistical characterization of devices operating at 400 MHz, with the geometry described in Table 4.6 and $L_c = 7 \lambda$	104
Table 4.12: Lithium Niobate thickness distribution from NGK.	106
Table 5.1: Multi-BVD fitting coefficients ($C_0 = 115.9 \text{ fF}$)	117
Table C.1: MATLAB [®] code for stress gradient extraction.	146

LIST OF FIGURES

Figure 1.1: (a) Historical growth of devices connected to the Internet. Recent analysis forecast 1 trillion devices connected by 2035 [NCTA]; (b) forecast of the mobile data consumption for the years 2016 – 2021. The CAGR (Compound Annual Aggregate Rate) is 47% [Cisco VNI Mobile Data Traffic Forecast]; (c) forecast of the increase in LTE bands for the years 2016 – 2021 [Akoustic Technologies, Inc.]; and (d) annual revenue (in billion dollars) of the RF filters market for the years 2015 - 2021. RF filters represent the largest and the fastest growing portion of the entire RFFE market [Mobility Experts 2016].....2

Figure 1.2: (a) Example of distributed network relying on wireless nodes: Unattended Ground Sensors for war-zone monitoring [3]; and (b) goal of the N-ZERO program: extend battery life of Unattended Ground Sensors from month to years [2]. The flattening of battery lifetime for low event activity in synchronous WuRx is due to the fixed energy consumption of the scheduled wake-up.3

Figure 1.3: Ultra-low-power Radio Survey 2005 – 2015 [4].....4

Figure 1.4: Typical architecture of an asynchronous WuRx in constitutive blocks (RFFE, mixing stage and baseband circuitry) and different options for its synthesis [5]. Ideally, active components are implemented only in the stage operating at baseband frequency to minimize power consumption.....5

Figure 1.5: Example of different piezoelectric MEMS resonators: (a) Scandium-doped Aluminum Nitride Film Bulk Acoustic Resonator (FBAR) fabricated at CMU Nanofab; (b) LiNbO₃ Surface Acoustic Wave (SAW) resonator developed for the acousto-optic gyroscope described in [12]; and (c) LiNbO₃ Laterally Vibrating Resonator (LVR) [13]..7

Figure 2.1: Block diagram of the RMR envisioned at CMU [18].11

Figure 2.2: Schematic representation of the RFFE of a WuRx implementing a matching network interfaced with the capacitive input of a mixing stage. The capacitor losses are represented by a parallel resistance to ground.12

Figure 2.3: Representation of a real inductor.....13

Figure 2.4: Representation of a matching network constituted by a transformer with a parallel inductor.14

Figure 2.5: (a) Butterworth-Van Dyke (BVD) model and its schematic representation; (b) admittance response of a 1-port resonator (blue), a capacitor (red), and 1-port resonator interfaced in series with a capacitor (yellow). The operating frequency shifts to higher frequency when the resonator is implemented as a matching network, and its motional resistance increases; and (c) operating frequency (f_{RF}) normalized over the natural frequency of a resonator (f_s) for different k_t^2 and C_{load}/C_0 ratios.....16

Figure 2.6: (a) Optimized ratio between the static capacitance and the load (α^{-1}) as a function of k_t^2 and Δ . Higher k_t^2 , f_s , Q_s , and C_{load} concur in decreasing the optimal static capacitance for a given load; and (b) pulling factor as a function of k_t^2 for different levels of Δ . k_p follows the same trend as α^{-1}18

Figure 2.7: BVD model of a 2-port resonator.....19

Figure 2.8: Representation of a matching network constituted by a transformer with a parallel resonator.....21

Figure 2.9: Optimal C_0 over C_{load} ratio as a function of the electromechanical coupling of the resonator.....22

Figure 2.10: Comparison between different matching networks architectures for a fixed $C_{load} = 1$ pF.....	23
Figure 2.11: (a) Equivalent electrical model of a MEMS demodulator; (b) SEM picture of a CMOS-MEMS demodulator fabricated with a $0.18 \mu\text{m}$ CMOS process [8]; and (c) schematic of the SCS resonator described in [27] and implemented in the RMR described in [5].....	25
Figure 2.12: (a) Equivalent model of a CMOS TIA. The static capacitance of a previous stage (C_s) is included; and (b) block diagram of the CMOS circuitry described in [5]. ...	27
Figure 2.13: Complete schematic of the RMR analyzed in this section.....	28
Figure 2.14: Simulated RMR sensitivity as a function of the resonator natural frequency (ω_s) and different demodulator frequencies (ω_r), for $C_0 = C_d = C_s = 500$ fF. The other RMR parameters are reported in Table 2.1.....	30
Figure 2.15: (a) Numerical optimization of the RMR sensitivity as a function of C_d and C_s ; and (b) simulated gain provided by the RF resonator to the input C_d of the demodulator. G is maximized for smaller C_d and is not affected by C_s . The optimal C_0 closely follows C_d as reported in Section 2.1.3.....	31
Figure 3.1: Laterally Vibrating Resonators made of different piezoelectric material: (a) X-cut Lithium Niobate LVRs. The edge reflectors are necessary to fully harness the maximum electromechanical coupling of the material; (b) Y-cut Lithium Niobate; and (c) 20% Scandium-doped Aluminum Nitride.....	34
Figure 3.2: Top view of the typical embodiment of a Laterally Vibrating Resonator (LVR). A bottom electrode under the resonator plate can be present or not according to the desired excitation method.....	35
Figure 3.3: (a) Thickness Field Excitation mode and equivalent electrical circuit representing the static capacitance (C_0) of the device. Such capacitance is effectively the series of the capacitances of each terminal; and (b) Lateral Field Excitation mode and equivalent electrical circuit representing the static capacitance. In this case, C_0 is given by the parallel capacitance between the IDEs pairs.....	37
Figure 3.4: TFE vs LFE capacitance per unit area for different piezoelectric materials. ...	40
Figure 3.5: (a) Voltage gain as a function of natural resonant frequency (f_s) for fixed load ($C_{load} = 1$ pF); (b) voltage gain as a function of the capacitive load for a fixed natural resonant frequency ($f_s = 50$ MHz); and (c) voltage gain as a function of the static capacitance (C_0) for fixed load ($C_{load} = 1$ pF) and frequency ($f_s = 50$ MHz), for different FoMs. Higher FoMs are desirable to reduce the optimal size of the resonators and to enhance the gain.....	41
Figure 3.6: Fabrication process of 1-port AlN LVRs: (1) Bottom electrode patterning via sputtering and lift-off; (2) AlN reactive sputtering; (3) AlN patterning via Cl-based RIE or ion milling; (4) top electrode patterning via sputtering and lift-off; and (5) XeF ₂ isotropic etching release.....	43
Figure 3.7: Microscope image of a 500 MHz 1-port AlN LVR.	44
Figure 3.8: (a) Admittance response of an in-band spurious-free 1-port LVR operating around 250 MHz. The reported k_t^2 is defined as $\pi^2/2 \cdot f_s/f_p \cdot \tan^{-1}(\pi/2 \cdot f_s/f_p)$; and (b) admittance response of a 1-port LVR exhibiting high Q_s and in-band spurious modes. As reported in Appendix B, in-band spurious can affect the measured k_t^2 . The k_t^2 reported in this figure was calculated after de-embedding the effect of the spurious mode.	45
Figure 3.9: (a) Microscope image of a 2-port 20% Sc-doped AlN resonator operating around 500 MHz. VIAs are added to ground the bottom electrode; and (b) SEM image of a 1-port resonator operating around 500 MHz.	47

Figure 3.10: (a) Detail of the sidewall angle of a 20% Sc-doped AlN LVR; (b) etch byproduct flakes hanging from the release trench; and (c) Failure of a 1-port LVR due to the elevate film stress gradient.....47

Figure 3.11: Admittance responses of a 20% Sc-doped AlN resonator operating (a) around 250 MHz; and (b) around 500 MHz.48

Figure 3.12: (a) EM coupling of TFE lateral mode (3-1) as a function of orientation for Y-cut Lithium Niobate. A global maximum exists at $\theta = 0^\circ$; and (b) relative dielectric constant in the vertical direction as a function of orientation. The global maximum for ϵ_r coincides with the k_t^2 maximum (cfr. Appendix D for details on matrix rotations).50

Figure 3.13: Fabrication process of 1-port Y-cut LVRs: (1) Sputtering of a uniform film of Pt on top of an HR Si wafer; (2) SAB of LN film on top of the Si substrate and film polishing and trimming; (3) LN patterning via ion milling; (4) reactive sputtering and patterning of AlN via wet etch; (5) top electrode patterning via sputtering and lift-off; and (6) XeF₂ isotropic etching release.....51

Figure 3.14: SEM image of a fabricated 1-port Y-cut LVR with zoom-in of the anchor, bus and finger-to-bus gap region. A 1 μm AlN patterned layer is deposited to reduce the parasitics introduced by the presence of an unpatterned bottom electrode.52

Figure 3.15: (a) Representation of the feedthrough parasitic capacitance (C_f) in a 1-port BVD model; and (b) contour plot of the equivalent dielectric relative constant ($\epsilon_{r,eq}$) of a stacking of Y-cut and AlN as a function of the material thicknesses (t_{LN} and t_{AlN} respectively).....53

Figure 3.16: Admittance responses of Y-cut LN resonator operating (a) around 200 MHz; and (b) around 400 MHz. De-embedding of C_0 , k_t^2 and Q_s is reported in Table 3.1.....54

Figure 3.17: (a) EM coupling of LFE lateral mode (1-1) as a function of orientation for X-cut Lithium Niobate. A global maximum exists at $\theta = 30^\circ$; (b) Relative dielectric constant in the lateral direction as a function of orientation. The global maximum for ϵ_r does not coincides with the k_t^2 maximum.55

Figure 3.18: Fabrication process of 1-port X-cut LVRs: (1) SAB of LN on HR Si and polishing; (2) LN patterning via ion milling; (3) top electrode patterning via sputtering and lift-off; and (4) XeF₂ isotropic etching release.56

Figure 4.1: Active area required by X-cut LVRs to match different capacitive loads assuming a parallel plate capacitor, $C_0 = C_{load}$, $c = 0.3$, $v_p = 5,800$ m/s, $t_{LN} = 2$ μm , $N_p = 1$, and $\epsilon_r = 40$60

Figure 4.2: COMSOL[®] models of LVRS operating around 100 MHz with an aperture of: (a) 3 λ ; and (b) 11 λ . PML boundaries are also pictured (outer frame).....63

Figure 4.3: COMSOL[®] simulated quality factors (Q_s) as a function of (a) aperture (L_e); and (b) Number of pairs (N_p).64

Figure 4.4: Zoom-in of resonance peaks of simulated X-cut LN LVRs for different values of aperture: (a) $L_e = 3$ λ ; (b) $L_e = 10$ λ ; and (c) $L_e = 11$ λ . Shorter plates exhibit more anchor losses (a) than slender plates (c).65

Figure 4.5: COMSOL[®] model (with reference system) of the standard resonator with PML boundary conditions. The resonator parameters are listed in Table 4.1.66

Figure 4.6: SEM pictures of: (a) individual X-cut LVRs. The depicted devices are part of the anchor variation test. Grounds were wire-bonded before measurements to provide a common reference to the VNA ports; and (b) a device constituted by 9 arrayed standard resonators. A large metal bus is implemented to connect the terminals of each device....67

Figure 4.7: (a) Detail of the anchor region of a resonator; and (b) angled SEM image picturing the edge of a resonator. The measured sidewall angle (φ) is greater than 80° . Devices fabricated via ion milling experience irregular patterning in the corner region due to sharp-tip effect. Lift-off residuals are also noticeable, but their impact on performance

was considered negligible given their small size with respect to the operating wavelength.67

Figure 4.8: Impact of different geometrical variables on the Q_s of fabricated 50 MHz devices: (a) aperture (L_e); (b) anchors width (W_a); and (c) finger-to-bus gap (g)..... 69

Figure 4.9: Impact of electrode coverage (c) of fabricated 50 MHz devices on: (a) quality factor (Q_s); (b) electromechanical coupling (k_t^2); and (c) Figure of Merit. 69

Figure 4.10: (a) Scatter plot of devices tested in air (blue dots) and under vacuum (red dots). Devices measured under vacuum showed a 20% increase in Q_s ; and (b) quality factor of a resonator with optimized geometry as a function of pressure. Maximum performance are attained in the sub-Torr range. 70

Figure 4.11: (a) Admittance response of the optimized X-cut LVR (measured in vacuum) showing the highest Figure of Merit recorded during the testing phase. COMSOL[®] simulation of the device under investigation is reported, showing good agreements between numerical prediction and experimental measurements. A feedthrough capacitance of 20 fF and a frequency shift of 0.2 MHz were added to consider the effects of non-idealities neglected by the FEA model; and (b) admittance response of X-cut LVRs with different g 71

Figure 4.12: (a) Quality factor as a function of temperature for different investigated devices; (b) AlSiCu Resistivity (ρ) as a function of temperature; and (c) resonant frequency as a function of temperature..... 72

Figure 4.13: SEM picture of tested X-cut LVRs failed during cryogenic tests due to stresses induced by thermal contraction. Note that in this set of devices, ground pads on opposite sides of the resonator were connected via wirebonds. 73

Figure 4.14: Wide-span admittance response of an optimized X-cut LVR measured under vacuum. Identified modes and resonant frequencies (f_s) are reported. Harmonics of the S_0 mode are present at multiple integers of the anti-resonance frequency of the main mode (f_p). 73

Figure 4.15: (a) Admittance response of an array constituted by 9 optimized parallel LVRs, measured in air; and (b) SEM image of identical standard resonators measured to characterize the statistical distribution of f_s , Q_s , k_t^2 and C_0 75

Figure 4.16: Impact of the number of elements recorded during the break-test on these measured quantities: (a) quality factor; (b) electromechanical coupling; and (c) static capacitance. 76

Figure 4.17: COMSOL[®] simulated admittance response capturing the impact of Al thickness (t_m) on the spurious modes at (a) around 200 MHz; and (b) around 1 GHz. The out-of-band mode showcased at around 1.2 GHz for $t_m = 300$ nm is a thickness mode and it is not caused by the metal thickness. 77

Figure 4.18: (a) Extended results of the COMSOL[®] investigation on the effect of Al thickness (t_m) on the severity of spurious modes. Red dots represent simulations showcasing severe spurious modes (as in Fig. 4.17); and (b) maximum theoretical k_t^2 as a function of frequency and metal thickness. t_m does not impact the maximum achievable electromechanical coupling. 78

Figure 4.19: Modified fabrication process for X-cut LVRs: (1) SAB substrate fabrication; (2) top electrode sputtering and patterning via RIE; (3) ion milling patterning; and (4) XeF₂ isotropic release. 80

Figure 4.20: Comparison between: (a) lithographically defined reflectors; and (b) self-aligned reflectors..... 82

Figure 4.21: SEM of fabricated X-cut LVRs operating around: (a) 100 MHz; (b) 200 MHz; (3) 400 MHz; and (4) 550 MHz. 83

Figure 4.22: Effect of fabrication process non-idealities on 200 MHz: (a) right reflector; (b) left reflector. The 200 nm misalignment between the etch mask and the top electrode mask is clearly visible. (c) Effects of fabrication non-idealities on a 1 GHz device. The etching of the right electrode caused low yield rate and failure on most of the devices.	83
Figure 4.23: (a) Measured electromechanical coupling (k_t^2) as a function of h/λ ratio; and (b) dispersion curve measured on X-cut LN (YZ 30°) LVRs.....	84
Figure 4.24: Scatterplots of the measured quality factors on devices operating at different frequencies.	85
Figure 4.25: Effect of the aperture (L_e) on Q_s for devices measured: (a) in air; (b) in vacuum.	85
Figure 4.26: Effect of the anchors width (W_a) on the quality factor measured in air for devices with an aperture of: (a) $L_e = 3 \lambda$; (b) $L_e = 7 \lambda$; and (c) $L_e = 11 \lambda$	86
Figure 4.27: Effect of the anchors width (W_a) on the quality factor measured in vacuum for devices with an aperture of: (a) $L_e = 3 \lambda$; (b) $L_e = 7 \lambda$; and (c) $L_e = 11 \lambda$	87
Figure 4.28: Effect of the fingers-to-bus gap (g) for resonator with a plate length (L) of 10λ on: (a) Q_s , measured in air; (b) Q_s , measured in vacuum; and (c) electromechanical coupling (k_t^2).	87
Figure 4.29: Effect of the fingers-to-bus gap (g) for resonator with a plate length (L) of 14λ on: (a) Q_s , measured in air; (b) Q_s , measured in vacuum; and (c) electromechanical coupling (k_t^2).	88
Figure 4.30: Effects of coverage (c) on X-cut LVRs operating around 400 MHz on: (a) Q_s ; and (b) k_t^2	89
Figure 4.31: Fabricated X-cut LVRs operating around: (a) 100 MHz; and (b) 200 MHz.	89
Figure 4.32: Fabricated X-cut LVRs operating around: (a) 400 MHz; and (b) 550 MHz.	90
Figure 4.33: Fabricated X-cut LVRs operating around: (a) 800 MHz; and (b) 1 GHz.	90
Figure 4.34: Quality factor of aperture variations measured at different temperatures for devices operating: (a) around 100 MHz; (b) around 200 MHz; and (c) around 400 MHz.	91
Figure 4.35: Quality factor of anchors variations (with fixed $L_e = 3 \lambda$) measured at different temperatures for devices operating: (a) around 100 MHz; (b) around 200 MHz; and (c) around 400 MHz.	91
Figure 4.36: Quality factor of anchors variations (with fixed $L_e = 7 \lambda$) measured at different temperatures for devices operating: (a) around 100 MHz; (b) around 200 MHz; and (c) around 400 MHz.	92
Figure 4.37: Admittance response of the resonator exhibiting the recorded highest Q_s at base temperature (10 K).	92
Figure 4.38: Extracted quality factor (Q_{air}) due to air damping.	93
Figure 4.39: Equivalent resistive network of a LFE LVR.	94
Figure 4.40: Equivalent resistive network of an array constituted by parallel LFE LVRs.	96
Figure 4.41: Quality factor measured in vacuum (Q_{vac}) and at base temperature ($Q_{10\text{K}}$), and unloaded quality factor (Q_u) for different apertures at: (a) 100 MHz; and (b) 200 MHz.	97
Figure 4.42: Quality factor measured in vacuum (Q_{vac}) and at base temperature ($Q_{10\text{K}}$), and unloaded quality factor (Q_u) for different apertures at: (a) 400 MHz; and (b) 550 MHz.	98
Figure 4.43: Quality factor as a function of anchor width (W_a) measured at base temperature (10 K) for different frequencies and values of aperture: (a) $L_e = 3 \lambda$; (b) $L_e = 7 \lambda$; (c) $L_e = 11 \lambda$	99
Figure 4.44: Admittance response of devices with different anchor width ($W_a = 0.25$ and 2λ) and an aperture of: (a) $L_e = 3 \lambda$; (b) $L_e = 7 \lambda$; and (c) $L_e = 11 \lambda$	99

Figure 4.45: Quality factor measured in vacuum (Q_{vac}) and at base temperature (Q_{10K}), and unloaded quality factor (Q_u) for different apertures and anchor width dimensions: (a) $W_a = 0.25 \lambda$; and (b) $W_a = 2 \lambda$	100
Figure 4.46: Monte Carlo simulations of an array of resonators generated from the randomly distributed parameters listed in Table 4.4 and recorded Q_{as} as a function of the number of elements.....	102
Figure 4.47: One-factor-at-time Monte Carlo simulations showing the impact of Q_s , k_t^2 , f_s , and C_0 variability on the Q_{sa} : (a) average quality factor (μ_{Qas}); and (b) standard deviation (σ_{Qas}).....	102
Figure 4.48: Modified Monte Carlo simulations of an array of resonators generated from the randomly distributed parameters listed in Table 4.4 and recorded Q_{as} as a function of the number of elements, including the effects of the interconnects.....	104
Figure 4.49: (a) Admittance responses of arrays of resonators operating around 400 MHz with different number of elements in parallel; and (b) zoom-in on the resonance peaks.....	105
Figure 4.50: Spilt surface fitting of the resonant frequencies extracted from COMSOL [®] simulations for devices operating: (a) around 50 MHz; and (b) around 400 MHz.....	105
Figure 4.51: Comparison between: (a) the spline surface fitting of the data reported in Table 4.12; and (b) the LN wafer used during the fabrication process.....	106
Figure 4.52: Simulated parabolic 3D distribution of sputtered metal thickness.....	107
Figure 4.53: Simulated resonant frequencies as a function of the number of tests for: (a) 50 MHz devices; and (b) 400 MHz devices.....	108
Figure 5.1: Modified model of the MEMS-based matching network described in Section 2.1.3 including parasitic resistances (R_p) and capacitances (C_p) to ground.....	110
Figure 5.2: Simplified model of the parasitics (R_p and C_p) between the signal (S) and ground (G) pads.....	112
Figure 5.3: ADS Momentum simulations of: (a) parasitics resistance to ground (R_p); and (b) parasitic capacitance to ground (C_p) as a function of frequency.....	112
Figure 5.4: Admittance response (measured in vacuum) of the resonator exhibiting the highest Figure of Merit (FoM) ever recorded for a devices in the VHF range.....	113
Figure 5.5: MATLAB [®] simulations of the expected gain as a function of the capacitive load (C_{load}) according to Y_{12} parameters (solid line) and BVD model fitting (dashed line). ...	114
Figure 5.6: Simulated gain as a function of different parasitic resistances to ground (R_p) for a load of: (a) 300 fF; (b) 700 fF; and (c) 1 pF.....	114
Figure 5.7: (a) Simulated gain for a C_{load} of 1 pF given as a function of the parameters reported in Fig. 4.16; and (b) relationship between the array quality factor (Q_{as}) and the number of elements.....	116
Figure 5.8: Multi-BVD model of a 1-port LVR. R_{ms} , L_{ms} , and C_{ms} represent the motional parameters of the spurious modes.....	117
Figure 5.9: (a) Simulated admittance response of 1-port LVR operating around 50 MHz considering only the main S_0 mode (blue) and including 7 in-band spurious modes (red); and (b) phases of the simulated resonators.	117
Figure 5.10: (a) Simulated admittance responses of a resonator without spurious modes (blue), with spurious modes (red), and after pulling in presence of spurious modes (orange) ; and (b) split peak due to the presence of an in-band spurious mode.	118
Figure 5.11: (a) Contour plot of the admittance of a resonator as a function of the anti-resonance frequency of a spurious mode ($f_s = 50$ MHz, $Q_s = 5,000$, $k_t^2 = 0.3$ and $C_0 = 70$ fF); and (b) analytical simulation of the frequency pulling.	121
Figure 5.12: Multi-BVD model in series with a load capacitance, as in the matching network described in Section 2.1.3.	121

Figure 5.13: (a) : (a) Contour plot of the admittance of a pulled resonator as a function of the anti-resonance frequency of a spurious mode ($f_s = 50$ MHz, $Q_s = 5,000$, $k_t^2 = 0.3$ and $C_0 = 70$ fF); and (b) analytical simulation of the frequency pulling. 123

Figure 5.14: (a) Magnitude of the voltage amplifications generated by the main mode peak (blue line) and spurious mode peak (red line) as a function of the frequency distance between modes; and (b) frequency pulling as a function of the frequency distance between a main and a spurious mode. 124

Figure 5.15: Magnitude of the voltage amplifications generated by the main mode peak and the spurious mode peak as a function of spurious mode quality factor (Q_{ss}). 125

Figure 5.16: Magnitude of the voltage amplifications generated by the main mode peak and the spurious mode peak as a function of spurious mode EM coupling (k_{ts}^2). 125

Figure 5.17: (a) Simulated gain implementing the spurious-free BVD model (blue line) and the Multi-BVD model (red line) reported in Fig. 5.9 for a load of 1 pF; and (b) ratio between the gain in presence of spurious (G_s) vs. spurious-free gain (G_{sf}). 126

Figure 5.18: Simulated gain for the models reported in Fig. 9 for two loads: (a) 100 fF; and (b) 1 pF. 127

Figure 5.19: (a) Schematic of the series-parallel (L-network) approach; and (b) L-network implementation in a matching network. 128

Figure 5.20: (a) L-network topology; and (b) admittance responses of the two resonators (blue and red line, overlapped), of the parallel resonator loaded by C_{load} of 1 pF (orange), and of the L-network response 130

Figure 5.21: Contour plot of the simulated gain as a function of the static capacitance of R1 (C_{01}) and R2 (C_{02}). 133

Figure 5.22: (a) Voltage gain as a function of the static capacitance for $C_{01} = C_{02}$ (blue line), representing a L-network implementing two identical resonators, and for $C_{02} = 0$ (red line), which represents a series approach; and (b) maximum gain as a frequency mismatch between R1 and R2; and (c) zoom-in of the central region of Fig. 5.22b. 134

Figure 5.23: Admittance responses of the resonators implemented in the L-network simulations. 135

Figure 5.24: Simulated gains based on Y_{12} data (solid line) and BVD fitting (dashed line) for the L-network configuration and the series configuration implementing the devices reported in Fig. 5.23. Discrepancies in the pulled frequencies between the series and the L-network approach are due to uncertainty in the BVD fitted parameters. 135

Figure B.1: (a) Multi-BVD model of a 1-port LVR. R_{ms} , L_{ms} , and C_{ms} represent the motional parameters of the spurious modes; and (b) multi-BVD model interfaced in series with a capacitive load. 143

Figure C.1: Measured beam deflection and cropped beam. 145

Figure E.1: Geometrical model for the overetch calculation. 155

CHAPTER 1: INTRODUCTION

The long-envisioned dream of an hyperconnected world, where an increasing quantity of information is available in real-time, is becoming a reality. The extension of the Internet connectivity to the Internet of Things (IoT) is a natural evolution towards a more advanced capability of remotely monitoring and controlling the environment through physical devices and everyday objects [1][2].

The number of devices connected to the Internet already grew from 1 million devices in 1992 to 42 billion in 2019 (Fig. 1.1a), with forecasts of 1 trillion devices connected by 2035. This exponential growth is largely motivated by the diffusion of smartphones in the 2000s and, more recently, by the development of IoT applications, such as wireless networks of sensors in consumer electronics. The larger number of connected devices comes with the necessity of higher data rate communication links. The global mobile data traffic increased from 7 to 24 exabytes per month between 2016 and 2019 and is expected to grow by 47% annually for the upcoming years (Fig. 1.1b). This growth directly translates into the demand of a higher number of LTE and 5G bands (Fig. 1.1c), and the need for more complex Radio Frequency Front-End (RFFE) modules in phones. For this reason, the demand for RF filters kept increasing over the past few years, and it is expected to further grow in the future (Fig. 1.1d). Ultimately, 5G and IoT emerging applications are driving the research on novel RFFE architectures and electronic components. For example, tunable and reconfigurable filters operating above few GHz would be a desirable solution to synthesize compact RFFE modules for mobile communications and allow faster data transfer. Research is currently active in identifying and developing the key hardware technologies for this purpose.

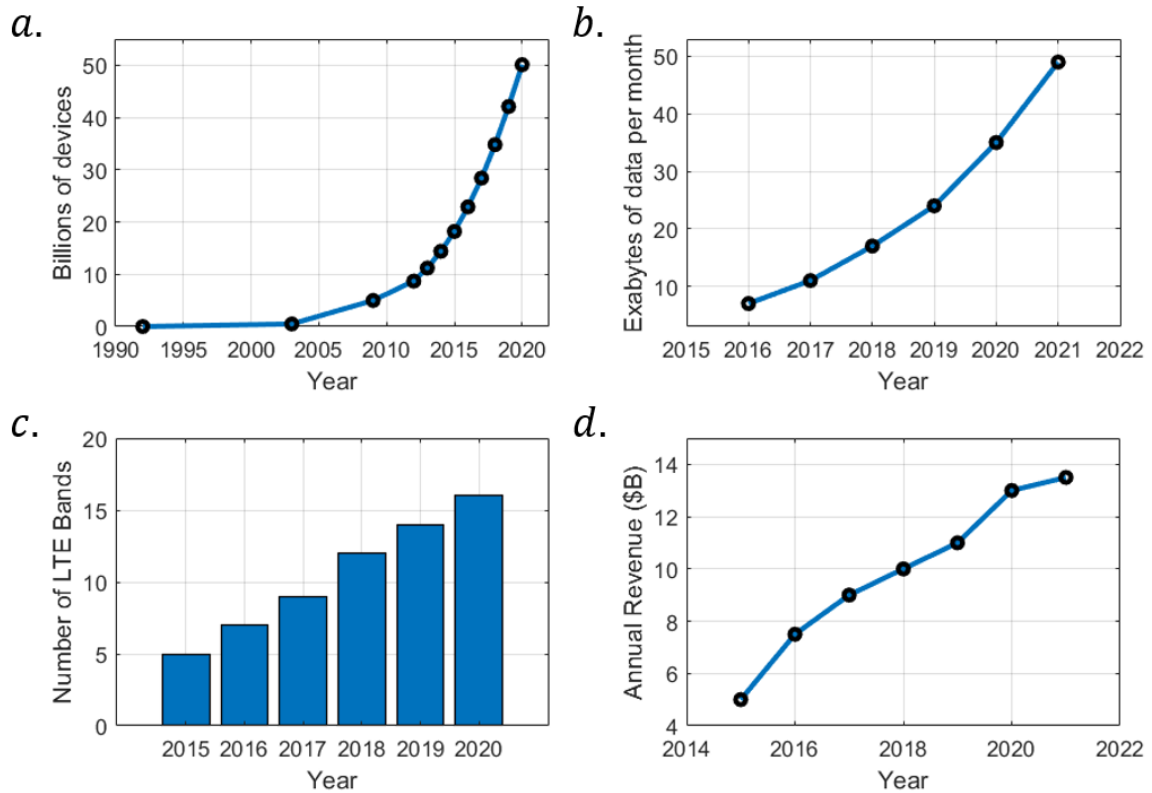


Figure 1.1: (a) Historical growth of devices connected to the Internet. Recent analysis forecast 1 trillion devices connected by 2035 [NCTA]; (b) forecast of the mobile data consumption for the years 2016 – 2021. The CAGR (Compound Annual Aggregate Rate) is 47% [Cisco VNI Mobile Data Traffic Forecast]; (c) forecast of the increase in LTE bands for the years 2016 – 2021 [Akoustic Technologies, Inc.]; and (d) annual revenue (in billion dollars) of the RF filters market for the years 2015 - 2021. RF filters represent the largest and the fastest growing portion of the entire RFFE market [Mobility Experts 2016].

1.1. The N-ZERO Project Challenge

Ultra-low-power (ULP) and high sensitivity receivers are another example of extremely interesting solutions for applications relying on large distributed networks of wireless nodes [3], such as Unattended Ground Sensors (UGS) for military infrastructure monitoring and border protection in active war zones (Fig. 1.2a). Often these sensors are deployed to monitor infrequent but critical event (~tens per day), with no previous knowledge of the event occurrence. The need for continuous, event-driven sensing poses serious challenges in terms of UGS battery lifetime.

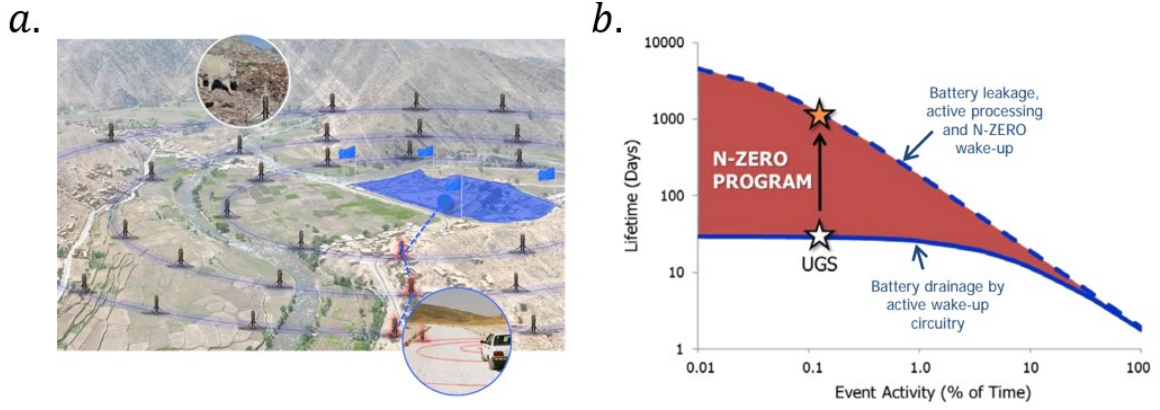


Figure 1.2: (a) Example of distributed network relying on wireless nodes: Unattended Ground Sensors for war-zone monitoring [3]; and (b) goal of the N-ZERO program: extend battery life of Unattended Ground Sensors from month to years [2]. The flattening of battery lifetime for low event activity in synchronous WuRx is due to the fixed energy consumption of the scheduled wake-up.

In fact, state-of-the-art synchronous receivers show a limited efficiency due to the high power consumption of the wake-up circuitry compared to the sensor total power consumption if the event activity is lower than 10% of the total time (Fig. 1.2b). A simple model to estimate the lifetime of a battery is reported in [2] (Eq. 1.1). For a fixed battery capacity (Q_{bat}), the lifetime of the battery (T_{bat}) is a function of the event activity (N), the active time (t_{on}) and the current consumption in the active and sleep states (I_{active} and I_{sleep} respectively), plus the self-discharge rate of the battery ($I_{leakage}$). If N tends to zero, the battery duration is substantially limited by power consumption of the wake-up circuitry in the sleep state.

$$T_{bat} = \frac{Q_{bat}}{N t_{on} I_{active} + (1 - N t_{on}) I_{sleep} + I_{leakage}} \quad (1.1)$$

Despite the development of more efficient scheduling algorithms, the continuous sensing and processing of irrelevant data limits the duration of UGS batteries. Furthermore, the replacement of these nodes is often impractical and directly translates to larger maintenance costs that undermine the feasibility of military missions relying on them.

These considerations fostered the interest on novel sensors and receivers architectures capable of performing continuous, event-driven sensing with near zero power consumption (N-ZERO project) [3]. The goal of the N-ZERO project is to exploit the energy contained in the RF trigger signature itself to detect the event of interest while maintaining a low false alarm rate (FAR).

1.2. Wake-Up Radio Receivers (WuRx)

Always-on, asynchronous Wake-Up Radio Receivers (WuRx) attaining high sensitivity (-100 dBm) and ultra-low-power consumption (~tens of nW, comparable to the self-discharge rate of a battery) are an attractive technology to extend battery-life by several orders of magnitude (Fig. 1.2b). When an incoming RF signature is detected, the WuRx triggers the sensing electronics, which performs the measurement only when required.

In spite of investigations into ULP radios for the last two decades, all pre-2016 demonstrations showed a clear trade-off between power consumption and sensitivity (~1 decade in power for 20 dB of sensitivity, Fig. 1.3).

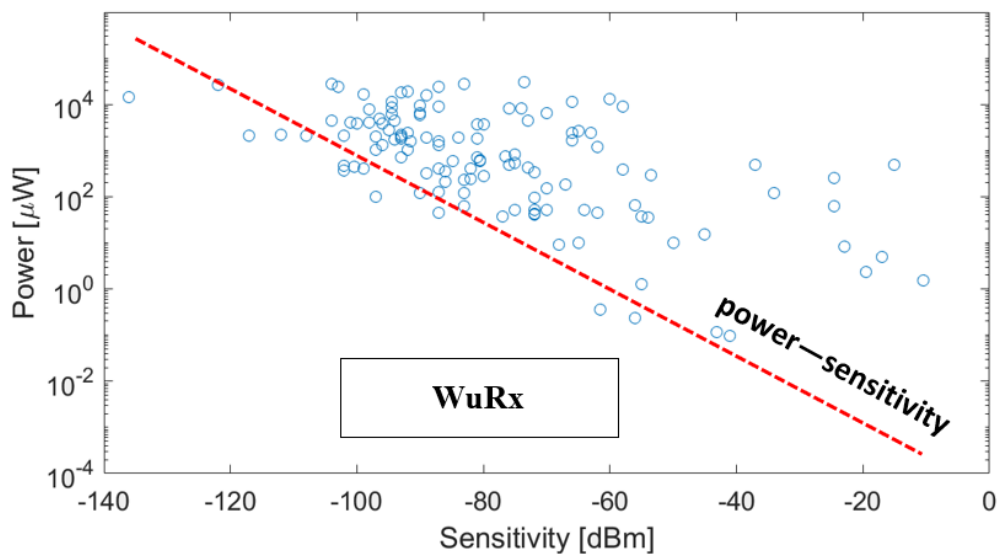


Figure 1.3: Ultra-low-power Radio Survey 2005 – 2015 [4].

In the last few years, novel RF WuRx architecture operating between hundreds of MHz and few GHz have been proposed to break this paradigm. The strict available power budget lead to a converge in WuRx topologies, which often consist in an RF Matching Network (MN), a mixing stage (such as an envelope detector or a demodulator) and a Baseband (BB) Amplifier. Fig. 1.4 reports different options for each building block constituting a typical ULP asynchronous WuRx [5][6].

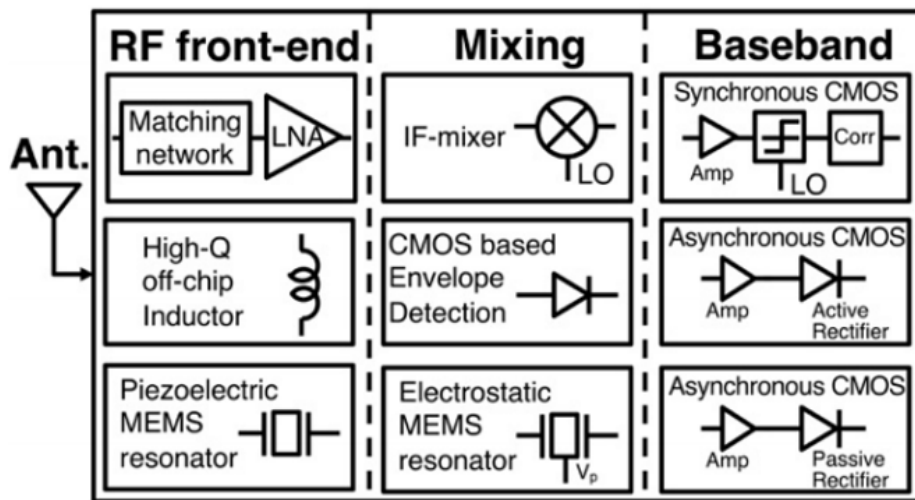


Figure 1.4: Typical architecture of an asynchronous WuRx in constitutive blocks (RFFE, mixing stage and baseband circuitry) and different options for its synthesis [5]. Ideally, active components are implemented only in the stage operating at baseband frequency to minimize power consumption.

The ability to continuously screen the RF spectrum with near zero power consumption heavily relies on the optimization of the active components (ideally a sole BB amplifier operating in subthreshold regime) and passive voltage amplification techniques in the RF Front-End (RFFE). For this reason, active stages such as RF Low Noise Amplifier (LNA) are generally not implemented due to their large power consumption ($\sim\mu\text{W}$). As far as the RFFE is concerned, existing approaches rely on different types of passive matching network, including transformers, LC tanks, and piezoelectric MEMS resonators, which interface the $50\ \Omega$ source resistance of the antenna with the input impedance of the mixing stage. This input impedance is usually a complex

value, represented by a large resistor to ground in parallel with a capacitor. If the inductive component of the MN is properly selected, it is possible to resonate out this capacitance, cancelling it over a narrow frequency range while providing passive voltage amplification (or gain, G) of the RF signature. Both the operating 3dB-bandwidth and the gain presented to the input of the ED are ultimately determined by the loaded quality factor (Q) of the matching network.

For the mixing stage, several solutions have been investigated to perform the down-conversion of the signal from RF to baseband. The most common ones involve an Intermediate Frequency (IF) mixer [2], a CMOS-based Envelope Detector (ED) [7] or an electrostatic MEMS demodulator [8] (Fig. 1.4). IF mixers are widely implemented in RF systems, but the large power consumption associated with the presence of a Local Oscillator (LO) makes their implementation in ULP WuRx impractical. The near-zero power consumption of CMOS-based Envelope Detector (ED) and electrostatic MEMS demodulator makes those solution more feasible for the synthesis of ultra-low-power WuRx [2][5].

Ultimately, the signal detection can be performed by means of baseband correlator [9], comparators [10], active or passive rectifiers [5], or switches [11]. If not passive, all the components operating at baseband must operate in deep subthreshold regime to minimize power consumption.

1.3. MEMS Resonators as Matching Networks

Micromechanical (MEM) piezoelectric acoustic resonators are an appealing solution for impedance matching networks due to their wide range of operation (tens of MHz to few GHz), high quality factor at resonance (Q_s), compact footprint and low motional resistance (R_m). Surface Acoustic Wave (SAW) and Bulk Acoustic Wave (BAW) resonators have already proven to be key

building blocks for a wide range of electronic components, especially in RF filtering applications. The performance of these components can be exploited in different MN by operating them as inductors close to their resonance (f_s) or anti-resonance frequency (f_p). This will allow the replacement of large, low Q , discrete inductors and will provide larger signal voltage boost, leading to higher sensitivity and low power consumption. Despite the availability of successful commercial products, including Aluminum Nitride (AlN) Film Bulk Acoustic Resonators (FBARs), WuRx are driving the demand for devices with improved performance beyond the current state-of-the-art MEMS resonators .

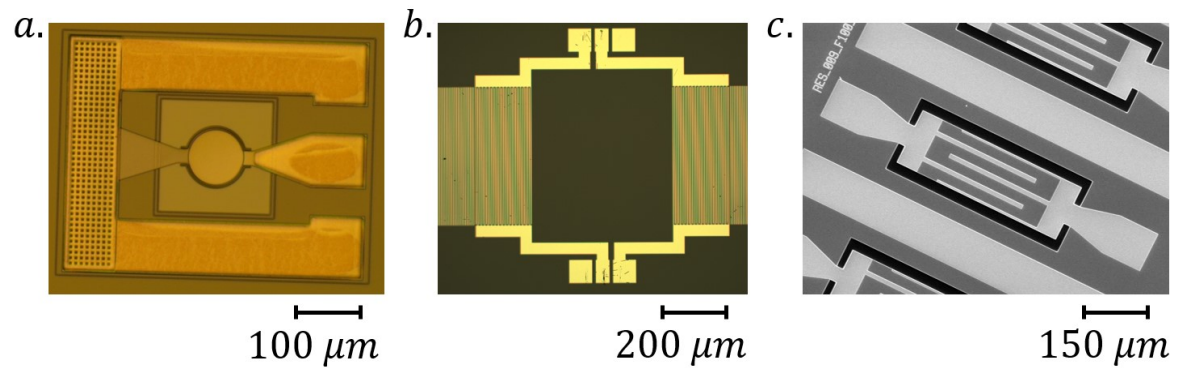


Figure 1.5: Example of different piezoelectric MEMS resonators: (a) Scandium-doped Aluminum Nitride Film Bulk Acoustic Resonator (FBAR) fabricated at CMU Nanofab; (b) LiNbO₃ Surface Acoustic Wave (SAW) resonator developed for the acousto-optic gyroscope described in [12]; and (c) LiNbO₃ Laterally Vibrating Resonator (LVR) [13].

At the resonator level, this performance is controlled by three parameters: the quality factor (Q_s), the electromechanical coupling (k_t^2), and the static capacitance (C_0). The quality factor represents the level of energy dissipation of the system and directly impacts the Insertion Losses (IL) and the bandwidth of the system (BW) in narrow band applications. The electromechanical coupling represents the capability of converting energy from the mechanical to the electrical domain and sets the bandwidth in filtering applications. The static capacitance defines the energy stored in the electrical domain and must be chosen according to the frequency of operation and the load characteristics for proper impedance matching. The product of the quality factor (Q_s) and the

electromechanical coupling (k_t^2) defines the Figure of Merit (FoM), one of the most widely used metrics to define the performance of piezoelectric MEMS resonator.

As highlighted in [14][15], WuRx employing MEMS resonators in the RFFE require resonators capable of simultaneously exhibiting high quality factor and high electromechanical coupling or, overall, large Figure of Merit. The FoM contributes, with the frequency of operation and the static capacitance, in determining the motional resistance (R_m) of the device, and ultimately the losses introduced when implementing MEMS-based matching networks. Since C_0 is usually selected to match the value of the capacitive input of the mixing stage, and the frequency is determined by the spectrum availability, the Figure of Merit is, with the MN architecture, the only lever available to decrease R_m and increase the passive voltage boost.

1.4. Thesis Outline

The dissertation is organized in the following chapters. In Chapter 2, the architecture of an asynchronous Ultra-low-power (ULP) Resonant Micromechanical Receiver (RMR) is described stage by stage and a first analytical description is provided for each block. Then, different matching networks based on discrete components and piezoelectric MEMS resonators are compared in terms of performance to identify the most suitable topology for the RMR. Ultimately, a numerical optimization of the RMR sensitivity is described to identify the key design parameters and the optimal operating point of each block of the WuRx.

In Chapter 3, piezoelectric MEMS Laterally Vibrating Resonators (LVRs) are introduced as elements to synthesize an RF matching network. The operating principles, the equivalent electrical model and the modeling of their static capacitance and series resistance are briefly described, such

as the impact of key parameters as Q_s , k_t^2 and C_0 on the voltage gain provided for a capacitive load representing the input impedance of an envelope detector. Different LVRs technologies are then compared in terms of Figure of Merit and fabrication process, with a focus on novel materials, such as Scandium-doped Aluminum Nitride alloys and Lithium Niobate crystalline cuts.

In Chapter 4, the design and performance of X-cut Lithium Niobate LVRs are investigated. Finite Elements Analysis is used to model the response of devices in the frequency range between 50 MHz and 550 MHz and define an experimental plan. Then, the response of fabricated devices is characterized and the impact of their geometry on Q_s , k_t^2 , and C_0 investigated. Vacuum and cryogenic measurements are presented, and the main sources of losses identified by comparing experimental results and theoretical models. The performance of arrays of optimized resonators to match to large input load capacitances are investigated, and the losses introduced by frequency mismatch between elements characterized.

In Chapter 5, direct measurements of the voltage gain provided by a matching network based on 1-port X-cut LVRs are presented and the impact of non-idealities (such as spurious modes) on the gain is discussed. Alternative topologies based on more compact resonators are introduced and tested.

In Chapter 6, the entire body of the Ph.D. work is summarized, and some future research directions are presented.

CHAPTER 2: RESONANT MICROMECHANICAL RECEIVER (RMR)

Ultra-low-power (ULP) wake-up radio receivers (WuRx) are a desirable solution to extend the battery lifetime of wireless sensors deployed in large, unattended networks, in order to reduce the maintenance costs of such infrastructure. WuRx are usually composed by three basic building blocks: RF front-end (RFFE), mixing and baseband.

Several approaches have been recently demonstrated [6][7][16][17], implementing various solutions for each of the main building blocks. Due to the strict available power budget (~ 10 nW), the only approach to simultaneously attain high sensitivity (-100 dBm) while minimizing power consumption is to reduce the implementation of active stages in favour of passive solutions.

An interesting approach is the asynchronous Resonant Microelectromechanical Receiver (RMR) developed at Carnegie Mellon University and extensively described in [5]. The system relies on resonant micro-electromechanical systems: the RFFE is implemented with a piezoelectric MEMS resonator, which provides for passive voltage amplification, impedance matching and aggressive filtering, while the mixing stage is realized with an electrostatically actuated MEMS demodulator. This approach allows exploiting the passive voltage boost provided by the piezoelectric MEMS and the non-linearity introduced by the electrostatic MEMS for the demodulation utilizing the energy contained in the RF signature itself. The only active stage contemplated in the RMR architecture is the baseband circuitry, which could be either a voltage amplifier or a transimpedance amplifier

(TIA). To keep the power consumption in the order of few nW, the CMOS circuitry is designed to operate in the subthreshold regime.

The carrier frequency (ω_c) is set to match the resonant operating frequency of the piezoelectric resonator (ω_{RF}), and is selected in the range between 50 MHz and 1 GHz. This range of frequency is of particular interest due to the availability of bands in the spectrum, and as a trade-off between performance and antenna dimensions. The baseband frequency (ω_m) is selected to match the resonant frequency of the demodulator (ω_r), which is usually set in the tens of kHz range as a trade-off between device footprint, performance and CMOS efficiency.

A schematic of the RMR is reported in Fig. 2.1. In this chapter, the main blocks will be analyzed and their mathematical model described to identify the main design parameters to attain ULP WuRx exhibiting a desired sensitivity of -100 dBm for a given power budget of 10 nW.

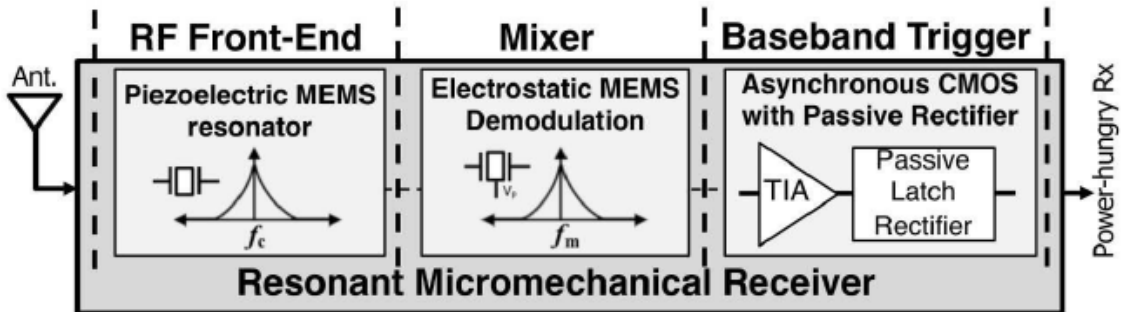


Figure 2.1: Block diagram of the RMR envisioned at CMU [18].

2.1. Matching Network (MN)

Matching Networks (MN) are a fundamental stage in each WuRx topology. Their main goal is to interface the impedance of the antenna (usually 50Ω) with the high input impedance of the mixing stage, which is often constituted by a capacitor in parallel with a large resistor (Fig. 2.2). The most important metrics to define the efficiency of a passive MN are the gain provided to the

input of the following stage, their loaded quality factor (Q) and their footprint, which becomes particularly relevant for applications such as small, easily deployable wireless nodes.

One of the most interesting features of passive matching networks is the capability of providing voltage boost to the input signal with no power consumption. This amplification is possible either by implementing a resonant circuit or through a transformer.

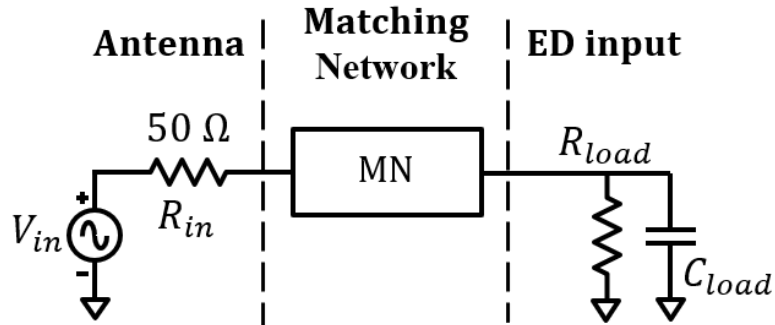


Figure 2.2: Schematic representation of the RFFE of a WuRx implementing a matching network interfaced with the capacitive input of a mixing stage. The capacitor losses are represented by a parallel resistance to ground.

In the first case, an inductive element is interfaced with a load capacitor to cancel its reactance over a narrow range of frequency, which is ultimately defined by the Q of the matching network. Over this bandwidth, the input impedance seen by the voltage source (*i.e.*, the RF signature) is minimized and mostly real, allowing a large current to flow across the MN and the load. Under these operating conditions, the reactive components of the system store and release energy at the same pace, building up a large peak voltage which can be sensed by a following stage [6]. The maximum attainable gain, and thus the signal boost, is given by the ratio of the input impedance of the mixing stage over the impedance seen by the voltage source at resonance.

In the second case, a transformer is introduced between the antenna and the input of the mixing stage to decrease the input impedance seen by the primary and increase the voltage at the secondary [6]. The voltage gain is, in this case, a function of the turn ratio (N) of the transformer and of the

ratio between the squared root of the output and input impedances, which defines the maximum attainable gain.

As mentioned before, the quality factor of the matching networks plays an important role in defining the maximum achievable gain, since it directly affects the resistance witnessed at resonance by the RF signature, but also impacts the 3-dB bandwidth of the system. For this reason, Q must be selected accordingly to the desired modulation speed [18].

In this section, several matching network topologies will be compared in terms of passive voltage amplification, loaded Q and footprint to identify the most suitable solution for the RMR under investigation.

2.1.1. Series Inductor (LC Tank)

The simplest matching network [6] is the LC tank and it is constituted by an inductor (L) in series with the input capacitive load of the ED (Fig. 2.3).



Figure 2.3: Representation of a real inductor.

The inductor must be properly sized according to the load capacitance (C_{load}) and the frequency of operation (ω) as captured by Eq. 2.1. Since the inductor has a limited quality factor (Q_i), it is necessary to define the associated losses (R_L , Eq. 2.2). The maximum achievable gain is thus given by the ratio between the impedance of the load and the impedance seen at resonance, which is the sum of R_{in} and R_L .

$$L = \frac{1}{\omega^2 C_{load}} \quad (2.1)$$

$$R_L = \frac{\omega L}{Q_L} = \frac{1}{\omega C_{load} Q_L} \quad (2.2)$$

$$G = \left| \frac{1}{\omega C_{load} (R_{in} + R_L)} \right| \quad (2.3)$$

The main limitations of this approach are the low quality factor of discrete inductors, usually lower than 100 [19], and their footprint.

2.1.2. Transformer with Parallel Inductor

Another approach successfully implemented in [20] synthesizes a matching network by interfacing the input impedance of the mixing stage with a parallel inductor (L) at the secondary of a transformer (Fig. 2.4). A parallel resistor (R_p) represents the losses introduced by the inductor, similarly to R_L described in Section 2.1.1.

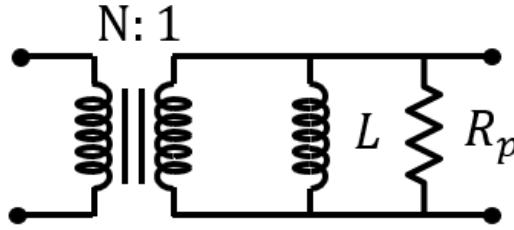


Figure 2.4: Representation of a matching network constituted by a transformer with a parallel inductor.

The transformer turn ratio (N , Eq. 2.4), is defined as the ratio between the windings at the primary (N_1) and the windings at the secondary (N_2). As reported in [21], the gain is maximized when R_p' (R_p seen at the primary) is equal to the impedance of the source ($R_{in} = 50 \Omega$), as reported by Eq. 2.5. This relationship is fundamental to define the turn ratio of the transformer when sizing

the system. Voltages at the secondary can be expressed according to Eq. 2.6, and the maximum achievable gain by Eq. 2.7.

$$N = \frac{N_1}{N_2} = \frac{V_1}{V_2} = \frac{I_2}{I_1} \quad (2.4)$$

$$R'_p = R_p N^2 = R_{in} = 50 \Omega \quad (2.5)$$

$$V_2 = \frac{V_1}{N} = V_{in} \frac{R_p N^2}{R_{in} + R_p N^2} \frac{1}{N} = \frac{V_{in}}{2} \sqrt{\frac{R_p}{R_{in}}} \quad (2.6)$$

$$G = \frac{V_2}{V_{in}} = \frac{1}{2} \sqrt{\frac{R_p}{R_{in}}} \quad (2.7)$$

This solution suffers of the same limitations of the LC tank. It is worth noticing that it is not necessary to resonate out the input capacitance of the mixing stage to attain passive voltage gain, especially if its impedance is much larger than R_{load} . In this case, the same analysis is valid assuming R_p equal to R_{load} .

2.1.3. 1-port MEMS Series Resonator

The typical behavior of a 1-port piezoelectric MEMS resonator is captured by the equivalent Butterworth-Van Dyke (BVD) electrical model (Fig. 2.5a). C_0 represents the static capacitance of the device, while R_m , C_m , and L_m respectively the motional resistance, capacitance and inductance [22]. The motional parameters are function of various combinations of 4 parameters (Eq. 2.8 – 2.10): C_0 , the electromechanical coupling coefficient (k_t^2), the quality factor at resonance (Q_s), and the resonant frequency ($\omega_s = 2\pi f_s$). Different definitions can be adopted to define the k_t^2 [23], and will be clearly stated throughout the dissertation.

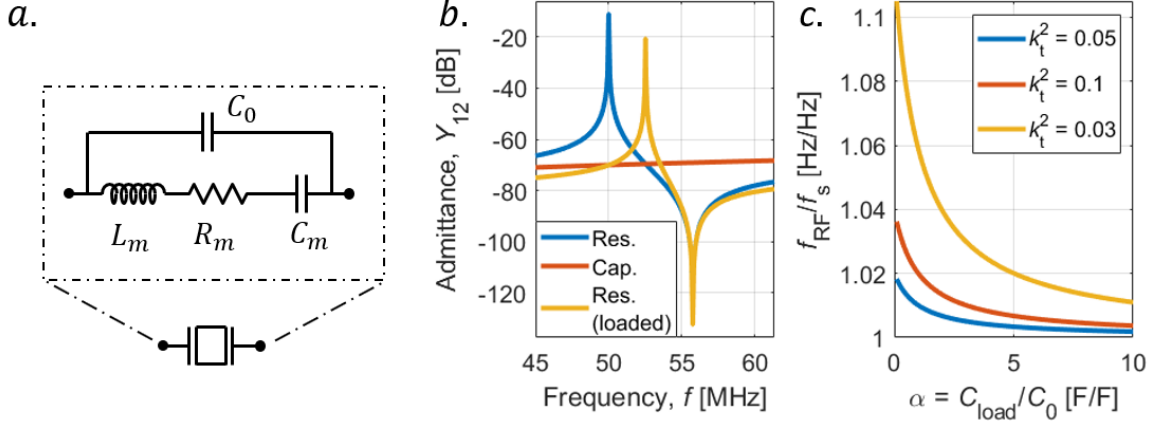


Figure 2.5: (a) Butterworth-Van Dyke (BVD) model and its schematic representation; (b) admittance response of a 1-port resonator (blue), a capacitor (red), and 1-port resonator interfaced in series with a capacitor (yellow). The operating frequency shifts to higher frequency when the resonator is implemented as a matching network, and its motional resistance increases; and (c) operating frequency (f_{RF}) normalized over the natural frequency of a resonator (f_s) for different k_t^2 and C_{load}/C_0 ratios.

$$R_m = \frac{\pi^2}{8} \frac{1}{k_t^2 C_0 Q_s \omega_s} \quad (2.8)$$

$$L_m = \frac{\pi^2}{8} \frac{1}{k_t^2 C_0 \omega_s^2} \quad (2.9)$$

$$C_m = \frac{8}{\pi^2} k_t^2 C_0 \quad (2.10)$$

$$Y = \frac{1}{Z_R} = j\omega C_0 + \frac{1}{R_m + j\omega L_m + \frac{1}{j\omega C_m}} \quad (2.11)$$

An example of admittance response of a 1-port resonator (Eq. 2.11) is reported in Fig. 2.5b. The characteristic response presents a series resonance (f_s) and an anti-resonance frequency (f_p) due to the presence of C_0 in parallel with the motional branch.

The simplest approach to synthesize a matching network with a piezoelectric MEMS resonator is to interface it in series with a capacitive load, as reported in Fig. 2.2. In this configuration the device operates as a high- Q inductor effectively cancelling out the imaginary impedance of the load (assuming $R_{load} \gg (\omega C_{load})^{-1}$). This allow a large current to flow in the motional branch to build up a large voltage across the load, which can be sensed by the mixing stage input. As highlighted in

Fig. 2.5b, the frequency of operation ($\omega_{RF} = 2\pi f_{RF}$) differs from the natural frequency of the resonator. The quality factor of the resonator is usually function of frequency [24], thus the Q measured at ω_{RF} could be different from Q_s . For simplicity, in the present dissertation the quality factor is assumed constant.

The pulling of the operating frequency is due to the need of the imaginary part of the resonator impedance (Z_R) to exactly match the value of the complex impedance of the load (Z_{load}). At ω_{RF} (Eq. 2.12), the passive voltage gain provided to the input load is a function of the impedance ratio between Z_{load} and the resistance of the antenna ($R_{in} = 50 \Omega$) plus the losses introduced by the resonator operating at ω_{RF} (Eq. 2.13). Such losses are a function of R_m , modulated by a pulling factor (k_p) greater than 1 and dependent on both C_0 and C_{load} (Eq. 2.14).

$$\omega_{RF} = \omega_s \sqrt{\frac{C_0 + C_{load} + C_m}{C_0 + C_{load}}} \quad (2.12)$$

$$G = \frac{Z_{load}}{R_{in} + Z_R + Z_{load}} = \left| \frac{1}{\omega_{RF} C_{load} (R_{in} + \text{Re}\{Z_R\})} \right| \quad (2.13)$$

$$\text{Re}\{Z_R\} = k_p R_m = \left(\frac{C_{load} + C_0}{C_{load}} \right)^2 R_m \quad (2.14)$$

Assuming constant C_{load} , Q_s , k_r^2 , and ω_s , the maximum achievable gain is merely a function of the static capacitance C_0 , which must be carefully selected to maximize the voltage boost [25]. It is possible to find an analytical solution to the problem by deriving Eq. 2.13 in respect to C_0 (Eq. 2.15). Eq. 2.15 allows a single global maximum which can be found by numerically solving the quadratic Eq. 2.16, where α represents the ratio between the capacitive load and the static capacitance (Eq. 2.17), K^2 the piezoelectric coupling (Eq. 2.18) [26][23], and Δ the ratio between the quality factor of the resonator and the equivalent quality factor of C_{load} evaluated at ω_s , including the losses deriving from the presence of R_{in} (Eq. 2.19).

$$\max G = \min \frac{1}{G} \rightarrow \frac{d}{dC_0} \left[\frac{1}{j\omega_{RF}(R_{in} + k_p R_m)} \right] = 0 \quad (2.15)$$

$$\alpha^4 + \alpha^3(2 + K^2) + \frac{\alpha^2}{2}(K^2 - \Delta K^4) - 2\alpha(1 + K^2) - (3 + K^2) = 0 \quad (2.16)$$

$$\alpha = \frac{C_{load}}{C_0} \quad (2.17)$$

$$K^2 = \frac{8}{\pi^2} k_t^2 \quad (2.18)$$

$$\Delta = C_{load} R_{in} Q_s \omega_s = \frac{Q_s}{Q_c |_{\omega=\omega_s}} \quad (2.19)$$

Fig. 2.6 reports the value of the optimal values of α^{-1} and the pulling factor (k_p) for different values of k_t^2 and Δ . For typical values of a high-performance X-cut Lithium Niobate resonator [13], $\alpha = 1.35$, $C_{0,opt} = 0.75 \cdot C_{load}$, and $k_p = 3$. Interestingly, when k_t^2 tends to 0, and consequently K^2 , Eq. 2.16 can be solved analytically. The solution is $\alpha = 1$, $C_{0,opt} = C_{load}$, and $k_p = 4$, meaning that in case of resonators exhibiting low k_t^2 , the gain is maximized when the static capacitance perfectly matches the load, and that the motional resistance at ω_{RF} becomes larger by a factor of 4.

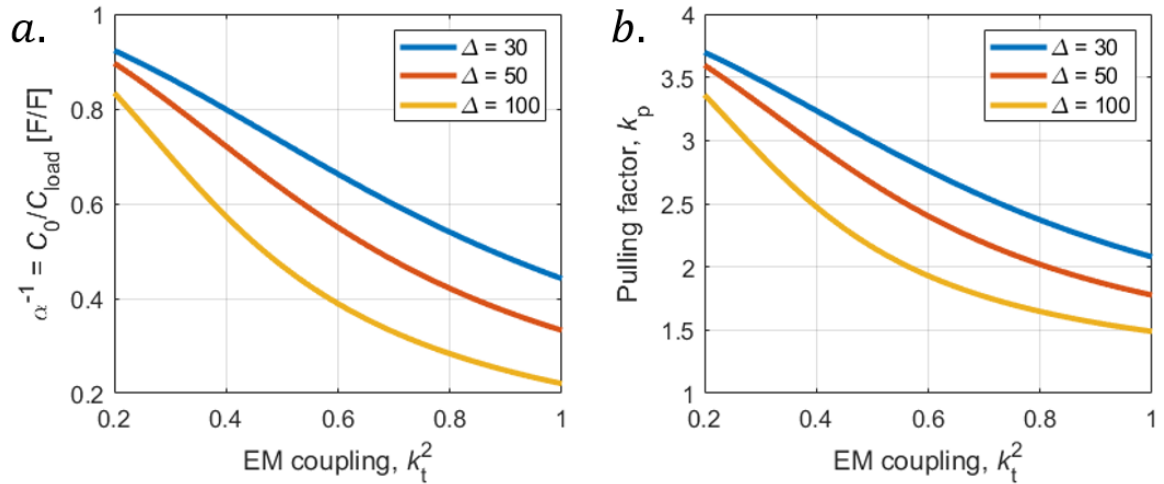


Figure 2.6: (a) Optimized ratio between the static capacitance and the load (α^{-1}) as a function of k_t^2 and Δ . Higher k_t^2 , f_s , Q_s , and C_{load} concur in decreasing the optimal static capacitance for a given load; and (b) pulling factor as a function of k_t^2 for different levels of Δ . k_p follows the same trend as α^{-1} .

The main advantages of this solution over the ones introduced in Section 2.1.1 and 2.1.2 are the more compact footprint, which allows for a reduction of the area occupied by the MN, and larger Q if high-performance MEMS resonators are employed.

2.1.4. 2-port MEMS Resonator

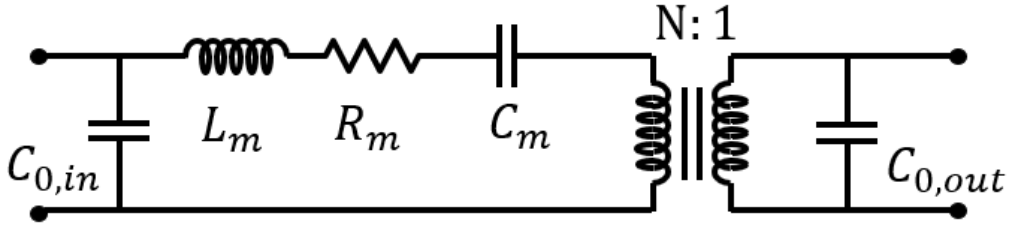


Figure 2.7: BVD model of a 2-port resonator.

The behavior of a 2-port MEMS resonator is captured by the Butterworth-Van Dyke (BVD) model reported in Fig. 2.7. Similarly to 1-port BVD model, R_m , L_m and C_m represents the motional resistance, inductance and capacitance, while $C_{0,in}$ and $C_{0,out}$ respectively the capacitances of the input and output ports. In the 2-port case, the motional parameters (Eq. 2.20 – 2.22) are both function of $C_{0,in}$ and $C_{0,out}$, and are usually reported at the primary or at the secondary of a transformer representing the transduction between the electrical and the mechanical domain. A turn ratio (N) is commonly used to represent the ratio between the input and the output capacitances (Eq. 2.23).

$$R_m = \frac{\pi^2}{8} \frac{1}{k_t^2 Q_s \omega_s} \frac{N+1}{N} \frac{1}{C_{0,in}} \quad (2.20)$$

$$L_m = \frac{\pi^2}{8} \frac{1}{k_t^2 \omega_s^2} \frac{N+1}{N} \frac{1}{C_{0,in}} \quad (2.21)$$

$$C_m = \frac{8}{\pi^2} k_t^2 \frac{N}{N+1} C_{0,in} \quad (2.22)$$

$$N = \frac{C_{0,in}}{C_{0,out}} \quad (2.23)$$

For a 2-port resonator, the output capacitance directly sums up to C_{load} to determine the load impedance (Z_{load}). The value of such impedance referred to the primary of the transformer and the voltage across it can be expressed respectively as Eq. 2.24 and 2.25. The total gain can be easily calculated as the ratio of the voltage measured across Z_{load} at the secondary (V_2) and the voltage source (V_{in}) as captured by Eq. 2.26.

$$Z'_{load} = \frac{1}{j\omega(C_{0,out} + C_{load})N^2} \quad (2.24)$$

$$V'_{load} = \frac{Z'_{load}}{R_{in} + \left(R_m + j\omega L_m + \frac{1}{j\omega C_m} + Z'_{load} \right) \parallel \frac{1}{j\omega C_{0,in}}} \quad (2.25)$$

$$G = \left| \frac{V_2}{V_{in}} \right| = \left| \frac{\frac{Z_{load}}{N}}{R_{in} + \left(R_m + j\omega L_m + \frac{1}{j\omega C_m} + \frac{Z_{load}}{N^2} \right) \parallel \frac{1}{j\omega C_{0,in}}} \right| \quad (2.26)$$

Similarly to the 1-port resonator described in Section 2.1.3, the operating frequency (ω_{RF}) of a 2-port resonator implemented in a MN differs from the natural resonant frequency of the device due to the pulling operating by the series capacitive load. The frequency can be expressed according to Eq. 2.27, where α represents the ratio between the capacitive load and the output capacitance (Eq. 2.28).

$$\omega_{RF} = \omega_s \sqrt{\frac{(\alpha + 1)(N + 1) + K^2}{(\alpha + 1)(N + 1)}} \quad (2.27)$$

$$\alpha = \frac{C_{load}}{C_{0,out}} = \frac{NC_{load}}{C_{0,in}} \quad (2.28)$$

To provide for passive voltage amplification, the imaginary part of the parallel between the $C_{0,in}$ and the motional branch in series with Z'_{load} must be equal to zero (Eq. 2.29). Differently from the

1-port resonator case, the losses introduced by the matching network are not amplified by the frequency pulling and are equal to the motional resistance, R_m (Eq. 2.30). The overall gain can thus be expressed as reported in Eq. 2.31.

$$\text{Im}g \left\{ \left(R_m + j\omega L_m + \frac{1}{j\omega C_m} + Z'_{load} \right) \parallel \frac{1}{j\omega C_{o,in}} \right\} = 0 \quad (2.29)$$

$$\text{Re} \left\{ \left(R_m + j\omega L_m + \frac{1}{j\omega C_m} + Z'_{load} \right) \parallel \frac{1}{j\omega C_{o,in}} \right\} = R_m \quad (2.30)$$

$$G = \left| \frac{1}{\omega(C_{o,in} + C_{load}N)(R_{in} + R_m)} \right| \quad (2.31)$$

Eq. 2.31 shows that a MN implementing a 2-port resonator instead of a 1-port device does not offer a significant advantage. Despite the absence of a pulling factor, 2-port devices exhibit a larger motional resistance for a fixed static capacitance (Eq. 2.20) and increase the load that needs to be resonated out, ultimately decreasing the gain. A decrease in N helps reducing the total load, at the expenses of a higher motional resistance. For this reason, 2-port resonators exhibit performance similar to 1-port resonators, with the cons of a more complicated topology and fabrication process.

2.1.5. Transformer with Parallel Resonator

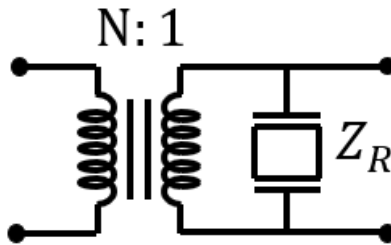


Figure 2.8: Representation of a matching network constituted by a transformer with a parallel resonator.

A more advanced matching network architecture implements a combination of the transformer approach described in Section 2.1.2 and the 1-port resonator approach described in Section 2.1.3.

The system is composed by a resonator interfaced in parallel with the input of the mixing stage at the secondary of a transformer (Fig. 2.8). The MEMS resonator is effectively employed as an inductor and the gain can still be expressed according to Eq. 2.7. In contrast to the series approach described in Section 2.1.3, the 1-port resonator is operated at its anti-resonance frequency ($\omega_p = 2\pi f_p$, Eq. 2.32) to synthesize a large resistance R_p , which can be expressed according to Eq. 2.33.

$$\omega_p = \omega_s \sqrt{\frac{C_0 + C_{load} + C_m}{C_0 + C_d}} \quad (2.32)$$

$$R_p = |Z_R|_{\omega=\omega_p} = \frac{Q_s \left(\frac{C_m}{C_0 + C_{load}} \right)}{\omega_s (C_0 + C_{load} + C_m)} \quad (2.33)$$

It is possible to calculate the value of C_0 that maximizes R_p (and thus the gain) similarly to the process reported in Section 2.1.3, by solving Eq. 2.34. Results are captured by Eq. 2.35.

$$\max R_p \rightarrow \frac{d}{dC_0} \left[\frac{Q_s K^2 C_0}{\omega_s (C_0 + C_{load}) (C_0 + C_{load} + K^2 C_0)} \right] = 0 \quad (2.34)$$

$$C_0 = \frac{C_{load}}{\sqrt{1 + K^2}} \quad (2.35)$$

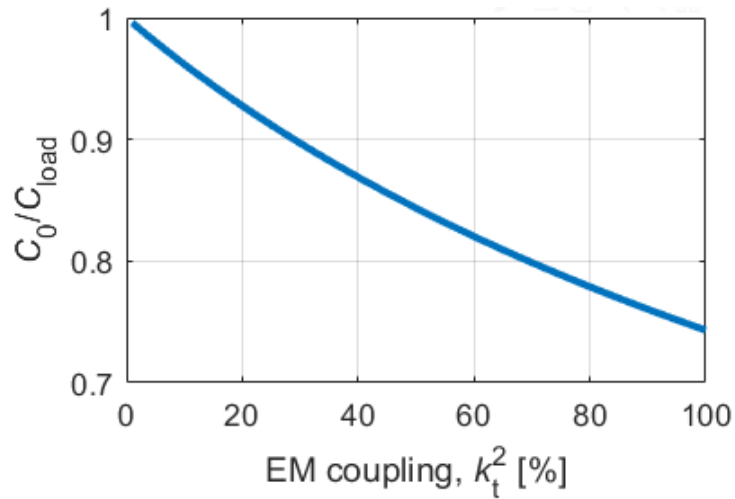


Figure 2.9: Optimal C_0 over C_{load} ratio as a function of the electromechanical coupling of the resonator.

Assuming $k_t^2 = 0.3$, $C_{0,opt} = 0.9 C_{load}$ (Fig. 2.9). Differently from the optimal C_0 found for the series resonator approach, the optimal point is frequency independent.

2.1.6. Matching Networks Comparison

The different architectures described in the previous sections are analytically compared to identify the most suitable topology for the implementation of a matching network in the RFFE of a WuRx. The most important metrics are the gain provided to the load and the footprint of the MN.

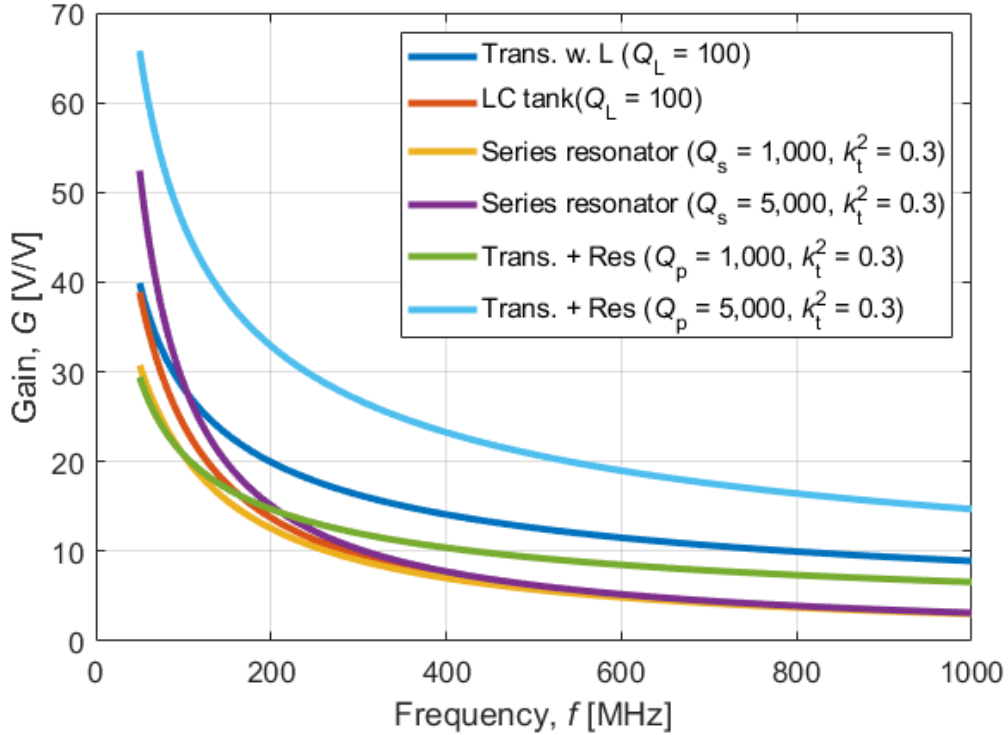


Figure 2.10: Comparison between different matching networks architectures for a fixed $C_{load} = 1$ pF.

For the analytical comparison, the Q_L of discrete inductors was set to 100 [5], while the quality factors (Q_s and Q_p) of piezoelectric resonators were varied between 1,000 and 5,000 according to existent literature [14], with a fixed k_t^2 equal to 30%. Transformers were assumed ideal and lossless for the current analysis. C_{load} was set to 1 pF, which represents the typical load of an ED [20]. The

static capacitance of piezoelectric resonators was set to match their optimal value according to the analysis reported in the previous sections.

As highlighted by Fig. 2.10, the LC tank and the transformer with a parallel inductor outperform any resonator-based architecture for Q_s and Q_p in the order of 1,000. A direct comparison between the series losses introduced by an LC tank and a series resonator approach (Eq. 2.36) shows how the FoM of the resonator must be at least greater than $k_p Q_L$ to provide for a larger gain (Eq. 2.37). For $Q_L = 100$ and $k_p \sim 3$ [14], the FoM of a 1-port resonator must be greater than 300.

$$R_L = k_p R_m \quad (2.36)$$

$$FoM = k_t^2 Q_s > k_p Q_L \quad (2.37)$$

A similar comparison can be performed between the approaches implementing a parallel inductor and a parallel resonator. In this case, the parallel resistance of the parallel inductor must be set equal to the resistance synthesized at the resonator anti-resonance (Eq. 2.38). The relationship between Q_p and Q_L is expressed by Eq 2.39. Assuming $k_t^2 = 30\%$, Q_p must be roughly 15 times higher than Q_L to provide similar results.

$$R_p = \frac{Q_L}{\omega C_{load}} = \frac{Q_p K^2 C_0}{\omega_p (C_0 + C_{load})(C_0 + C_{load} + K^2 C_0)} \quad (2.38)$$

$$Q_p > \frac{4 + 2K^2}{K^2} Q_L \quad (2.39)$$

System based on piezoelectric resonators with high Q_s and Q_p ($\sim 5,000$) show higher gains than other architectures especially at low frequency (< 100 MHz).

The smaller footprint of MEMS devices, due to the absence of any large, external component (such as a transformer), point out to the series approach as the most suitable MN for the RMR under investigation. Despite higher theoretical performance, the presence of severe spurious at the anti-

resonance of demonstrated high performance devices [13] limits the implementation of architectures combining a transformer and a parallel resonator. Furthermore, as emphasized in Fig. 2.10, this approach would equally benefit of the development of high Figure of Merit resonators, which is the main goal of the present dissertation.

2.2. Electrostatic MEMS demodulator

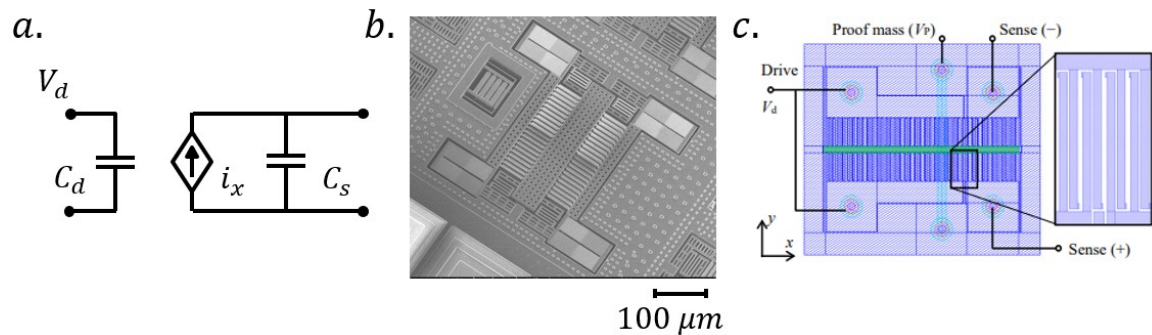


Figure 2.11: (a) Equivalent electrical model of a MEMS demodulator; (b) SEM picture of a CMOS-MEMS demodulator fabricated with a $0.18 \mu m$ CMOS process [8]; and (c) schematic of the SCS resonator described in [27] and implemented in the RMR described in [5].

The mixing stage of the RMR is implemented with an electrostatic high- Q MEMS resonator operating at ω_r that takes the place of an Envelope Detector (ED) in more conventional WuRx designs. Different MEMS-based demodulator have been demonstrated in the past [28][29][30], but the RMR described in [5] offers the first implementation of such systems in the chain of a WuRx.

The non-linearity of an electrostatic parallel-plate capacitor is exploited to down-convert a modulated signal from RF to baseband without power consumption. The force (F_{el}) generated across the combs of a capacitive electrostatic drive (C_d) is, in fact, proportional to the square of the voltage (V_d) applied across C_d [8]. For a signal modulated at $\omega_c \pm \omega_m$, such force presents a component at the baseband signal frequency (Eq. 2.40).

$$F_{el} = \frac{1}{2} V^2(t) \frac{dC_d}{dx} \propto \left(\frac{1 + \cos(2\omega_m t)}{2} + \cos(\omega_m t) + 1 \right) \quad (2.40)$$

If ω_m is set equal to the resonant frequency of the MEMS demodulator (ω_r), F_{el} is maximized and can be exploited to generate a large motional current (i_x) at the output sense combs of the microelectromechanical structure (Eq. 2.41). This behavior is captured by the equivalent electrical circuit reported in Fig 2.11a, where i_x is represented as a voltage controlled current source. The magnitude of the output current is a function of operating frequency (ω_r), the input drive (C_d) and output sense capacitances (C_s), their movable airgaps (g_d and g_s), the demodulator quality factor (Q_x), its total and equivalent mechanical stiffness in the direction of motion (k_{mech} and k_{eqx}), and the polarization voltage applied to the structure (V_p). The polarization voltage (Eq. 2.42) must be carefully selected to avoid instability, which is defined by the pull-in voltage (V_{pi}) [8]. For this reason, a safety factor η (<0.9) is generally included when defining the operational V_p .

$$i_x = \frac{\delta C_s}{\delta x} \frac{\delta x}{\delta t} V_p = \frac{1}{2\pi} \frac{C_s C_d \omega_r Q_x}{g_s g_d k_{eqx}} V_p V_d^2 \quad (2.41)$$

$$V_p = \eta V_{pi} = \eta \sqrt{\frac{8k_{mech} g_s^2}{27C_s}} \quad (2.42)$$

Two different designs have been demonstrated for the mixing stage of the RMR described in [5]. In the first design [8], a CMOS-MEMS demodulator was fabricated utilizing the six-metal TowerJazz 0.18 μm CMOS process. The main advantage of this approach is the integration between MEMS and CMOS circuitry, which allows for an easier system integration and lower parasitics. The relatively low quality factor (Q_x) and capacitance per unit area attained [5] fostered the investigation of a demodulator implemented in thick Single-Crystal-Silicon (SCS). SCS resonators realized with the ‘‘Epi-Seal’’ process offer better impedance matching and larger capacitance [27] at the expenses of a three-chips WuRx solution [5].

2.3. CMOS TIA

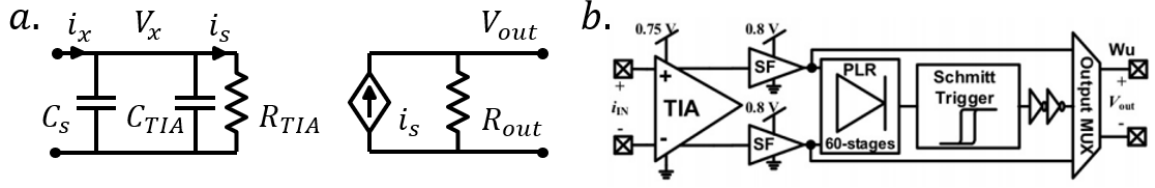


Figure 2.12: (a) Equivalent model of a CMOS TIA. The static capacitance of a previous stage (C_s) is included; and (b) block diagram of the CMOS circuitry described in [5].

The last stage of the RMR is constituted by a CMOS Transimpedance Amplifier (TIA) followed by a Passive Latch Rectifier (PLR). The wake up signal is generated by passively rectifying the motional current generated at baseband by the MEMS resonant demodulator.

The aim of the TIA is to provide sufficient voltage boost to the signal (V_{out}) before presenting it to the input stage of the PLR. The TIA can be modeled to first approximation as a current controlled voltage source (Fig. 2.12). A portion (i_s) of the motional current (i_x) generated at the sensing comb of the demodulator flows into the TIA transimpedance (R_{TIA}), which is later converted into a voltage (Eq. 2.43) via the TIA output resistance (R_{out} , Eq. 2.44).

$$V_{out} = i_s R_{out} \quad (2.43)$$

$$R_{out} = \frac{1}{\lambda I_{DC}} \quad (2.44)$$

$$i_s = i_x \frac{\frac{1}{j\omega_r(C_s + C_{TIA})}}{R_{TIA} + \frac{1}{j\omega_r(C_s + C_{TIA})}} \quad (2.45)$$

R_{out} represents the output impedance of the TIA and is a function of the CMOS biasing current (I_{DC}) and of the channel-length modulation parameter (λ). The value of R_{out} cannot be arbitrarily selected since the biasing current is strongly limited by the power budget of the system, which translates in an $I_{DC} \sim 1$ nA, while λ is a function of the adopted CMOS technology (~ 0.7). The

design of R_{TIA} is critical since a lower resistance allows for more transimpedance gain, but reduces the current (i_s) flowing into the TIA. If R_{TIA} gets too close to the impedance of the sensing comb, more current will flow into C_s , ultimately reducing V_{out} (Eq. 2.43). Therefore, a trade-off between performance and power consumption is necessary to identify an optimal design point. For the selected technology (TowerJazz 0.18 μm CMOS), the maximum R_{TIA} and R_{out} were set to 2.15 M Ω and 1.4 G Ω to comply with the power budget.

The TIA is followed by a Source Follower (SF) stage operating in deep subthreshold regime, which drives a multi-stage Passive Latch Rectifier (PLR). The SF is necessary to decouple the TIA and the capacitive load introduced by the rectifier stages, which was set to 60 in a trade-off between latching time and triggering voltage (~ 1 V). According to [5], a V_{out} of 40-45 mV is necessary at the input of the PLR to trigger the comparator (Schmitt trigger) at the end of the CMOS chain (Fig. 2.12b).

2.4. RMR Numerical Optimization

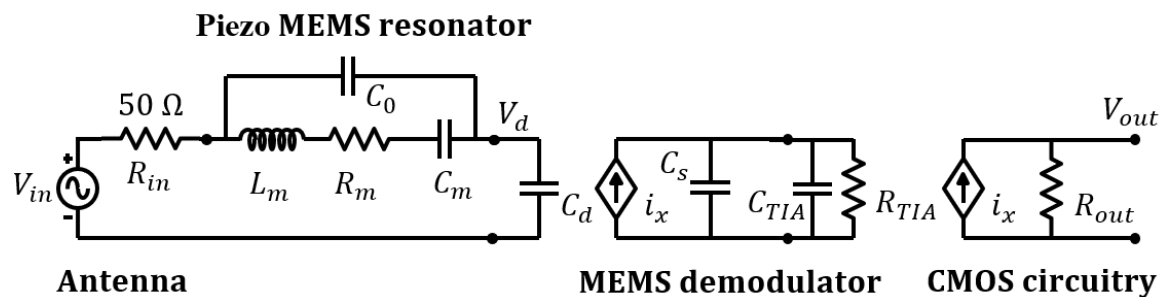


Figure 2.13: Complete schematic of the RMR analyzed in this section.

Fig. 2.13 reports the final simplified schematic of a Resonant Microelectromechanical Receiver composed by a series piezoelectric MEMS resonator implemented in the RFFE matching network, an electrostatic MEMS resonant demodulator and a CMOS circuitry. This last stage includes a ULP

TIA, a passive latch rectifier and a Schmitt trigger to provide a wake-up signal to the sensing electronic.

The relationships defining the passive voltage amplification (G) in the MN, the current generated at the output of the demodulator (i_x) and the voltage presented at the input of the PLR by the TIA (V_{out}) are captured by Eq. 2.46 – 2.48.

$$G = \left| \frac{V_d}{V_{in}} \right| = \frac{1}{j\omega_{RF}C_d \left(R_s + \frac{(C_d + C_0)^2 \pi^2}{C_d^2} \frac{1}{8 \omega_s C_0 k_t^2 Q_s} \right)} \quad (2.46)$$

$$i_x = \frac{1}{2\pi} \frac{C_s C_d \omega_r Q_x}{g_s g_d k_{eqx}} \eta \sqrt{\frac{8k_{mech}g_s^2}{27C_s}} V_d^2 \quad (2.47)$$

$$V_{out} = \frac{i_x}{\lambda_{DC}} \frac{\frac{1}{j\omega_r(C_s + C_{TIA})}}{R_{TIA} + \frac{1}{j\omega_r(C_s + C_{TIA})}} \quad (2.48)$$

Table 2.1: List of RMR fixed parameters.

Parameters					
RF MEMS resonator		MEMS demodulator		CMOS TIA	
Target sensitivity (dB)	-100 dBm	Quality Factor (Q_x)	1,500	TIA input capacitance (C_{TIA})	10 fF
Operating frequency (ω_{RF})	50 – 400 MHz	Drive and sense airgaps (g_d/g_s)	217 nm	Ch. Modulation factor (λ)	0.7
Quality Factor (Q_s)	1,500	Resonant Frequency (ω_r)	20 – 100 kHz	TIA output impedance (Z_{out})	1.4 G Ω
EM coupling (k_t^2)	0.3	Equivalent stiffness (k_{eqx})	17 N/m	Biasing current (I_{DC})	1 nA
Parasitics	150 fF	Mechanical stiffness (k_{mech})	60 N/m	Transimpedance (R_{TIA})	2.15 M Ω
		Safety coefficient (η)	0.85	Parasitics	30 fF

In order to maximize the receiver sensitivity, the MEMS voltage amplifier operating frequency (ω_{RF}), its static capacitance (C_0), the MEMS demodulator resonant frequency (ω_r), and its drive (C_d) and sense static capacitances (C_s) must be optimized according to the system constraints. The

assumptions made for the other parameters and the ranges of investigation for the carrier and baseband frequencies are reported in Table 2.1 and are extrapolated from prior experimental results [31][8]. TIA parameters are set to comply with a power budget of 10 nW.

An important constraint derives from the need of having a demodulator frequency (ω_r) smaller than the 3 dB bandwidth of the carrier frequency. This constraint is required to allow the modulation of the RF signature and sets a limit for the maximum loaded quality factor of the RF MEMS resonator that can be implemented in the RFFE (Eq. 2.49). As an example, Q_s as high as 10,000 can be sustained for R_m in the order of few Ω s, assuming $k_p = 4$, $f_{RF} = 50$ MHz and $f_r = 20$ kHz.

$$Q_{max} = Q_s \frac{k_p R_m}{k_p R_m + R_{in}} = \frac{\omega_{RF}}{\omega_r} \quad (2.49)$$

Fig. 2.14 shows the impact of the RF carrier frequency and the demodulator frequency on the expected WuRx sensitivity for $C_0 = C_d = C_s = 500$ fF, with Q_{max} set by Eq. 2.49. Operating at lower ω_{RF} (~ 50 MHz) yields higher sensitivity, due to the larger impedance conversion that can be attained at RF between the 50Ω input resistance and a fixed capacitive load.

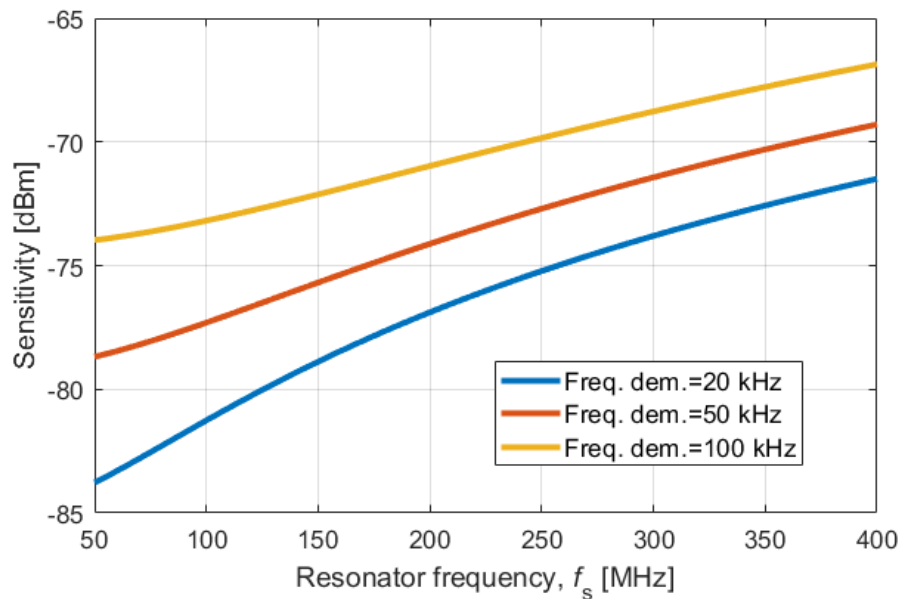


Figure 2.14: Simulated RMR sensitivity as a function of the resonator natural frequency (ω_s) and different demodulator frequencies (ω_r), for $C_0 = C_d = C_s = 500$ fF. The other RMR parameters are reported in Table 2.1.

Lower ω_r (~ 20 kHz) improve the system sensitivity mostly because of the TIA bandwidth, as well as a slightly higher voltage gain attainable in the MN, at the sidebands are closer to the carrier frequency. Despite the analysis shows that operating at the lowest possible frequency is advantageous by a sensitivity standpoint, consideration related to the antenna size, the piezo MEMS resonator and MEMS demodulator footprints, and the spectrum availability must be taken into account when selecting the carrier frequency. For the purpose of this dissertation, the carrier and modulation frequencies were respectively set around 50 MHz and 20 kHz, to showcase the capabilities of the RMR architecture.

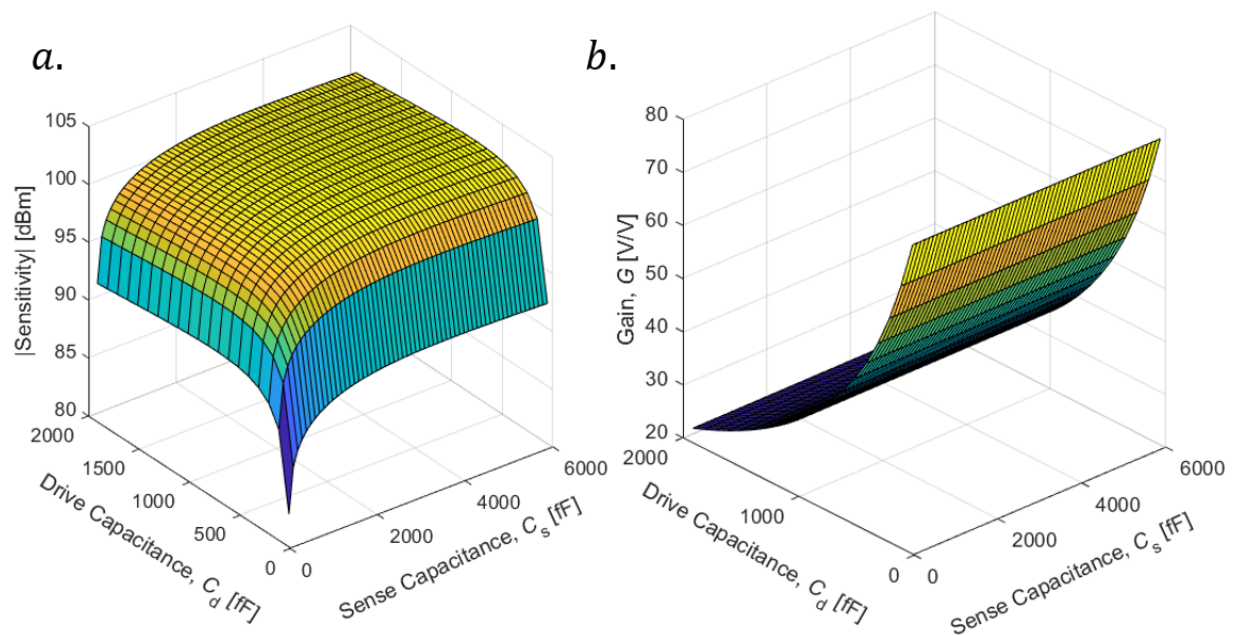


Figure 2.15: (a) Numerical optimization of the RMR sensitivity as a function of C_d and C_s ; and (b) simulated gain provided by the RF resonator to the input C_d of the demodulator. G is maximized for smaller C_d and is not affected by C_s . The optimal C_0 closely follows C_d as reported in Section 2.1.3.

The sensitivity of the RMR as a function of the sizing of the RF MEMS resonator (C_0) and demodulator (C_d and C_s) is reported in Fig. 2.4a.

According to the numerical optimization reported in Fig. 2.15a, the optimal sensitivity is achieved for a demodulator drive capacitance (C_d) of 500 fF, as a trade-off between the gain which

can be provided by the MN (Fig. 2.15b) and the motional current generated at the output of the demodulator (i_x). The sense capacitance (C_s) should be increased up to the point its equivalent impedance matches the input impedance of the TIA (~ 3.7 pF). For the case under examination, a C_d of 500 fF corresponds to an optimal RF MEMS static capacitance (C_0) of roughly 400 fF. More realistically, due to system integration parasitic capacitances, C_d should be assumed close to 1 pF, which closely resemble the typical load of a WuRx ED [20].

The numerical optimization proves that our proposed RMR architecture is capable of sensitivities approaching -100 dBm for a large range of resonator and demodulator capacitances (Fig. 2.4a), proving its robustness to parasitics. More importantly for the purpose of this dissertation, it provides the design range in terms of Q_s , k_t^2 and C_0 for the resonators to be implemented in the MN of the RMR.

CHAPTER 3: PIEZOELECTRIC MEMS

RESONATORS TECHNOLOGIES

Piezoelectric-based acoustic MEMS resonators have been widely investigated and became commercially successful products, with devices deployed in RF filters, duplexers and oscillators. Quartz crystal oscillators for time-reference applications and Surface Acoustic Wave (SAW) resonators for RF filters were the most notable pioneering solution based on acoustic devices. In most recent times, Aluminum Nitride (AlN) Film Bulk Acoustic Resonators (FBARs) set the technological threshold for mobile filtering applications, which is projected to become the largest market for these devices in the years to come (Fig. 1.1d).

The challenge to enhance filter performance in terms of lower insertion losses (IL) and wider bandwidth (BW), and the development of matching networks based on piezoelectric MEMS for novel IoT applications is fostering the investigation of new classes of resonators based on different acoustic modes. Among those, the most notable are the fundamental symmetric mode (S_0) [31], fundamental shear horizontal wave (SH_0) [15], Bulk Acoustic Wave (BAW) [32], Incredible High Performance (IHP) SAW [33], and Thickness Shear Mode (TSM) [34]. The need for compact resonators with higher Q_s and k_t^2 is also spurring interest for new classes of materials, such as doped-AlN alloys [35][36], thin films of Lithium Niobate (LiNbO_3 , or LN) [37], Lead Zirconate Titanate (PZT) [38], and Gallium Nitride (GaN) [39]. Especially for Scandium-doped Aluminum Nitride ($\text{Sc}_x\text{Al}_{1-x}\text{N}$) alloys and LN resonators, research is currently focused on overcoming fabrication constraints and device performance, which are still far from the theoretical maximum.

This chapter focuses on Laterally Vibrating Resonators (LVRs), a promising class of devices which exhibits good Q_s and k_t^2 for different piezoelectric material and fabrication versatility, making them an ideal solution for prototyping. The main excitation modes and the key geometrical features, and their effect on the devices static capacitance (C_0), are later introduced. Finally, resonators fabricated with different material technologies are compared to identify the solution that would maximize the gain in the RFFE of the WuRx described in Chapter 2.

3.1. Laterally Vibrating Resonators (LVRs)

Laterally Vibrating Resonators (LVRs) operating in the symmetric mode (S_0) are an appealing solution for filtering and novel IoT applications due compact footprint, high performance (FoM) in the frequency range of interest, and low motional resistance (R_m). Differently from FBAR resonators, LVRs frequency can be defined lithographically, allowing multi-frequency fabrication per die on substrates with various thicknesses. The promising results reported in preliminary studies [40][35][41][31] and their characteristics make LVRs ideal candidates for use in matching networks of WuRx receivers.

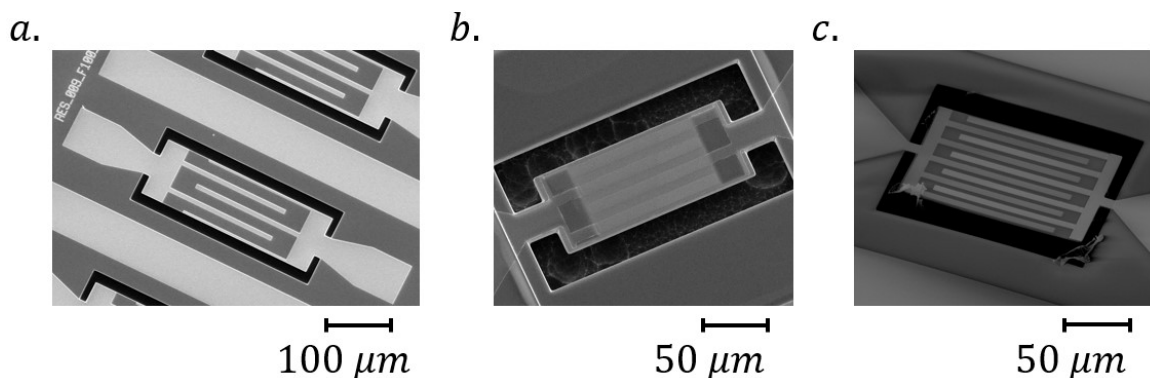


Figure 3.1: Laterally Vibrating Resonators made of different piezoelectric material: (a) X-cut Lithium Niobate LVRs. The edge reflectors are necessary to fully harness the maximum electromechanical coupling of the material; (b) Y-cut Lithium Niobate; and (c) 20% Scandium-doped Aluminum Nitride.

The typical embodiment for an LVR consists in a thin suspended plate of piezoelectric material, tethered to the substrate via longitudinal anchors (Fig. 3.2). The piezoelectric medium is excited via metallic Interdigitated Electrodes (IDEs) or Transducers (IDTs) which are patterned on the top surface. Similarly to SAW resonators, the resonant frequency is set to first approximation by the distance between the longitudinal symmetry axis of the metallized fingers, which is defined as pitch (p). The pitch must equal half of the acoustic wavelength (λ) of the desired mode, which can be estimated accordingly to Eq. 3.1, knowing the speed of propagation of wave in the medium (v_p).

$$\lambda = \frac{v_p}{f_s} \quad (3.1)$$

Several parameters, such as plate length (L), width (W), substrate thickness (h), anchors width (W_a) and length (L_a), and metal thickness (t_m) define the resonator mechanical stiffness, ultimately affecting its resonant frequency.

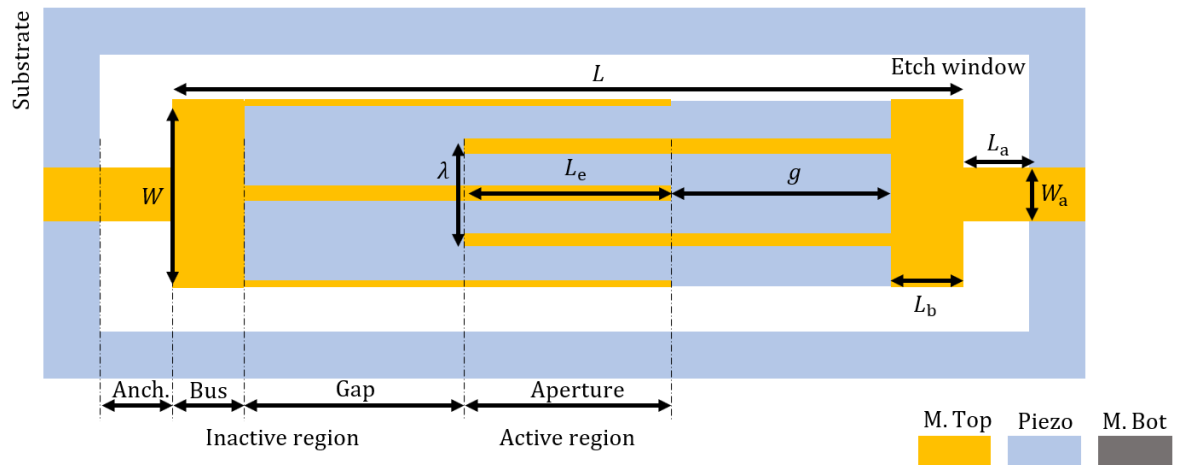


Figure 3.2: Top view of the typical embodiment of a Laterally Vibrating Resonator (LVR). A bottom electrode under the resonator plate can be present or not according to the desired excitation method.

The ratio between the width of the IDEs and the pitch (metallized vs. total area) is named electrode coverage (c). A patterned or unpatterned bottom electrode can be present or not, according to the desired excitation method and fabrication process.

This class of devices relies simultaneously on the direct and inverse piezoelectric effect for its functioning. When the frequency of the RF signature matches the mechanical resonance set by the IDT spacing, the signal is transduced in the acoustic domain at the input port as a standing wave. The acoustic wave propagates in the medium and is later re-converted in the electromagnetic domain at the output terminal.

In more details, five regions can be identified in a typical LVR geometry:

- Active region, or aperture (L_c);
- Finger-to-bus gap (g);
- Bus length (L_b);
- Anchors;
- Routing.

The active region is defined by the IDEs and is the area where piezoelectric transduction occurs. Ideally, all the energy is confined in this region to maximize the quality factor and electromechanical coupling of the resonator. The finger-to-bus gap represents the distance between the termination of the IDEs belonging to one port and the bus of the opposite port, which acts as an interconnect between all the fingers belonging to the same terminal. The sum of lengths of the aperture, the two gaps and bus defines the length of the plate (L), while the number of fingers (and edge reflectors if present, Fig 3.1a) sets the plate width. The width of a resonator can be expressed according to Eq. 3.2, where N_p represents the number of finger pairs. Reflectors account for half a finger when defining the number of pairs.

$$W = \frac{\lambda}{2}(N_p + 1) \quad (3.2)$$

Different anchor geometries can be implemented to connect the plate to the substrate [42][43]. The simplest solution is the adoption of two symmetrical anchors positioned perpendicularly to the wave propagation direction. Together with the gap and bus length, anchors' length and width define the acoustic boundary conditions of the resonator. It was proven, for different technologies, that the sizing of the passive regions is fundamental in synthesizing a $\lambda/4$ transformer [44][45] to minimize the anchor losses, thus maximizing the resonator quality factor.

3.1.1. Static Capacitance (C_0) Modeling and Excitation Mode

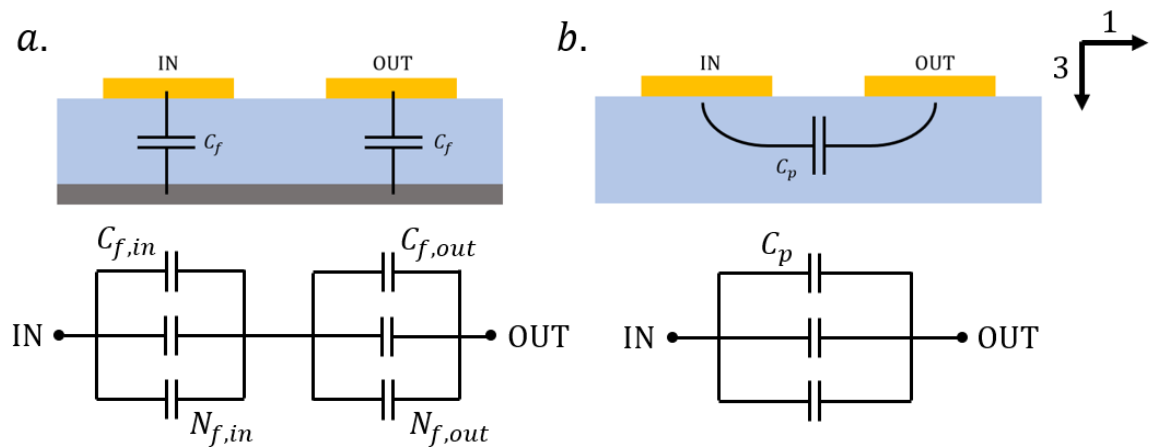


Figure 3.3: (a) Thickness Field Excitation mode and equivalent electrical circuit representing the static capacitance (C_0) of the device. Such capacitance is effectively the series of the capacitances of each terminal; and (b) Lateral Field Excitation mode and equivalent electrical circuit representing the static capacitance. In this case, C_0 is given by the parallel capacitance between the IDEs pairs.

The static capacitance of the resonator (C_0) plays a major role with Q_s and k_t^2 in determining the performance of piezoelectric MEMS-based matching network, as described in Section 2.1.3. Its value must be properly selected according to the MN architecture and the mixing stage input load to maximize the impedance transformation, thus maximizing the gain. For this reason, an accurate model for C_0 is required to guide the design of devices matched to a given C_{load} . Two excitation methods are usually exploited in S_0 modes LVR (Fig. 3.3): Thickness Field Excitation (TFE) and

Lateral Field Excitation (LFE). The desired mode of vibration, and thus the excitation method, determines the exploited piezoelectric coefficient, and the IDT and plate geometries. In order to synthesize an LVR operating in pure S_0 mode, the h/λ ratio should be kept below 0.05 [46].

In resonator relying on Thickness Field Excitation (Fig. 3.3a), the electric field is applied in the vertical direction (3) to generate a standing acoustic wave in the lateral direction (1). The piezoelectric coefficient exploited is d_{31} [26]. Assuming perfect coupling into the piezoelectric film, k_t^2 can be estimated according to Eq. 3.3 [26], where s_{11} is the compliance of the material in the lateral direction at constant electric field (E).

$$k_t^2 = \frac{d_{31}^2}{s_{11}^E \varepsilon_{r_3}^T \varepsilon_0} \quad (3.3)$$

In this configuration, a bottom electrode is desirable to define the potential of the bottom surface and better drive the electric field in the desired direction. It is possible to exploit the d_{31} coefficient even without a bottom electrode, at the expenses of a lower coupling coefficient [46].

For 1-port LVRs with bottom electrode, a simple C_0 model can be derived neglecting any fringe effect. The capacitance of each finger (C_f) can be modeled as parallel plate capacitor (Eq. 3.4), where $\varepsilon_0 \varepsilon_r$ is the dielectric permittivity of the piezoelectric medium, λ is the acoustic wavelength, L_e is the aperture and c is the finger coverage. The overall static capacitance, C_0 , can be estimated as the series combination between the capacitance of the input and output IDTs (Eq. 3.5), considering the number of fingers at each terminal ($N_{f,in}$ and $N_{f,out}$) and their respective capacitance per finger ($C_{f,in}$ and $C_{f,out}$).

$$C_f = \frac{\varepsilon_0 \varepsilon_r L_e \lambda c}{2h} \quad (3.4)$$

$$C_0 = \frac{N_{f,in} N_{f,out} C_{f,in} C_{f,out}}{N_{f,in} C_{f,in} + N_{f,out} C_{f,out}} \quad (3.5)$$

Differently from TFE resonators, devices operating with Lateral Field Excitation (LFE) exploit an electric field which is mainly directed in the horizontal direction (1). In this case, the piezoelectric coefficient of interest is d_{11} and k_t^2 can be estimated according to Eq. 3.6.

$$k_t^2 = \frac{d_{11}^2}{s_{11}^E \varepsilon_r^T \varepsilon_0} \quad (3.6)$$

A vertical direction (3) component is usually present due to the direction of the electric field in the medium. Thus, C_0 is both a function of the dielectric constants in the 1 and 3 directions (ε_{r1} and ε_{r3} , respectively). For $h/\lambda < 0.05$, it is possible to assume that the electric field is mainly constrained in the lateral direction, and that an approximated value for the capacitance of a pair of IDTs (C_p) can be estimated with a parallel plate capacitor model (Eq. 3.7).

$$C_0 = C_p N_p = \frac{2\varepsilon_0 \varepsilon_r L_e h}{\lambda(1-c)} N_p \quad (3.7)$$

If the h/λ ratio is greater than 0.05, the parallel plates approximation is no more valid, and a different model is required [47]. In such case, C_0 can be more accurately described by Eq. 3.8, where ε_{eff} represents the effective permittivity (Eq. 3.9) and $K(x)$ the elliptical integral of the parameter x [48]. The other parameters introduced to defined C_0 and ε_{eff} (q , k_0 , k_1 , k_0' , and k_1') are reported in Eq. 3.10 – 3.13.

$$C_0 = \varepsilon_0 \varepsilon_{eff} \frac{K(k_0')}{K(k_0)} L_e N_p \quad (3.8)$$

$$\varepsilon_{eff} = 1 + q(\varepsilon_r - 1) \quad (3.9)$$

$$q = \frac{1}{2} \frac{K(k_1') K(k_0)}{K(k_1) K(k_0')} \quad (3.10)$$

$$k_0 = \frac{1-c}{1+c} \quad (3.11)$$

$$k_1 = \frac{\tanh\left[\frac{\pi}{8}(1-c)\frac{\lambda}{h}\right]}{\tanh\left[\frac{\pi}{8}(1+c)\frac{\lambda}{h}\right]} \quad (3.12)$$

$$k'_i = \sqrt{1 - k_i^2} \quad (3.13)$$

Compared to TFE resonators, LFE suffer of lower capacitance per unit area (Fig. 3.4). This mean that in order to match the capacitance of demonstrated ED (~ 1 pF) and maximize the gain, larger structures are required. Differently from TFE, where a thinner piezoelectric film is required to increase the capacitance per unit area, thicker film help increasing LFE devices C_0 . Unfortunately, such increment does not scale linearly with h , and thicker film proven to be harder to etch, leading to poorer sidewall angles and lower Q_s .

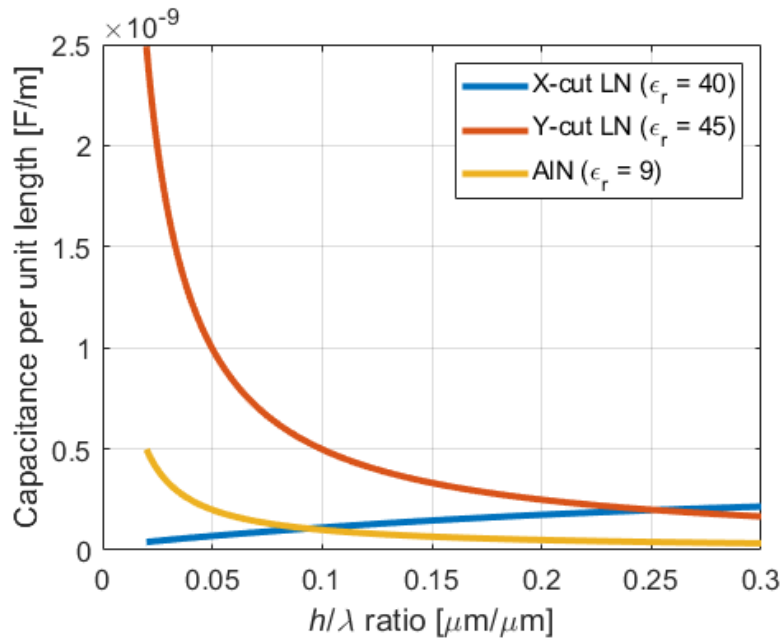


Figure 3.4: TFE vs LFE capacitance per unit area for different piezoelectric materials.

3.1.2. Impact of FoM and C_0 on Voltage Amplification

As highlighted in Section 2.1.3, the gain provided by a 1-port MEMS-based matching network to a fixed capacitive input load (C_{load}) is a function of the Figure of Merit (FoM), the resonant

frequency and its static capacitance (C_0). An optimal value of C_0 exists for a given C_{load}, f_s and FoM (Fig 2.6), such as a proper sizing of the resonator is necessary to maximize the MN performance. In order to identify the most suitable LVR technology, it is fundamental to understand the impact of the FoM and of C_0 on the gain as a function of C_{load} and the frequency of operation (f_{RF}).

Fig. 3.5a reports the analytical simulation of the gain provided by a 1-port resonator to a fixed input load of 1 pF as a function of the operating frequency, for different values of FoM. A high FoM is desirable, especially at lower frequency, to minimize both R_m and k_p , which significantly contribute in determining the insertion losses of the MN. The same conclusion can be derived considering the gain provided to variable load (Fig. 3.5b) for a fixed frequency ($f_s = 50$ MHz). As mentioned beforehand, the FoM also impacts the C_0 optimal point (Fig. 3.5c). Interestingly, the gain characteristic is relatively flat around the point of optimum C_0 , meaning that smaller resonator can be employed without significant reduction in gain if necessary.

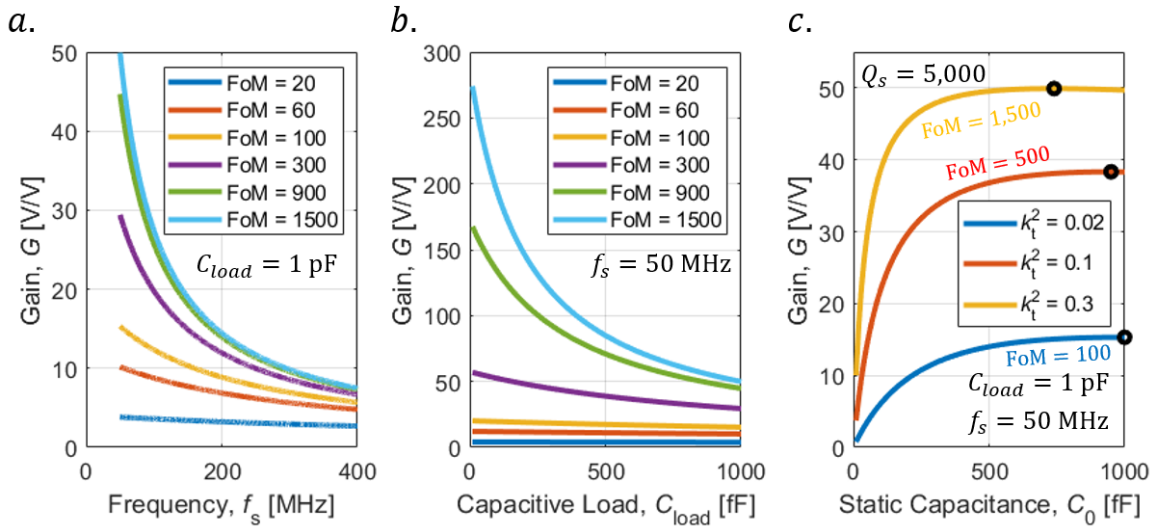


Figure 3.5: (a) Voltage gain as a function of natural resonant frequency (f_s) for fixed load ($C_{load} = 1$ pF); (b) voltage gain as a function of the capacitive load for a fixed natural resonant frequency ($f_s = 50$ MHz); and (c) voltage gain as a function of the static capacitance (C_0) for fixed load ($C_{load} = 1$ pF) and frequency ($f_s = 50$ MHz), for different FoMs. Higher FoMs are desirable to reduce the optimal size of the resonators and to enhance the gain.

3.2. Comparison between LVRs Technologies

Numerical simulations point out that resonator with a FoM of at least 500 in the frequency range of interest (50 – 400 MHz), and with static capacitances in the order of C_{load} , are necessary to attain large passive voltage amplification in 1-port MEMS-based matching networks. In the present section, different demonstrated and experimental LVRs technologies will be compared in terms of FoM, static capacitance and fabrication process to identify the most promising solution to be implemented in the RFFE of novel WuRx.

3.2.1. Aluminum Nitride (AlN)

The advancements in reactive sputtering technology and the development of high-quality thin film of Aluminum Nitride (AlN) at the end of the 90s fostered the research on innovative RF MEMS devices to enable large scale mobile communication. Film Bulk Acoustic Resonators (FBARs) [49] are the brightest example of a successful, commercial product that revolutionized an existing market segment (in this case, the RF filtering niche). The constant need for lower Insertion Losses (IL) and higher fractional bandwidths led to the study of FBARs alternatives. In this framework, the first Contour Mode Resonators (CMRs), the class of resonators LVRs can be ascribed to [22], were demonstrated [50]. Despite significant improvements from preliminary results [40], both in terms of Figure of Merit and understanding of the device physics, AlN LVRs have not been able to attain performance similar to FBARs ($Q_s = 4,000$ and $k_t^2 = 7\%$ [5]). Q_s in the order of 2-3,000 are generally reported in literature for 1 μm thick film operating in the hundreds of MHz range [44], with a maximum k_t^2 of 2% (FoM $\sim 40 - 60$). Q_s up to 4,500 have been demonstrated for thicker films, but at the expenses of k_t^2 (0.7%) and capacitance per unit area [40]. More recently, research focused on

hybrid modes to enhance the electromechanical coupling, with promising results [51][52], but still far from the target set by cutting-edge applications, such as 5G filtering solutions or MEMS-based matching networks for IoT WuRx.

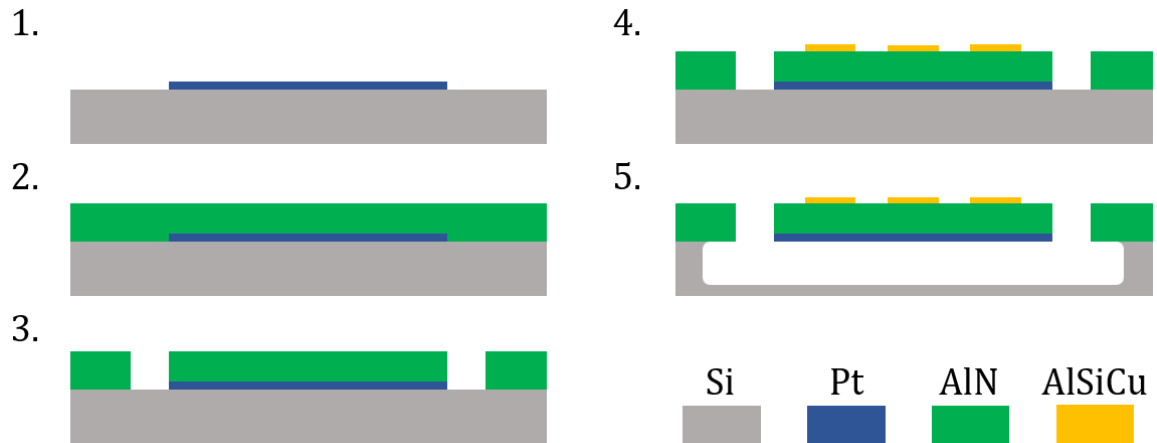


Figure 3.6: Fabrication process of 1-port AlN LVRs: (1) Bottom electrode patterning via sputtering and lift-off; (2) AlN reactive sputtering; (3) AlN patterning via Cl-based RIE or ion milling; (4) top electrode patterning via sputtering and lift-off; and (5) XeF₂ isotropic etching release.

The typical fabrication process of an AlN LVRs is reported in Fig. 3.6. As first step, the platinum (Pt) bottom electrode is patterned on top of a high resistivity silicon (Si) wafer using DC sputtering and lift-off (step 1 in Fig. 3.6). The thickness of the bottom electrode is set as a fraction of the piezoelectric film thickness as a trade-off between the electrical loading introduced and the necessity of having a plane substrate for a correct growth of the AlN crystals. Pt thicknesses in the order of 100 nm are usually adopted for 1 μm thick films [53]. To ensure adhesion between the metallic layer and the silicon surface, 10 nm of Chromium (Cr) are pre-sputtered. Chromium is preferred over other adhesion layer materials, such as Titanium (Ti), due to its compatibility with hydrofluoric acid (HF), which is often used to strip silicon dioxide (SiO₂) masks. Successively, a uniform, thin film of AlN is deposited via reactive sputtering on top of the wafer (step 2 in Fig. 3.6). A negative photoresist (PR) soft mask is then patterned on top of the piezoelectric film for the definition of the release pit. A hard mask made of SiO₂ can be used instead of a PR soft one, at the

expenses of a more complicated fabrication process. The LVRs geometry is then patterned via chlorine (Cl) based Reactive Ion Etching (RIE, step 3 in Fig. 3.6) or ion milling. Successively, the aluminum-silicon-copper (AlSiCu) top electrode and the interconnects are patterned via DC sputtering and lift-off (step 4 in Fig. 3.6). Similarly to the bottom electrode, the optimal AlSiCu thickness is a trade-off between electrical and mass loading, and it is a function of the piezoelectric film thickness. For 1 μm AlN films, 200 to 300 nm of AlSiCu is an optimal choice to reduce series resistance without affecting the electromechanical coupling. The resonator is finally released via xenon difluoride (XeF_2) isotropic etch (step 5 in Fig. 3.6), which removes the Si underneath the plate from the release pit. A more detailed description of the fabrication process, including recipes and etch rates, is reported in Appendix A. An example of a fabricated device is reported in Fig. 3.7.

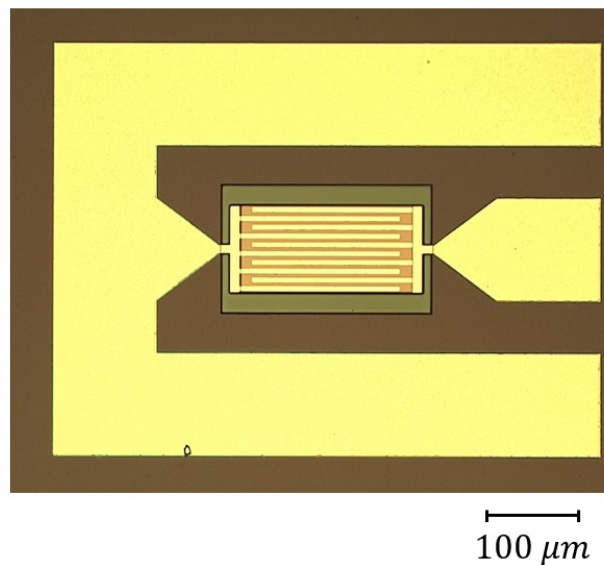


Figure 3.7: Microscope image of a 500 MHz 1-port AlN LVR.

AlN 1-port LVRs fabricated as a testbench at CMU Nanofab Facility exhibited Q_s as high as 3,910 and k_t^2 of 2%, for an overall FoM of 78 (Fig. 3.8). These results are consistent with the performance reported in literature, which are far from the specs required by the MEMS-based matching networks previously described, especially in terms of k_t^2 .

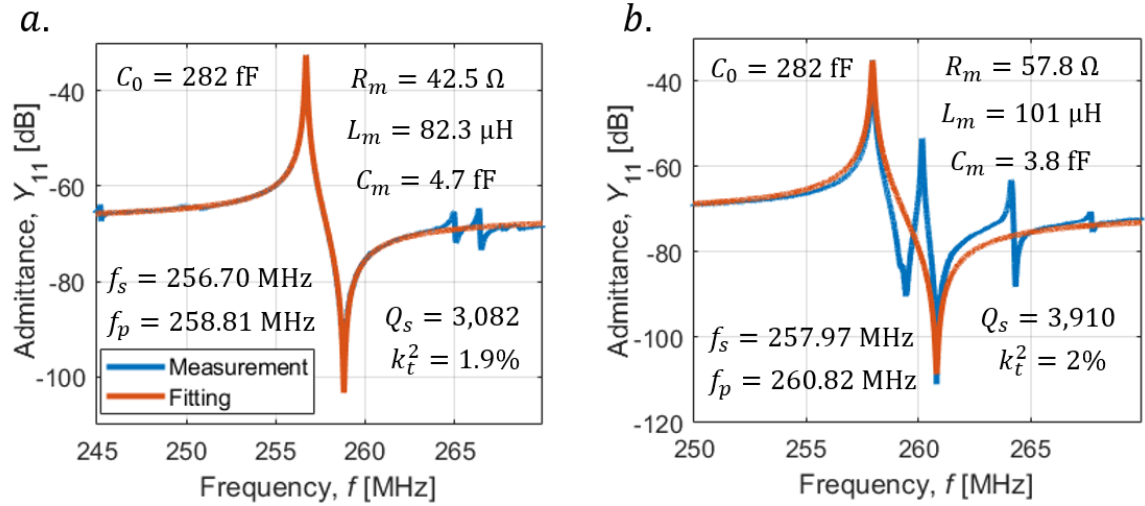


Figure 3.8: (a) Admittance response of an in-band spurious-free 1-port LVR operating around 250 MHz. The reported k_t^2 is defined as $\pi^2/2 \cdot f_s/f_p \cdot \tan^{-1}(\pi/2 \cdot f_s/f_p)$; and (b) admittance response of a 1-port LVR exhibiting high Q_s and in-band spurious modes. As reported in Appendix B, in-band spurious can affect the measured k_t^2 . The k_t^2 reported in this figure was calculated after de-embedding the effect of the spurious mode.

3.2.2. Scandium-doped Aluminum Nitride (ScAlN)

Doping is an appealing solution to increase the intrinsic k_t^2 of AlN films. Electromechanical coupling enhancement has been theoretically predicted [54], and different alloys investigated for this purpose [55][56]. Among all the possible dopants, Scandium (Sc) has proven to be the most attractive element due to its low inclusion energy [36] and theoretical k_t^2 improvement. In fact, the presence of Sc modifies the AlN Wurtzite structure, decreasing its Young's modulus, while increasing its dielectric and piezoelectric constants [55]. This phenomenon is valid up to approximately 40% Sc-doping ($\text{Sc}_{0.4}\text{Al}_{0.6}\text{N}$), where the Wurtzite structure transitions into rock-salt structure, which does not exhibit piezoelectricity.

Sc-doped AlN films are interesting over other piezoelectric materials not only in terms of performance, but also for their CMOS compatibility. High-quality, sputterable thin film of ScAlN at different concentrations, which can be machined with similar technologies already developed for

AlN, are in fact the most ideal solution for mass production of consumer electronic components, since their implementation on production lines would require significantly lower investments.

The most promising results showed LVRs with k_t^2 of 4.5% and Q_s of 1,300 - 1,600 between 200 and 500 MHz [35][36] for a doping around 20%, and k_t^2 up to 8% for 40% doping in the GHz range for Lamb Wave resonators [57]. These values of k_t^2 are respectively 2x and 4x higher than the typical performance of an AlN LVR.

The fabrication process for 20% Sc-doped AlN ($\text{Sc}_{0.2}\text{Al}_{0.8}\text{N}$) LVRs is virtually identical to the process flow described in Fig. 3.6 for an AlN resonator. The process developed at CMU Nanofab starts with the sputtering and lift-off of 100 nm of Pt for the definition of the floating bottom electrodes of 1-port resonators (step 1 in Fig. 3.6). 10 nm of Cr are used as adhesion layer to allow compatibility with HF-based processes. The reactive sputtering (step 2 in Fig. 3.6) of the 1 μm piezoelectric thin film was performed externally by Advanced Modular Systems (AMS) [58]. The Sc-doped films proven to have a sensibly higher selectivity to standard Cl-based RIE (step 3 in Fig. 3.6) recipes commonly used, showing a reduced etch rate of 50 nm/min compared to the 200 nm/min registered for AlN resonator with identical geometry. A 2.5 μm SiO_2 hard mask is patterned in place of a thick ($\sim 5 \mu\text{m}$) soft mask, to avoid PR overheating and issues during the mask removal process. The remaining oxide layer ($\sim 500 \text{ nm}$) is later removed with a buffered HF solution, which does not attack AlN nor ScAlN films. Both the top electrode patterning (4) and the resonator release (step 5 in Fig. 3.6) are identical to the steps reported for AlN devices. Microscope and SEM pictures of fabricated devices are reported in Fig. 3.9. Sidewall angle (φ) were estimated around 70° (Fig. 3.10a). A value of φ as close as possible to 90° is associated with higher Q_s and lower damping.

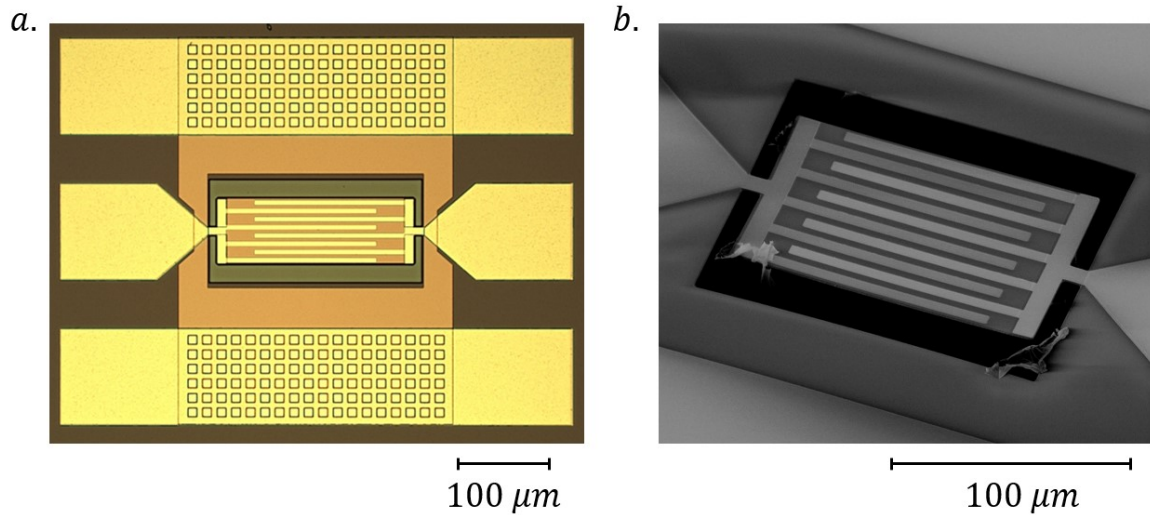


Figure 3.9: (a) Microscope image of a 2-port 20% Sc-doped AlN resonator operating around 500 MHz. VIAs are added to ground the bottom electrode; and (b) SEM image of a 1-port resonator operating around 500 MHz.

Visual inspection of fabricated devices highlighted two main fabrication issues: etch byproducts redeposition and out-of-plane bending. The residuals consist in thin flakes hanging from the resonator and release pit edges (Fig. 3.10b), which became visible only after the release process. Energy-dispersive X-Ray Spectroscopy (EDX) analysis found an elevated concentration of Boron (B) in the flakes, pointing out to the Cl-based RIE, which implements BCl_3 in the dry etching chemistry. The physical mechanism of flakes formations, which tend to disappear over time, has not been identified, nor their impact on the resonators' performance. Devices fabricated adopting ion milling in place of RIE did not show byproducts after release [53].

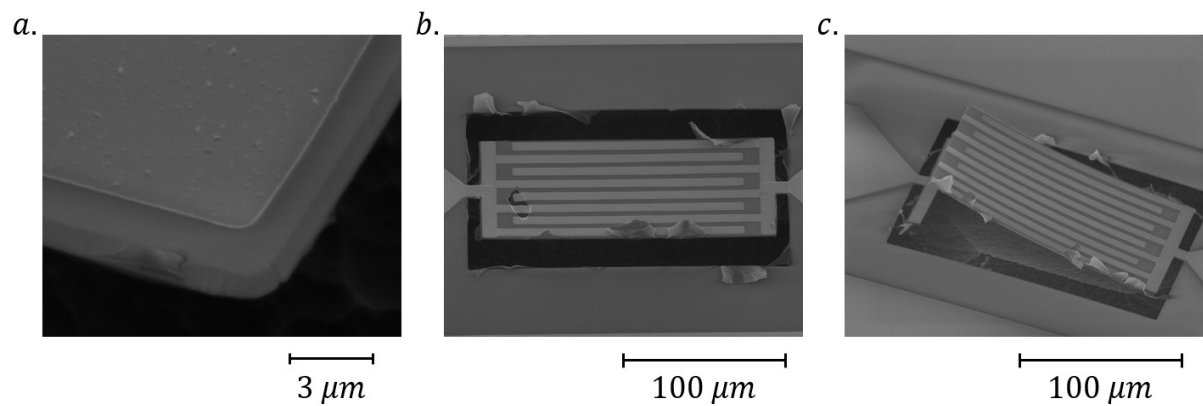


Figure 3.10: (a) Detail of the sidewall angle of a 20% Sc-doped AlN LVR; (b) etch byproduct flakes hanging from the release trench; and (c) Failure of a 1-port LVR due to the elevated film stress gradient.

Stress gradient generated along the thickness direction caused out-of-plane bending in all fabricated devices (Fig. 3.10b) and, in some cases, catastrophic failure of the resonators (Fig. 3.10c). Such stress was estimated around 1 GPA/ μm from test structures included in the tape-out (cfr. Appendix C).

Fabricated devices exhibited a maximum Q_s of 1,240 and k_t^2 of 4.5% at 250 MHz, and a maximum Q_s of 1,500 and k_t^2 of 3.6% at 500 MHz (Fig. 3.11). Further investigations [53] implementing a modified fabrication process did not show any significant improvement in terms of quality factor, and similar values of k_t^2 . Despite improvements on the electromechanical coupling, such FoM (~ 60) are comparable to the performance achieved on AlN LVRs, which makes these devices not suitable for the application targeted in this dissertation.

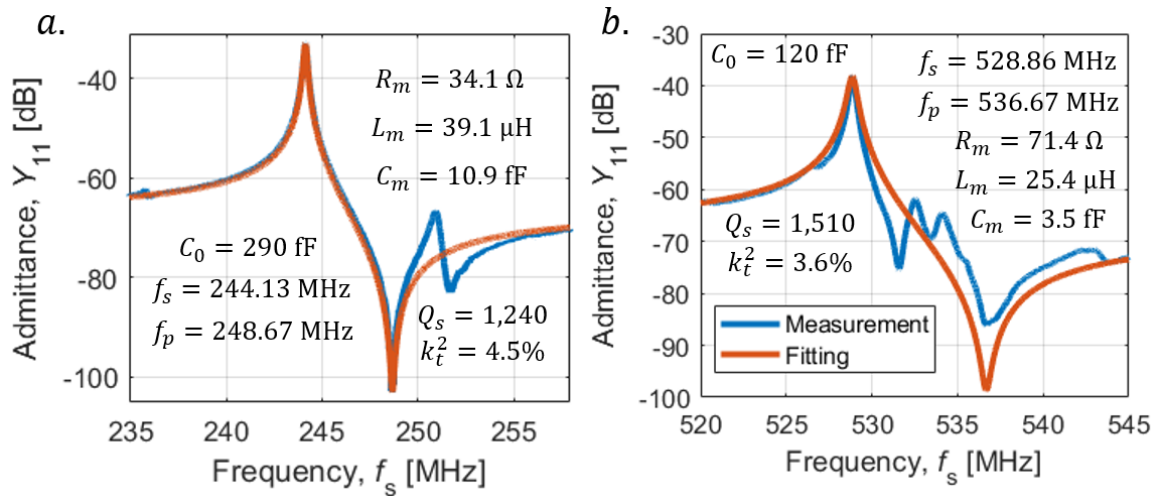


Figure 3.11: Admittance responses of a 20% Sc-doped AlN resonator operating (a) around 250 MHz; and (b) around 500 MHz.

In conclusion, further improvements are necessary to fully harness the potential of Sc-doped AlN films. Recorded Q_s are generally lower than the values recorded in identical AlN devices, meaning that losses mechanism have not been fully identified. Sputtering technology also needs to be improved to provide almost stress-free, high quality ScAlN films that can be reliably

implemented in production lines for mass production. Ultimately, the fabrication process needs to be further refined, with the development of reliable dry or wet etching procedures.

3.2.3. Y-cut Lithium Niobate (LN)

Different cuts and orientations of bulk Lithium Niobate (LiNbO_3 or LN) have been widely used for the fabrication of Surface Acoustic Wave (SAW) resonators in the past decades due to their high intrinsic k_t^2 [59]. In recent years, LN based piezoelectric thin films have been extensively explored for the development of high coupling and high performance resonators [60][61]. Unfortunately, sputtering is not a viable solution since the c-axis oriented (Z-cut) LN is of limited interest, due to the low k_t^2 of lateral modes [62]. For this reason, researchers have focused on thin film transfer technologies to fabricate LN substrates varying from hundreds of nm to few μm . Two technologies have mostly been investigated to fabricate thin film of various LN orientation on Si or SiO_2 carriers: ion-slicing and Surface Activated Bonding (SAB). Ion-slicing [63] implements Helium (He) implanted ions to generate cracks at a controlled depth. The wafer is later bonded to a carrier wafer. Slicing is finally completed by heating up the stacking in a furnace, allowing the cracks generated by the implantation to propagate across the entire wafer diameter. This technique, although very promising for the making of thin, uniform films, resulted in limited transfer yields and material properties that did not match the film bulk values. Another appealing solution is Surface Activated Bonding. In this case, a LN wafer is bonded on a carrier wafer (usually Si or SiO_2) by means of plasma. Two thin layers (~ 10 nm) of SiO_2 and polysilicon are respectively sputtered on the back of

the LN wafer and the carrier to ensure adhesion. As last step, the desired thickness is achieved by Chemical Mechanical Polishing (CMP) and laser trimming to reduce the surface roughness to a few nm. Devices fabricated on SAB wafers showed better performance over ion-sliced ones [31], and have lately become the standard for research and commercial applications.

Among the different cuts, Y-cut Lithium Niobate is of particular interest due to its high d_{31} piezoelectric coefficient and dielectric constant ϵ_{r3} , which makes it a perfect candidate for the making of TFE LVRs. Differently from sputtered AlN thin film, which exhibit an in-plane symmetry due to the c-axis oriented columnar structure, transfer Y-cut films show a high in-plane anisotropy. For this reason, the k_t^2 is a function of the wave propagation direction (θ). Fig. 3.12 shows the dependency of k_t^2 and ϵ_r as a function of θ . Parameters are maximized for $\theta = 0^\circ$ (0° XZ).

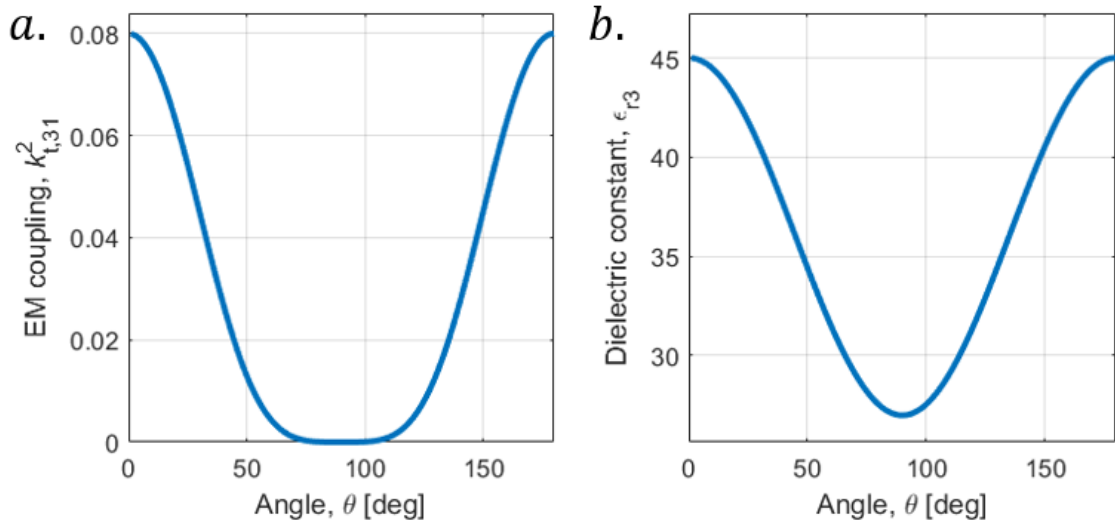


Figure 3.12: (a) EM coupling of TFE lateral mode (3-1) as a function of orientation for Y-cut Lithium Niobate. A global maximum exists at $\theta = 0^\circ$; and (b) relative dielectric constant in the vertical direction as a function of orientation. The global maximum for ϵ_r coincides with the k_t^2 maximum (cfr. Appendix D for details on matrix rotations).

To allow the making of TFE LVRs, the SAB process developed for LN thin film was modified to integrate a Pt layer beneath the piezoelectric layer, as reported in [41]. Despite its theoretical

feasibility, patterned bottom electrodes have not been demonstrated with SAB technologies up to date, due to the surface planarity required by film transferring techniques.

The fabrication process is reported in Fig. 3.13. A thin film of Pt (100 nm) is sputtered on top of a high resistivity (HR) wafer (step 1 in Fig. 3.13). Successively, the LN thin film is transferred on top of the carrier (step 2 in Fig. 3.13) with the SAB process previously described. The process was performed externally by NGK Insulators, Ltd. The patterning of 1-port LVRs is performed with ion milling (step 3 in Fig. 3.13) using a 2 μm SiO_2 hard mask for 1 μm thick LN films. The remaining oxide is later stripped with fluorine based RIE.

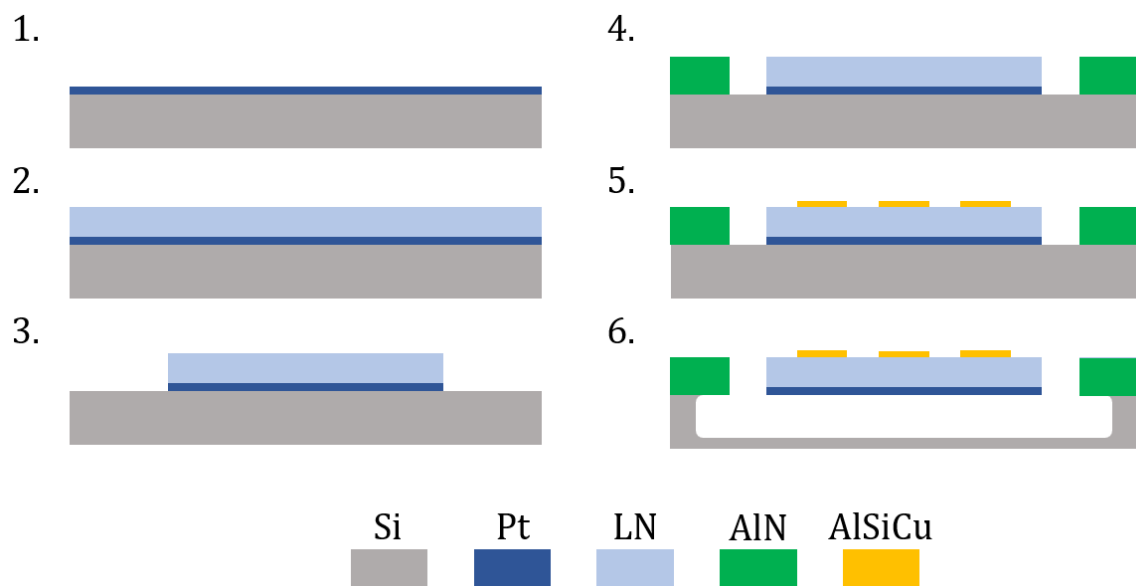


Figure 3.13: Fabrication process of 1-port Y-cut LVRs: (1) Sputtering of a uniform film of Pt on top of an HR Si wafer; (2) SAB of LN film on top of the Si substrate and film polishing and trimming; (3) LN patterning via ion milling; (4) reactive sputtering and patterning of AN via wet etch; (5) top electrode patterning via sputtering and lift-off; and (6) XeF_2 isotropic etching release.

Differently from AN resonators, most of LN around the resonator plate is removed to reduce the amount of parasitic capacitance introduced. To define a rigid, outer frame, a 1 μm film of AN is sputtered on top of the patterned plates. Such layer is later patterned and etched (4) with a wet

process using CD-26 heated up to 55°C and a soft mask of AZ4400. CD-26 contains 2.4% of tetramethyl-ammonium-hydroxide (TMAH), which is able to etch AlN at a rate of about 200 nm/min without attacking Pt or LN. Patterning of top IDEs (5) and resonator release (6) follows the same procedure described for AlN LVRs. A SEM picture of fabricated devices is shown in Fig. 3.14.

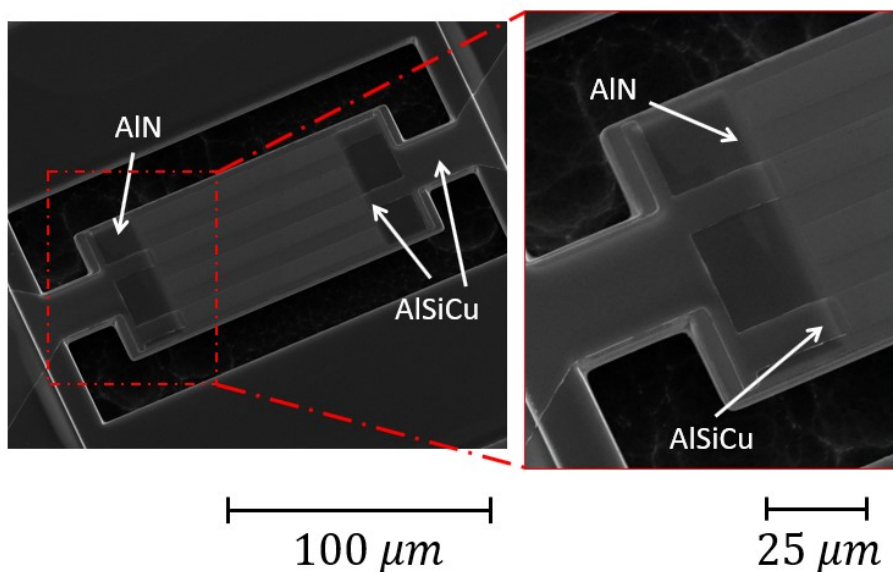


Figure 3.14: SEM image of a fabricated 1-port Y-cut LVR with zoom-in of the anchor, bus and finger-to-bus gap region. A 1 μm AlN patterned layer is deposited to reduce the parasitics introduced by the presence of an unpatterned bottom electrode.

As highlighted in Fig. 3.14, AlN is patterned on top of the LN plate up to the gap region. This design choice is implemented to reduce the impact of parasitic capacitance between the terminals of the device. The lack of a patterned bottom electrode, combined with the high relative dielectric constant of Y-cut LN ($\epsilon_r = 45$), adds a feedthrough capacitance component (C_f , Fig. 3.15a) in parallel with the static capacitance of the resonator (C_0) which effectively decreases the measured k_t^2 ($k_{t,m}^2$, Eq. 3.14). The addition of a layer of AlN, which presents a lower dielectric constant ($\epsilon_r = 9$) helps decreasing the effective ϵ_r ($\epsilon_{r,eq}$, Eq. 3.15) as reported in Fig. 3.15b, ultimately reducing C_f .

$$k_{t,m}^2 = k_t^2 \frac{C_0}{C_0 + C_f} \quad (3.14)$$

$$\epsilon_{r,eq} = \frac{\epsilon_{r,LN} \epsilon_{r,AlN}}{t_{AlN} \epsilon_{r,LN} + t_{LN} \epsilon_{r,AlN}} (t_{AlN} + t_{LN}) \quad (3.15)$$

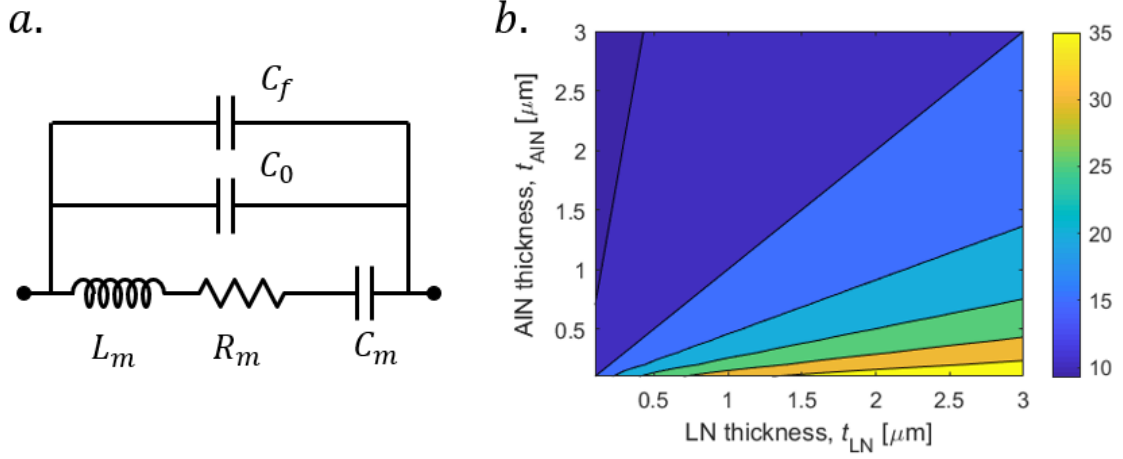


Figure 3.15: (a) Representation of the feedthrough parasitic capacitance (C_f) in a 1-port BVD model; and (b) contour plot of the equivalent dielectric relative constant ($\epsilon_{r,eq}$) of a stacking of Y-cut and AlN as a function of the material thicknesses (t_{LN} and t_{AlN} respectively).

Fabricated devices at 220 and 440 MHz exhibited Q_s around 1,100 – 1,200 and k_t^2 close to 5%, lower than the theoretical prediction (Fig. 3.16). De-embedding was performed on measured data to identify the impact of parasitic feedthrough capacitances (C_f) and electrical loading on k_t^2 and Q_s respectively (Table 3.1). The static capacitance model captured by Eq. 3.5 was utilized to estimate C_0 for both the resonators. C_f was estimated subtracting the estimated value from the measured C_0 . Estimation based on the overlapping area of the bottom electrode and the metallic traces, considering the effective dielectric constant ($\epsilon_{r,eq}$) reported in Eq. 3.15, provided similar results. The series resistance (R_s) model introduced in Section 4.3.2 was similarly used to estimate the electrical loading introduced by the IDTs and the routing.

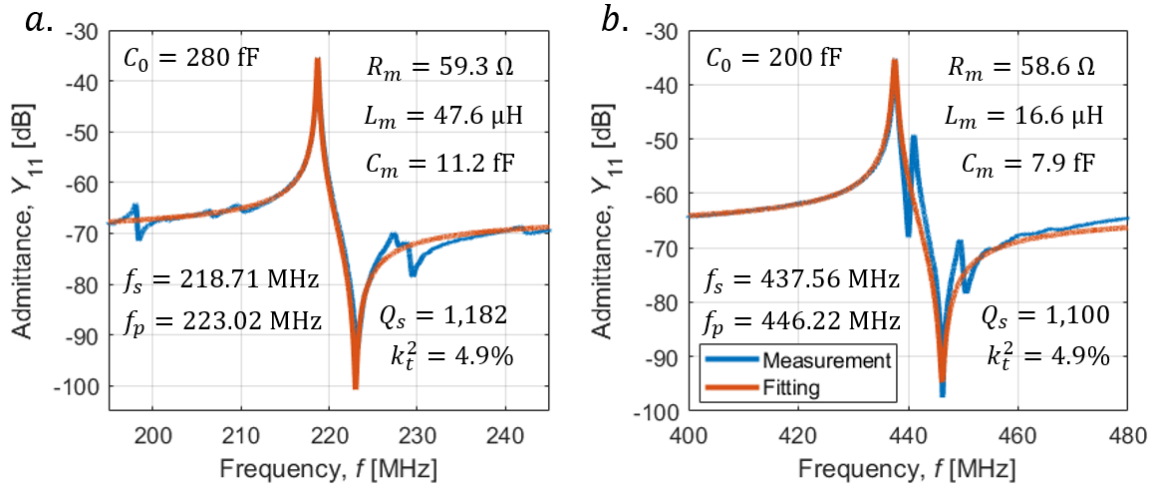


Figure 3.16: Admittance responses of Y-cut LN resonator operating (a) around 200 MHz; and (b) around 400 MHz. De-embedding of C_0 , k_t^2 and Q_s is reported in Table 3.1.

Table 3.1: Measured parameters, geometrical dimensions and estimated R_s , C_0 and C_f for the devices reported in Fig. 3.16. De-embedded k_t^2 and Q_s are also reported.

Parameter	220 MHz	440 MHz
Measured static capacitance (C_0)	280 fF	200 fF
Measured motional resistance (R_m)	59.3 Ω	58.6 Ω
Measured EM coupling (k_t^2)	4.9%	4.9%
Measured quality factor (Q_s)	1,182	1,100
Wavelength (λ)	27 μm	27 μm
Anchors width (W_a)	20.25 μm	9.75 μm
Anchors length (L_a)	20.75 μm	10.25 μm
Number of fingers (N_f)	2	3
Coverage (c)	0.5	0.5
Gap (g)	18.5 μm	7.55 μm
Aperture (L_c)	135.5 μm	104.5
Metal thickness (t_m)	200 nm	300 nm
Modeled static capacitance	180 fF	90 fF
Modeled series resistance (R_s)	10 Ω	5.7 Ω
Feedthrough capacitance (C_f)	100 fF	110 fF
Spurious-free k_t^2	4.9%	3.4%
De-embedded k_t^2	7.6%	7.5%
De-embedded Q_s	1,426	1,220
Figure of Merit (FoM)	58	54
De-embedded FoM	110	92

The de-embedded k_t^2 for both resonators was estimated around 7.5%, close to the theoretical maximum of 8% reported in Fig. 3.12a. De-embedded Q_s show that electrical loading for the geometry under examination has a limited impact on the device performance. Fabrication

complexity and the overall low FoMs recorded (around 60 before de-embedding) show that the state-of-the-art Y-cut LN does not outperform AlN devices, despite promising improvements in terms of k_t^2 .

3.2.4. X-cut Lithium Niobate (LN)

X-cut Lithium Niobate (LN) is another interesting material that has been widely investigated over the past few years for the fabrication of resonators in the hundreds of MHz and low GHz range operating in different modes [63][64].

Differently from Y-cut LN, X-cut LN is appealing due to its high d_{11} piezoelectric coefficient, which can be exploited by LFE LVRs. Fig. 3.17 reports k_t^2 and ϵ_r as a function of the wave propagation direction (θ).

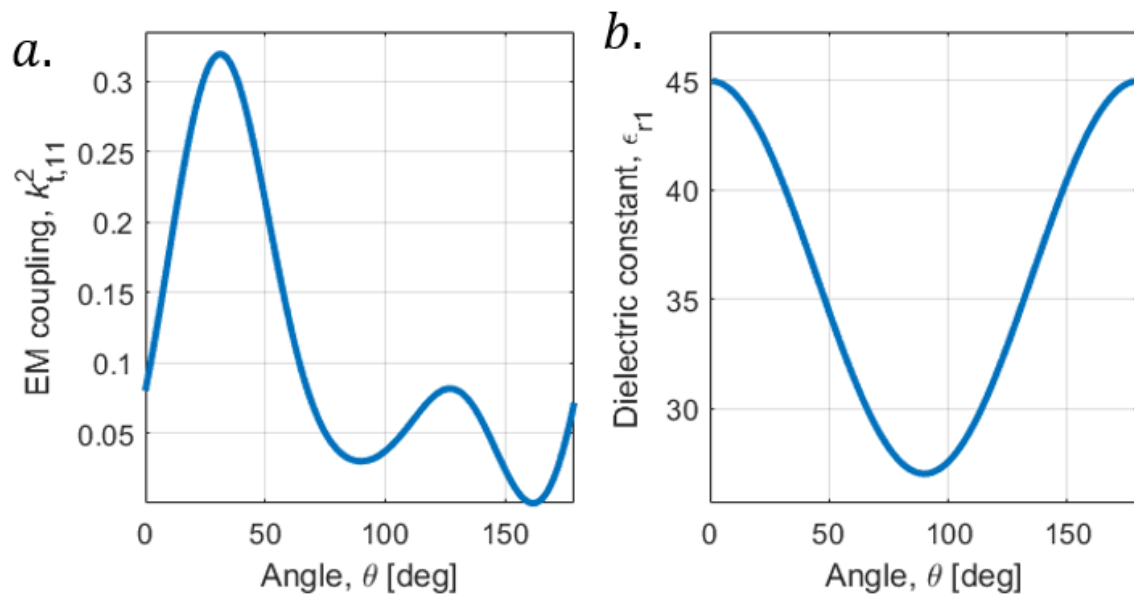


Figure 3.17: (a) EM coupling of LFE lateral mode (1-1) as a function of orientation for X-cut Lithium Niobate. A global maximum exists at $\theta = 30^\circ$; (b) Relative dielectric constant in the lateral direction as a function of orientation. The global maximum for ϵ_r does not coincide with the k_t^2 maximum.

A global maximum for the electromechanical coupling exists for $\theta = 30^\circ$ (YZ 30°), as reported in [62]. The dielectric constant is maximized for $\theta = 0^\circ$, and its equal to 40 at the point of maximum k_t^2 , 4x greater than AlN.

The simplest fabrication process for X-cut LFE LVRs is reported in Fig. 3.18 and consists of two masks, three steps process. Ion-slicing or SAB are used to fabricate a thin film of X-cut LN on top of a carrier, usually high resistivity Si (step 1 in Fig. 3.18). The resonator plates are then patterned with ion milling using a soft PR mask. For 1 μm thick films, 2.5 μm of AZ4210 are sufficient to ensure a good sidewall profile and the complete etch of the lithium niobate. The top electrode is patterned similarly to the procedure described for AlN and Y-cut, with the sputtering and lift-off of a film of AlSiCu (step 2 in Fig. 3.18). Ultimately, resonators are released with a XeF_2 isotropic etching (step 3 in Fig. 3.18).

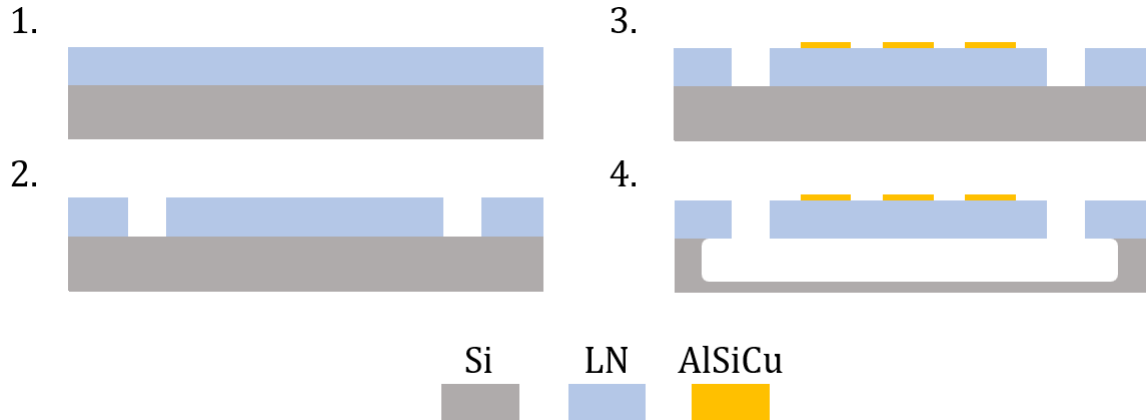


Figure 3.18: Fabrication process of 1-port X-cut LVRs: (1) SAB of LN on HR Si and polishing; (2) LN patterning via ion milling; (3) top electrode patterning via sputtering and lift-off; and (4) XeF_2 isotropic etching release.

Preliminary investigation [65] performed prior to the work described in this thesis demonstrated X-cut LVRs operating in the S_0 mode with k_t^2 of 11.5% and Q_s of 475 around 500 MHz (FoM = 55) on substrates fabricated with ion-slicing technology. Further improvements achieved k_t^2 of 30% and Q_s of 1,200 around 400 MHz (FoM = 360) on SAB substrates.

3.3. Conclusions and Figure of Merit (FoM) Remarks

Table 3.2 summarizes the performance achieved by each technology described in this section in terms of achieved k_t^2 , Q_s and FoM. Among all the demonstrated LVRs, X-cut Lithium Niobate is the most promising in terms of FoM and, thus, passive voltage amplification in the RFFE of the WuRx described in Section 2.

Table 3.2: Recap of the performance demonstrated by the most notable LVRs technologies. $\text{Sc}_{0.4}\text{Al}_{0.6}\text{N}$ and X-cut LN properties and performance are presented as reported in [57] and [66].

Material	Theor. k_t^2	Meas. k_t^2	Q_s	Mode	ϵ_r	CMOS compatible	FoM
AlN	2%	2%	3,900 (250 MHz)	TFE	9	Yes	78
$\text{Sc}_{0.2}\text{Al}_{0.8}\text{N}$	4%	4.5%	1,500 (500 MHz)	TFE	11	Yes	67
$\text{Sc}_{0.4}\text{Al}_{0.6}\text{N}$	10%	8%	-	TFE	13	Yes	-
Y-cut LN (0° XZ)	8%	4.9%	1,200 (200 MHz)	TFE	45	Hybrid	58
X-cut LN (30° YZ)	30%	30%	1,200 (400 MHz)	LFE	40	Hybrid	360

The main disadvantages of such technology are the relatively low capacitance per unit area (Fig. 3.4), and the need for hybrid integration for CMOS interfacing. Both these limitations can be easily overcome if the FoM of X-cut LN LVRs is sensibly larger than any other technology. As highlighted in Fig. 3.5, capacitance matching between C_0 and C_{load} can be traded off for suboptimal, high gains which outperform resonator with smaller FoMs. Similarly, hybrid integration can be tolerated despite the larger parasitics introduced.

In conclusion, preliminary investigation on X-cut Lithium Niobate S_0 mode devices outperformed any other demonstrated LVR technology, thanks to the simultaneously high k_t^2 and

Q_s , which contribute to the overall Figure of Merit. Since the maximum theoretical k_t^2 was demonstrated [31], Q_s is the only remaining lever to further enhance the FoM and, overall, the performance achievable by these devices when implemented in MEMS-based matching networks. This topic is thoroughly discussed in Chapter 4.

CHAPTER 4: X-CUT LITHIUM NIOBATE LVRs

The first demonstration of X-cut Laterally Vibrating Resonators operating in the S_0 mode is reported in [63], where k_t^2 of 8.2% and Q_s around 140 at 530 MHz were attained. Following investigations [67] reported similar electromechanical couplings (9%) at higher frequency (~720 MHz), with similar Q_s . The introduction of active reflectors helped improving k_t^2 up to 12% [65], with Q_s greater than 400 at 500 MHz. Weighted electrodes and improvements in the machining process, in particular on the sidewall angle of LVR suspended plates, made possible the fabrication of devices which exhibited simultaneously high k_t^2 (21%) and high Q_s (~1,300) in the same frequency range [60].

More recently, advancements in the SAB process for the production of thin films, combined with the previous knowledge developed for LN LVRs design and fabrication [68], led to the demonstration of resonators which exhibited k_t^2 close to the theoretical maximum (30%), combined with high Q_s (>1,200) [31][66] around 400 MHz.

Despite the incredibly high electromechanical coupling exhibited, X-cut LVRs have suffered from relatively low Q_s compared to other available technologies based on piezoelectric materials, including AlN FBARs and LVRs (~4,000) [40][69], IHP SAW [70], and crystalline quartz resonators [71]. The values measured for current state-of-the-art resonators are in fact far from the main sources of losses (electron-phonon dissipation, piezoelectric-semiconductor loss, air damping, Akhieser damping, and thermo-elastic damping) reported in [72], and generally from the expected performance of devices fabricated on single crystal substrate, rather than sputtered films.

Preliminary investigation performed with Finite Element Analysis (FEA) in COMSOL[®] using Perfectly Matched Layer (PML) boundary conditions, highlighted Q_s greater than 20,000 for the anchor losses alone [72]. These facts hint that a thorough characterization of damping mechanism is necessary to fully understand the limitation of such technology and synthesize LVRs that can exhibit Q_s greater than few thousands.

As highlighted in Section 3.3, for IoT applications, Q_s must be maximized while preserving a high k_t^2 to maximize the overall Figure of Merit, while roughly matching the static capacitance of the device to the one of the input load (C_{load}). This last constrain is particularly severe for X-cut LVRs operating in the LFE mode due to their low capacitance per unit area. Fig. 4.1 reports the required area to match different loads, as a function of the operating frequency. Especially for large loads and low frequency of operation, the dimension of the resonators poses serious challenges in terms of design and fabrication and could severely impact their performance.

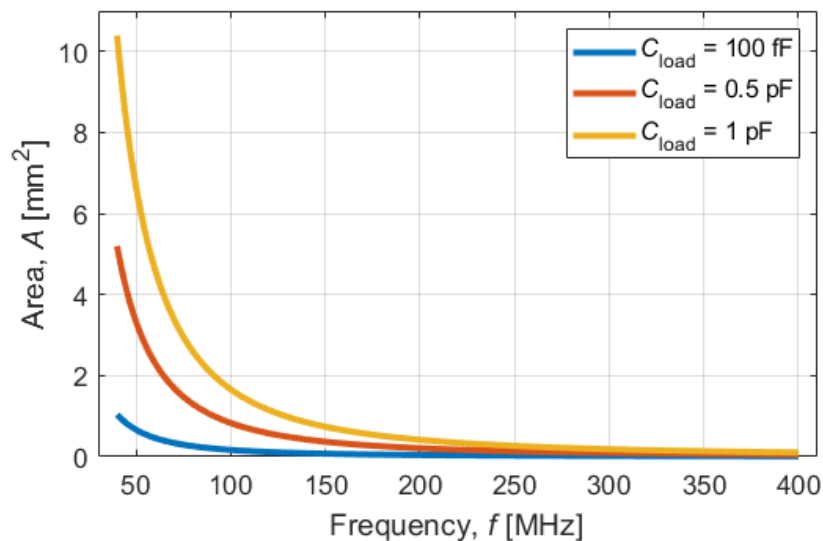


Figure 4.1: Active area required by X-cut LVRs to match different capacitive loads assuming a parallel plate capacitor, $C_0 = C_{load}$, $c = 0.3$, $v_p = 5,800$ m/s, $t_{LN} = 2$ μ m, $N_p = 1$, and $\epsilon_r = 40$.

Following these considerations, it becomes clear that the design of an optimized X-cut LVRs to be implemented in the MN of a ULP WuRx must take into account the trade-off between the operating frequency, matching to C_{load} , size, fabrication complexity, and the need to maximize k_t^2 and Q_s simultaneously.

In the first part of this chapter, preliminary studies on 50 MHz devices are reported. These studies are further expanded up to 550 MHz in the following section. A few devices operating around 800 MHz and 1 GHz are also demonstrated. In the third and last section, the main sources of damping are investigated according to the data collected on all the fabricated resonators.

4.1. Design and Fabrication of 50 MHz devices

According to the RMR optimization reported in Section 3.1.2, a frequency of 50 MHz was selected for the preliminary investigation of high performance X-cut LVRs. This frequency offers a sweet spot for the system level demo. In fact, lower frequencies offer a larger impedance conversion, thus larger gain, for a fixed C_{load} , which ultimately increases the system sensitivity. Furthermore, no restrictions were provided by the project funder on the design and sizing of the antenna, which would have otherwise limited the implementation of system operating below few hundreds MHz.

From a resonator stand-point, lower frequencies are generally associated with lower damping [73], thus larger Q_s can be achieved to showcase the potential of a technology. Larger devices are also less sensitive to lithography misalignments and overetch, which have proven to impact the quality factor of LVRs [72]. Compared to higher frequency resonators, which have usually a far

more compact footprint, 50 MHz devices are more prone to breakage due to the stresses induced by the sputtered metal traces on top of the thin piezoelectric film. Therefore, the preliminary investigation on large devices also serves to testbench the fabrication process regarding this specific issue.

For the example under examination, a reference C_{load} of 1 pF was assumed for the sizing of the X-cut LVRs, to simulate the typical input capacitance of a MEMS demodulator or CMOS ED [20]. A static capacitance (C_0) of 1 pF was also targeted for the sake of simplicity. Different approaches can be implemented to increase the total capacitance of an X-cut LVR operating in the LFE mode: 1) Increase the electrode coverage (c); 2) increase the thickness of the piezoelectric film (t_{LN}); 3) increase the aperture (L_e) and thus the area of transduction; 4) Increase the number of pairs (N_p); and 5) arraying a finite number of individual resonators (N_{el}) in parallel.

Increasing the finger coverage proved to be a counter-productive choice since larger values of c are associated with a severe k_t^2 reduction, as reported in [72]. Differently from TFE modes, where a thinner piezoelectric film is required to increase the capacitance per unit area, thicker films help increasing the C_0 for devices operating in the LFE mode. Unfortunately, the increase in C_0 does not scale linearly with t_{LN} as reported in Section 3.1.1. Furthermore, thicker film machining renders plate patterning more complex and leads to poorer sidewall angles, which are a fundamental feature in LVRs to attain high Q_s . For this reason, a maximum thickness of 2 μm was set as a limit for the fabrication of 50 MHz devices. Similarly to c , the choice of L_e and N_p impacts the anchor losses and therefore the overall Q_s . The effects of geometry on Q_s can be reasonably investigated via Finite Element Analysis (FEA) to identify an optimal geometry.

The investigation reported in this Section is based on the preliminary work reported in [31] and [66]. The results highlighted will be further expanded and extended to higher frequency in the following sections.

4.1.1. COMSOL[®] Simulations

The device active region, or aperture (L_e), and the number of fingers pairs (N_p) were identified as the most interesting parameters to vary to increase the static capacitance (C_0) of individual resonators, as mentioned in Chapter 3 and in the introduction of the present chapter. The impact of these geometry features on the quality factor (Q_s) was investigated via COMSOL[®] Finite Element Analysis (FEA) to provide significative insights on the optimal design of X-cut LVRs. The energy leakage through the anchors was modeled via Perfectly Matched Layers (PMLs) strategically positioned around the resonator frame, as reported in Fig. 4.2.

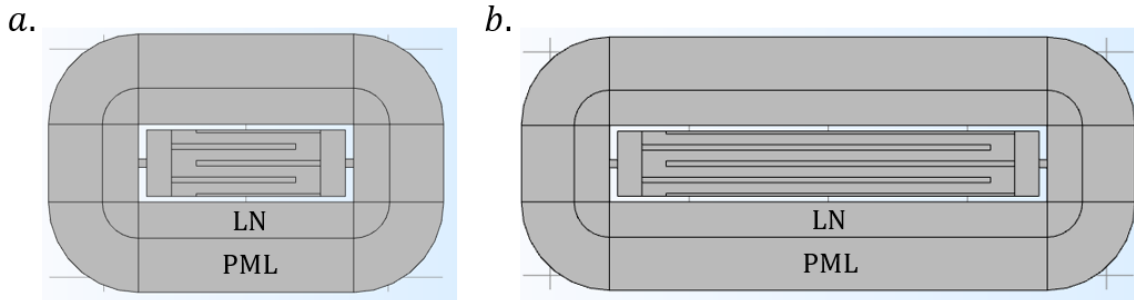


Figure 4.2: COMSOL[®] models of LVRs operating around 100 MHz with an aperture of: (a) 3λ ; and (b) 11λ . PML boundaries are also pictured (outer frame).

Two sets of simulations were designed to independently verify the impact of L_e and N_p on the quality factor (Q_s). A λ of 116 μm was set to ensure the device operation around 50 MHz. The aperture was swept from 3λ to 13λ for a constant number of fingers pairs equal to 3, while the N_p was swept from 3 to 11 for a constant L_e of 11λ . The fingers-to-bus gap (g) and the bus length (L_b) were set to 0.75λ according to previous investigation on AlN LVRs [74] to maximize acoustic

reflection. Anchors width (W_a) and length (L_a) were set to 0.25λ . The LN substrate thickness was fixed to $2 \mu\text{m}$, which represents an optimal tradeoff between ease of fabrication and maximum achievable capacitance per unit area. Ultimately, the top electrode metal was fixed to 200 nm to reduce the impact of any series resistance (R_s) without impacting the main resonance [75].

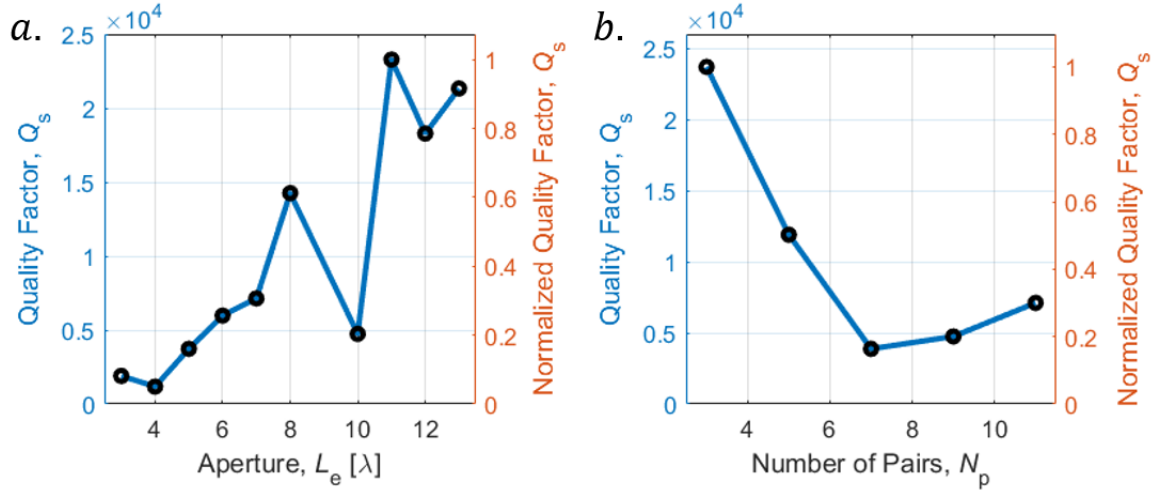


Figure 4.3: COMSOL® simulated quality factors (Q_s) as a function of (a) aperture (L_e); and (b) Number of pairs (N_p).

The aperture simulation (Fig. 4.3a) highlighted that longer plates for fixed N_p showcase higher Q_s . The maximum Q_s ($\sim 25,000$) was recorded for $L_e = 11 \lambda$. Plates with aperture larger than 13λ were not investigated due to concern regarding electrical loading and fabrication yield rate. While increasing N_p theoretically helps increasing the static capacitance of the device (Eq. 3.7 – 3.8), COMSOL® simulations showed a drastic reduction in Q_s (Fig. 4.3b) for devices with larger number of fingers. Intuitively, slender geometries help better confining the vibrational energy in the central region of the resonator (Fig. 4.4a vs. Fig. 4.4c), reducing anchor leakage phenomena.

Interestingly, the simulation of the expected Q_s as a function of L_e is strongly not monotone, showing large performance dips at $L_e = 10$ and 12λ . This phenomenon can be explained by closely looking at the admittance response of the simulated resonators and at the mode shape exhibited by the plates at resonance (Fig. 4.4b). The strong anisotropy exhibited by the lithium niobate crystal,

which is reflected by the density of the piezoelectric matrices [76], makes LN LVRs more prone in exhibiting spurious modes compared to other material technologies. Transversal modes have proven to be particularly severe in conventional plate geometries, causing mode conversion [77] and Q_s degradation when too close to the resonant frequency. This phenomenon is very well captured by the mode shape reported in Fig. 4.4b for an aperture (L_e) equal to 10λ .

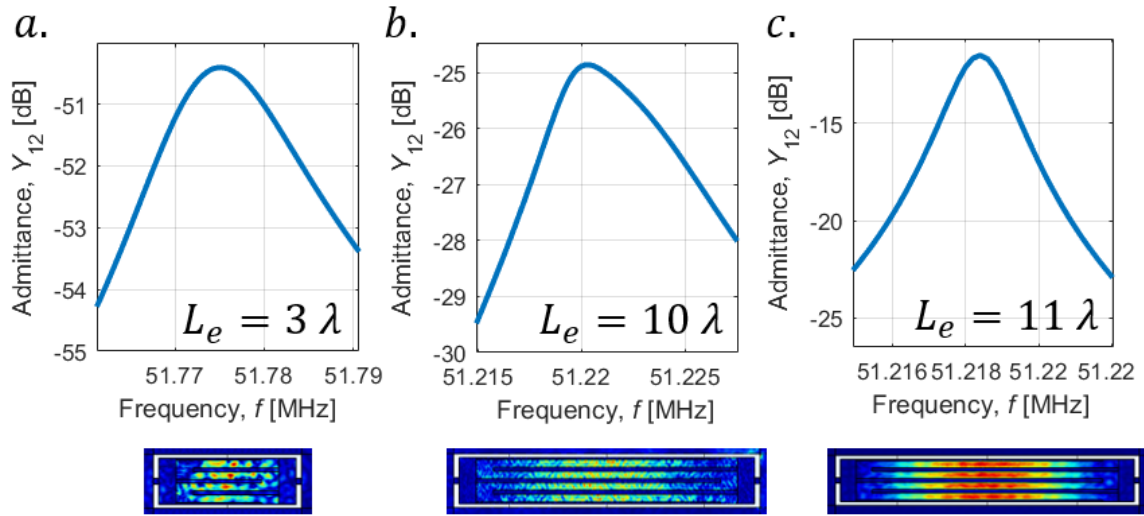


Figure 4.4: Zoom-in of resonance peaks of simulated X-cut LN LVRs for different values of aperture: (a) $L_e = 3 \lambda$; (b) $L_e = 10 \lambda$; and (c) $L_e = 11 \lambda$. Shorter plates exhibit more anchor losses (a) than slender plates (c).

4.1.2. Experimental Plan and Fabrication

According to the results provided by COMSOL[®] FEA simulations, an optimized geometry to maximize Q_s while maintaining high k_t^2 and modest C_0 is identified (Fig. 4.5). Throughout this section, this geometry is referred to as the optimized or standard geometry. The design parameters of such device are reported in Table 4.1.

Starting from the standard resonators, four different experimental plans were designed to investigate the impact of geometry on Q_s , varying one-factor-at-a-time: aperture (L_e), anchor width (W_a), gap (g), and coverage (c). Table 4.1 reports the variations of each parameter from the standard geometry. Since the optimized geometry shows a static capacitance (C_0) of about 110 fF, according

to FEA simulations, an array of 9 resonators was also included in the tape-out to attain a device with a total capacitance of 1 pF.

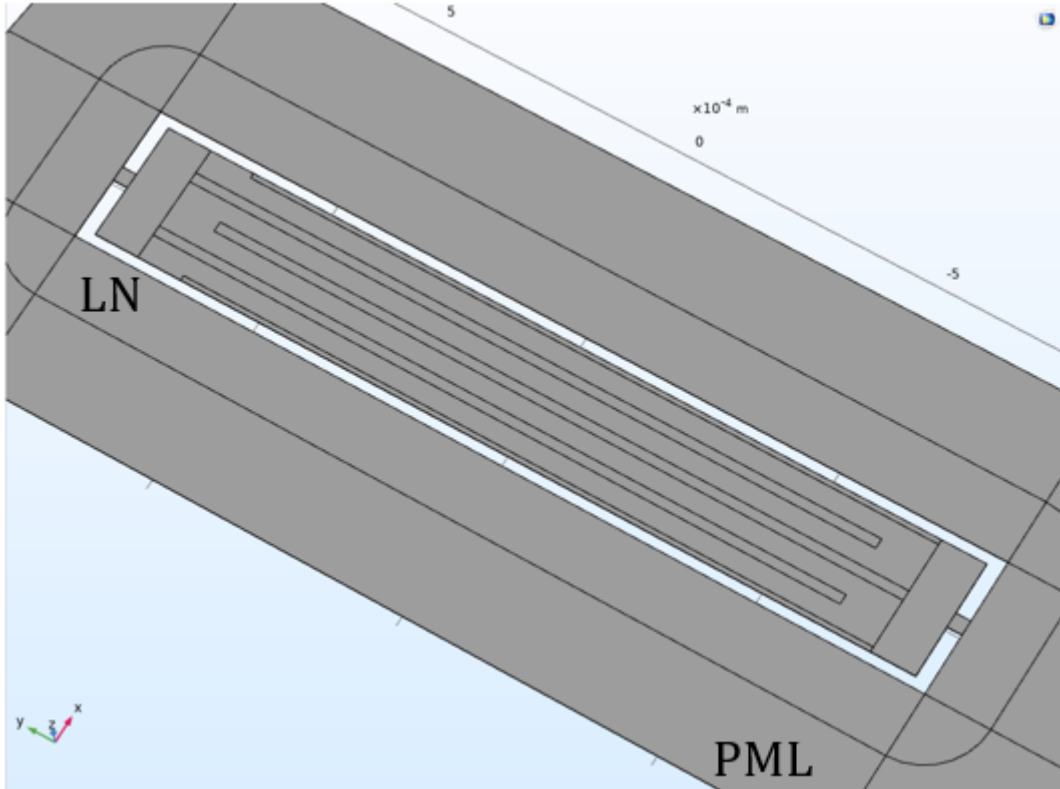


Figure 4.5: COMSOL[®] model (with reference system) of the standard resonator with PML boundary conditions. The resonator parameters are listed in Table 4.1.

Table 4.1: Standard geometry parameters.

Variable	Value	Variable	Value
Wavelength (λ)	116 μm	Nominal frequency (f_s)	50 MHz
Aperture (L_c)	11 λ	Plate length (L)	14 λ
Number of pairs (N_p)	3	Plate width (W)	2 λ
Bus length (L_b)	0.75 λ	Gap (g)	0.75 λ
Anchor width (W_a)	0.25 λ	Anchor length (L_a)	0.25 λ
Coverage (c)	0.3	Substrate thickness (t_{LN})	2 μm
Metal thickness (t_m)	200 nm		

Table 4.2: Experimental parametric investigation.

Variable	Values
Anchor width (W_a)	0.125 – 0.25 – 0.375 – 0.5 – 0.675 0 – 0.75 λ
Gap ^a (g)	0.25 – 0.75 – 1.25 – 1.75 – 2.25 – 2.75 λ
Coverage (c)	0.3 – 0.5 – 0.8
Aperture (L_c)	8 – 11 – 14 λ

^aFor the gap study, the length of the plate was fixed to $L = 16 \lambda$ instead of 14 λ .

Devices were fabricated with the process described in Section 3.2.4 on a 2 μm X-cut LN substrate provided by NGK. Details of the fabrication process are reported in Appendix A.

SEM pictures of individual and arrayed fabricated resonators are reported in Fig. 4.6. Due to the dimensions of the resonators, the overetch ($\sim 0.5 \mu\text{m}$) can be considered negligible (Fig. 4.7). The measured sidewall angle of fabricated devices (φ) is greater than 80° (Fig. 4.7a), a value which is commonly considered optimal for the minimization of losses and spurious modes generated by the backscattering of acoustic waves [78].

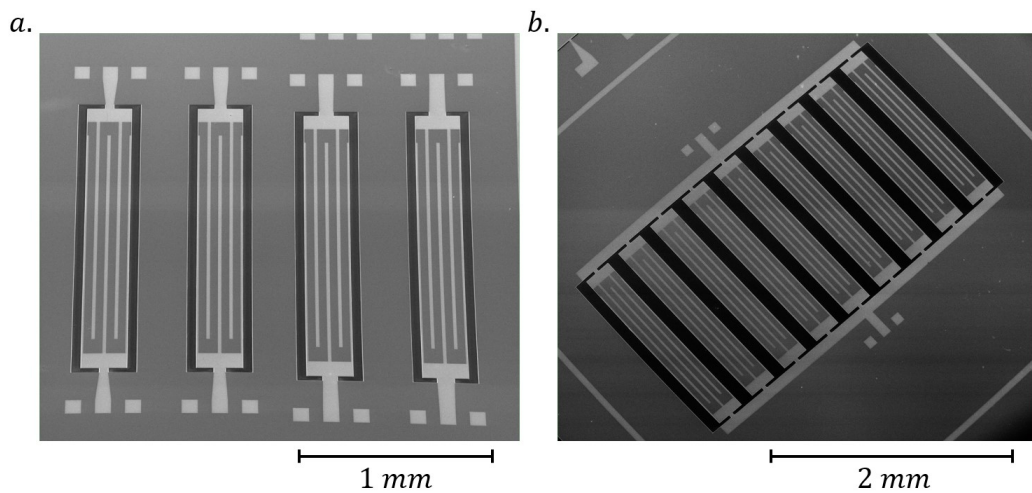


Figure 4.6: SEM pictures of: (a) individual X-cut LVRs. The depicted devices are part of the anchor variation test. Grounds were wire-bonded before measurements to provide a common reference to the VNA ports; and (b) a device constituted by 9 arrayed standard resonators. A large metal bus is implemented to connect the terminals of each device.

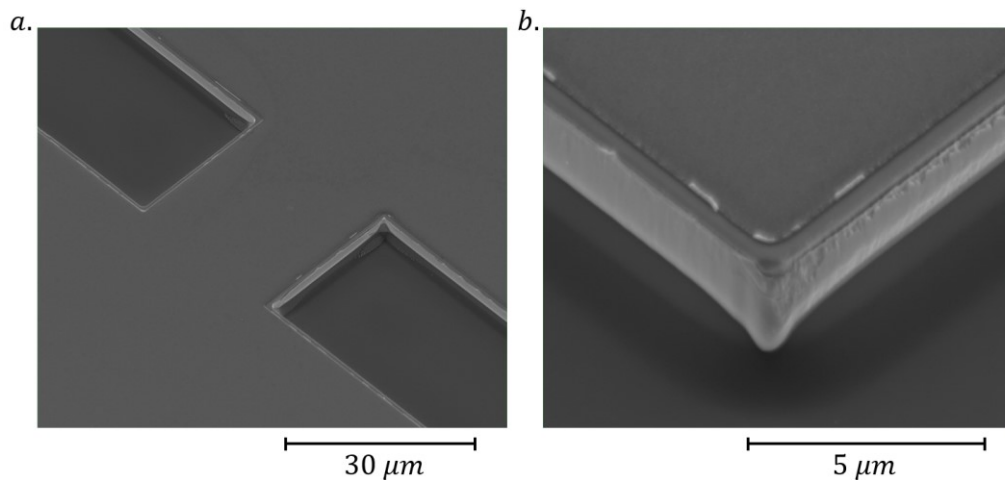


Figure 4.7: (a) Detail of the anchor region of a resonator; and (b) angled SEM image picturing the edge of a resonator. The measured sidewall angle (φ) is greater than 80° . Devices fabricated via ion milling experience irregular patterning in the corner region due to sharp-tip effect. Lift-off residuals are also noticeable, but their impact on performance was considered negligible given their small size with respect to the operating wavelength.

4.1.3. Device Characterization

Fabricated devices were wafer-probed in laboratory conditions ($T = 293$ K and $P = 760$ mTorr), in vacuum ($T = 293$ K, $P < 10^{-3}$ Torr) and at different temperatures (as low as 130 K) with GSG150 probes in a 2-port configuration to extract their characteristic response. S-parameters were recorded with an Agilent N5230A VNA and later converted into Y-parameters via software (MATLAB®). 95% Confidence Intervals (95% C.I., or 2σ) are reported when more than 5 data points were collected.

The impact of device aperture (L_e) is reported in Fig. 4.8a. A global optimum exists for $L_e = 11 \lambda$ and confirms the intuition of the existence of a trade-off between anchor losses and the electrical loading introduced by the IDTs. This point of trade-off is expected to be a different value of L_e for different frequencies for a fixed geometry in terms of λ , since R_s does not scale as R_m over frequency.

Anchors losses have been widely investigated as damping mechanism in AlN LVRs [44]. According to COMSOL® simulations, slender plates help attaining higher Q_s due to a better acoustic energy confinement. Under this hypothesis, the effect of anchors should be negligible for relatively long resonators ($L_e > 7 \lambda$ at 50 MHz). This effect was never shown in AlN LVRs due to the difficulty of fabricating devices with a high L/W ratio, mainly related to the intrinsic stress gradient introduced by the reactive sputtering techniques necessary to fabricate thin piezoelectric films. According to experimental data (Fig. 4.8b), W_a does not impact Q_s for devices with an L_e of 11λ .

As for the anchor width, the gap size (g) was previously identified as a key parameter affecting the amount of energy leaking through the substrate [45], and ultimately Q_s . Fabricated devices with fixed plate length ($L = 16 \lambda$) show a clear relationship between quality factor and gap, as reported

in Fig. 4.8c. Similarly to L_e , a larger gap is believed to facilitate the energy confinement in the resonator active region, hence enhancing Q_s while reducing the energy leakage through the anchors.

Interestingly, larger gaps do not impact the k_t^2 , up to $g = 2.75 \lambda$.

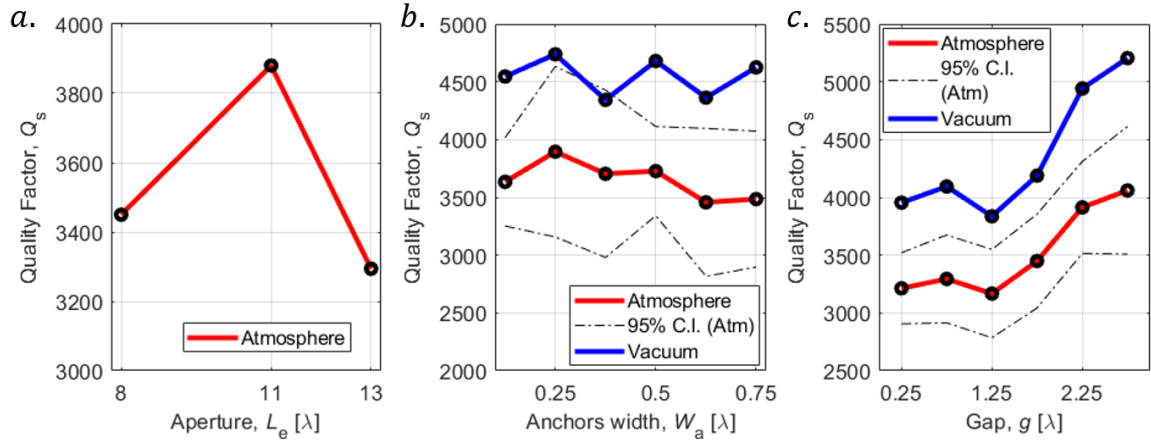


Figure 4.8: Impact of different geometrical variables on the Q_s of fabricated 50 MHz devices: (a) aperture (L_e); (b) anchors width (W_a); and (c) finger-to-bus gap (g).

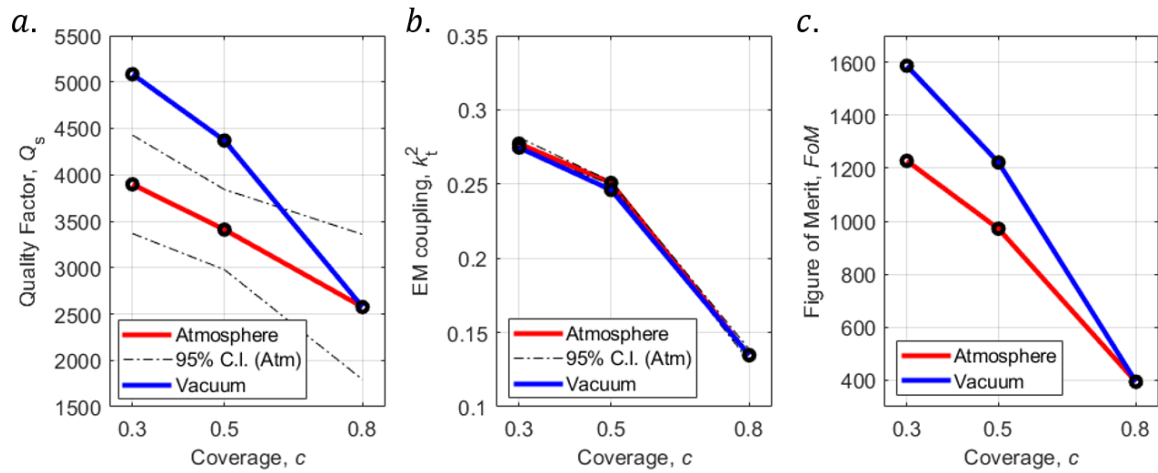


Figure 4.9: Impact of electrode coverage (c) of fabricated 50 MHz devices on: (a) quality factor (Q_s); (b) electromechanical coupling (k_t^2); and (c) Figure of Merit.

Lastly, the effects of coverage on Q_s were investigated. A larger coverage is desirable since it increase the achievable capacitance per unit area, both for resonators operating in TFE and LFE mode. Unfortunately, the optimal coverage that maximizes k_t^2 for S_0 mode X-cut LVRs is achieved for $c = 0.3$ as reported in previous publications [65]. As reported in Fig. 4.9a, there is no advantage

in operating with larger coverage because the quality factor closely follows the reduction in k_t^2 (Fig. 4.9b). This effect directly translates to a reduction of the Figure of Merit as c increases (Fig. 4.9c).

Quality factors in the order of 4,500 - 5,000 were consistently recorded on devices with different geometries measured under vacuum, with an average increase of 20% from atmosphere condition (Fig. 4.10). Air damping proved to be a significant source of losses only above few Torrs, making commercially available vacuum package a viable solution to fully harness the performance of these devices (Fig. 4.10b).

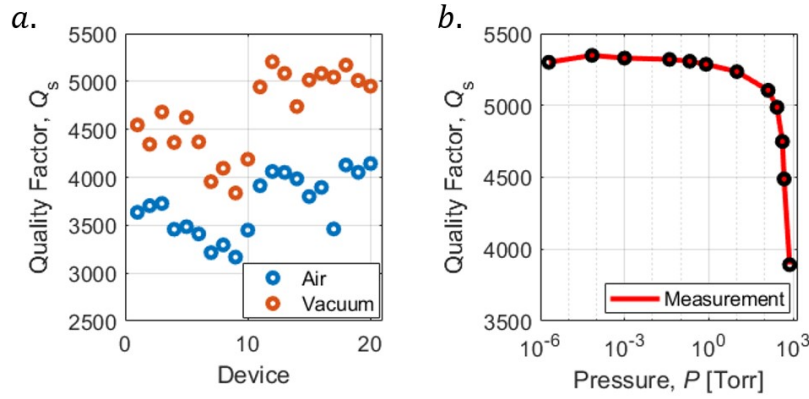


Figure 4.10: (a) Scatter plot of devices tested in air (blue dots) and under vacuum (red dots). Devices measured under vacuum showed a 20% increase in Q_s ; and (b) quality factor of a resonator with optimized geometry as a function of pressure. Maximum performance are attained in the sub-Torr range.

Electromechanical couplings as high as 28% were recorded on devices with a coverage (c) equal to 0.3. The k_t^2 was estimated with the arctangent method (Eq. 4.1), which provides the most conservative results and complies with the BVD model reported in Section 2.1.3.

$$k_t^2 = \frac{\pi f_s}{2 f_p} \arctan\left(\frac{\pi f_s}{2 f_p}\right) \quad (4.1)$$

As reported in [23], for low intrinsic k_t^2 , methods tend to converge to a unique value. This approximation is no more valid when the electromechanical coupling surpasses 10%. Previous results on X-cut LVRs [66] showing k_t^2 as high as 30% utilized a different definition, reported by

Eq. 4.2. Adopting this definition for the devices under examination would provide values of k_t^2 as high as 31.5%, which has been reported in literature [79].

$$k_t^2 = \frac{\pi^2}{4} \left(1 - \frac{f_s}{f_p} \right) \quad (4.2)$$

Measurements in vacuum of optimized devices highlighted resonators exhibiting both high Q_s and k_t^2 . The device showing the highest recorded Figure of Merit at 50 MHz, defined by Eq. 4.3 [26], is reported in Fig. 4.11. k_{eff}^2 represents the effective coupling coefficients [23] and is defined by Eq. 4.4. All the measured devices experience severe in-band spurious modes, which have been accurately predicted by COMSOL® FEA preliminary investigations. Interestingly, the quality factors of such spurious are reduced for lower gap values and maximized for larger g , as the Q_s of the S_0 mode (Fig. 4.11b).

$$FoM = Q_s \left(\frac{k_{eff}^2}{1 - k_{eff}^2} \right) \quad (4.3)$$

$$k_{eff}^2 = \frac{f_p^2 - f_s^2}{f_p^2} \quad (4.4)$$

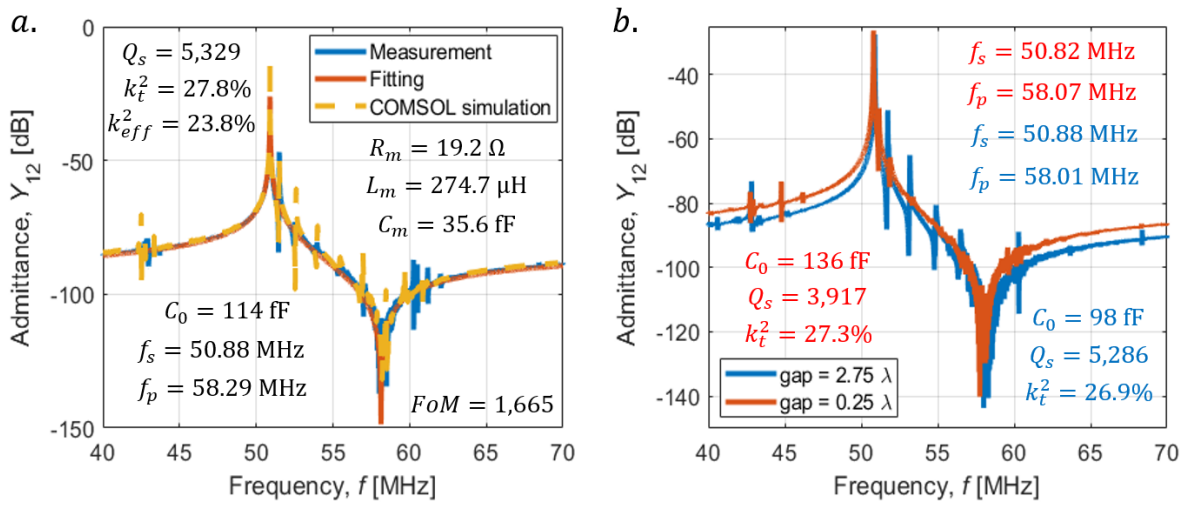


Figure 4.11: (a) Admittance response of the optimized X-cut LVR (measured in vacuum) showing the highest Figure of Merit recorded during the testing phase. COMSOL® simulation of the device under investigation is reported, showing good agreements between numerical prediction and experimental measurements. A feedthrough capacitance of 20 fF and a frequency shift of 0.2 MHz were added to consider the effects of non-idealities neglected by the FEA model; and (b) admittance response of X-cut LVRs with different g .

Cryogenic measurements performed between 130 K and 293 K on devices with different geometries found a strong linear dependency between the quality factor and the temperature (Fig. 4.12a), especially in the 130 K – 250 K range. AlSiCu resistivity was extracted from de-embedding structures included in the tape-out (Fig. 4.12b) as a function of temperature in the range 180 – 293 K. The high Q_s recorded at 130 K (up to 10,000) and the linear behavior hints that the electrical loading introduced by the IDEs plays a major role as a damping factor in determining the measured Q_s . No measurements were performed below 130 K due to the sudden breakage of devices at the interface of the release region, likely due to stresses induced by thermal contraction (Fig. 4.13). Starting from the cryogenic measurement of an optimized device, the linear and quadratic Temperature Coefficients of Frequency (TCF_1 and TCF_2 , respectively) were extracted (Fig. 4.12c). The model adopted to describe the change in resonant frequency as a function of the temperature is captured by Eq. 4.5, where f_{s0} represents the series resonant frequency measured at $T_0 = 293$ K. Results are in line with the values reported in literature of X-cut Lithium Niobate resonators [72], with measured TCF_1 and TCF_2 of -75 ppm/K and -121 ppb/K², respectively.

$$f_s(T) = f_{s0}[1 + TCF_1(T - T_0) + TCF_2(T - T_0)^2] \quad (4.5)$$

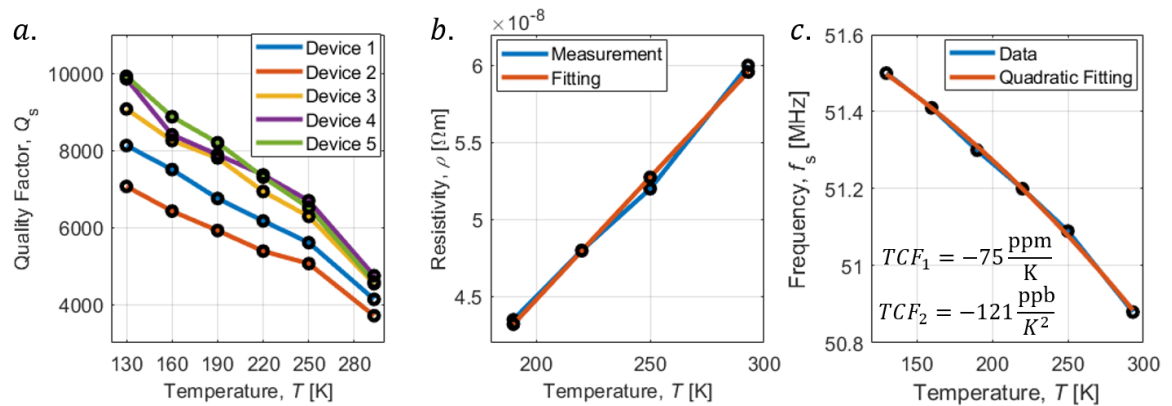


Figure 4.12: (a) Quality factor as a function of temperature for different investigated devices; (b) AlSiCu Resistivity (ρ) as a function of temperature; and (c) resonant frequency as a function of temperature.

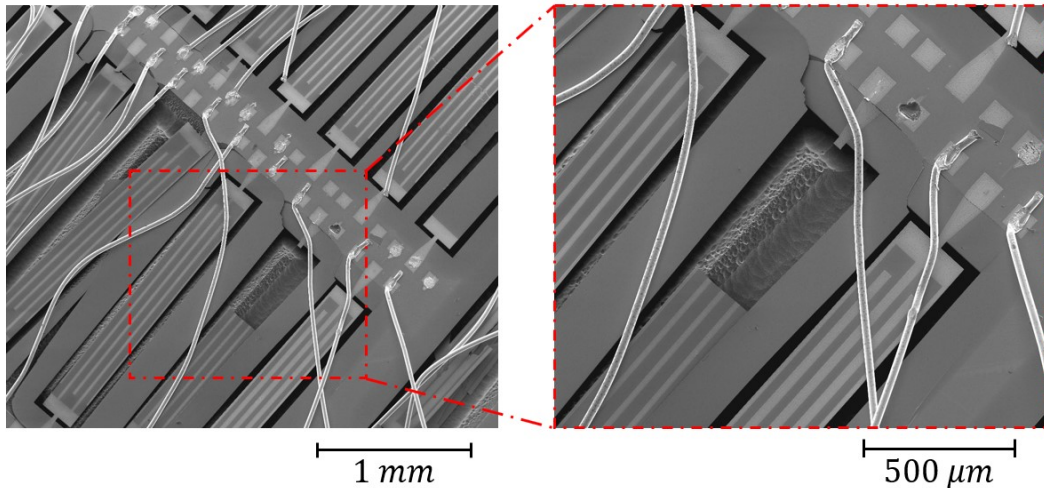


Figure 4.13: SEM picture of tested X-cut LVRs failed during cryogenic tests due to stresses induced by thermal contraction. Note that in this set of devices, ground pads on opposite sides of the resonator were connected via wirebonds.

A wide-span measurement was also performed on the fabricated device exhibiting the best performance in terms of Figure of Merit (Fig. 4.14). Weak SH_0 mode and its first harmonic were recorded around 33 and 103 MHz, respectively. Odds harmonic of the S_0 mode were recorded at integer multiples of the anti-resonant frequency (f_p), as the 2nd and 4th harmonics. These modes proven to be very weak and highly damped and are likely present due to fabrication non-idealities.

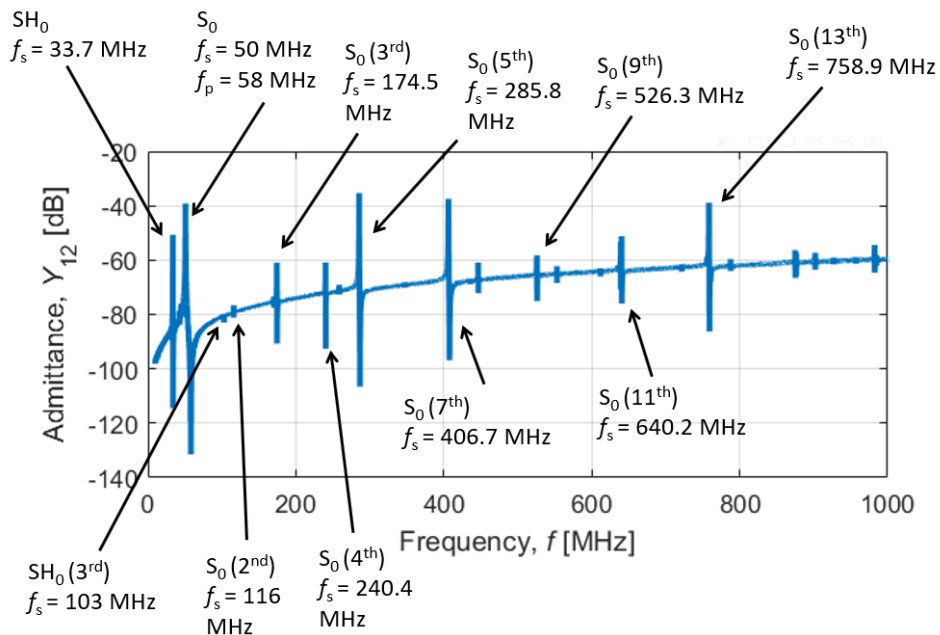


Figure 4.14: Wide-span admittance response of an optimized X-cut LVR measured under vacuum. Identified modes and resonant frequencies (f_s) are reported. Harmonics of the S_0 mode are present at multiple integers of the anti-resonance frequency of the main mode (f_p).

Table 4.3 recaps f_s , Q_s , k_t^2 and the $f_s \cdot Q_s$ product for all the identified modes. Q_s were recorded only for modes showing clear responses at resonance to allow 3-dB extraction. Harmonics of the S_0 mode, and in particular the 3rd, 5th, 9th and 11th showed particularly high $f_s \cdot Q_s$ products, comparable to values reported in literature [80], which could be exploited for the fabrication of low noise oscillators.

Table 4.3: Identified modes exhibited by an optimized X-cut LVR and main extracted parameters. Modes at 33.72, 102.99, 115.99, 240.35, and 406.1 MHz showed noisy or split peaks, which prevented the extraction of Q_s .

Mode	Harmonic	f_s [MHz]	Q_s	k_t^2	$f_s \cdot Q_s$	Notes
SH ₀	1	33.72	-	2.18%	-	Noisy peak
S ₀	1	50.88	5,329	27.8%	2.7e11	Highest FoM recorded
SH ₀	3	102.99	-	-	-	Noisy peak
S ₀	2	115.99	-	-	-	Noisy peak
S ₀	3	174.46	22,630	0.27%	4e12	-
S ₀	4	240.35	-	0.13%	-	Noisy peak
S ₀	5	285.7	5,300	1.06%	1.5e12	-
S ₀	7	406.81	-	0.73%	-	Noisy peak
S ₀	9	526.25	23,600	0.07%	1.3e13	-
S ₀	11	640.18	16,410	0.15%	1e13	-
S ₀	13	758.81	2,200	0.26%	1.7e12	-

4.1.4. Arrays Performance

The admittance response of an array measured in air constituted by 9 optimized elements is reported in Fig. 4.15a. Compared to an individual resonator, arrays showcase a sensibly lower Q_s (~1,800 vs. 4,000) and thus a reduced Figure of Merit. Data collected from identical copies of the optimized resonator, not arrayed in a single structure (Fig. 4.15b) pointed out that frequency mismatch between elements is likely the cause of quality factor degradation experienced by arrays. Table 4.4 recaps the statistical variations recorded for f_s , Q_s , k_t^2 and C_0 in 8 identical, adjacent resonators, and the resonant frequency recorded for each device. While measured Q_s , k_t^2 and C_0

variations can be considered modest, the mismatch in f_s is considered severe enough to impact the array performance.

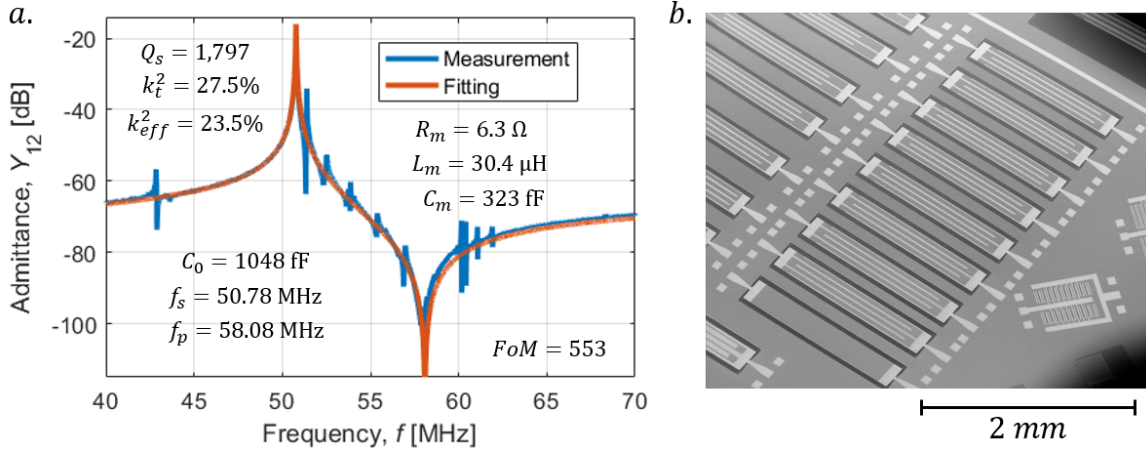


Figure 4.15: (a) Admittance response of an array constituted by 9 optimized parallel LVRs, measured in air; and (b) SEM image of identical standard resonators measured to characterize the statistical distribution of f_s , Q_s , k_t^2 and C_0 .

Table 4.4: Statistical distribution of f_s , Q_s , k_t^2 and C_0 measured on 8 identical standard resonators. Resonant frequency as a function of the position are also reported.

Variable		Average (μ)			Standard deviation (σ)			
Resonant frequency (f_s)		50.844 MHz			0.004 MHz			
Quality factor (Q_s)		3,900			50			
EM coupling (k_t^2)		0.27			0.003			
Static capacitance (C_0)		115.7 fF			0.89 fF			
Device	1	2	3	4	5	6	7	8
f_s [MHz]	50.8430	50.8412	50.84555	50.8410	50.8409	50.8444	50.8466	50.8486

To prove this hypothesis, an in-air break-test was performed on the resonator array. Devices were manually broken starting from the outer elements towards the inner ones. The admittance was measured after each iteration, for a total of 9 distinct measurements. As reported by Fig. 4.16a, Q_s sharply increases as the number of elements decreases, while k_t^2 remains overall constant (Fig. 4.16b). As expected, C_0 linearly varies with the number of elements (Fig. 4.16c).

The test pointed out that a relationship between the number of elements (N_{ei}) and Q_s exists, likely due to frequency mismatch between parallel devices. Such source of degradation will be further investigated, among other losses mechanisms, in Section 4.3.5.

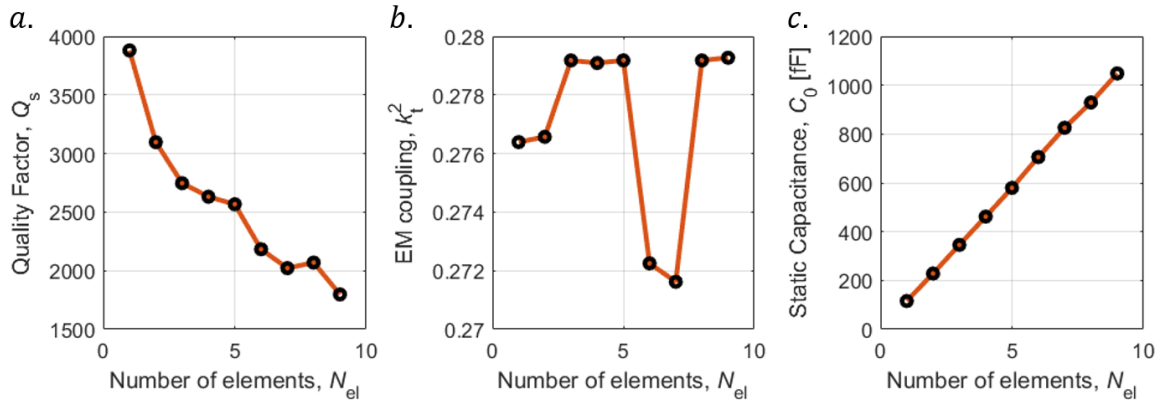


Figure 4.16: Impact of the number of elements recorded during the break-test on these measured quantities: (a) quality factor; (b) electromechanical coupling; and (c) static capacitance.

4.2. Design and Fabrication of Higher Frequency Devices

4.2.1. Experimental Plan and Fabrication

The incredibly high performance attained with 50 MHz X-cut LVRs, which exhibit Figure of Merits more than four times higher compared to commercially available resonators [13], fostered the investigation of devices at higher frequency, which can be exploited for IoT, filtering and time referencing applications. The experimental plan developed for 50 MHz devices was extended up to 1 GHz to validate the design and the results attained at low frequencies. Table 4.5 reports the investigated frequencies, including the selected wavelengths. COMSOL[®] FEA simulations were performed on the optimized geometry reported in Table 4.1 to identify the λ that approached the desired operating frequencies. For each f_s , the relative pitch (p), finger width and reflector width (assuming $c = 0.3$), which also represents the minimum feature size of the device, are also reported.

Table 4.5: Investigated frequencies and rounded wavelengths for S_0 mode resonators.

Frequency (f_s)	Wavelength (λ)	Pitch (p)	Fingers width ($c = 0.3$)	Reflectors width ($c = 0.3$)
50 MHz	116 μm	58 μm	17.4 μm	8.7 μm
100 MHz	56 μm	28 μm	8.4 μm	4.2 μm
200 MHz	30 μm	15 μm	4.5 μm	2.25 μm
400 MHz	15 μm	7.5 μm	2.25 μm	1.13 μm
550 MHz	11 μm	5.5 μm	1.65 μm	0.83 μm
800 MHz	8 μm	4 μm	1.2 μm	0.6 μm
1 GHz	6 μm	3 μm	0.9 μm	0.45 μm

Since preliminary results at 50 MHz pointed out that the electrical loading coming from the interconnects and the IDEs is one of the main sources of Q_s degradation, a study on the variation of top electrode metal thickness (t_m) was performed via FEA. Investigations on AlN LVRs demonstrated the impact of different metals and thicknesses on damping (especially TED [81]) and electromechanical coupling. COMSOL[®] simulations (assuming $t_{LN} = 2 \mu\text{m}$, aluminum as top electrode metal and the optimal geometry reported in Table 4.1) highlighted a dependency between spurious modes and metal thickness (t_m). The analysis shows that thicker electrodes are associated with more severe in band spurious modes (Fig. 4.17) across the entire frequency range of interest.

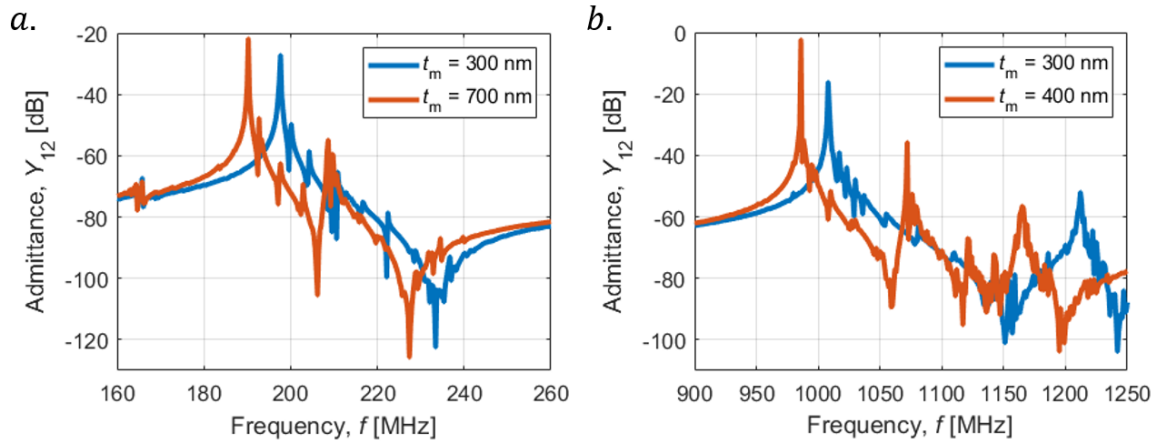


Figure 4.17: COMSOL[®] simulated admittance response capturing the impact of Al thickness (t_m) on the spurious modes at (a) around 200 MHz; and (b) around 1 GHz. The out-of-band mode showcased at around 1.2 GHz for $t_m = 300 \text{ nm}$ is a thickness mode and it is not caused by the metal thickness.

Furthermore, the maximum tolerable thickness before the insurgence of unwanted modes is a function of the resonant frequency as reported in Fig. 4.18a, meaning that low h/λ ratios can handle thicker electrodes, and further reduce R_s . In order to minimize the fabrication complexity, a thickness of 300 nm was selected. Interestingly, the k_t^2 is not affected by the metal thickness (Fig. 4.18b), likely due to the positioning of the electrodes at the anti-nodes of the generated standing wave [82].

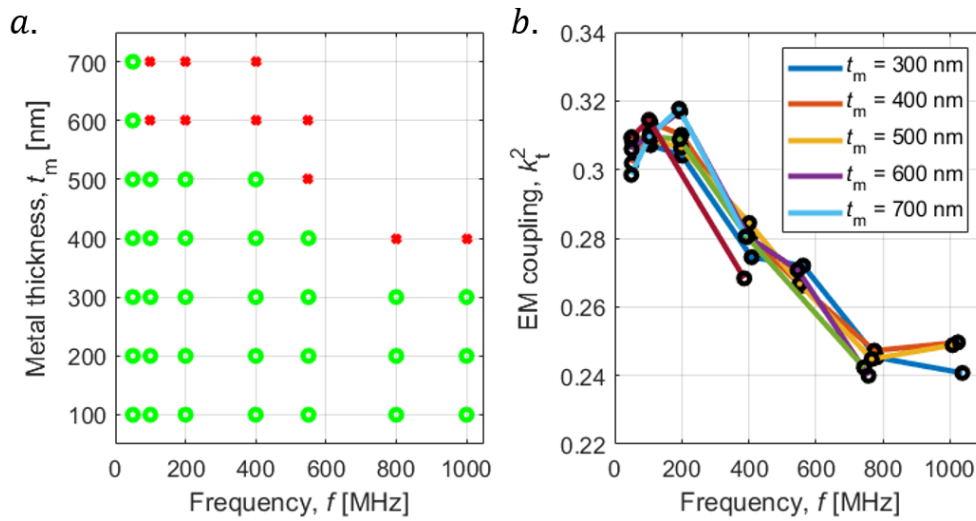


Figure 4.18: (a) Extended results of the COMSOL[®] investigation on the effect of Al thickness (t_m) on the severity of spurious modes. Red dots represent simulations showcasing severe spurious modes (as in Fig. 4.17); and **(b)** maximum theoretical k_t^2 as a function of frequency and metal thickness. t_m does not impact the maximum achievable electromechanical coupling.

Similarly to the experimental plan implemented for 50 MHz devices, a standard geometry was identified (Table 4.6) and variations were designed around such geometry. Few 50 MHz devices with different apertures (L_e) and gaps (g) were included in the tape-out (Table 4.7) to verify the results attained in previous runs. The main set of variations for each frequency under investigation is reported in Table 4.8 and includes more extended aperture, anchor width and gap tests compared to the preliminary tests reported in Section 4.1. The anchor width (W_a) test is performed in fact with three different levels of aperture, to quantify the impact of anchor losses on plates with different aspect ratios. The gap variation test is performed on plates with two different lengths (10 and 14 λ)

for similar reasons. Due to the compactness of devices operating at higher frequency, more data points were included both for L_e and g tests.

Table 4.6: Standard geometry constant parameters.

Variable	Value	Variable	Value
Number of pairs (N_p)	3	Plate width (W)	2λ
Bus length (L_b)	0.75λ	Gap (g)	0.75λ
Anchor width (W_a)	0.25λ $0.75 \lambda (>400$ MHz)	Anchor length (L_a)	0.25λ $0.75 \lambda (>400$ MHz)
Coverage (c)	0.3	Substrate thickness (t_{LN})	1 - 2 μm
Metal thickness (t_m)	300 nm		

Table 4.7: Experimental plan for 50 MHz devices.

50 MHz variations experimental plan		
Variable (primary)	Variable (secondary)	Values
Aperture (L_e)	-	3 - 7 - 11 λ
Gap (g)	-	0.25 - 0.75 - 2.25 - 3.75 λ

Table 4.8: Experimental plan for 100, 200, 550 and 800 MHz devices.

100, 200, 550, and 800 MHz variations experimental plan			
Variable (primary)	Value	Variable (secondary)	Value
Aperture (L_e)	3 - 5 - 7 - 9 - 11 - 13 λ	-	-
Anchor width (W_a)	0.25 - 0.5 - 0.75 - 1 - 1.25 - 1.5 - 1.75 - 2 λ	Aperture (L_e)	3 - 7 - 11 λ
Gap ^I (g)	0.25 - 0.75 - 1.25 - 1.75 - 2.25 - 2.75 - 3.25 - 3.75 λ	Plate length (L)	10 λ
Gap ^{II} (g)	0.25 - 0.75 - 1.25 - 1.75 - 2.25 - 2.75 - 3.25 - 3.75 - 4.25 - 4.75 - 5.25 - 5.75 λ	Plate length (L)	14 λ

Experimental test on devices operating at 400 MHz and 1 GHz was further expanded, with the inclusion of coverage (c) variations in addition to a denser aperture (L_e) test (Table. 4.9). Arrays with different numbers of elements (N_{el}) and repetition of devices were included for statistical variation analysis.

Table 4.9: Experimental plan for 400 MHz and 1 GHz devices.

400 MHz and 1 GHz variations experimental plan			
Variable (primary)	Value	Variable (secondary)	Value
Aperture (L_e)	3 – 4 – 5 – 6 – 7 – 8 – 9 – 10 – 11 – 12 – 13 – 14 λ	-	-
Anchor width (W_a)	0.25 – 0.5 – 0.75 – 1 – 1.25 – 1.5 – 1.75 – 2 λ	Aperture (L_e)	3 – 7 – 11 λ
Gap ^I (g)	0.25 – 0.75 – 1.25 – 1.75 – 2.25 – 2.75 – 3.25 – 3.75 λ	Plate length (L)	10 λ
Gap ^{II} (g)	0.25 – 0.75 – 1.25 – 1.75 – 2.25 – 2.75 – 3.25 – 3.75 – 4.25 – 4.75 – 5.25 – 5.75 λ	Plate length (L)	14 λ
Coverage (c)	0.1 – 0.2 – 0.3 – 0.4 – 0.5 0.8	Aperture (L_e)	3 – 7 – 11 λ

By a fabrication stand-point, the investigation of X-cut LN LVRs poses serious challenges. The width of the active reflectors, necessary to exploit the substrate high piezoelectric coupling, approaches sub-micron dimensions slightly above 400 MHz, assuming $c = 0.3$ (Table 4.5). This fact, combined with the need of increasing the top electrode thickness to minimize R_s , makes the lift-off of the IDTs an impractical solution. To accommodate for smaller feature sizes, the process flow described in Section 4.1.2 was modified, as depicted in Fig. 4.19.

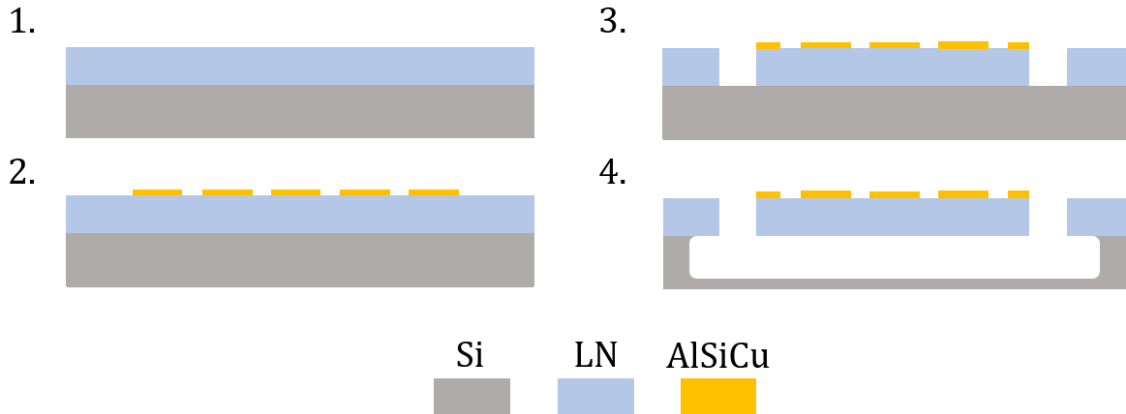


Figure 4.19: Modified fabrication process for X-cut LVRs: (1) SAB substrate fabrication; (2) top electrode sputtering and patterning via RIE; (3) ion milling patterning; and (4) XeF₂ isotropic release.

In this improved fabrication process, a thin film (300 nm) of AlSiCu is first sputtered on top of the LN surface. The IDTs and interconnects are then patterned via Cl-based Reactive Ion Etching (RIE) using a dark field mask and a positive, thin resist (S1805) to resolve minimum feature sizes up to 500 nm (step 2 in Fig. 4.19). The fabrication of the IDTs before the LN etching process also minimizes any contamination of the top surface, which can impact the adhesion of the metallic film and thus the resonator performance. The top electrode is then masked by the thick PR layer used to pattern the resonator plate, to protect it during the ion milling step (step 3 in Fig. 4.9). Devices are ultimately released via XeF₂ isotropic etch (step 4 in Fig. 4.9). A more accurate description of the fabrication process is reported in Appendix A.

Despite fabrication process improvements, reflectors patterning above 400 MHz still posed severe challenges due to the proximity of the minimum feature size to the maximum resolution allowed by the i-line stepper currently available at the CMU Nanofab Facility (0.5 μm). To bypass this issue, devices at 550 MHz, 800 MHz and 1 GHz were taped-out with reflectors having the same width as the central fingers. In this configuration, named “self-aligned reflectors”, the correct dimensioning of the outer IDTs relies on the patterning of the resonator plates via ion milling, which effectively serves to etch the unnecessary portion of the reflectors. A comparison between the regular reflector layout and the self-aligned version is reported in Fig. 4.20. This approach heavily relies on the alignment accuracy of the lithographic tool, and on the accurate prediction of the lateral overetch (Fig. 4.20) during ion milling. An overetch of 0.5 μm was added on each edge of the resonator anchors and plate according to previous experiments. A simplified analytical model for the calculation of the overetch is reported in Appendix E.

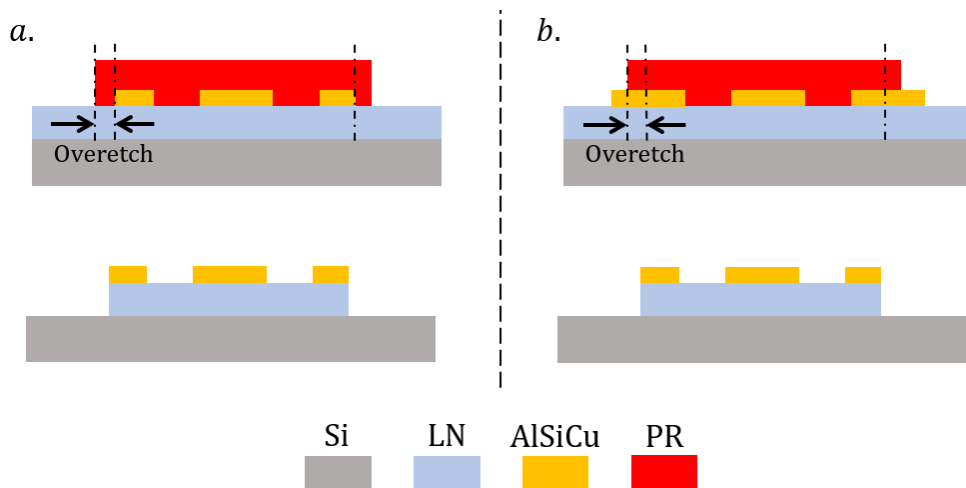


Figure 4.20: Comparison between: (a) lithographically defined reflectors; and (b) self-aligned reflectors.

Fig. 4.21 reports various examples of fabricated devices on 1 μm and 2 μm thick X-cut LN films, at different frequencies. Devices in the range 50 – 550 MHz proven to be working, validating both the approaches for the electrode patterning. Unfortunately, due to misalignment during the lithographic definition of the resonator plates, devices operating above 550 MHz showcase a partially etch reflector. Such misalignment was quantified to be 200 nm and is visible both in devices operating at relatively low frequency (200 MHz, Fig. 4.22a-b) and high frequency (1 GHz, Fig. 4.22c). The impact of the misalignment is particularly severe in the latter case, since the damage sensibly narrows one of the edge active reflectors, disconnecting it from the bus. This effect causes a change in the electrical boundary condition, which results in the excitation of different modes with lower coupling coefficients and the insurgence of split peaks.

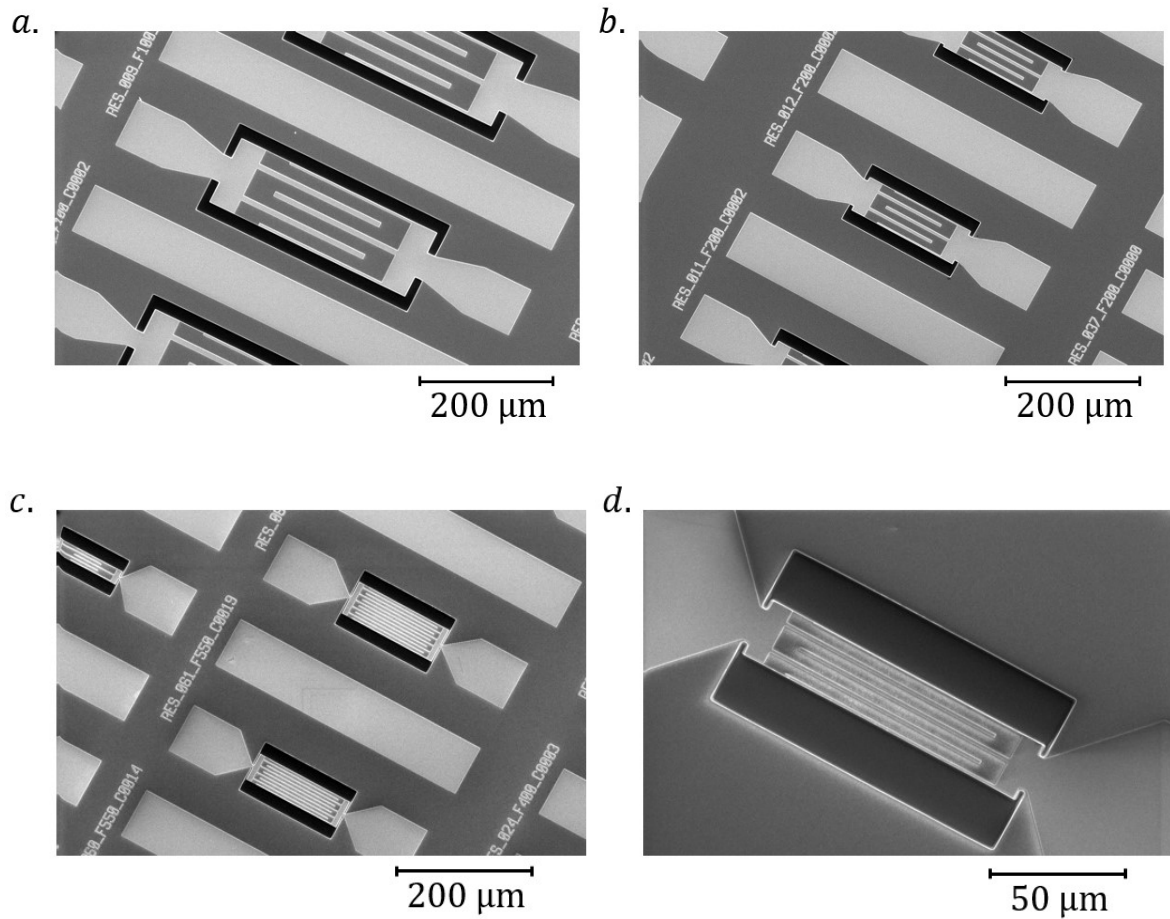


Figure 4.21: SEM of fabricated X-cut LVRs operating around: (a) 100 MHz; (b) 200 MHz; (3) 400 MHz; and (4) 550 MHz.

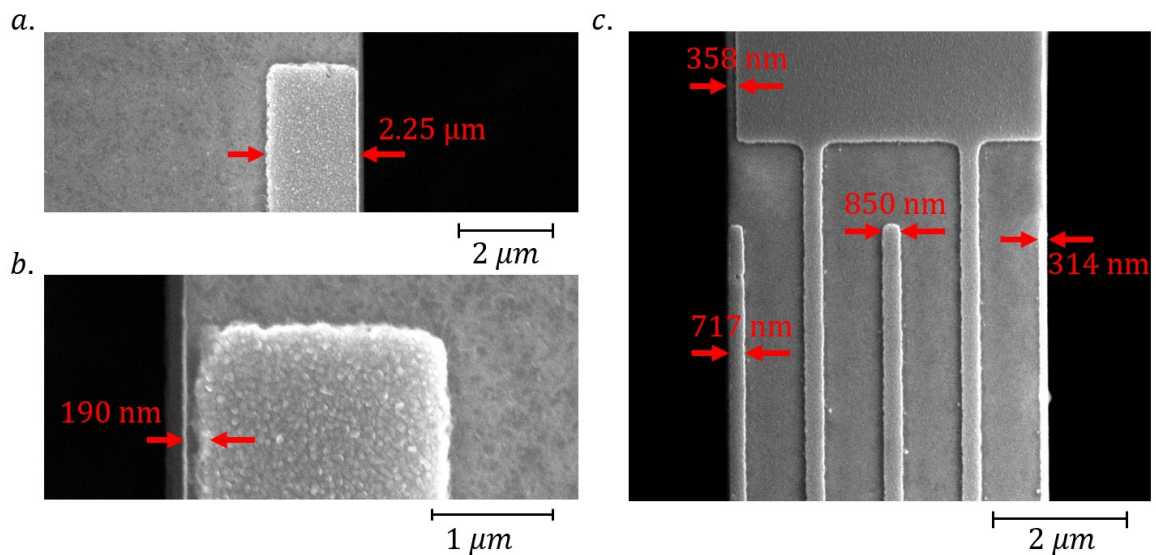


Figure 4.22: Effect of fabrication process non-idealities on 200 MHz: (a) right reflector; (b) left reflector. The 200 nm misalignment between the etch mask and the top electrode mask is clearly visible. (c) Effects of fabrication non-idealities on a 1 GHz device. The etching of the right electrode caused low yield rate and failure on most of the devices.

4.2.2. Device Characterization

Fabricated devices were characterized with the approach described in Section 4.1.3. The investigation focused on devices fabricated on 1 μm , which showed a better yield and more consistent results after preliminary measurements. Measurements in atmosphere, vacuum and at cryogenic temperature (50 K) were performed on most devices. Compared to previous cryogenic measurements on 50 MHz resonators, devices at higher frequencies did not suffer from breakage due to thermally induced stresses. A subset of devices, consisting in anchor variations (with an aperture of 3 and 7 λ) and aperture variations were measured from laboratory conditions (293 K) to cryogenic temperature (50 K) in step of 40 K to evaluate the change in Q_s as a function of temperature (T). Few devices were measured at a base temperature of 10 K.

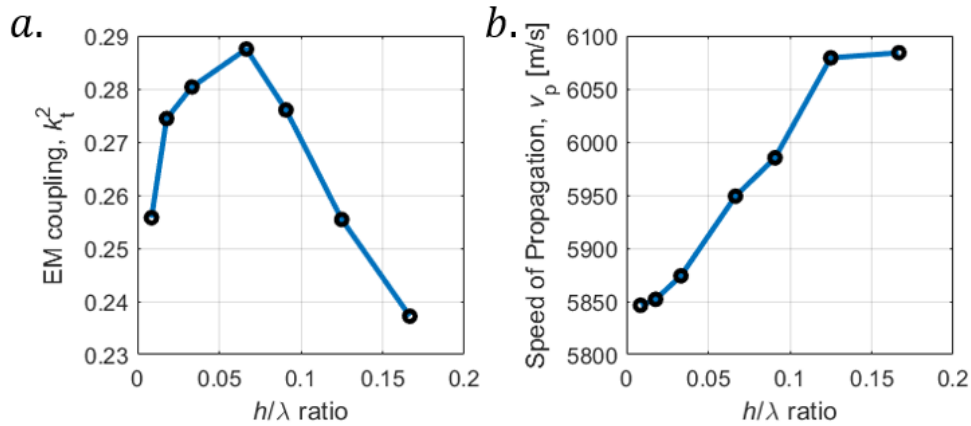


Figure 4.23: (a) Measured electromechanical coupling (k_t^2) as a function of h/λ ratio; and (b) dispersion curve measured on X-cut LN (YZ 30°) LVRs.

The measured average electromechanical coupling (k_t^2) and the average speed of propagation (v_p) evaluated during preliminary measurements are reported in Fig. 4.23. The results are consistent with the values reported in literature [62] and the COMSOL[®] simulations summarized in Fig. 4.18. Fig. 4.24 reports four scatterplots showing the measured quality factor in air and in vacuum for

every tested device, divided by resonant frequency. As expected, air damping has a larger impact on devices operating at lower frequency. Air damping will be analyzed in detail in Section 4.3.1.

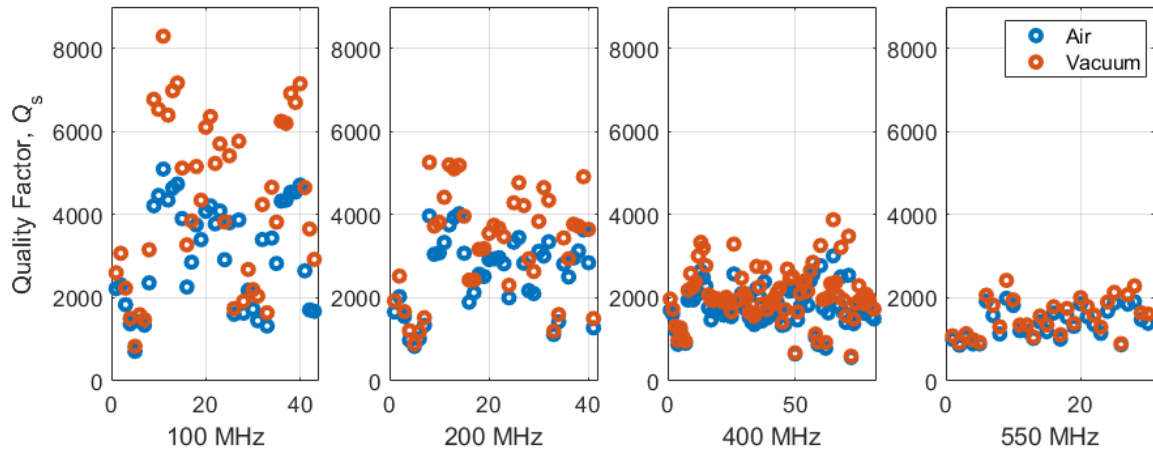


Figure 4.24: Scatterplots of the measured quality factors on devices operating at different frequencies.

The effect of the aperture (L_e) on the quality factor is reported in Fig. 4.25. The measurements closely follow the trends previously reported for 50 MHz resonators. In general, a global maximum can be identified for each different frequency. As discussed in Section 4.1.3, the point of maximum Q_s represents a tradeoff between anchor losses and electrical loading.

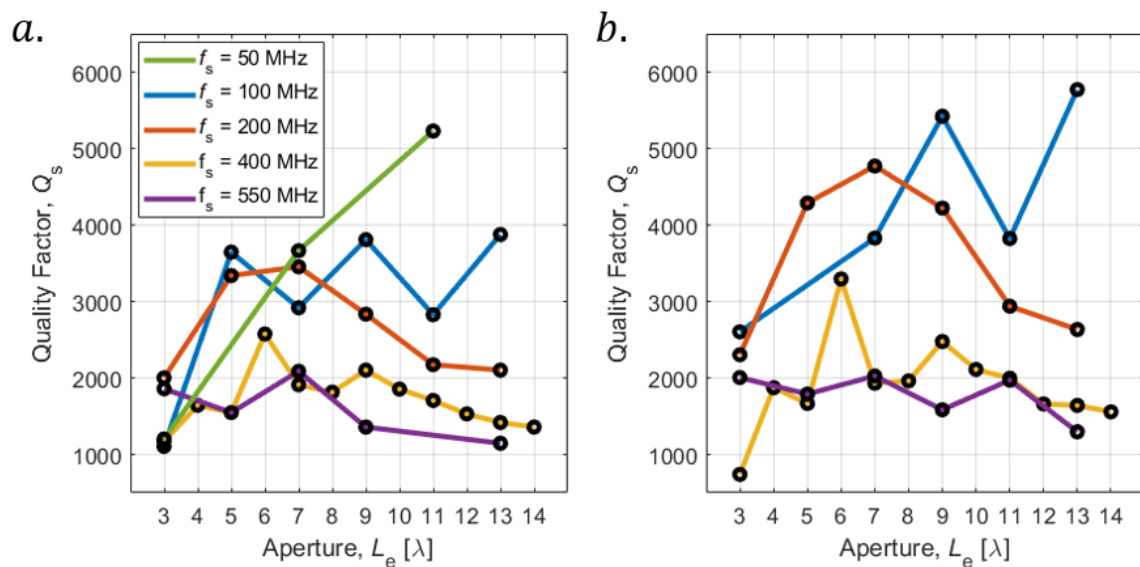


Figure 4.25: Effect of the aperture (L_e) on Q_s for devices measured: (a) in air; (b) in vacuum.

For a fixed geometry, electrical losses do not scale with frequency, being dependent as first approximation by the number of squares and the metal thickness. Vice versa, R_m does scale inversely with frequency if C_0 and the FoM are assumed constant, meaning that higher frequency devices experience larger resistive losses. For this reason, devices at lower frequencies showcase lower Q_s for smaller values of L_e .

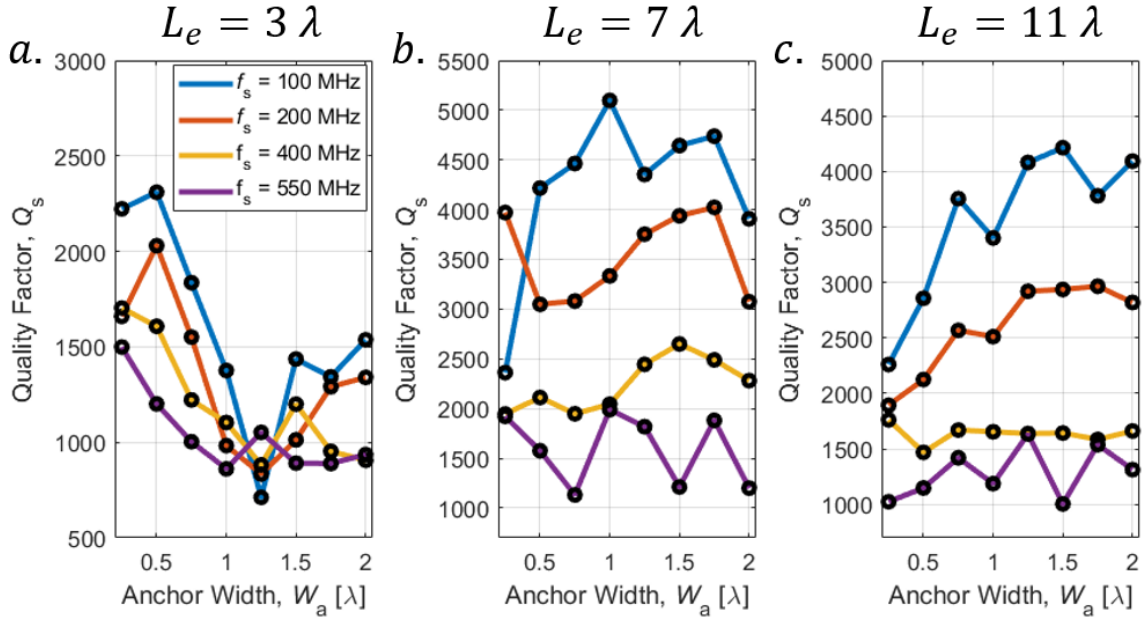


Figure 4.26:Effect of the anchors width (W_a) on the quality factor measured in air for devices with an aperture of: (a) $L_e = 3\lambda$; (b) $L_e = 7\lambda$; and (c) $L_e = 11\lambda$.

Fig. 4.26 and 4.27 report the results of anchor width (W_a) variations in air and vacuum, respectively. W_a was swept from 0.25λ to 2λ (fully anchored configuration) for three different levels of aperture (3, 7 and 11λ). As highlighted in Fig. 4.26a and 4.27a, shorter devices are more prone in exhibiting lower Q_s for larger values of W_a , while longer devices seem less affected ($L_e = 7\lambda$, Fig. 4.26b and 4.27b) or show the opposite trend ($L_e = 11\lambda$, Fig. 4.26c and 4.27c). The measurements confirm the intuition reported in Section 4.1 that anchor losses are a strong function of the ratio between the length (L) and the width (W) of the plate. Intuitively, smaller values of W_a prevent energy leaking via the substrate in shorter resonators, thus increasing Q_s . In larger resonator,

shorter anchors introduce more electrical loading, which partially explains the trends reported in

Fig. 4.26b-c and 4.27b-c.

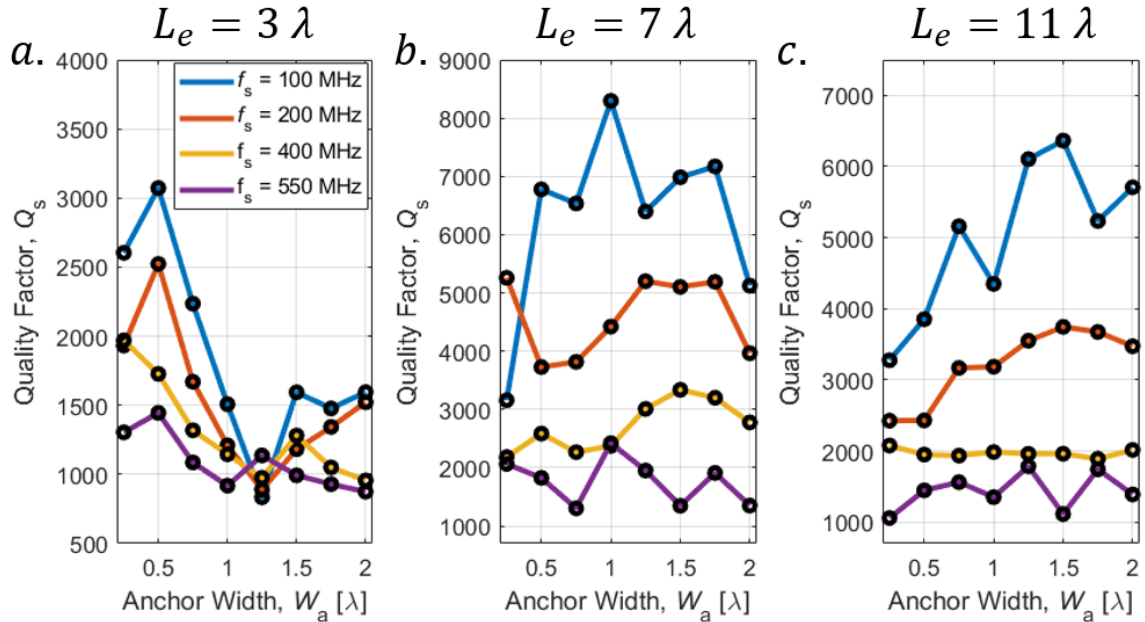


Figure 4.27: Effect of the anchors width (W_a) on the quality factor measured in vacuum for devices with an aperture of: (a) $L_e = 3\lambda$; (b) $L_e = 7\lambda$; and (c) $L_e = 11\lambda$.

Measurements in air and vacuum of gap (g) variations on plates with a total length (L) of 10λ and 14λ are reported in Fig. 4.28 and 4.29, respectively.

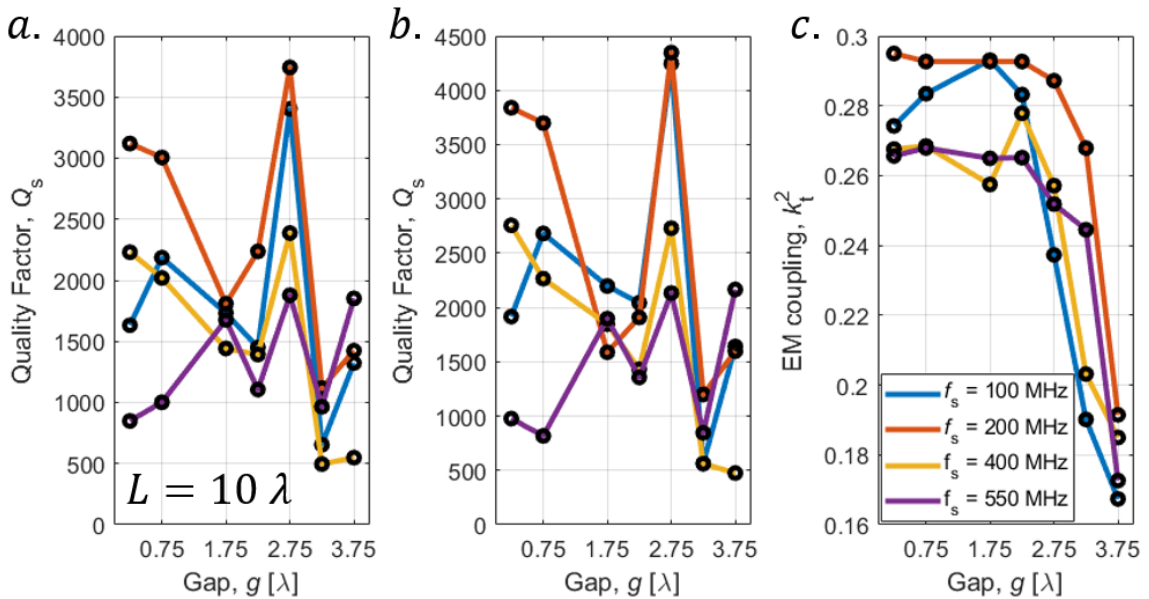


Figure 4.28: Effect of the fingers-to-bus gap (g) for resonator with a plate length (L) of 10λ on: (a) Q_s , measured in air; (b) Q_s , measured in vacuum; and (c) electromechanical coupling (k_t^2).

Trends closely follows the results measured on 50 MHz devices. For $L = 10 \lambda$, Q_s is maximized for $g = 2.75 \lambda$, and abruptly drops for large fingers-to-bus distances (Fig. 4.28a-b). The electromechanical coupling (k_t^2) follows a similar trend (Fig. 4.28c). Measurements of gap variations on resonators with $L = 14 \lambda$ (Fig. 4.29), reported maximum Q_s around $3.25 - 3.75 \lambda$ (except for $f_s = 200$ MHz), as well as k_t^2 reduction beyond this optimal point. Since the plate length is fixed, the aperture decreases as the gap increases according to Eq. 4.6. Since $L_b = 0.75 \lambda$, an optimal L_e of 3λ and 5λ can be calculated for $L = 10 \lambda$ and 14λ , respectively. This means that an aperture of at least $0.3 - 0.35 L$ is necessary to ensure an optimal transduction of the piezoelectric material.

$$L_e = L - 2(g + L_b) \quad (4.6)$$

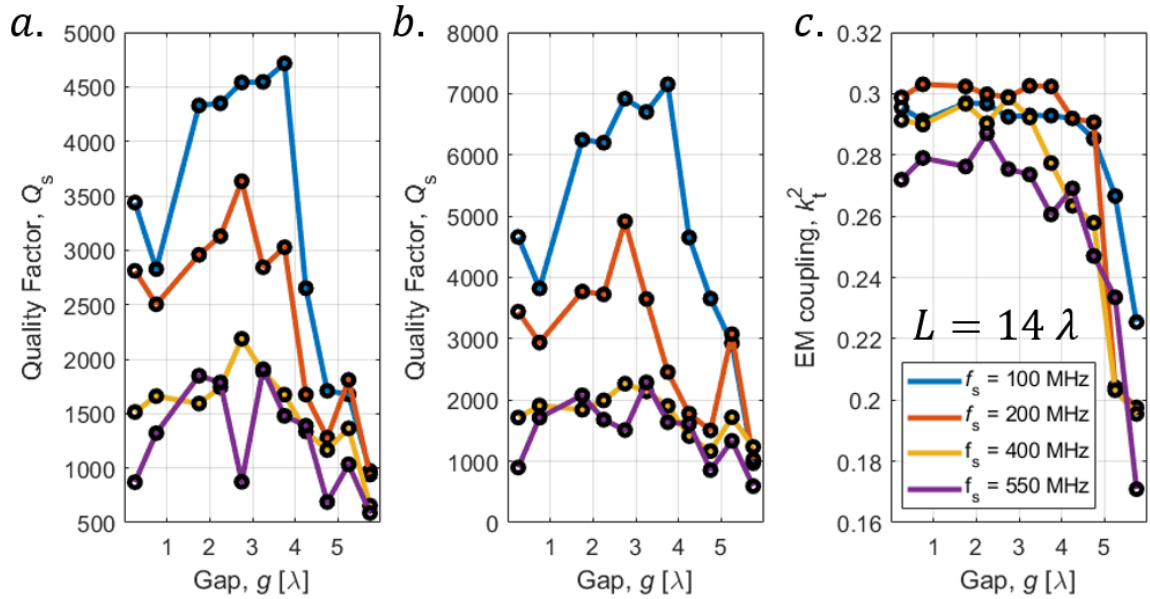


Figure 4.29: Effect of the fingers-to-bus gap (g) for resonator with a plate length (L) of 14λ on: (a) Q_s , measured in air; (b) Q_s , measured in vacuum; and (c) electromechanical coupling (k_t^2).

Coverage variations on 400 MHz devices highlighted similar trends to the subset investigated at 50 MHz (Fig. 4.30). The electromechanical coupling (k_t^2) is maximized for $c = 0.3$, as widely reported in literature [72]. Q_s is maximized between $c = 0.3$ and $c = 0.5$, hinting that slightly larger

coverages can be implemented without Figure of Merit degradation, increasing the capacitance per unit area.

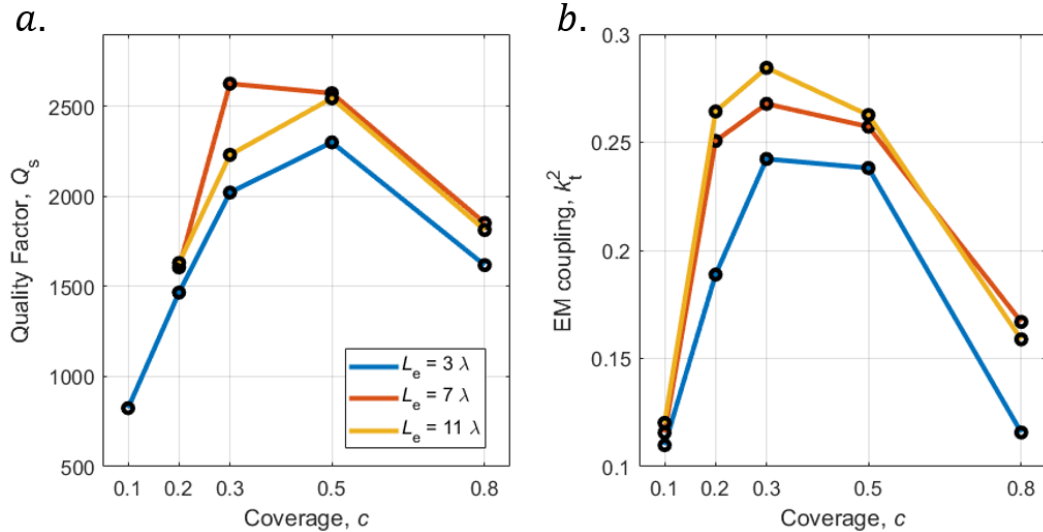


Figure 4.30: Effects of coverage (c) on X-cut LVRs operating around 400 MHz on: (a) Q_s ; and (b) k_t^2 .

The best measured devices (in vacuum) for each frequency are reported in Fig. 4.31 - 4.33. Figure of Merits of 2,688, 1,741, 964 and 751 were recorded for devices operating at 100, 200, 400 and 550 MHz, respectively. At the time of this thesis, these values represent the highest FoM ever recorded for devices operating at Very High Frequency (VHF) and Ultra High Frequency (UHF). Good Q_s ($> 1,000$) and FoMs (> 240) were also recorded on few devices operating at 800 MHz and 1 GHz, despite the poor active reflectors patterning (Fig. 4.22)

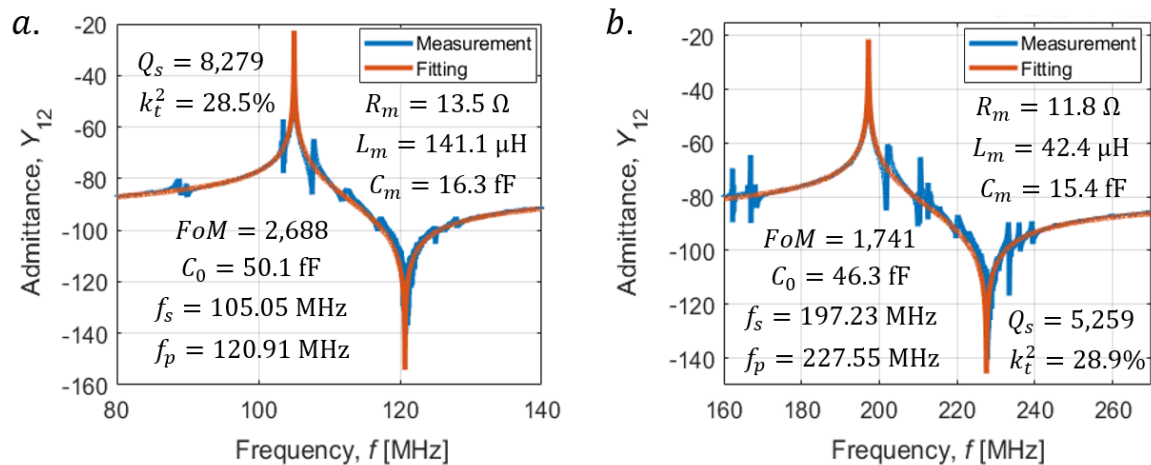


Figure 4.31: Fabricated X-cut LVRs operating around: (a) 100 MHz; and (b) 200 MHz.

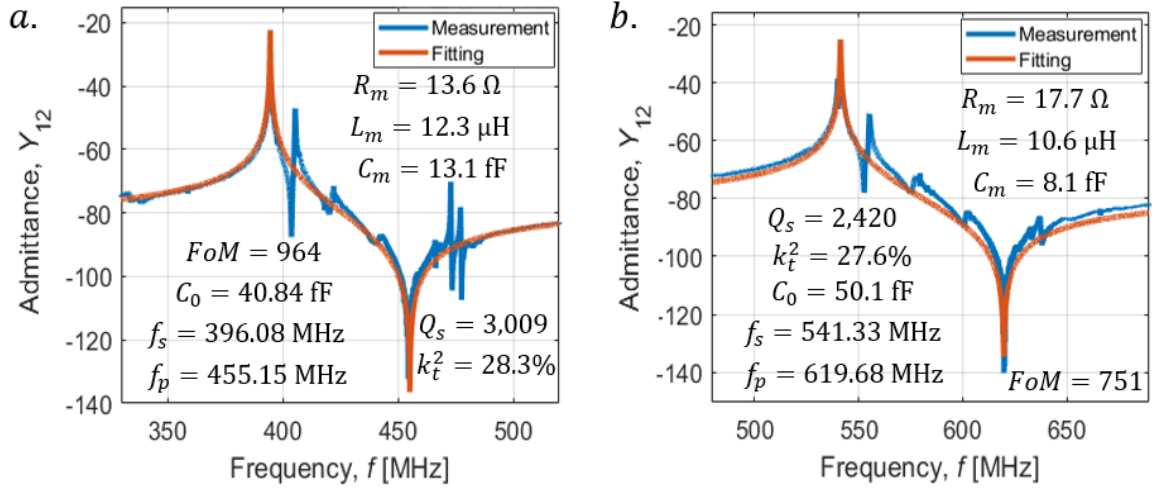


Figure 4.32: Fabricated X-cut LVRs operating around: (a) 400 MHz; and (b) 550 MHz.

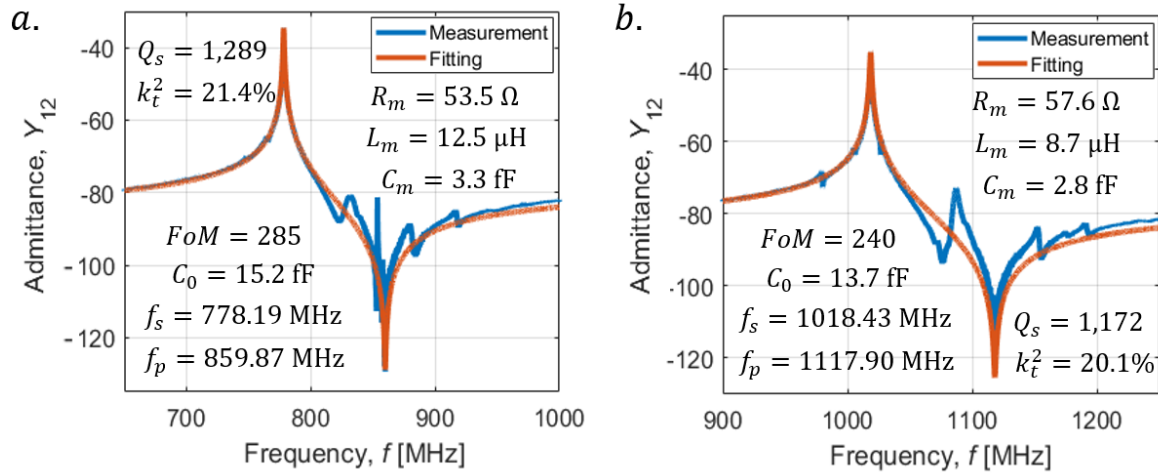


Figure 4.33: Fabricated X-cut LVRs operating around: (a) 800 MHz; and (b) 1 GHz.

A subset of devices (aperture test and anchor tests with $L_e = 3 \lambda$ and 7λ) at different frequencies (100, 200, and 400 MHz) was monitored throughout the entire cooling process to 50 K, in steps of 40 K, to characterize the Q_s variation as a function of frequency. Fig. 4.34 shows the results of the aperture variations at different frequencies and temperatures. On average, devices operating at lower frequencies and with larger apertures show more consistent Q_s increments. Trends appear to be roughly linear, considering that a normalized standard deviation (σ/μ) of 8% was measured on high Q_s ($> 15,000$) resonators.

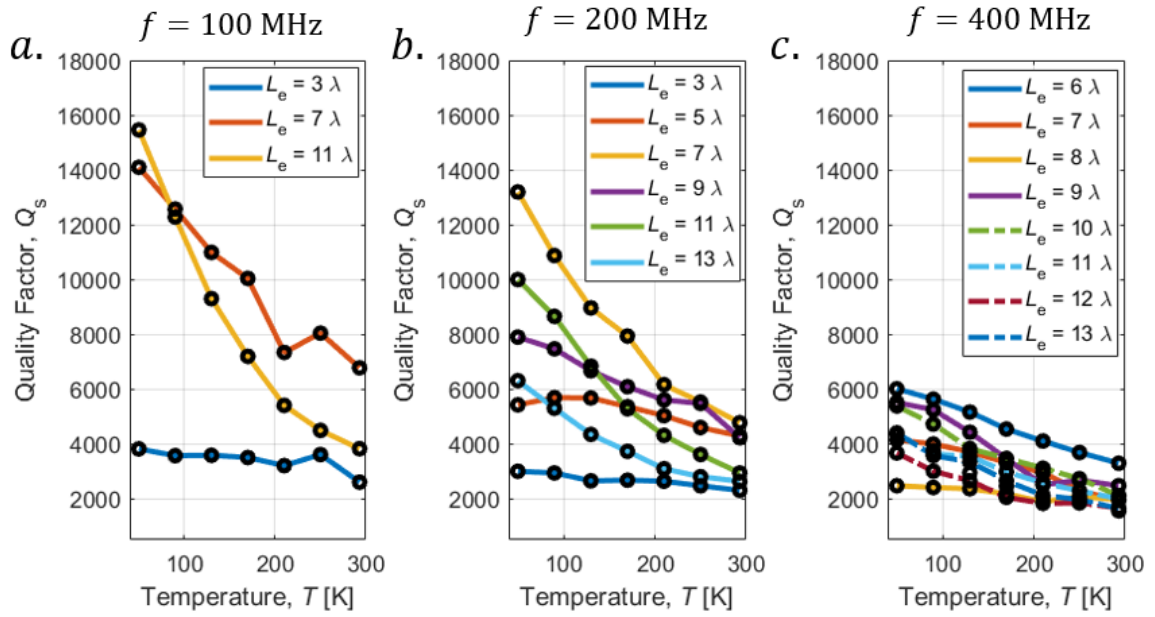


Figure 4.34: Quality factor of aperture variations measured at different temperatures for devices operating: (a) around 100 MHz; (b) around 200 MHz; and (c) around 400 MHz.

This phenomenon hints that electrical loading plays a fundamental role in determining the quality factor of devices at room temperature, when anchor losses are minimized (*i.e.*, when $L_e > 3\lambda$). Measurements of anchor variations (Fig. 4.35 and 4.36) strongly support this hypothesis, showing trends that are consistent with the aperture test reported in Fig. 4.34.

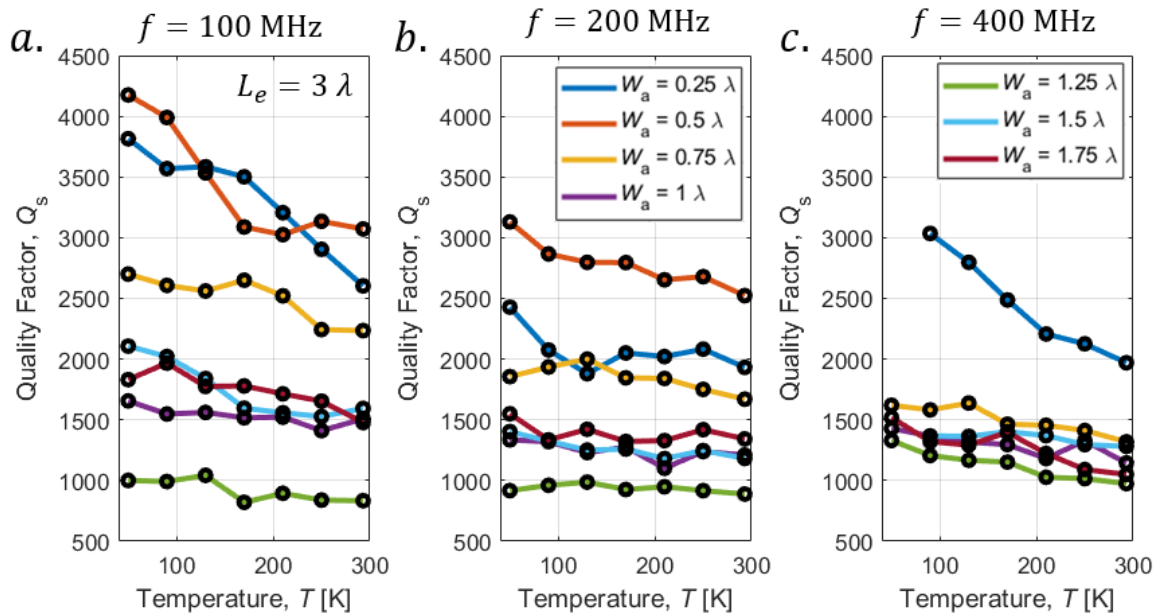


Figure 4.35: Quality factor of anchor variations (with fixed $L_e = 3\lambda$) measured at different temperatures for devices operating: (a) around 100 MHz; (b) around 200 MHz; and (c) around 400 MHz.

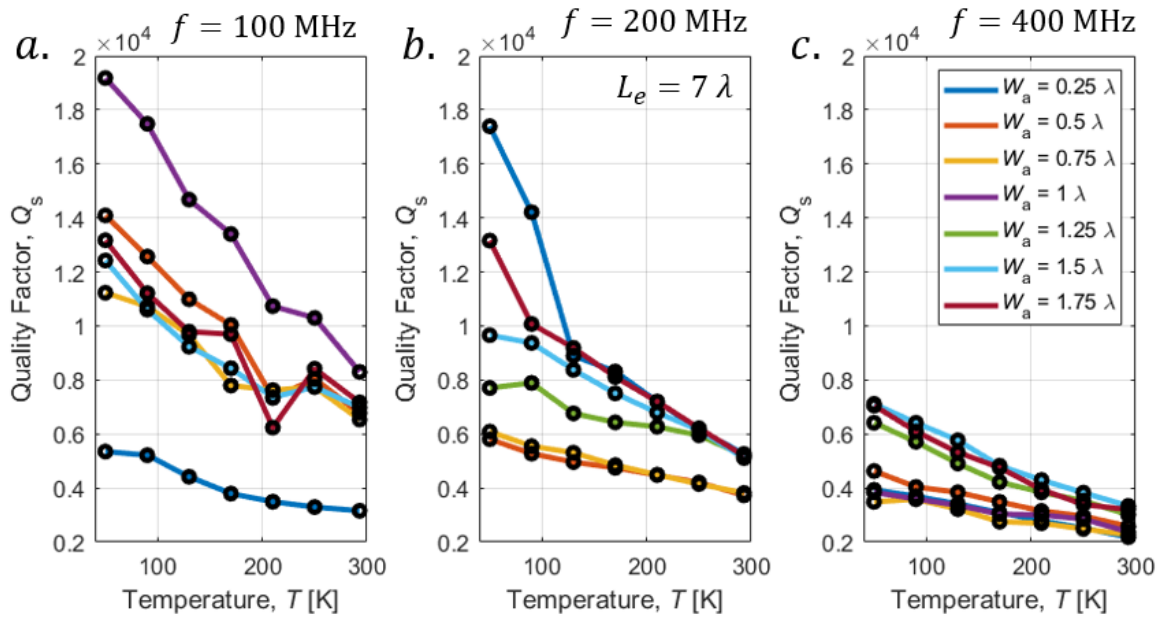


Figure 4.36: Quality factor of anchors variations (with fixed $L_e = 7 \lambda$) measured at different temperatures for devices operating: (a) around 100 MHz; (b) around 200 MHz; and (c) around 400 MHz.

The best cryogenic measurements recorded for devices operating around 100 MHz is reported in Fig. 4.37, with a zoom-in of the resonance peak. The highest Q_s recorded ($> 26,000$) is comparable with the anchor losses estimated by COMSOL models (Fig. 4.3).

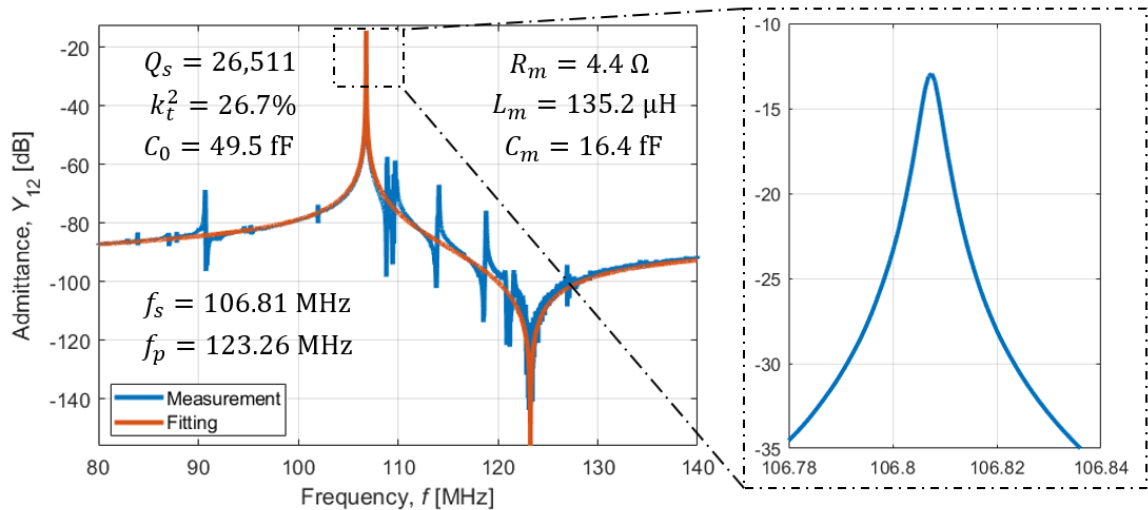


Figure 4.37: Admittance response of the resonator exhibiting the recorded highest Q_s at base temperature (10 K).

4.3. Characterization of Damping Mechanism

4.3.1. Air Damping

Air damping was estimated according to the air and vacuum measurements reported in the previous section (scatterplots of Fig. 4.24). The air damping (Q_{air}) was estimated according to Eq. 4.7, where Q_{atm} and Q_{vac} represent the resonator quality factors measured in air and in vacuum, respectively.

The measured median Q_{air} is reported in Fig. 4.38. The median is adopted instead of a simple mean to minimize the impact of outliers and measurement uncertainty. The measured Q_{air} was later fit to a square root function (Eq. 4.8). Trends are consistent with simple viscous damping measurements reported in literature [73].

$$Q_{air} = \frac{1}{\left(\frac{1}{Q_{atm}} - \frac{1}{Q_{vac}}\right)} \quad (4.7)$$

$$Q_{air}(f) = a\sqrt{f} + b \quad (4.8)$$

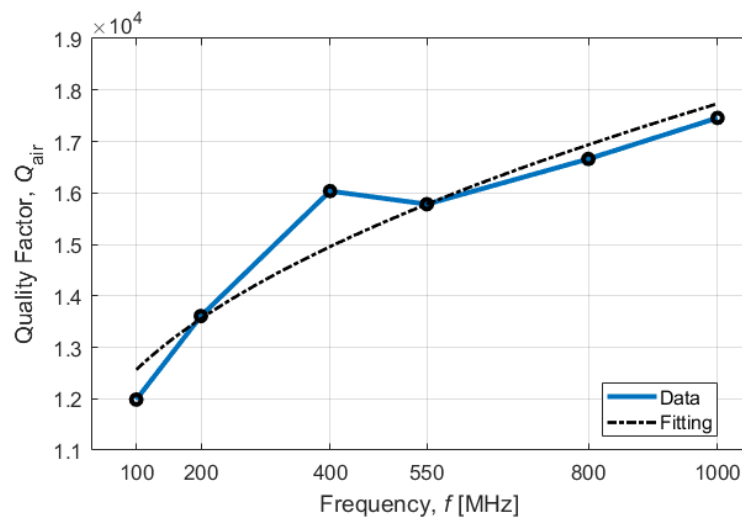


Figure 4.38: Extracted quality factor (Q_{air}) due to air damping.

4.3.2. Series Resistance Modeling

Devices which exhibit a large Figure of Merit (FoM) combined with relatively large capacitance (C_0) are extremely susceptible to any series resistance (R_s) introduced by interconnects and IDEs due to their low motional resistance (R_m , Eq 2.8). If R_m is comparable or lower than R_s , the measured or loaded quality factor (Q_s) is mainly limited by the electrical loading rather than any other damping mechanism. It is possible to estimate the unloaded quality factor (Q_u) according to Eq. 4.9 [74], where R_m represents the measured motional resistance, while the difference between R_m and R_s determine the unloaded motional resistance.

$$Q_u = Q_s \frac{R_m}{R_m - R_s} \quad (4.9)$$

In order to properly estimate Q_u , a series resistance (R_s) model was developed by dividing the distributed loading of the resonator into smaller lumped components. Fig. 4.39 shows a direct comparison between the resonator topology and the equivalent resistive network.

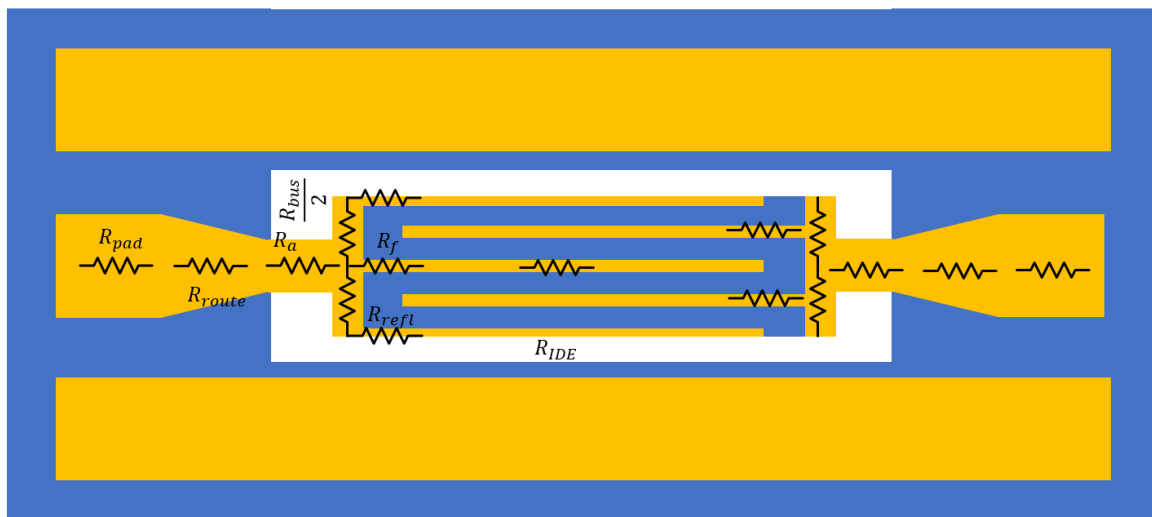


Figure 4.39: Equivalent resistive network of a LFE LVR.

All the components beside the loading introduced by the IDTs were estimated according to Ohm's law (Eq. 4.10), where L , W and t represents respectively the length, width and thickness of a metallic trace. The modeled resistance (R_s , Eq. 4.11) accounts for the resistance introduced by the pads (R_{pad}), pads-anchor routing (R_{route}), anchors (R_{anc}), bus (R_{bus}), fingers extending in the gap region (R_{gap} , Eq. 4.12), and by the IDEs (R_{IDE} , Eq. 4.13). The model of the interdigitated transducers is based on the work reported in [83].

$$R = \frac{\rho L}{Wt} \quad (4.10)$$

$$R_s = 2 \left(R_{pad} + R_{route} + R_{anc} + \frac{R_{bus}}{4} + R_{gap} \right) + R_{IDE} \quad (4.11)$$

$$R_{gap} = \frac{2}{\sum \frac{1}{R_{fi}}} = \frac{4\rho g}{\lambda c t_m} \frac{1}{(N_p + 1)} \quad (4.12)$$

$$R_{IDE} = \frac{4}{3} \frac{\rho L_e}{\lambda c t_m} \frac{1}{N_p} \quad (4.13)$$

Table 4.10 reports the parameters adopted for L and W for each lumped resistance considered in the model. L_{pad} , W_{pad} and L_{route} respectively represents the length and width of the probing pads and the length of the metallic trace connecting the pads to the anchors (Fig. 4.21a). An example of the value of each resistance of the described mode is also reported, along with the geometry of the analyzed resonator. For the case under consideration, most of the series resistance is introduced by the IDEs, which contributes for roughly 60% of the overall electrical loading. While the resistances introduced by traces can be minimized up to the bus region by increasing the metal thickness, the gap and the transduction region are particularly sensitive to mass loading effects, which can ultimately lead to FoM degradation and the insurgence of spurious modes.

Table 4.10: Lengths and widths of each element of the resistive network depicted in Fig. 4.39. For the estimation of the resistance of each component, the following geometry was investigated: $\lambda = 56 \mu\text{m}$, $L_{\text{route}} = 76 \mu\text{m}$, $L_{\text{pad}} = W_{\text{pad}} = 80 \mu\text{m}$, $L_a = W_a = g = L_b = 0.75\lambda$, $L_c = 13\lambda$, $N_p = 3$, $c = 0.3$, $t_m = 300 \text{ nm}$, and $\rho = 5.7\text{e-}8 \Omega\cdot\text{m}$.

Element	Length (L)	Width (W)	Resistance (R)
R_{pad}	$0.5L_{\text{pad}}$	W_{pad}	0.10Ω
R_{route}	L_{route}	$0.5(W_{\text{pad}}+W_a)$	0.30Ω
R_{anc}	L_a	W_a	0.19Ω
R_{bus}	W	L_b	0.13Ω
R_f	g	$0.5\lambda c$	0.95Ω
R_{refl}	g	$0.25\lambda c$	1.9Ω
R_{gap}	-	-	0.48Ω
R_{IDE}	L_c	$0.5\lambda c$	3.67Ω
R_s	-	-	6.04Ω

An equivalent resistive model for an array of resonators was also developed starting from the R_s estimated for the individual device (Fig. 4.15b). Compared to a single resonator, the array topology reported in Fig. 4.40 is constituted by a fixed number of elements (N_{el}) connected via a long metallic bus. The distributed resistance introduced by the interconnects can be modeled via smaller lumped resistances (R_t) connecting the anchors of each parallel resonators. In this case, the resistance of the single resonator (R_{res}) is slightly lower than R_s (Eq. 4.11) since R_{pad} and R_{route} are accounted for the entire array, and not for each parallel resonator.

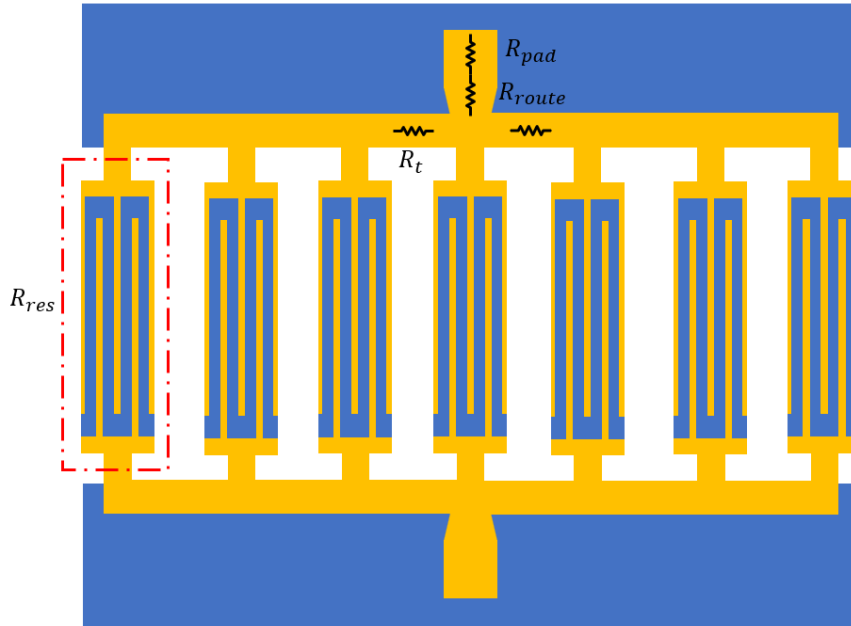


Figure 4.40: Equivalent resistive network of an array constituted by parallel LFE LVRs.

4.3.3. Impact of Electrical Loading

The series resistance model described in Section 4.3.2 was applied to understand the results of the aperture variations tests for which various resonator quality factors were measured in vacuum (Q_{vac}) and at base temperature (10 K, Q_{10K}). A contact resistance (R_{c0}) of 2Ω , extrapolated from de-embedding structures with different lengths, was added to the R_s reported in Eq. 4.11. The unloaded quality factor (Q_u) was later calculated for devices operating at 100, 200, 400, and 550 MHz according to Eq. 4.14.

$$Q_u = Q_{vac} \frac{R_{m_{mes}}}{(R_{m_{mes}} - R_s - R_{c0})} \quad (4.14)$$

Results are reported in Fig. 4.41 and 4.42. Q_u closely follows the measured data at cryogenic temperature (Q_{10K}) for all the frequencies under examination. Discrepancies between the unloaded quality factor (Q_u) and the quality factor measured at base temperature (Q_{10K}) are likely due to measurement errors in vacuum (*e.g.*, see $L_e = 11 \lambda$ at 100 MHz, Fig. 4.41a). As expected, longer devices are more vulnerable to electrical loading than shorter resonators.

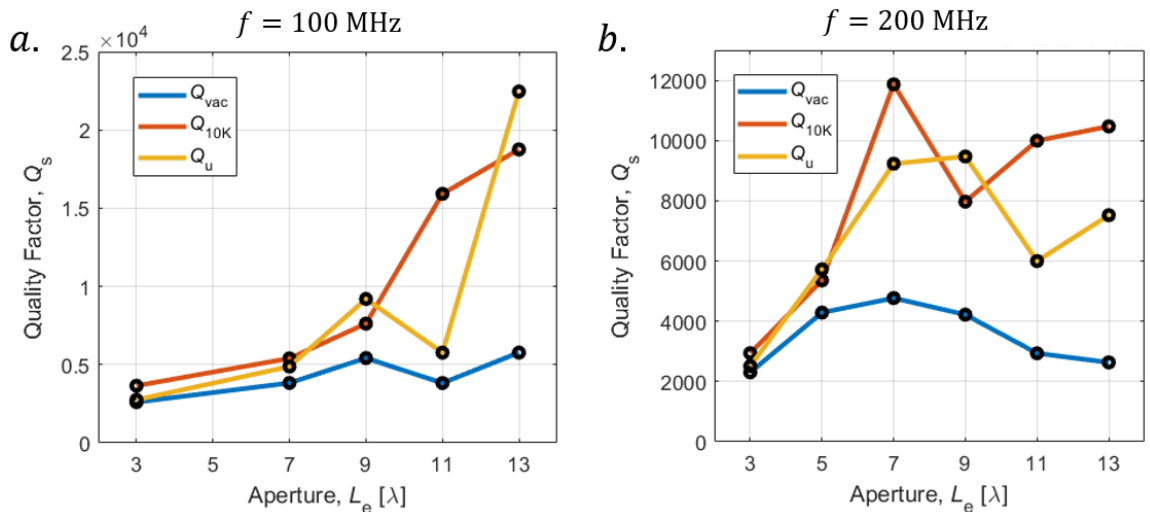


Figure 4.41: Quality factor measured in vacuum (Q_{vac}) and at base temperature (Q_{10K}), and unloaded quality factor (Q_u) for different apertures at: (a) 100 MHz; and (b) 200 MHz.

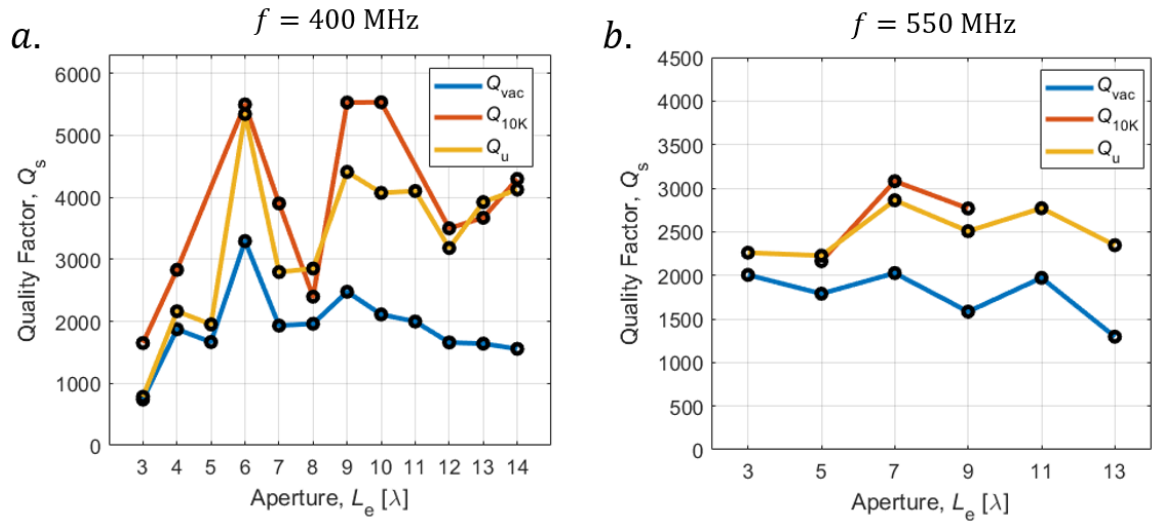


Figure 4.42: Quality factor measured in vacuum (Q_{vac}) and at base temperature (Q_{10K}), and unloaded quality factor (Q_u) for different apertures at: (a) 400 MHz; and (b) 550 MHz.

4.3.4. Anchor Losses

Ultimately, the impact of anchor geometry on the quality factor is investigated. Fig. 4.43 reports the measured quality factor at base temperature (10 K) on anchor width variations for different frequencies and apertures. At this temperature, any thermally-related damping mechanism (including electrical loading and TED) are considered negligible compared to the acoustic losses due to energy leaking in the substrate (Eq. 4.15).

$$Q_s|_{10K} = \frac{1}{\sum \frac{1}{Q_i}} \sim Q_{anch} \quad (4.15)$$

Fig. 4.43 reports the measured quality factors. The trends closely follow the results recorded in atmosphere and vacuum, meaning that anchor losses are the most limiting mechanism for shorter plates, while they do not play a significant role for slender resonators. Quality factors recorded on devices exhibiting $L_e = 7 \lambda$ and 11λ (Fig. 4.43b and 4.43c) do not show significant trends, likely due to the impact of fabrication non-idealities and mode conversion phenomena.

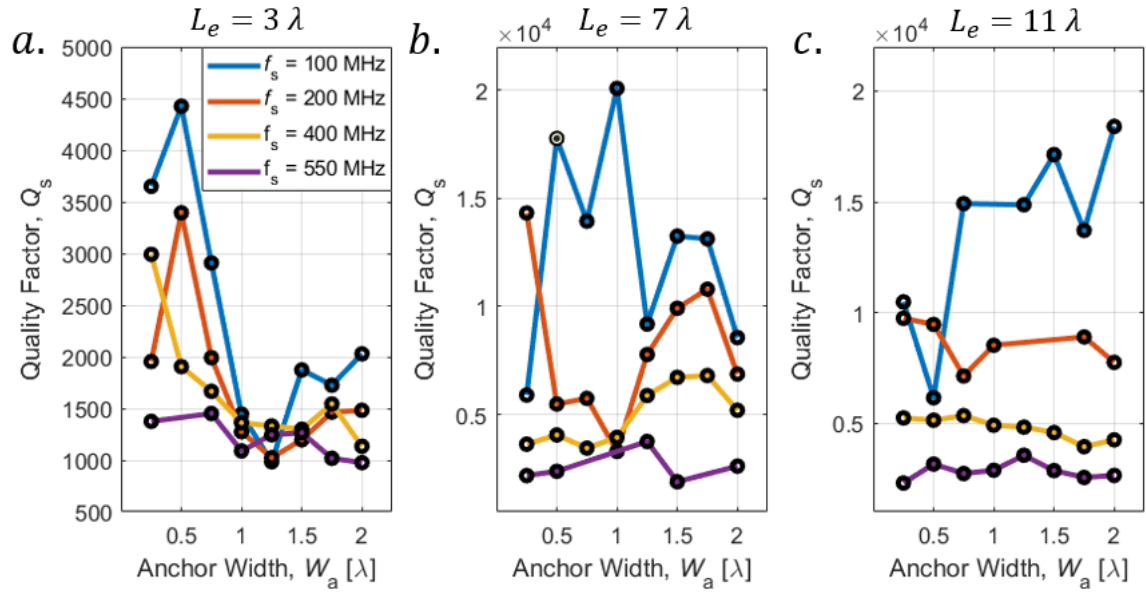


Figure 4.43: Quality factor as a function of anchor width (W_a) measured at base temperature (10 K) for different frequencies and values of aperture: (a) $L_e = 3 \lambda$; (b) $L_e = 7 \lambda$; (c) $L_e = 11 \lambda$.

Fully anchored devices were proven to exhibit less aggressive spurious responses, likely due to the suppression of transversal modes at the expenses of maximum attainable quality factor (especially for smaller values of L_e). Fig. 4.44 reports the characteristic response of three resonators with different anchors ($W_a = 0.25 \lambda$ and 2λ)

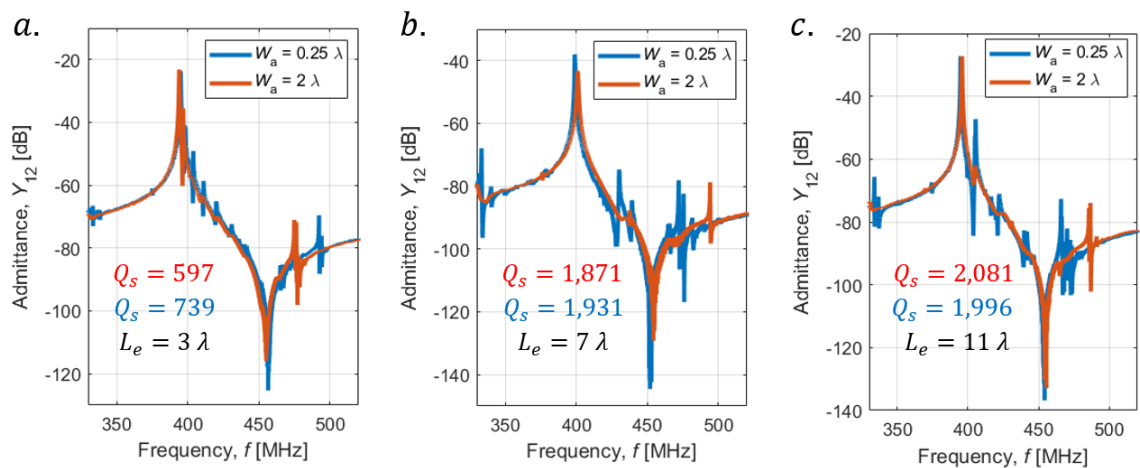


Figure 4.44: Admittance response of devices with different anchor width ($W_a = 0.25$ and 2λ) and an aperture of: (a) $L_e = 3 \lambda$; (b) $L_e = 7 \lambda$; and (c) $L_e = 11 \lambda$.

Fig. 4.45 reports the comparison between the vacuum measurements (Q_{vac}) and cryogenic measurements (Q_{10K}) performed on two subsets of devices operating around 400 MHz with different

apertures and anchors widths. As reported before, shorter anchors width ($W_a = 0.25$, Fig. 4.45a) devices with aperture $L_e < 5 \lambda$ exhibit larger anchor losses, due to the larger amount of energy leaking via the substrate. As the aperture increases, the quality factor measured at room temperature tends to decrease, while the Q_s measured at base temperature roughly flattens between 4,000 and 5,000, meaning that the electrical loading is the dominant damping mechanism. Different from devices with $W_a = 0.25 \lambda$, fully anchored resonators show a monotone increase in their Q_s at cryogenic temperature, meaning that the transition between the anchor losses dominated region and the electrical loading dominated region is smoother, due to the larger amount of energy leaking through the larger tethering width. For large values of aperture ($L_e > 11 \lambda$), the measured Q_s is substantially independent from the anchor geometry, meaning that almost no energy escapes the central portion of the resonator.

Interestingly, fully anchored devices do not show sharp drops in the quality factor as L_e increases, hinting that spurious modes play a fundamental role in determining the Q_s of some geometries, as previously suspected.

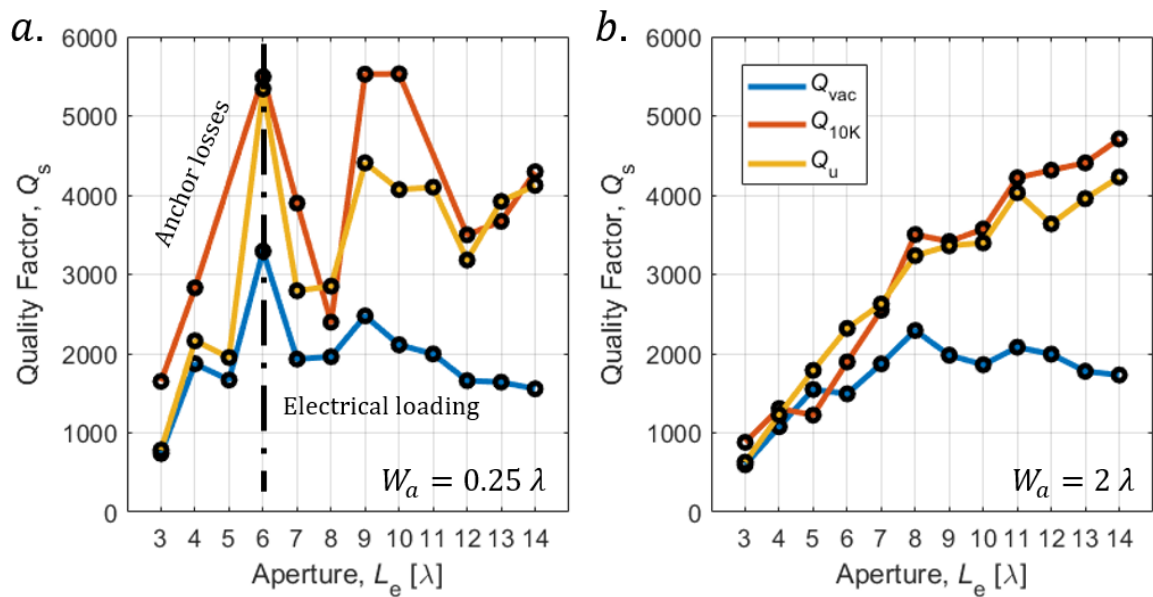


Figure 4.45: Quality factor measured in vacuum (Q_{vac}) and at base temperature (Q_{10K}), and unloaded quality factor (Q_u) for different apertures and anchor width dimensions: (a) $W_a = 0.25 \lambda$; and (b) $W_a = 2 \lambda$.

4.3.5. Frequency Mismatch in Arrays of Resonators

Measurements reported in Section 4.1.4 highlighted the impact of the number of elements (N_{el}) of an array of resonators on the measured quality factor (Q_{as}). Resonant frequency (f_s) mismatch between elements is suspected to be the primary source of Q_s degradation. To prove this hypothesis, the effect of statistically distributed parameters (f_s , Q_s , k_t^2 , and C_0) on the quality factor of an array constituted by N_{el} elements operating around 50 MHz is investigated with a Monte Carlo approach. N_{el} is varied from 1 to 9 to provide a direct comparison with the results reported in Section 4.1.4. A number of Monte Carlo simulations (N_{MC}) equal to 1,000 is performed for each N_{el} , for a total of 9,000 tests.

For each N_{el} , individual resonators are randomly generated according to the statistical distribution of f_s , k_t^2 , Q_s and C_0 reported in Table 4.4, which are then used to calculate randomly distributed motional parameters (R_m , L_m and C_m). The admittance of each array (Y_{array}) is then estimated by superimposing the response of the N_{el} randomly generated resonator responses (Eq. 4.16). The quality factor of the simulated array (Q_{as}) is later extracted with the 3 dB method from the admittance response.

$$Y_{array} = \sum_{i=1}^{N_{el}} Y_i = \sum_{i=1}^{N_{el}} \left(j\omega C_{0i} + \frac{1}{R_{m_i} + j\omega L_{m_i} + \frac{1}{j\omega C_{m_i}}} \right) \quad (4.16)$$

The average array quality factor ($\mu_{Q_{as}}$) and its standard deviation ($\sigma_{Q_{as}}$) are then calculated from the N_{MC} test replicates for each N_{el} . Fig. 4.46 reports the results of the Monte Carlo simulation (in form of box plots) compared to the Q_{as} measured in the break-test reported in Section 4.1.4. For low number of elements, the measured quality factor closely follows the value predicted by the

Monte Carlo simulation. Experimental data diverge from the theoretical model for larger number of elements due to the impact of interconnects as N_{el} increases (as explained in next paragraph).

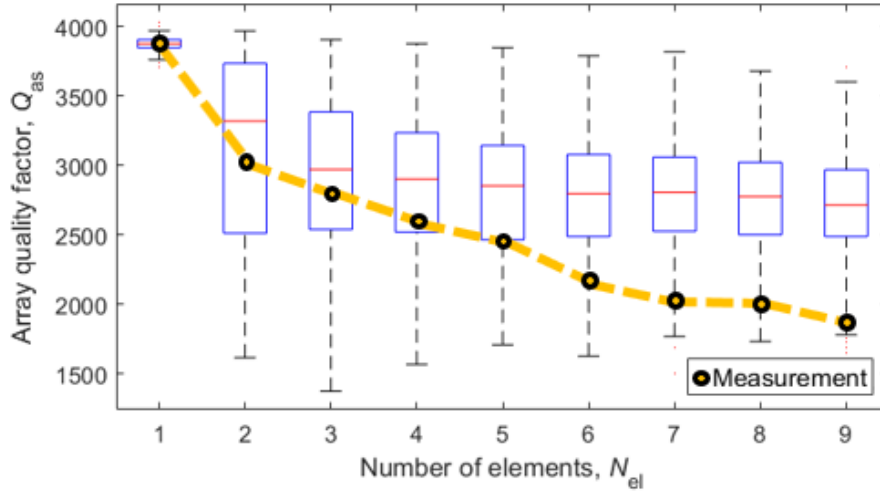


Figure 4.46: Monte Carlo simulations of an array of resonators generated from the randomly distributed parameters listed in Table 4.4 and recorded Q_{as} as a function of the number of elements.

One-factor-at-time (OFAT) Monte Carlo simulations, in which a single parameter is varied while the standard deviations of the others are set equal to zero, confirm that the mismatch in resonant frequency is the predominant Q_{sa} degradation mechanism (Fig. 4.47).

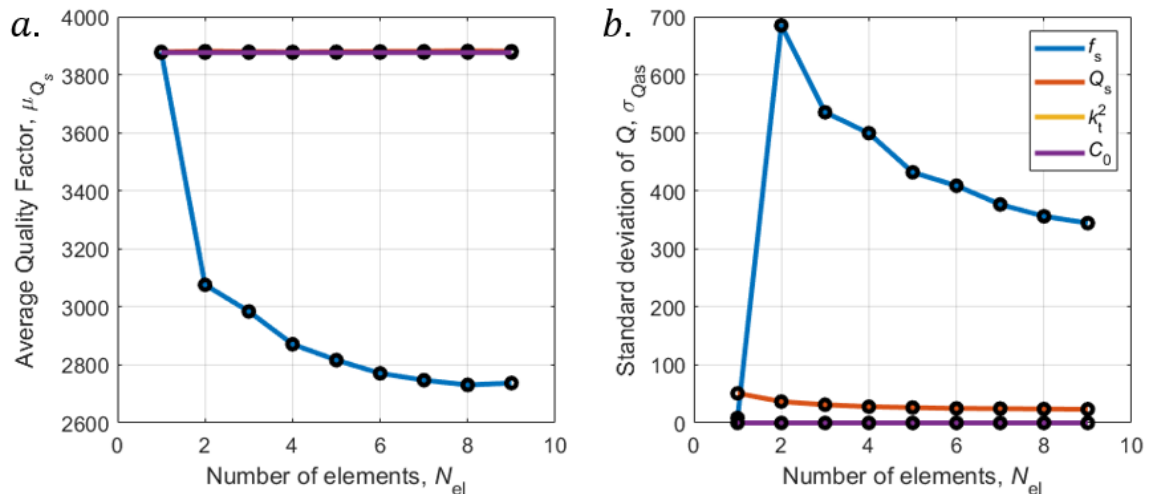


Figure 4.47: One-factor-at-time Monte Carlo simulations showing the impact of Q_s , k_t^2 , f_s , and C_0 variability on the Q_{sa} : (a) average quality factor ($\mu_{Q_{as}}$); and (b) standard deviation ($\sigma_{Q_{as}}$).

The Monte Carlo model previously described is further refined by including the impact of the interconnects connecting the array elements. The model closely follows the resistive electrical model developed for arrays of resonators described in Section 4.3.2. In the case under examination, the resistance of the resonator (R_{res}) is replaced by the randomly generated R_m . This approximation is valid since the randomly generated R_m is based on measurements performed in air and is not de-embedded of the series resistance (R_s) component. In this case, for each N_{el} , the array admittance (Y_{array}) is calculated according to Eq. 4.17, where $Y_{N_{el}}$ represents the last randomly generated resonator response (Y_i), while Y_{brx} and Y_{blx} respectively represents the admittances of the right and left branches of a symmetric device as the one reported in Fig. 4.1.2. The generic expression of the admittance of a branch (Y_b) is reported by Eq. 4.18, where N_b represents the number of elements in a branch (*i.e.*, 4 for an arrays of 9 elements), and R_t the trace resistance, estimated from the distance between the individual resonators anchors and the interconnects width and thickness. For the arrays reported in Section 4.1.4, R_t is estimated in 1.25Ω , given an anchor-anchor distance of 3λ ($348 \mu\text{m}$), an interconnect width of $100 \mu\text{m}$ and an AlSiCu thickness of 192 nm .

$$Y_{array} = Y_{N_{el}} + Y_{brx} + Y_{blx} \quad (4.17)$$

$$Y_b = \sum_{i=1}^{N_b} \left[\left(\frac{1}{\frac{1}{Y_{i-1}} + 2R_t} \right) + Y_i \right] \quad (4.18)$$

Fig. 4.48 reports the comparison between the measured data and the Monte Carlo simulation performed considering the impact of the metallic bus. Compared to Fig. 4.46, the experimental data almost coincide with the expected value of the estimated Q_{as} distribution, confirming that resistive losses due to interconnects play an important role in limiting the quality factor of arrays of resonators.

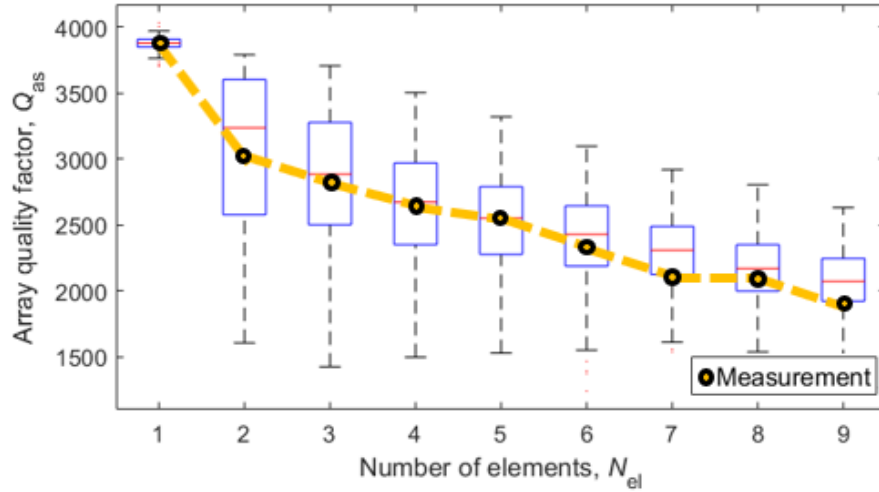


Figure 4.48: Modified Monte Carlo simulations of an array of resonators generated from the randomly distributed parameters listed in Table 4.4 and recorded Q_{as} as a function of the number of elements, including the effects of the interconnects.

Arrays operating around 400 MHz devices, fabricated on 1 μm X-cut Lithium Niobate, are also measured to validate the hypothesis that frequency mismatch is direct cause of Q_{as} degradation. As reported in Fig. 4.49, devices with different number of elements (N_{el}) show multiple peaks at resonance, confirming that frequency mismatch between elements is the fundamental reason limiting the quality factor of those devices. Resonators operating at higher frequencies are more prone to exhibit larger frequency variations due to their smaller features size, which make them more sensitive to substrate and metal thickness variations and fabrication non-idealities. Table 4.11 reports the statistical characterization of identical devices operating around 400 MHz with the optimized geometry reported in Table 4.6 and an aperture of 7λ . The resonant frequency standard deviation (σ_{f_s}) is estimated to be 357 kHz, or 900 ppm, more than 10 times the value recorded for 50 MHz devices [13].

Table 4.11: Statistical characterization of devices operating at 400 MHz, with the geometry described in Table 4.6 and $L_c = 7\lambda$.

Device	1	2	3	4	5	6	7	μ_{f_s}	σ_{f_s}
f_s [MHz]	397.735	398.483	397.996	398.198	398.245	397.853	397.414	397.989	0.3574

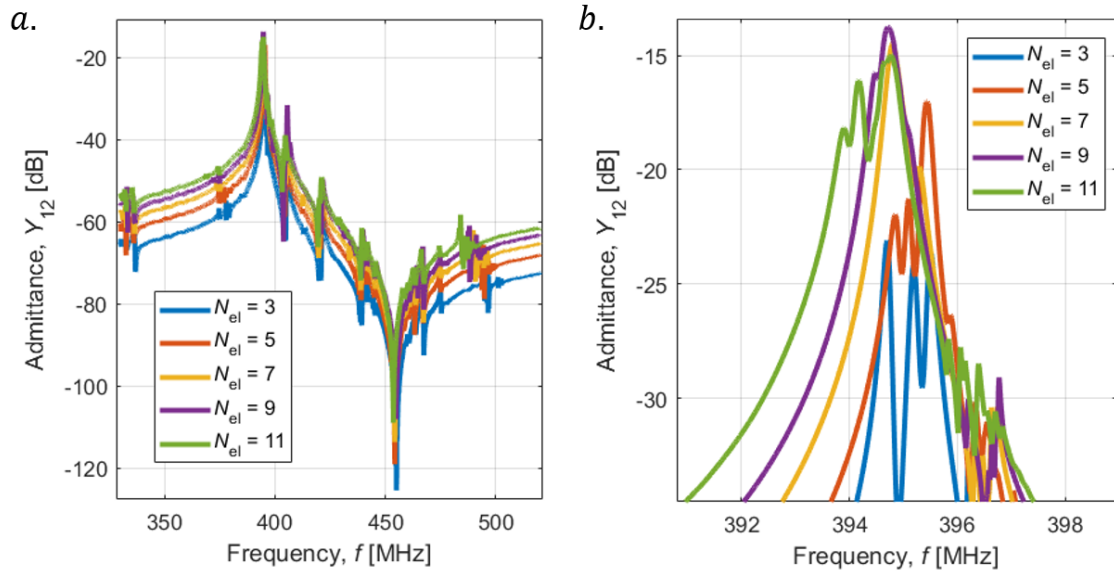


Figure 4.49: (a) Admittance responses of arrays of resonators operating around 400 MHz with different number of elements in parallel; and (b) zoom-in on the resonance peaks.

A hybrid analytical-experimental model is later developed to understand whether lithium niobate and metal thickness variations can be considered one of the major sources of these frequency variations. Devices with the optimized geometry reported in Table 4.6 are simulated via COMSOL[®] FEA operating around 50 MHz ($\lambda = 116 \mu\text{m}$) and 400 MHz ($\lambda = 15 \mu\text{m}$) and their resonant frequency (f_s) extracted for different LN thickness (0.5, 1, 2, and 3 μm) and top electrode metal thicknesses (100, 200, 300, and 400 nm of Al). Simulated data are later fitted with a spline surface ad reported in Fig. 4.50.

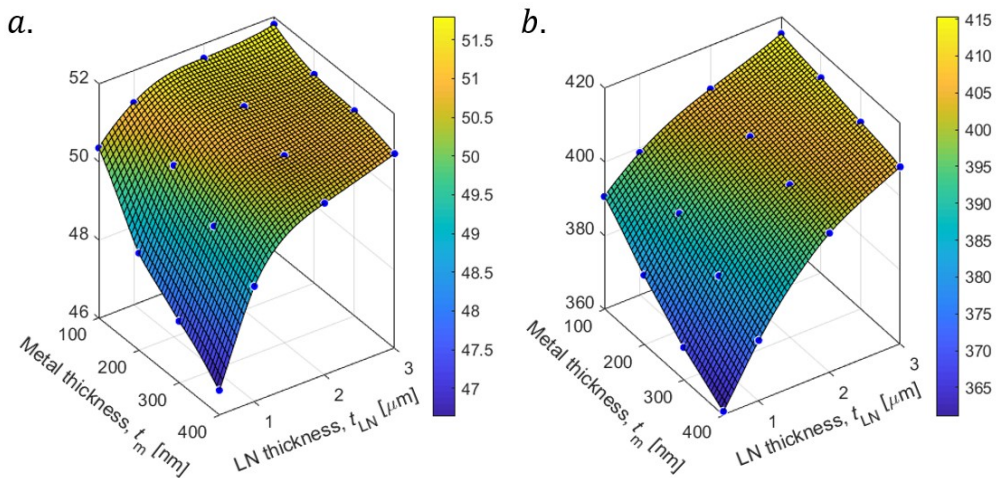


Figure 4.50: Spilt surface fitting of the resonant frequencies extracted from COMSOL[®] simulations for devices operating: (a) around 50 MHz; and (b) around 400 MHz.

The substrate thickness is characterized with a similar approach from the data provided by the vendor (Table 4.12), by fitting the data point with a spline surface. Fig. 4.51 reports the comparison between the fitting and actual X-cut LN wafer.

Table 4.12: Lithium Niobate thickness distribution from NGK.

Point	LN thickness [nm]	Point	LN thickness [nm]	Point	LN thickness [nm]
1	1540.3	8	1029.4	15	1009.8
2	1044.1	9	1135.0	16	903.9
3	1114.0	10	1378.0	17	1379.5
4	1351.5	11	1027.2	A	1403.4
5	1567.0	12	1149.1	B	1456.5
6	1445.0	13	1432.5	C	1247.6
7	1154.1	14	1324.1	D	1273.4

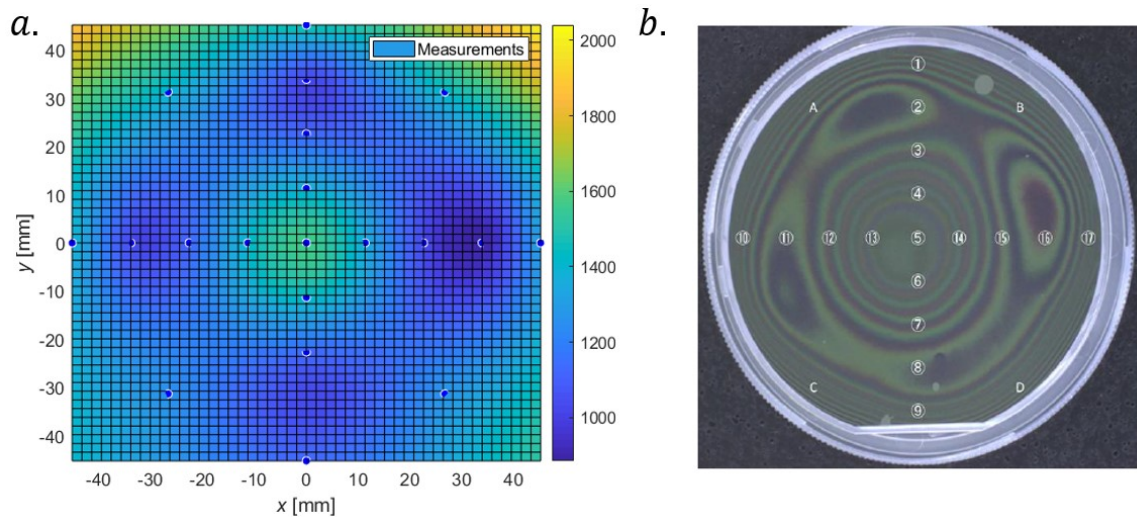


Figure 4.51: Comparison between: (a) the spline surface fitting of the data reported in Table 4.12; and (b) the LN wafer used during the fabrication process.

Ultimately, the metal thickness (t_m) variations across the wafer are characterized via direct measurement, assuming a parabolic 3D distribution over a wafer of radius R . Eq. 4.19 captures the dependency of t_m as a function of the cartesian coordinates x and y for a given wafer radius (R), metal thickness measured at center of the wafer (t_{max}), and metal thickness variation between the center and the wafer edge (Δt_m). Fig. 4.52 reports an example of simulated t_m distribution assuming $t_{max} = 300$ nm, $\Delta t_m = 40$ nm and $R = 2''$.

$$t_m(x, y) = \left(-\frac{\Delta t_m}{R^2}\right)(x^2 + y^2) + t_{max} \quad (4.19)$$

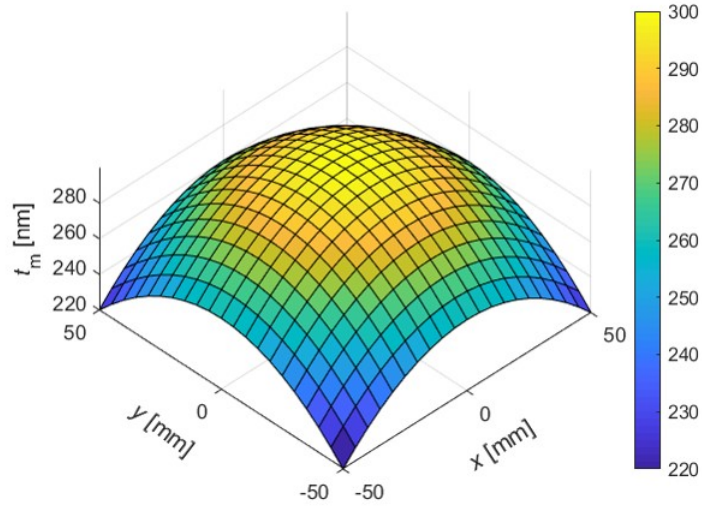


Figure 4.52: Simulated parabolic 3D distribution of sputtered metal thickness.

An algorithm is later developed to estimate the standard deviation of the resonant frequency as a function of the LN and top electrode metal thickness distributions. A random couple of x and y is selected within a circumference with a diameter of 3", to exclude the outer region of the wafer. Starting from this point, a number of points (N_p) set equal to 8 is sampled in the horizontal direction and the respective x_i and y_i recorded. These coordinates are used to extract the LN and metal thicknesses for each of the N_p points (according to the thickness profiles reported in Fig. 4.51 and 4.52) and estimate a statistical distribution for the t_{LN} and t_m . Starting from random values of t_{LN} and t_m extracted from these statistical distributions, the correspondent value of f_s , derived from the spline surface fitting reported in Fig. 4.50, are extracted. The test is repeated a number of times (N_f) equal to 1,000 to estimate the statistical distribution of f_s . For 50 MHz devices, a distance between resonators of 3λ is set for the sampling, while a t_{max} of 192 nm and a center-edge thickness variation of 40 nm is assumed according to experimental data. For 400 MHz devices, a distance equal to 4λ is set for the sampling, and a t_{max} of 290 nm with a center-edge variation of 60 nm is adopted for the metal distribution estimation. LN thickness distributions are fitted according to the data

provided by the manufacturer. Fig. 4.53 reports the results of frequency simulations performed on 50 MHz and 400 MHz devices as a function of the number of tests (N_f). The standard deviation (σ_{fs}) for 50 MHz devices predicted by the model is equal to 2.704 kHz, versus a measured σ of 4 kHz. 400 MHz simulated devices showed a predicted σ_{fs} of 89.383 kHz versus a recorded standard deviation of 397 kHz. While 50 MHz simulations closely follow the experimental data, 400 MHz predicted value is sensibly lower than experimental records.

The simulations confirm that lithium niobate and electrode metal thickness variations play a critical role in determining the resonant frequency of X-cut LN LVRs. These problematics can be addressed by an improvement of the thin film transfer technology, which is already implementing polishing and trimming to maintain the thickness variations in the order of few tens of nm. The discrepancies between measured and predicted frequency distributions can be attributed to the variability induced by lithographic and etching processes on the resonator geometrical dimensions. These fabrication non-idealities have a larger impact on higher frequency devices, as reported in Fig. 4.22, and could be partially addressed by utilizing more advanced lithographic equipment.

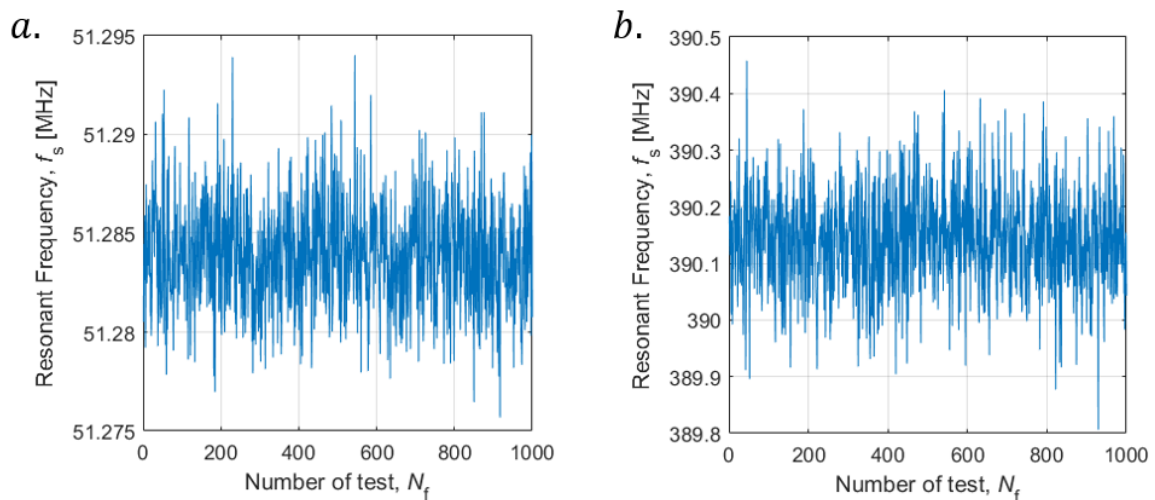


Figure 4.53: Simulated resonant frequencies as a function of the number of tests for: (a) 50 MHz devices; and (b) 400 MHz devices.

4.3.6. Conclusions on Damping Mechanism

In the present chapter, the main damping mechanism impacting X-cut LN LVRs operating between 50 and 550 MHz were investigated. Compared to traditional AlN LVRs, lithium niobate resonators experience larger losses due to electrical loading. The intrinsic quality factor of the piezoelectric thin film ($> 26,000$ at 100 MHz) and the large k_t^2 available for the mode of interest, minimize the motional resistance (R_m), making these devices more prone to experience Q_s degradation due to parasitic series resistances. No noticeable effects due to TED were recorded during the cryogenic measurements. The quality factor degradation over frequency, which is strongly highlighted in Fig. 4.35 and 4.36, hints that other losses mechanisms are playing a fundamental role in determining the Q_s of higher frequency devices.

CHAPTER 5: X-cut LVRs as Matching Networks

5.1. 1-port LVRs Gain

In Chapter 4, X-cut LVRs with record-breaking Figure of Merits are reported, making them an extremely appealing technology for the implementation of MEMS-based matching network. To assess the performance of fabricated devices, the gain provided by resonators implemented in the RFFE matching network are simulated from the gathered experimental data. To properly simulate the expected gain, it is necessary to fully characterize any parasitics between the path signal and the ground. A more accurate and widely used model for the matching network implementing a series 1-port resonator is depicted in Fig. 5.1. The model introduces a parasitic parallel resistance (R_p) and capacitance (C_p) to ground on both the input and the output port. These are the two main parasitic components that will have a direct impact on the RFFE gain.

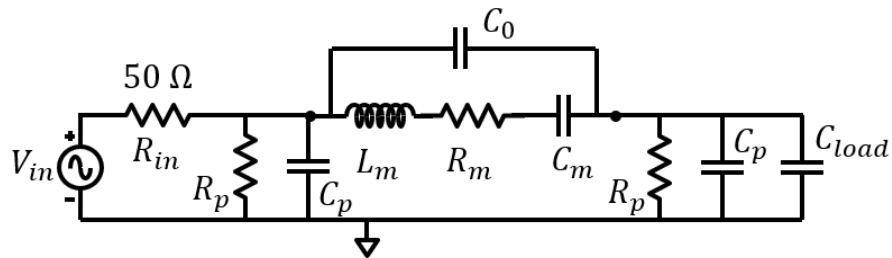


Figure 5.1: Modified model of the MEMS-based matching network described in Section 2.1.3 including parasitic resistances (R_p) and capacitances (C_p) to ground.

While C_p has been estimated in few tens of fF [66] and can be easily lumped into the design of C_{load} , the estimation of R_p results more challenging due to the limited dynamic range of most commonly used measurement instruments, including the VNA adopted for the device characterization. VNA measurements using an Intermediate Frequency (IF) bandwidth of 100 Hz

to reduce noise effects showed no differences between the R_p measured on an on-chip open test structure and the R_p measured with the probes lifted from the substrate, effectively limiting the maximum measurable value of R_p to be between 50 and 100 k Ω). Such value is clearly not compatible with experimental measurements of gains provided by devices fabricated on similar substrates and with identical pads configuration [5], since an R_p of 50 k Ω would shunt most of the current provided by the resonator to ground. For this reason, the extracted Y-parameters matrix cannot be readily used to estimate the passive voltage gain provided by the resonator to a given C_{load} . The model used in this section is captured by Eq. 5.1, where Z_{load} represents the impedance to ground at the output node (Eq. 5.2) and Z_R the impedance of the resonator, estimated from the measured Y_{12} data (Eq. 5.3).

$$G \cong \frac{Z_{load}}{Z_{load} + Z_R + R_{in}} \quad (5.1)$$

$$Z_{load} = \frac{1}{\left(j\omega C_{load} + j\omega C_p + \frac{1}{R_p}\right)} \quad (5.2)$$

$$Z_R = -\frac{1}{Y_{12}} \quad (5.3)$$

Both C_p and R_p can be to first approximation modeled as the parasitics between the signal and the ground pads, as reported in Fig. 5.2. Simulations performed on ADS Momentum, assuming a LN thickness (t_{LN}) of 2 μm , a Si thickness of 500 μm and a dissipation factor ($\tan\delta$) of 0.001 and 0.004 respectively for LN and Si, are reported in Fig. 5.3.

At 100 MHz, the resistance to ground extracted from the simulation is close to 140 dB, equal to 10 M Ω , while the parasitic capacitance was estimated to be about 20 fF, as confirmed by direct experiment. Assuming the validity of the reported simulation, R_p and C_p can both be neglected for

the gain simulation due to their high impedance compared to the variable of interest (C_{load}) at the frequencies under investigation.

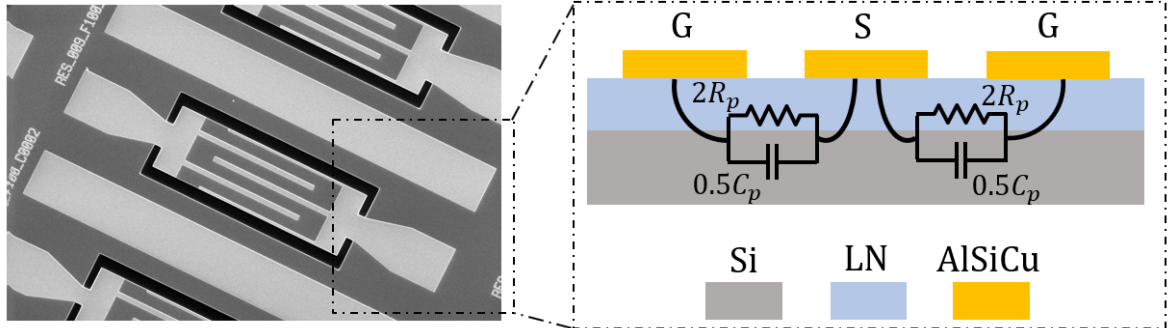


Figure 5.2: Simplified model of the parasitics (R_p and C_p) between the signal (S) and ground (G) pads.

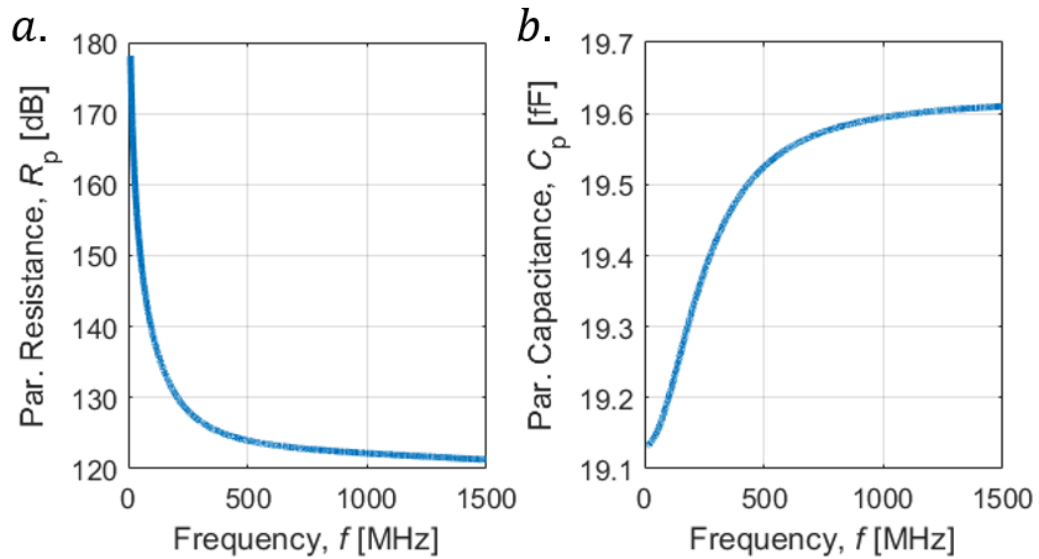


Figure 5.3: ADS Momentum simulations of: (a) parasitics resistance to ground (R_p); and (b) parasitic capacitance to ground (C_p) as a function of frequency.

5.1.1. 100 MHz LVRs Gain Simulation

The admittance response of the best measured device (in vacuum) operating around 100 MHz is reported in Fig. 5.4. With a Q_s greater than 8,000 and a k_t^2 of nearly 30%, it represents the resonator exhibiting the highest Figure of Merit (2,688) reported in literature [79] for devices operating in the Very High Frequency (VHF) range. The same reported Y_{12} data is used to simulate

the gain provided to a capacitive load when implementing the device in the matching network topology described in Section 2.1.3.

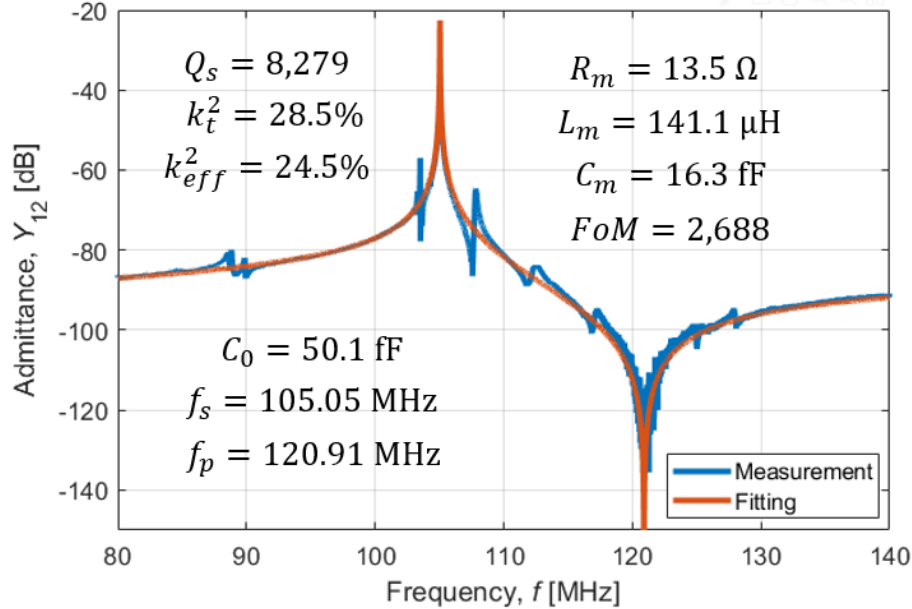


Figure 5.4: Admittance response (measured in vacuum) of the resonator exhibiting the highest Figure of Merit (FoM) ever recorded for a device in the VHF range.

Fig. 5.5 reports the results of the voltage amplification simulations, which are performed in MATLAB®. Four different capacitive loads (300, 500, 700 fF, and 1 pF) are selected to track the gain as the operating frequency (f_{RF}) moves from the anti-resonance (f_p) to the resonant frequency (f_s). Numerical simulation based on the device fitting reported in Fig. 5.5 are represented by dashed lines to highlight the differences from the theoretical solution.

Interestingly, the simulated gain attained for smaller capacitive loads is sensibly lower than the expected theoretical one (*i.e.*, 300 fF), while closely match the expected value for larger load values. This phenomenon can be explained by the presence of in-band spurious modes, which are known to cause gain degradation and peak splitting by interfering with the main mode. For a C_{load} of 300 fF and is in fact possible to distinguish two different peaks, one around 107 MHz, and another one closer to 108.5 MHz. Peak splitting and spurious modes impact on gain will be investigated more

in depth in Section 5.2. The discrepancy between the operating frequencies of simulated and theoretical peaks, which is estimated in 0.1 MHz ($<0.1\%$) is due to approximations in the estimations of the BVD motional parameters (L_m and C_m).

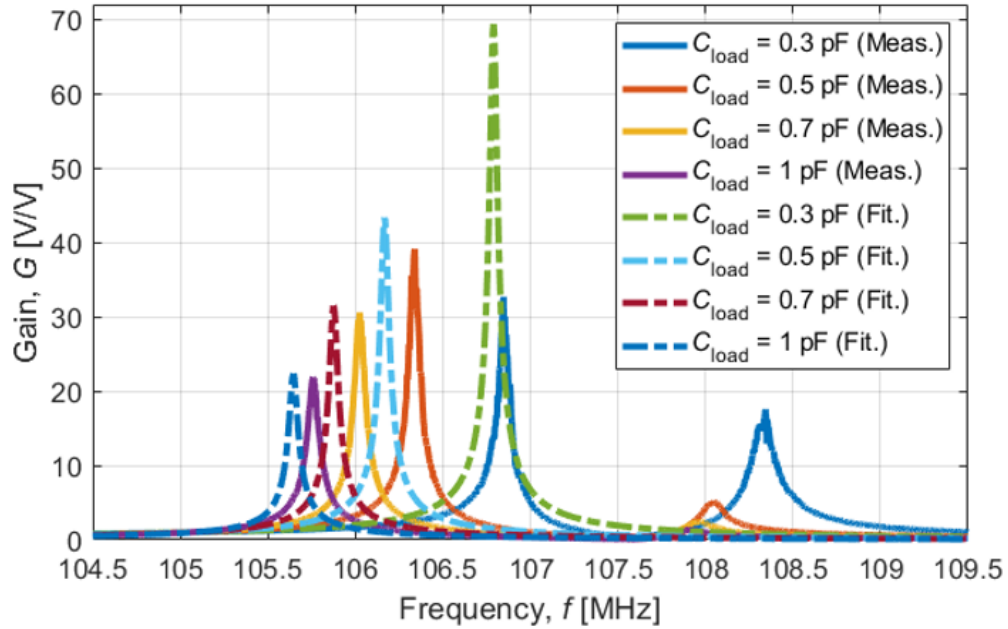


Figure 5.5: MATLAB[®] simulations of the expected gain as a function of the capacitive load (C_{load}) according to Y_{12} parameters (solid line) and BVD model fitting (dashed line).

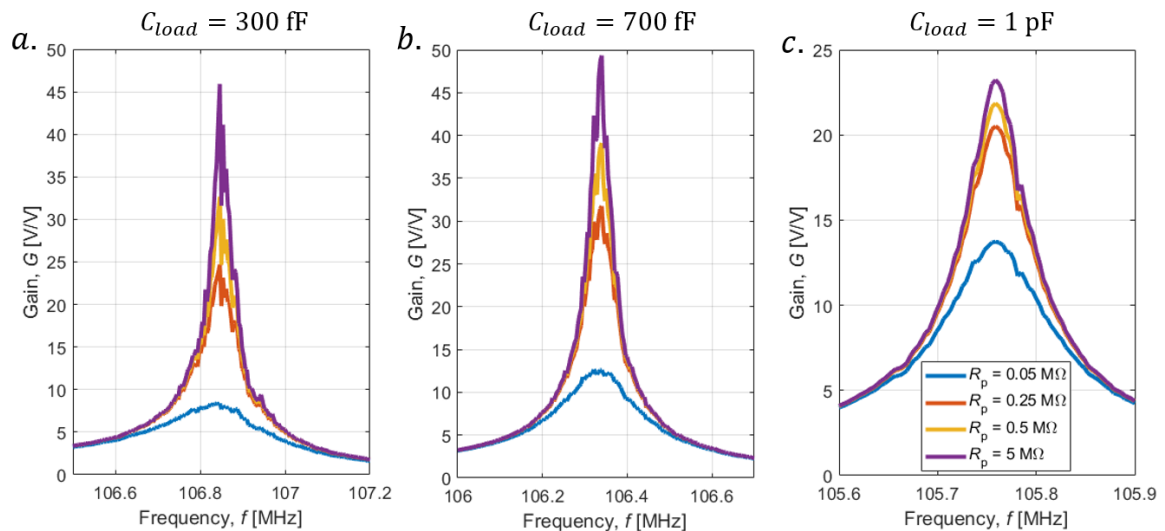


Figure 5.6: Simulated gain as a function of different parasitic resistances to ground (R_p) for a load of: (a) 300 fF; (b) 700 fF; and (c) 1 pF.

Ultimately, the impact of R_p on the simulated gain is investigated. Four different values of the parasitic impedances (50, 250, and 500 k Ω , and 5 M Ω) are simulated for three different capacitive loads (300 and 500 fF, and 1 pF). Results are reported in Fig. 5.6. As expected, low values of R_p impacts smaller loads by limiting the maximum achievable gain, which is ultimately set by the ratio between the load impedance and the source. For loads in the order of 1 pF, an R_p greater than 1 M Ω is considered sufficient to avoid significant gain reduction for large C_{load} (> 300 fF).

5.1.2. Considerations on Arrays

As thoroughly described in Section 4.3.5, arrays of resonators show a strong dependency between the quality factor (Q_{as}) and the number of elements (N_{el}) due to frequency mismatch between the individual devices. Fig. 5.7a shows the simulated gain of an array of devices exhibiting the Q_{as} reported in Fig. 5.7b and the k_t^2 and C_0 reported in Fig. 4.16, interfaced with a C_{load} of 1 pF. The voltage amplification is maximized for a number of arrayed resonators varying between 3 and 5, while sensibly drops for larger values of N_{el} and for individual devices. As discussed in Section 2.1.3, there is a suboptimal region in which the resonator is still able to provide large passive voltage amplification to a capacitive load, without being perfectly matched. The optimization reported in Section 2.1.3 is based on the hypothesis that Q_s is independent of C_0 . Since it is impossible to arbitrarily synthesize resonators with the desired static capacitance while attaining maximum Q_s , a trade-off between C_0 and Q_s exists. For this reason, operating with a smaller number of arrayed elements is often advantageous by a gain standpoint, since operating in the suboptimal region with a higher FoM overcomes the Q_s degradation introduced by a larger N_{el} .

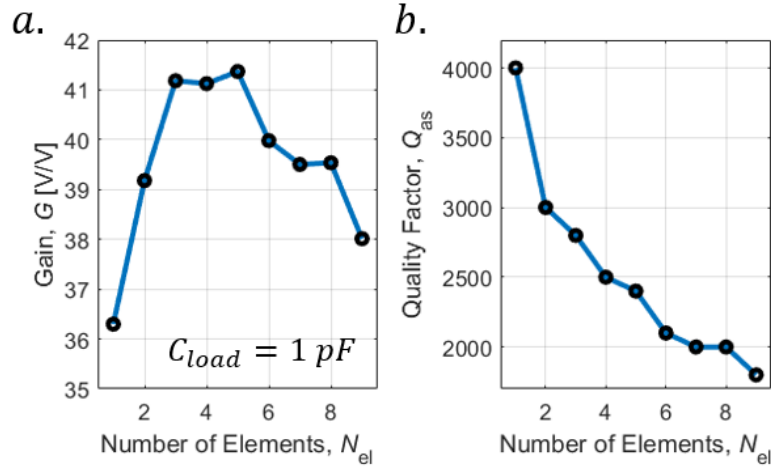


Figure 5.7: (a) Simulated gain for a C_{load} of 1 pF given as a function of the parameters reported in Fig. 4.16; and (b) relationship between the array quality factor (Q_{as}) and the number of elements.

5.2. Effects of Spurious Modes on Gain

Spurious modes are defined as any undesired mode exhibited by microelectromechanical resonators. In-band spurious modes are especially detrimental in filtering applications, since they increase the transmission losses in the pass band, causing signal attenuation and distortion. For this reason, the origin of such modes has been widely investigated [84][85], such as techniques to mitigate their impact [86] or predict their emergence [87]. As highlighted in Section 5.1, unwanted modes are harmful also for resonators implemented as narrow band matching networks, since they can cause peak splitting, frequency shift and gain attenuation compared to spurious-free devices. Unfortunately, the large intrinsic k_t^2 and the strong asymmetricity of the LN lattice makes X-cut LVRs particularly prone to exhibiting in and out-of-band spurious modes, as widely reported in literature [82]. Recent results showed devices fabricated on thin film of LN with spurious-free responses [15][88], but with limited Q_s compared to the devices operating at similar frequencies presented in Section 4.

The simplest approach to model the behavior of a resonator exhibiting spurious modes is via a Multi-BVD model (Fig. 5.8), in which each unwanted mode is represented by a parallel resonant branch [23]. A comparison between a spurious-free response (BVD model) and a Multi-BVD approach is reported in Fig. 5.9. The simulations are performed according to the measured data of a 50 MHz device (Table 5.1).

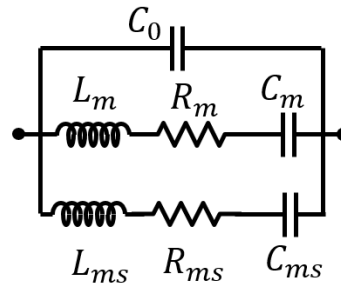


Figure 5.8: Multi-BVD model of a 1-port LVR. R_{ms} , L_{ms} , and C_{ms} represent the motional parameters of the spurious modes.

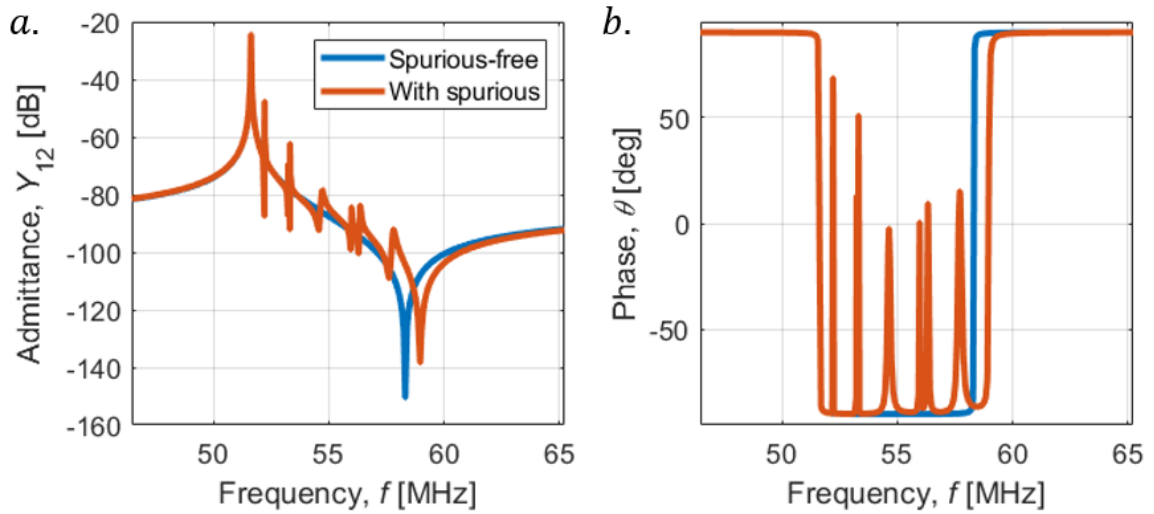


Figure 5.9: (a) Simulated admittance response of 1-port LVR operating around 50 MHz considering only the main S_0 mode (blue) and including 7 in-band spurious modes (red); and (b) phases of the simulated resonators.

Table 5.1: Multi-BVD fitting coefficients ($C_0 = 115.9$ fF)

i -th Mode	Frequency, f_s [MHz]	Frequency, f_p [MHz]	Quality Factor, Q_s	EM coupling, k_t^2
0 (S_0)	51.63	59.28	5,831	0.3
1	52.1677	52.2204	58,186	0.0025
2	53.215	53.244	7,067	0.0013
3	53.305	53.3235	28,490	0.0009
4	54.55	54.690	490	0.0063
5	55.965	55.98	2,294	0.0007
6	56.32	56.352	1,206	0.0014
7	57.75	57.785	439	0.0015

The impact of spurious modes on the admittance of a resonator when interfaced with a capacitive load can be illustrated by using a simplified model which accounts for a single spurious mode located closely to the operating frequency (f_{RF}). A capacitive load of 100 fF is selected for a resonator exhibiting Q_s , k_t^2 and f_s for the main mode as reported in Table 5.1. In case of spurious free response, the operating frequency is purely set by the capacitive load and it is close to 56.68 MHz. If a spurious mode with $f_{ss} = 55.6$ MHz, $Q_{ss} = 5,000$, and $k_{ts}^2 = 0.2\%$ is introduced in the model as an additional resonant branch, the proximity between the operating frequency of the main mode and the spurious causes a split peak (Fig. 5.10a), which directly translates into a pulling of the operating frequency and reduction of the maximum achievable gain (Fig. 5.10b). As a secondary effect, the presence of a spurious mode close to the anti-resonance causes a pulling of f_p , as shown in Fig. 5.9a.

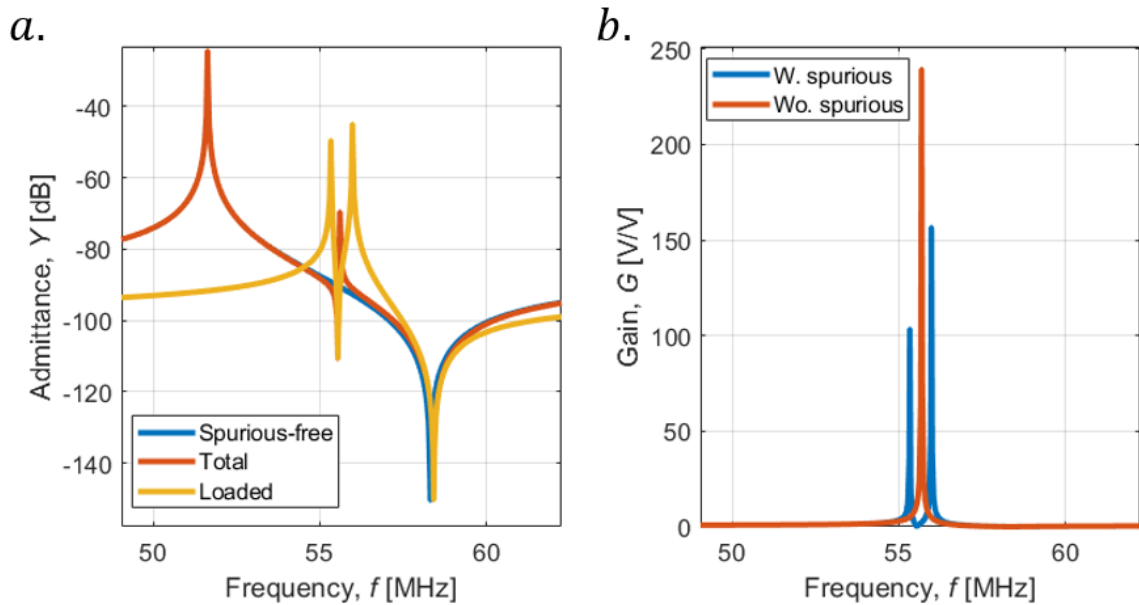


Figure 5.10: (a) Simulated admittance responses of a resonator without spurious modes (blue), with spurious modes (red), and after pulling in presence of spurious modes (orange); and (b) split peak due to the presence of an in-band spurious mode.

In this section, an analytical modeling of the pulled anti-resonant and operating frequency is presented to provide a physical explanation of the phenomenon. The effect of spurious modes key parameters (Q_{ss} , k_{ts}^2 , and f_{ss}) on the gain provided by a 1-port LVR when implemented in the matching network described in Section 2.1.3 is also investigated. A high Q_s resonator, exhibiting the modes reported in Table 5.1, is used as an example throughout the entire section.

5.2.1. Frequency Pulling Modeling

As highlighted in Fig. 5.94, the presence of spurious modes close to the anti-resonance causes the pulling of f_p , which complicates the extraction of k_t^2 [23]. Assuming $R_m = R_{ms} = 0$, the admittance of a two-branch Multi-BVD equivalent circuit can be modeled as in Eq. 5.4, where ω_{ss} represents the resonant frequency of the spurious mode.

$$Y = \frac{j\omega C_0 \left(1 - \frac{\omega^2}{\omega_s^2}\right) \left(1 - \frac{\omega^2}{\omega_{ss}^2}\right) + j\omega C_m \left(1 - \frac{\omega^2}{\omega_{ss}^2}\right) + j\omega C_{ms} \left(1 - \frac{\omega^2}{\omega_{ss}^2}\right)}{\left(1 - \frac{\omega^2}{\omega_s^2}\right) \left(1 - \frac{\omega^2}{\omega_{ss}^2}\right)} \quad (5.4)$$

Intuitively, the series resonances of the main and the spurious modes remain unaltered since they are represented by two conjugated couples of zeros. To calculate the anti-resonance, it is necessary to set the numerator equal to zero. Such equation can be rewritten as in Eq. 5.5, where ω_p and ω_{ps} (Eq. 5.6 and 5.7) represent the unpulled anti-resonant frequencies of the main and of the spurious modes, respectively. A more detailed derivation of the model is reported in Appendix B.

$$\omega^4 - \omega^2(\omega_p^2 + \omega_{ps}^2) + \omega_{ss}^2 \omega_p^2 + \omega_s^2 \omega_{ps}^2 - \omega_s^2 \omega_{ss}^2 = 0 \quad (5.5)$$

$$\omega_p = \omega_s \sqrt{\frac{C_0 + C_m}{C_0}} \quad (5.6)$$

$$\omega_{ps} = \omega_{ss} \sqrt{\frac{C_0 + C_{ms}}{C_0}} \quad (5.7)$$

An analytical expression can be found for the roots of Eq. 5.5, which respectively represent the pulled anti-resonance frequency of the main mode (ω_p' , Eq. 5.8) and of the spurious mode (ω_{ps}' , Eq. 5.9). Interestingly, the two pulled anti-resonances are equidistant from a central frequency (ω_{pc}), which is function of ω_p and ω_{ps} (Eq. 5.10), proportionally to a distance factor (δ_p , Eq. 5.11).

$$\omega_p' = \sqrt{\omega_{pc}^2 + \frac{1}{2} \sqrt{(\omega_p^2 + \omega_{ps}^2) - 4(\omega_{ss}^2 \omega_p^2 + \omega_s^2 \omega_{ps}^2 - \omega_s^2 \omega_{ss}^2)}} \quad (5.8)$$

$$\omega_{ps}' = \sqrt{\omega_{pc}^2 - \frac{1}{2} \sqrt{(\omega_p^2 + \omega_{ps}^2) - 4(\omega_{ss}^2 \omega_p^2 + \omega_s^2 \omega_{ps}^2 - \omega_s^2 \omega_{ss}^2)}} \quad (5.9)$$

$$\omega_{pc} = \sqrt{\frac{\omega_p^2 + \omega_{ps}^2}{2}} \quad (5.10)$$

$$\delta_p^2 = \frac{1}{2} \sqrt{(\omega_p^2 + \omega_{ps}^2) - 4(\omega_{ss}^2 \omega_p^2 + \omega_s^2 \omega_{ps}^2 - \omega_s^2 \omega_{ss}^2)} \quad (5.11)$$

Assuming constant ω_s , ω_p , and k_{ts}^2 , a variation of ω_{ss} (and consequently of ω_{ps}), generates an increment of δ_p^2 when ω_{ps} approaches ω_p , causing the divergence of the roots.

This phenomenon is captured by Fig. 5.11a, which represents the contour plot of the admittance response of a simulated resonator as a function of frequency (f), when varying the spurious mode anti-resonant frequency (f_{ps}). The numerical simulation is performed assuming a f_s of 51.63 MHz, a Q_s of 5,800, a k_{τ}^2 of 30%, and a C_0 of 115.9 pF for the main mode (as in Table 5.1), while the spurious quality factor (Q_{ss}) is set to 20,000, and its k_{ts}^2 to 0.63%. The resonant frequency of the spurious mode is calculated from the anti-resonance according to Eq. 4.1. As reported in Fig. 5.11a, the spurious mode has no influence on the anti-resonance of the main mode up to roughly 57 MHz,

when both f_p' and f_{ps}' start diverging. The analytical derivation of the pulled anti-resonant frequencies (Eq. 5.8 and 5.9) closely follow the numerical simulation (Fig. 5.11b).

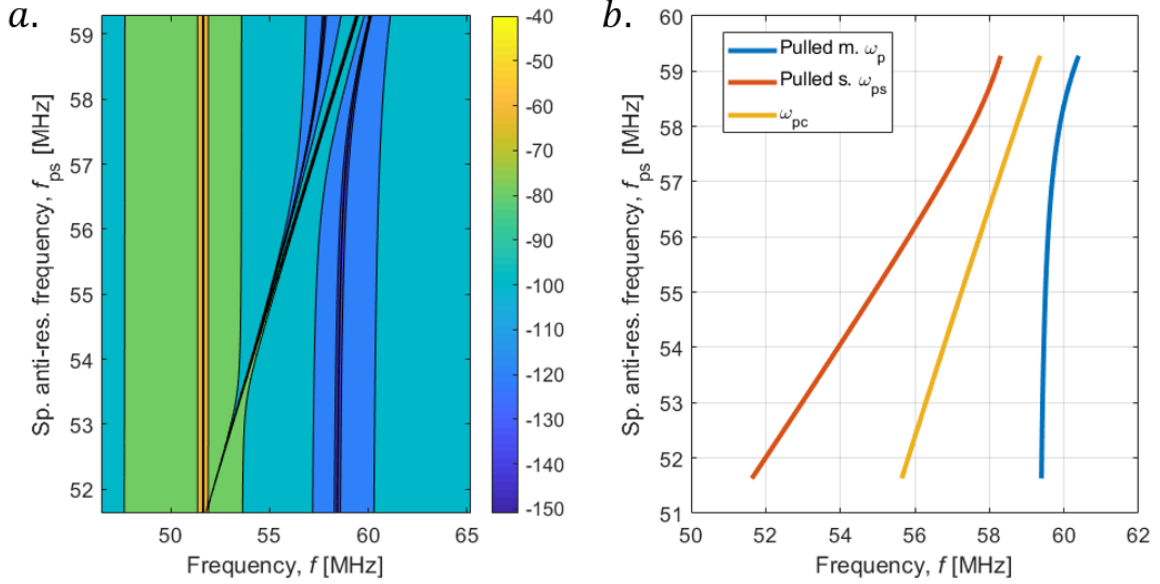


Figure 5.11: (a) Contour plot of the admittance of a resonator as a function of the anti-resonance frequency of a spurious mode ($f_s = 50$ MHz, $Q_s = 5,000$, $k_t^2 = 0.3$ and $C_0 = 70$ fF); and (b) analytical simulation of the frequency pulling.

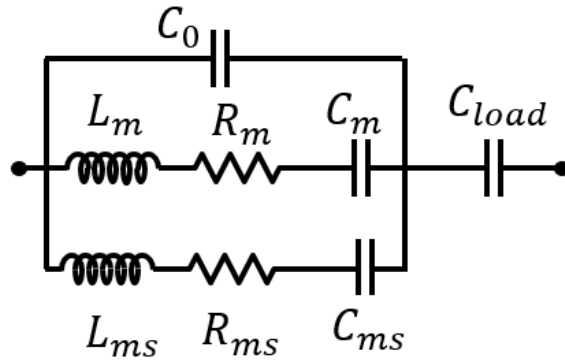


Figure 5.12: Multi-BVD model in series with a load capacitance, as in the matching network described in Section 2.1.3.

If a capacitive load is interfaced in series with the 1-port resonator (Fig. 5.12), as in the matching network series configuration described in Section 2.1.3, the resonant frequency of the main mode (f_s) and of the spurious mode (f_{ss}) are no longer decoupled and influence the operating frequency of the system. A mathematical expression similar to Eq. 5.4 can be found by setting the denominator of the admittance of the circuit represented in Fig. 5.12 equal to zero (Eq. 5.12). An equation similar

to Eq. 5.5 (Eq. 5.13) can be then derived, where ω_{RF} (Eq. 5.14) and ω_{RFs} (Eq. 5.15) represents the operating resonant frequency of the main and spurious modes, respectively, as described in Section 2.1.3.

$$j\omega \left[(C_{load} + C_0) \left(1 - \frac{\omega^2}{\omega_s^2} \right) \left(1 - \frac{\omega^2}{\omega_{ss}^2} \right) + C_m \left(1 - \frac{\omega^2}{\omega_{ss}^2} \right) + C_{ms} \left(1 - \frac{\omega^2}{\omega_s^2} \right) \right] = 0 \quad (5.12)$$

$$\omega^4 - \omega^2(\omega_{RF}^2 + \omega_{RFs}^2) + \omega_{RF}^2\omega_{ss}^2 + \omega_{RFs}^2\omega_s^2 - \omega_s^2\omega_{ss}^2 = 0 \quad (5.13)$$

$$\omega_{RF} = \omega_s \sqrt{\frac{C_{load} + C_0 + C_m}{C_{load} + C_0}} \quad (5.14)$$

$$\omega_{RFs} = \omega_{ss} \sqrt{\frac{C_{load} + C_0 + C_{ms}}{C_{load} + C_0}} \quad (5.15)$$

The mathematical derivation of the pulled resonance frequency of the main (ω_{RF}' , Eq. 5.16) and spurious (ω_{RFs}' , Eq. 5.17) modes follows the same steps described to find ω_p' and ω_{ps}' . Even in this case, the two pulled resonant frequencies are equidistant from a central pulled resonant frequency (ω_{RFC}) defined as in Eq. 5.18, proportionally to a distance factor (δ_{RF} , Eq. 5.19).

$$\omega_{RF}' = \sqrt{\omega_{RFC}^2 - \delta_{RF}^2} \quad (5.16)$$

$$\omega_{RFs}' = \sqrt{\omega_{RFC}^2 + \delta_{RF}^2} \quad (5.17)$$

$$\omega_{RFC} = \sqrt{\frac{\omega_{RF}^2 + \omega_{RFs}^2}{2}} \quad (5.18)$$

$$\delta_{RF}^2 = \frac{1}{2} \sqrt{(\omega_{RF}^2 + \omega_{RFs}^2) - 4(\omega_{ss}^2\omega_{RF}^2 + \omega_s^2\omega_{RFs}^2 - \omega_s^2\omega_{ss}^2)} \quad (5.19)$$

The effect of a moving spurious mode on the pulled operating frequencies (f_{RF}' and f_{RFs}') was investigated using the same approach described for the pulling anti-resonant frequencies. A load of 150 fF was introduced in the simulation to pull the main mode around 54 MHz. Similarly to the

results described by Fig. 5.11a, the operating frequency of the main mode (f_{RF}) gets pulled to lower frequencies until the anti-resonance is far enough (~ 1 MHz) from the peak of the main mode (Fig. 5.13a). As in Fig. 5.11b, the analytical model captured by Eq. 5.16 and 5.17 for f_{RF}' and f_{RFs}' matches the numerical simulation (Fig. 13b).

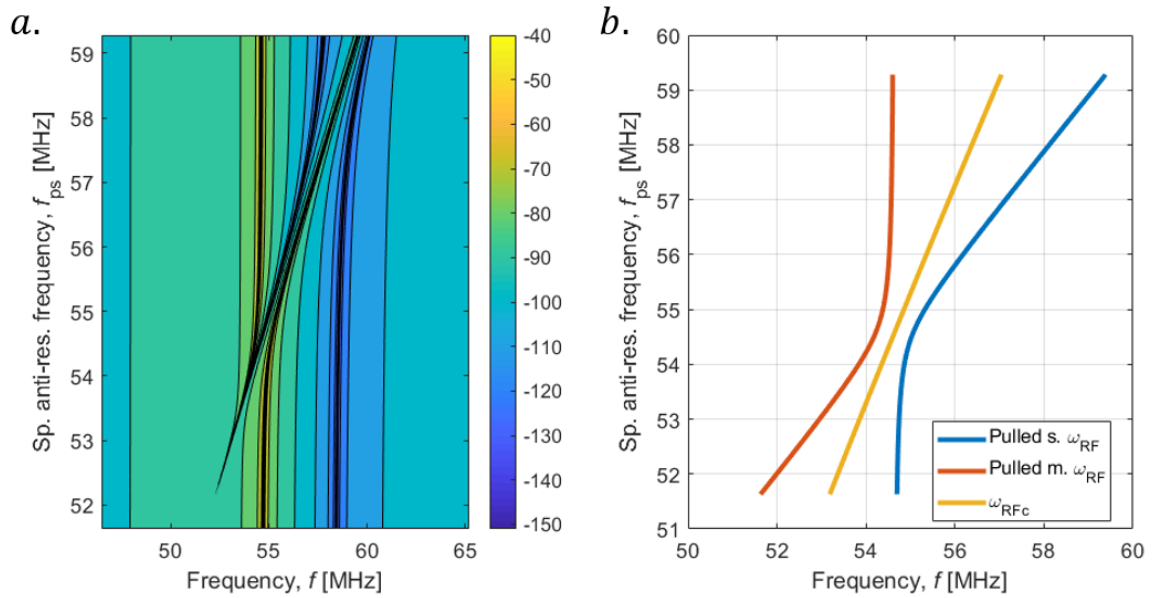


Figure 5.13: (a) : (a) Contour plot of the admittance of a pulled resonator as a function of the anti-resonance frequency of a spurious mode ($f_s = 50$ MHz, $Q_s = 5,000$, $k_t^2 = 0.3$ and $C_0 = 70$ fF); and (b) analytical simulation of the frequency pulling.

The analytical and numerical models developed in this section hint that while a complete suppression of spurious modes would be desirable by an application stand-point, their presence could be tolerated if such modes are positioned far enough from the operating frequency of the loaded resonator (or from its anti-resonance if implemented in a parallel configuration, as in the transformer described in Section 2.1.5).

5.2.2. Impact of Spurious Modes Key Parameters on Gain

The impact of the spurious mode key parameters (f_{ss} , Q_{ss} and k_{ts}^2) is numerically investigated assuming a spurious-free device operating around 50 MHz with the characteristics described in Table 5.1. A series capacitance of 100 fF is added in series with such resonator to set its operating frequency (ω_{RF}) to 55.68 MHz, as described in the introduction of the present chapter.

Fig. 5.14a reports the effect of the spurious resonant frequency (f_{ss}) on the gain peak due to the main mode (blue line) and the unwanted mode (red line). Q_{ss} and k_{ts}^2 are respectively fixed to 5,000 and 0.2%, while f_{ss} is expressed as a frequency variation (Δ) from the undisturbed operating frequency (f_{RF}) according to Eq. 5.20. As the spurious mode approaches f_{RF} , the gain of the main mode starts dropping, while the gain due to the unwanted mode increases. The worst case scenario is represented by a perfectly split peak, in which both the gains have the same magnitude.

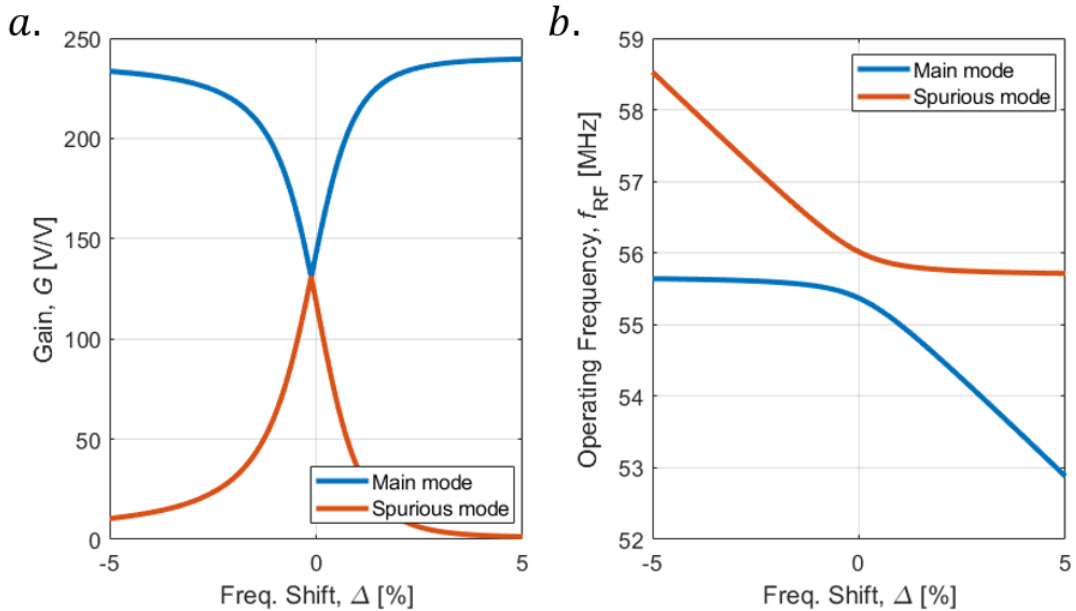


Figure 5.14: (a) Magnitude of the voltage amplifications generated by the main mode peak (blue line) and spurious mode peak (red line) as a function of the frequency distance between modes; and (b) frequency pulling as a function of the frequency distance between a main and a spurious mode.

As highlighted in Fig. 5.14a, a frequency shift of 2% is enough to keep the peaks separated (Fig. 5.14b) and limit the gain degradation introduced by the spurious mode.

$$\Delta = 1 - \frac{f_{ss}}{f_{RF}} \quad (5.20)$$

A variation in the quality factor of the spurious mode (Q_{ss}) impacts both the maximum achievable gain and the bandwidth over which the voltage amplification is reduced. Low Q_{ss} spurious modes are more deleterious than high Q_{ss} ones, since they cause a larger gain reduction of the main peak and increase in the bandwidth over which the gain is degraded (Fig. 5.15).

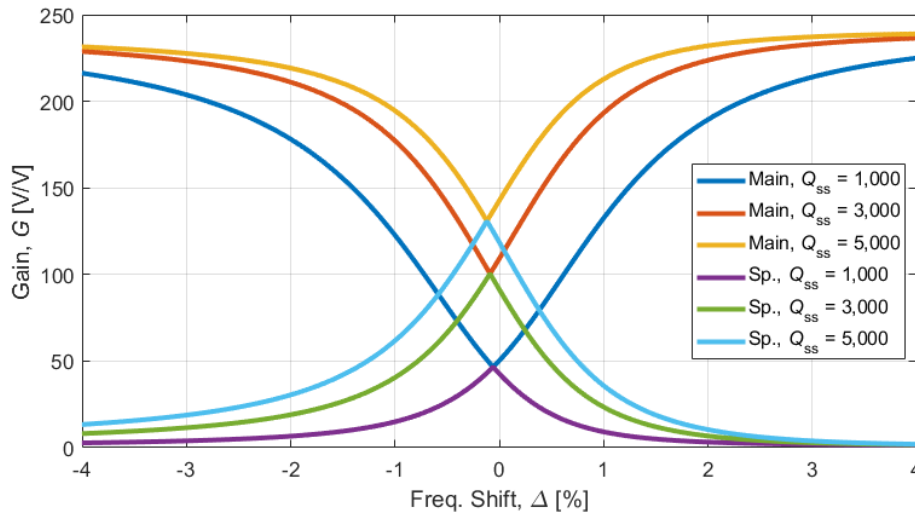


Figure 5.15: Magnitude of the voltage amplifications generated by the main mode peak and the spurious mode peak as a function of spurious mode quality factor (Q_{ss}).

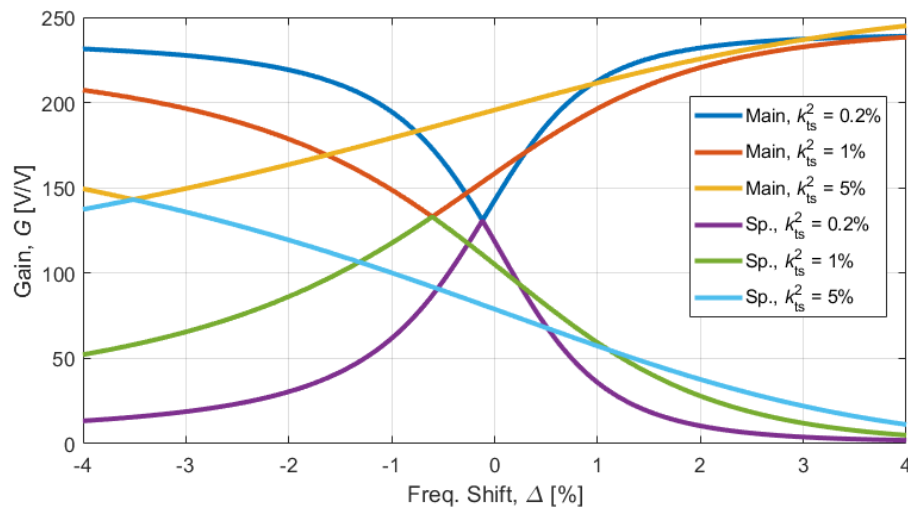


Figure 5.16: Magnitude of the voltage amplifications generated by the main mode peak and the spurious mode peak as a function of spurious mode EM coupling (k_{ts}^2).

The spurious modes electromechanical coupling (k_{ts}^2) has a similar effect on the bandwidth, while does not sensibly affect the maximum attainable gain (Fig. 5.16).

In conclusion, if a spurious mode cannot be fully suppressed, high Q_{ss} and low k_{ts}^2 spurious modes which are at least shifted by 2% from the spurious-free operating frequency are more tolerable by the matching network described in Section 2.1.3. For this reason, apodization techniques may not be an optimal solution since they extensively rely on the reduction of spurious modes quality factors to limit their impact [86]. While this approach is desirable for filtering applications, it worsen the impact of unwanted modes if they are not fully suppressed for the application targeted by this dissertation. One possible solution is to vary the geometrical dimensions affecting the spurious mode locations (*i.e.*, finger-to-bus gap) once a C_{load} , and thus a f_{RF} , is set.

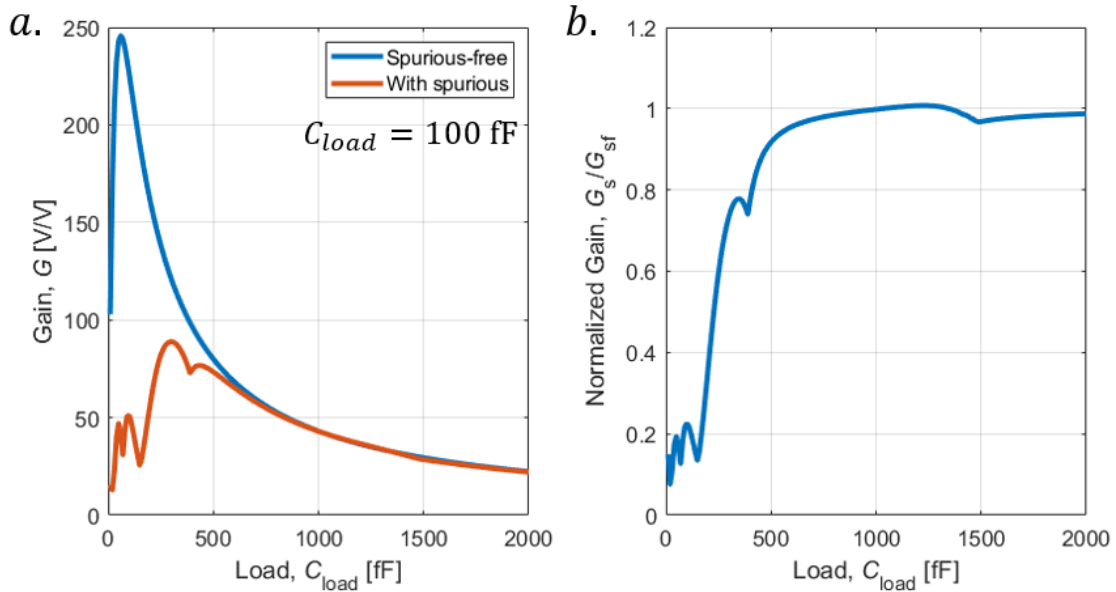


Figure 5.17: (a) Simulated gain implementing the spurious-free BVD model (blue line) and the Multi-BVD model (red line) reported in Fig. 5.9 for a load of 1 pF; and (b) ratio between the gain in presence of spurious (G_s) vs. spurious-free gain (G_{sf}).

These considerations can be extended to a full Multi-BVD model, as the one described in the introduction of the present chapter. In this case, the capacitive load (C_{load}) is swept from 10 fF to 2 pF. As reported in Fig. 5.17a, the spurious-free gain (G_{sf} , which accounts only for the main mode)

is maximized around a C_{load} of 150 fF, which represents the optimal load for a resonator with a C_0 of 115.9 fF. As expected, the gain drops as the load increases, due to the lower impedance transformation ratio. If spurious modes are present, the voltage gain (G_s) shows a large degradation for capacitive loads up to 500 fF. This phenomenon occurs since spurious modes close to the anti-resonance have experimentally proven to exhibit lower Q_{ss} than unwanted modes close to f_s . Fig. 5.17b reports the ratio between the gain attained in presence of spurious versus the spurious-free maximum attainable gain. These consideration hints that a trade-off between spurious modes and resonator size exists, and that it is convenient to operate in the suboptimal gain region (*i.e.*, with smaller resonators) for large loads to increase f_{RF} , moving the operating frequency away from the anti-resonance frequency. Two numerical examples for the resonator under examination are reported in Fig. 5.18, for 100 fF and 1 pF capacitive loads.

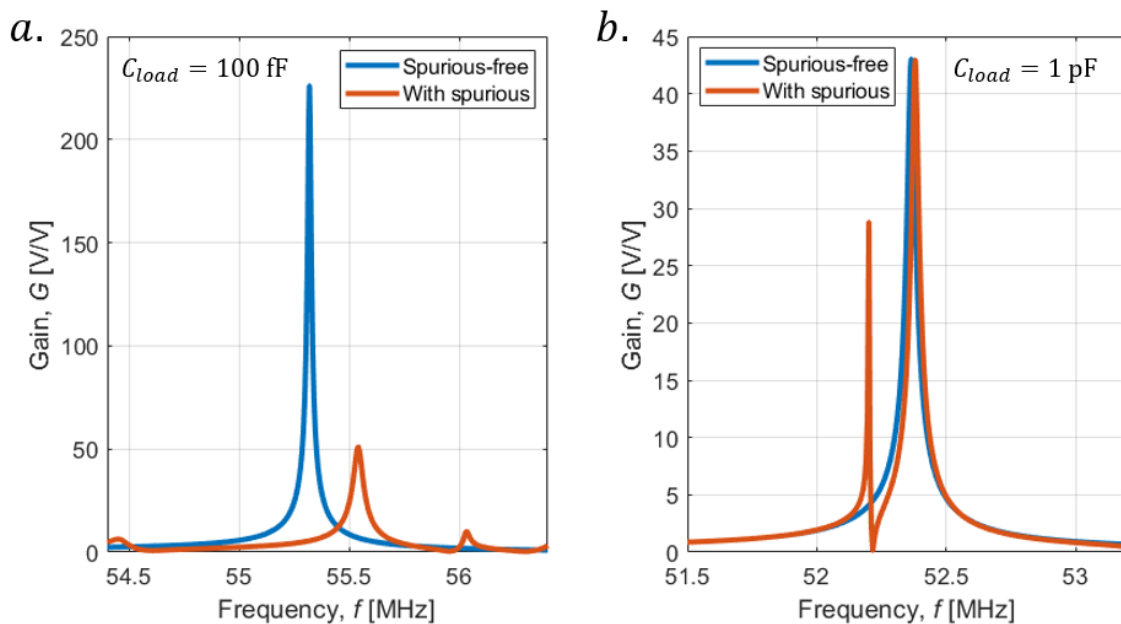


Figure 5.18: Simulated gain for the models reported in Fig. 9 for two loads: (a) 100 fF; and (b) 1 pF.

5.3. L-network Topology

As presented in the previous sections, there are limitation on the maximum achievable gains when attempting to properly match the static capacitance (C_0) of the resonator to large values of C_{load} . High quality factors, and consequently high FoMs, are in fact attained only for relatively small resonators with limited aperture (L_c) and number of finger pairs (N_p), due to the need of keeping a large L/W ratio while minimizing the impact of electrical loading. This problem worsens at higher frequencies, since the motional resistance (R_m) is inversely proportional to ω , while the series resistance (R_s) is only dictated by the device geometry and the top electrode metal thickness, which cannot be incremented arbitrarily (Fig. 4.18a). Fabrication non-idealities also impact devices operating at higher frequency more aggressively, limiting their performance. As reported in Sections 4.1.4 and 5.1.2, arrays of parallel resonators offer only minor advantages since their quality factor (Q_{sa}) is degraded by variations of the resonant frequency of the elements composing the array. Ultimately, resonators matched to the static capacitance of the load tends to operate closer to the anti-resonance region (Fig. 2.5), where spurious mode show lower Q_{ss} and are more likely to degrade the voltage boost provided by the matching network.

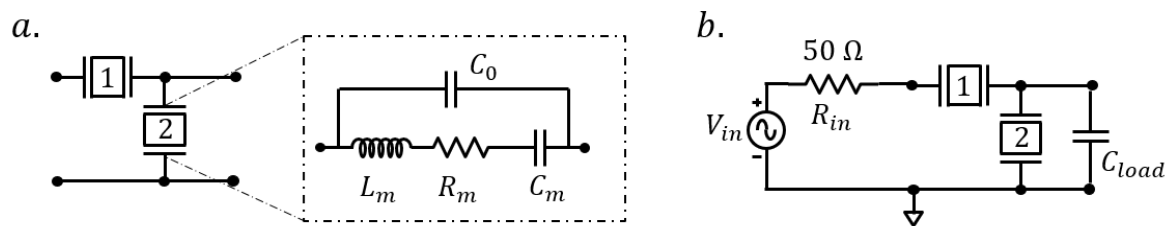


Figure 5.19: (a) Schematic of the series-parallel (L-network) approach; and (b) L-network implementation in a matching network.

For all these reasons, the development of more complex matching networks topologies [38], which can implement compact resonators exhibiting limited C_0 and incredibly high FoMs, is of

particular interest for the applications targeted by this dissertation. One possible solution consists in arranging a pair of resonators in an innovative series-parallel network configuration, or L-network, as reported in Fig. 5.19.

The L-network works similarly to the series approach described in Section 2.1.3, providing for impedance matching between the antenna ($R_{in} = 50 \Omega$) and a capacitive load (C_{load}). The ratio between the load and source impedances defines the maximum attainable gain, assuming the absence of insertion losses. In the L-network topology, a resonator (R2, Fig. 5.19a) operating in its inductive region is implemented in parallel with C_{load} to increase its impedance over a narrow bandwidth. The series resonator (R1, Fig. 5.19a) resonates out the parallel between R2 and C_{load} , allowing for a large current to flow and charge the effective load ($C_{load,eff}$). The $C_{load,eff}$ synthesized by a L-network is captured by Eq. 5.21, and ideally must be lower than C_{load} to provide any advantage by a voltage gain stand-point.

$$C_{load_{eff}} = C_{02} + C_{load} + \frac{1}{-\omega L_{m2} + j\omega R_{m2} + \frac{1}{C_{m2}}} \quad (5.21)$$

The same result could be attained by the introduction of a parallel inductor to resonate out C_{load} at the frequency of interest. This solution is fundamentally limited by the use of commercial or MEMS inductors, which exhibit quality factors (Q) between 50 and 200. Inductors with such low Q s introduce a small resistance in parallel to C_{load} , shunting the large current built up by the series resonator to ground. Instead, if the inductor in parallel with C_{load} is implemented with a very high FoM resonator, the aforementioned approach can function efficiently in a small form factor.

In this section, an analytical model is derived for the L-network topology, and differences with the series approach are highlighted. A numerical optimization is later performed to identify the

optimal design point for the series and parallel resonators. In conclusion, an example based on measured data is provided to validate the numerical model developed.

5.3.1. Analytical Modeling

An analytical model for the L-network configuration can be easily derived assuming that the static capacitances of the series and parallel resonators are equal ($C_{01} = C_{02}$). The admittances of the series resonator (Y_A , Fig. 5.20a) and of the loaded parallel resonators (Y_B , Fig. 5.20a) can be expressed according to Eq. 5.22 and 5.23. The total admittance can be readily calculated as the series of the two admittances (Eq. 5.24), and is represented in Fig. 5.20b.

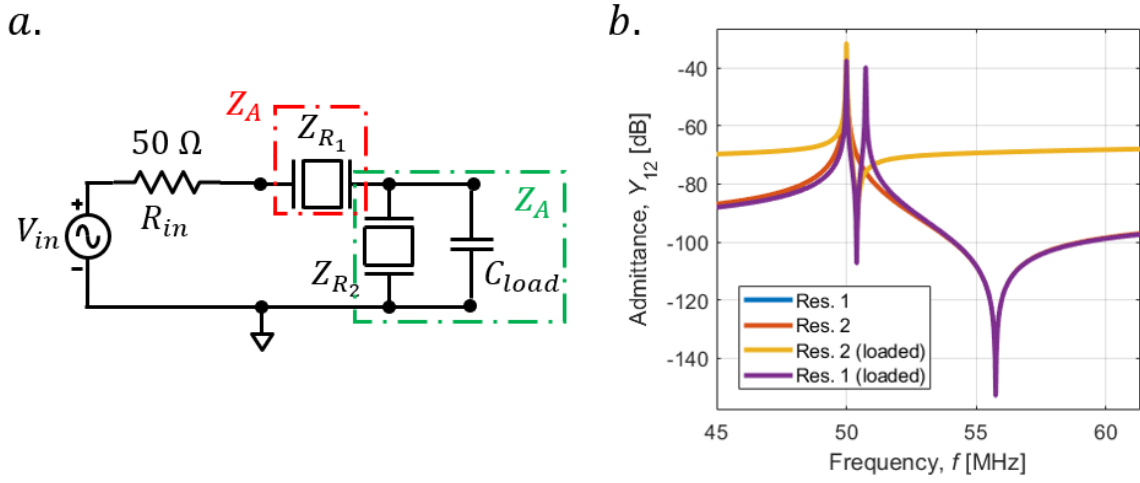


Figure 5.20: (a) L-network topology; and (b) admittance responses of the two resonators (blue and red line, overlapped), of the parallel resonator loaded by C_{load} of 1 pF (orange), and of the L-network response .

$$Y_A = \frac{1}{Z_A} = j\omega C_0 + \frac{1}{R_m + j\omega L_m + \frac{1}{j\omega C_m}} \quad (5.22)$$

$$Y_A = \frac{1}{Z_B} = j\omega C_0 + j\omega C_{load} + \frac{1}{R_m + j\omega L_m + \frac{1}{j\omega C_m}} \quad (5.23)$$

$$\frac{1}{Y} = \frac{1}{Y_A} + \frac{1}{Y_B} \quad (5.24)$$

As reported in Fig. 5.20b, the admittance presents two operating resonances and two anti-resonances. The first operating resonance lies at the natural frequency of the system (ω_s), while the second one (ω_{RF}) can be expressed by solving Eq. 5.25. Such frequency is expressed by Eq. 5.26, and closely resemble the operating frequency reported in Section 2.1.3 for a matching network based on a series resonator (Eq. 2.12). α represents the ratio between C_{load} and C_0 as previously discussed.

$$2j\omega C_0 \left(1 - \frac{\omega^2}{\omega_s^2}\right) + j\omega C_{load} \left(1 - \frac{\omega^2}{\omega_s^2}\right) + 2j\omega C_m = 0 \quad (5.25)$$

$$\omega_{RF} = \omega_s \sqrt{\frac{2C_0 + C_{load} + 2C_m}{2C_0 + C_{load}}} = \omega_s \sqrt{\frac{2 + \alpha + 2K^2}{2 + \alpha}} \quad (5.26)$$

Evaluating the real component of the inverse of Y_A (Z_A) leads to Eq. 5.27, which represents the insertion losses of the series resonator when operating at ω_{RF} . By manipulating Eq. 5.28, it is possible to define a pulling factor for Z_A (k_{pA}). Similarly to the k_p described for the series resonator matching network, k_{pA} multiplies the motional resistance (R_m) when the device is configured in series with a capacitive load.

$$\text{Re}\{Z_A\} = \frac{K^2}{\omega_s C_0 Q_s} \frac{1}{\left(1 + K^2 - \frac{2 + \alpha + 2K^2}{2 + \alpha}\right)^2} = k_{pA} R_m \quad (5.27)$$

$$k_{pA} = \frac{2 + \alpha^2}{\alpha^2} \quad (5.28)$$

The real component of Z_B is represented by a slightly different equation (Eq. 5.29). Curiously, the derived pulling factor results identical to k_{pA} (Eq. 5.30), meaning that both the resonators introduce the same losses when operating at ω_{RF} .

$$\text{Re}\{Z_B\} = \frac{K^2}{\omega_s C_0 Q_s} \frac{1}{\left[(1 + \alpha) \left(1 - \frac{2 + \alpha + 2K^2}{2 + \alpha}\right) + K^2\right]^2} = k_{pB} R_m \quad (5.29)$$

$$k_{p_B} = k_{p_A} = \frac{2 + \alpha^2}{\alpha^2} \quad (5.30)$$

Both k_{p_A} and k_{p_B} are higher than the pulling factor for the series topology (Eq. 2.14). Therefore, the gain attained by a L-network topology is a trade-off between the larger losses introduced by the series-parallel resonators and the effective load synthesized by the combination of the parallel resonator and C_{load} (which is smaller and allows for higher gains). Even if an analytical derivation of the optimal C_0 can be found, the complexity of the mathematical problem fostered the development of a numerical method to identify the impact of the key network parameters on the maximum attainable gain.

5.3.2. Numerical Optimization

The voltage gain provided by a L-network for a fixed C_{load} of 1 pF is numerically simulated with MATLAB[®]. To simplify the problem, all the variables are fixed except for the static capacitance of the series (C_{01}) and parallel resonators (C_{02}). The natural frequency (f_s) is fixed to 50 MHz, while Q_s and k_t^2 are respectively set to 5,000 and 30%, according to the experimental data showcased in Chapter 4. The static capacitances of the series (C_{01}) and of the parallel resonator (C_{02}) are then swept from 0 to 1 pF in steps of 10 fF. As clearly shown by the contour plot of the gain as a function of C_{01} and C_{02} (Fig. 5.21), a global optimal point exists when C_{01} and C_{02} approach 400 fF. Two cases of interest can be extracted from Fig. 5.21. In the first case (Fig. 5.22, blue line) the static capacitance of the two resonator is set equal ($C_{01} = C_{02}$), while in the second case (Fig. 5.22a, red line) the static capacitance of the parallel resonator is set to 0 (to simulate a series approach).

This comparison serves to benchmark the benefits introduced by the L-network over the series-only configuration.

As clearly shown in Fig. 5.22, the L-network offers two main advantages over a simple series configuration. If the capacitive load is large enough, the parallel-series topology provides a larger gain (+30%). Furthermore, the optimal point is achieved for smaller resonator static capacitance (400 fF vs. 740 fF). Smaller capacitance resonators have generally shown higher Q_s , both for individual devices and arrays [79]. It is interesting to note that the optimal solution occurs for two identical size resonators, which makes the L-network more amenable to large scale manufacturing.

Ultimately, the L-network also shows robustness in regards to frequency mismatch between series and parallel elements. Frequency mismatch has proven to be a relevant problem for arrays with large number of elements, as discussed in Chapter 4. As highlighted in Fig. 5.22b, the gain provided by the proposed configuration is almost independent of any frequency mismatch between the series and parallel resonators in the range of $\pm 20,000$ parts per million (ppm). Beyond this frequency range, the gain decreases monotonically until the L-network does not offer any advantage over a single series configuration.

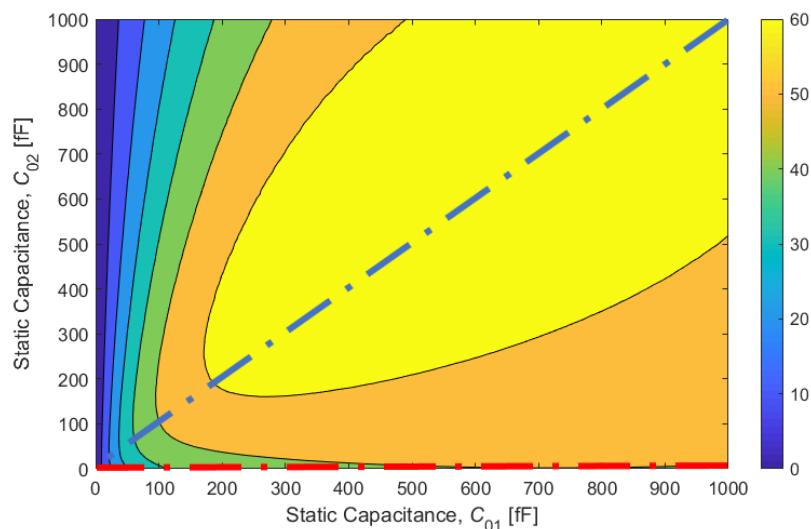


Figure 5.21: Contour plot of the simulated gain as a function of the static capacitance of R1 (C_{01}) and R2 (C_{02}).

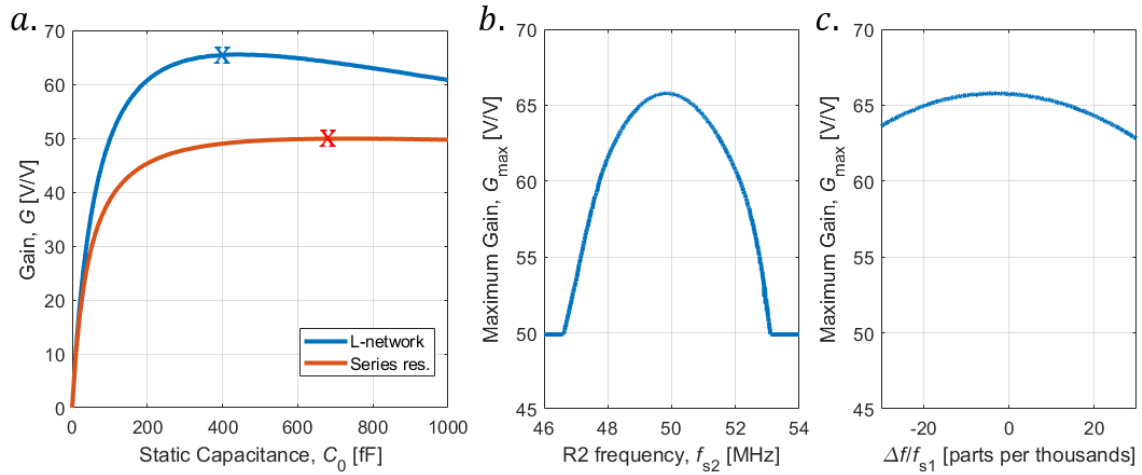


Figure 5.22: (a) Voltage gain as a function of the static capacitance for $C_{01} = C_{02}$ (blue line), representing a L-network implementing two identical resonators, and for $C_{02} = 0$ (red line), which represents a series approach; and (b) maximum gain as a frequency mismatch between R1 and R2; and (c) zoom-in of the central region of Fig. 5.22b.

5.3.3. System Demonstration

To validate the theoretical predictions described in Section 5.3.2, two identical resonators made out of 2 μm of X-cut Lithium Niobate on Silicon and operating around 50 MHz are characterized in air with the same approach described in Section 4.1.3. The two resonators exhibit quite similar performance with $<10\%$ variations in Q_s , $<3\%$ variations in k_t^2 , identical C_0 , and only 140 ppm of frequency difference (Fig. 5.23). It is important to note that the static capacitance of these devices does not match the optimal C_0 identified by numerical optimization. Nonetheless, as reported in Fig. 5.22a, this is still an operating point in which the L-network shows its benefits.

The gain is subsequently calculated with the same approach reported in Section 5.1. Starting from the measured Y-parameters matrix, an ideal voltage source (with 50 Ω impedance) and a capacitor with $C_{\text{load}} = 1$ pF are added to the input and output port respectively, and the gain across the capacitor extracted. As reported in Fig. 5.24, the L-network configuration shows a gain of 46

V/V, resulting in a net improvement of 30% compared to the best single resonator ($G = 35$ V/V).

These results outperform the gain achieved by any other similar technology for $C_{\text{load}} = 1$ pF.

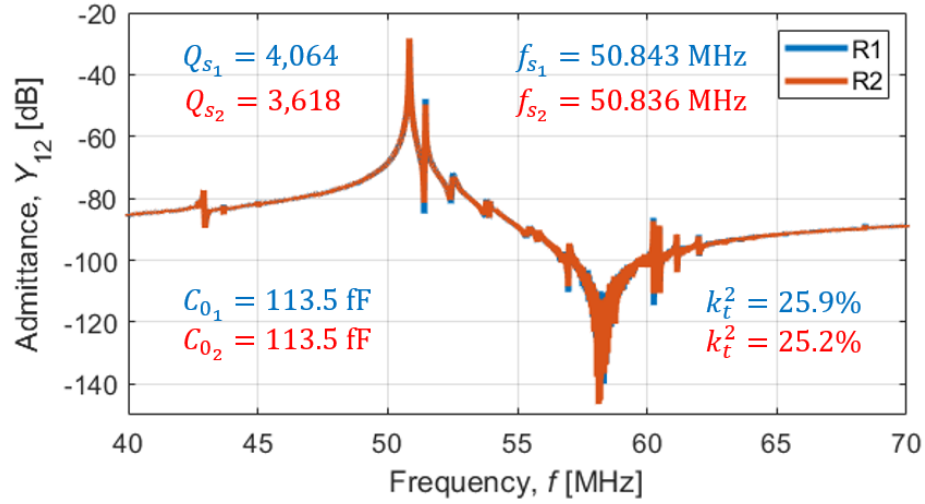


Figure 5.23: Admittance responses of the resonators implemented in the L-network simulations.

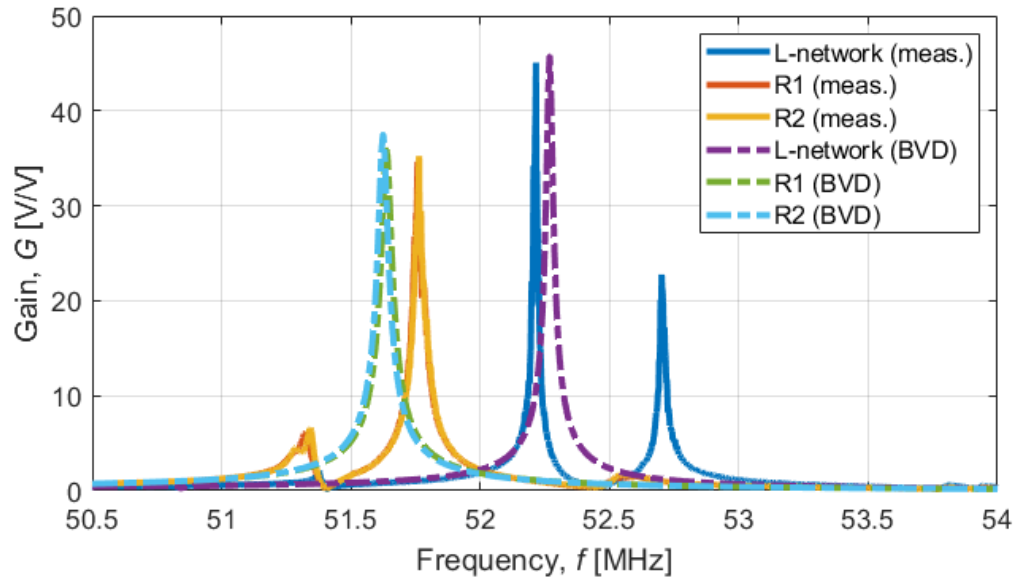


Figure 5.24: Simulated gains based on Y_{12} data (solid line) and BVD fitting (dashed line) for the L-network configuration and the series configuration implementing the devices reported in Fig. 5.23. Discrepancies in the pulled frequencies between the series and the L-network approach are due to uncertainty in the BVD fitted parameters.

CHAPTER 6: CONCLUSIONS AND FUTURE WORK

This dissertation presented the modeling, fabrication and characterization of high-performance X-cut Lithium Niobate Laterally Vibrating Resonators (LVRs) operating between 50 MHz and 550 MHz, to be implemented in the RFFE matching network of ultra-low power WuRx. Record-breaking Figure of Merits greater than 2,500 ($Q_s > 8,000$ and $k_t^2 > 28\%$) were demonstrated in vacuum on resonators operating around 100 MHz, the highest ever recorded for devices operating at Very High Frequency (VHF). The main sources of damping were characterized to identify an optimal device geometry as a function of design constraints and frequency of operation. Resonators aspect ratio (L/W) was proven to be fundamental in minimizing the anchor losses by reducing energy leakage through the substrate. Q_s greater than 26,000 were demonstrated at cryogenic temperature (10 K) on optimized devices. A tradeoff between anchor losses and electrical loading was demonstrated for resonators with a slender (high L/W ratio) geometry at different frequencies. The existence of this tradeoff severely limits the performance of these devices above 500 MHz due to the larger impact of any series resistance (R_s) on the motional resistance (R_m), which is frequency dependent.

The need for capacitance matching in the matching network for IoT application fostered the investigation of arrays of optimized resonators with larger C_0 , which showcased lower performance than the individual devices. Frequency mismatch between elements was identified as the main source of Q_s , and its impact investigated with a Monte Carlo statistical approach as a function of the resonator size.

Different MEMS-based matching network topologies were investigated to exploit the passive voltage amplification generated at resonance by fabricated devices when implemented in an RFFE matching network. To overcome the limitations of the limited static capacitances (50 – 100 fF) attained by high performance X-cut LVRs, a novel series-parallel matching network configuration (L-network) was investigated. This configuration showcased a 30% passive voltage amplification improvement (46 V/V) compared to a simple series topology (35 V/V) at 50 MHz, for a capacitive load of 1 pF.

Ultimately, the impact of spurious modes on the gain provided by X-cut LVRs when implemented in a matching network was investigated. Guidelines on the spurious modes quality factor, electromechanical coupling and resonant frequency were defined to minimize their impact on the passive voltage amplification.

6.1. Future Research Direction

The limited static capacitance showcased by demonstrated X-cut LN LVRs and the presence of severe in-band spurious modes and multiple higher order harmonics exhibiting high Q_s pose serious challenges for their implementation in commercial application.

As highlighted in Chapter 3 and 4, the excitation mode exploited by these high performance devices limits the maximum attainable capacitance per unit area. Arrays performance can be improved according to the models described in Section 4.3.5, with a more rigorous control of the fabrication process.

The incredibly high Q_s and k_t^2 showcased in the present work are nonetheless promising for the investigation of resonators fabricated with different cuts and orientations on different substrates,

thanks to the improvement of thin film machining processes. The high intrinsic Q_s and k_t^2 demonstrated could also be exploited by applications in which capacitance matching is not a requirement. If temperature stability is required, the large recorded TCF must be addressed by proper compensation.

A better understanding of spurious modes and how to suppress them is desirable for applications requiring a clean, broad bandwidth. The present work offers some hints on possible approach to minimize their impact.

In conclusion, a deeper investigation on losses mechanism as a function of frequency could provide better insights on the full potential of the technology discussed in this dissertation.

APPENDIX A: FABRICATION PROCESSES

A.1. Aluminum Nitride (AlN)

Step no.	Description	Material	Tool	Date
1	Sputtering	Pt	6J	-
Process				
	Thickness [nm]	Power [W]	Time [s]	Ar flow rate [sccm] and pressure [mTorr]
Cr pre-sputtering	-	200	300	25 - 5
Cr sputtering	10	100	35	25 - 5
Pt pre-sputtering	-	50	30	65 - 21
Pt sputtering	100	50	230	65 - 21
Notes				

Step no.	Description	Material	Tool	Date
2	Reactive sputtering	AlN	Tegal	-
Phase				
	Etching	Sputtering	Conditioning	
Time [s]	180	1038	200	
Power [W]	100 (RF)	7000 (AC) – 300 (DC)	5000 (AC)	
Current [A]	-	25 (AC) – 8.35 (DC)	13.1 (AC)	
Voltage [V]	-	336 (AC) – 30 (DC)	425 (AC)	
Tap	1	2	-	
Ar flow [sccm]	15	24.5	100	
N₂ flow [sccm]	-	32	-	
Pressure [mTorr]	1.96	3.32	6.77	
Notes				
1 μm AlN thick film				

Step no.	Description	Tool	Date
3	Etching (chlorine RIE)	Versaline	-
Recipe			
	ICP [W]	Bias [W]	Pressure [mTorr]
AlN etch	450	125	5
Time			
	Time	Post-etch	Post time
AlN etch	5 min	Argon flow	3 min
Notes			

Step no.	Description	Material	Tool	Date
4	Sputtering	AlSiCu	CVC	-
Recipe				
	Time	Thickness		
AlSiCu	300 s	100 nm		
Notes				
Sputter etch step (100 s) before deposition				

A.2. Scandium-doped Aluminum Nitride ($\text{Sc}_{0.2}\text{Al}_{0.2}\text{N}$)

Step no.	Description	Material	Tool	Date
1	Sputtering	Pt	6J	-
Process				
	Thickness [nm]	Power [W]	Time [s]	Ar flow rate [sccm] and pressure [mTorr]
Cr pre-sputtering	-	200	300	25 - 5
Cr sputtering	10	100	35	25 - 5
Pt pre-sputtering	-	50	30	65 - 21
Pt sputtering	100	50	230	65 - 21
Notes				

Step no.	Description	Tool	Date
2	Etching (chlorine RIE)	Versaline	-
Recipe			
	ICP [W]	Bias [W]	Pressure [mTorr]
AlN etch	600	350	5
Time			
	Cl₂ [sccm]	BCl₃ [sccm]	Ar [sccm]
	25	15	70
	O₂ [sccm]	Post-etch	Post time
	0	Argon flow	3 min
Notes			
1 st generation fab			

Step no.	Description	Tool	Date
2	Ion milling LN etch	Millatron	-
Current [μA]			
	Voltage [V]	Angle	Time
80	500	22.5	2 h
Monitoring			
End point			
Notes			
2 nd generation fab			

Step no.	Description	Material	Tool	Date
3	Sputtering	AlSiCu	CVC	-
Recipe				
	AKAlSiCu	Time	Thickness	
		300 s	100 nm	
Notes				
Sputter etch step (100 s) before deposition				

A.3. Y-cut Lithium Niobate (LN)

Step no.	Description	Material	Tool	Date
1	Sputtering	Pt	6J	-
Process				
	Thickness [nm]	Power [W]	Time [s]	Ar flow rate [sccm] and pressure [mTorr]
Cr pre-sputtering	-	200	300	25 - 5
Cr sputtering	10	100	35	25 - 5
Pt pre-sputtering	-	50	30	65 - 21
Pt sputtering	100	50	230	65 - 21

Step no.	Description	Tool	Date
2	Ion milling LN etch	Millatron	-
Current [μA]			
80	Voltage [V]	Angle	Time
	500	22.5	2 h
Monitoring			
End point			
Notes	1 μm LN thick film		

Step no.	Description	Material	Tool	Date
3	Reactive sputtering	AlN	Tegal	-
Phase				
	Etching	Sputtering	Conditioning	
Time [s]	180	1038	200	
Power [W]	100 (RF)	7000 (AC) – 300 (DC)	5000 (AC)	
Current [A]	-	25 (AC) – 8.35 (DC)	13.1 (AC)	
Voltage [V]	-	336 (AC) – 30 (DC)	425 (AC)	
Tap	1	2	-	
Ar flow [sccm]	15	24.5	100	
N₂ flow [sccm]	-	32	-	
Pressure [mTorr]	1.96	3.32	6.77	
Notes	1 μm AlN thick film			

Step no.	Description	Tool	Date
4	Etching (chlorine RIE)	Versaline	-
Recipe			
	ICP [W]	Bias [W]	Pressure [mTorr]
AlN etch	450	125	5
	Time		
	5 min		
Cl₂ [sccm]			
25	BCl₃ [sccm]	Ar [sccm]	O₂ [sccm]
	5	70	0
Post-etch			
Argon flow			
Post time			
3 min			
Notes			

Step no.	Description	Material	Tool	Date
3	Sputtering	AlSiCu	CVC	-
Recipe				
	Time	Thickness		
AKAlSiCu	300 s	100 nm		
Notes	Sputter etch step (100 s) before deposition			

A.4. X-cut Lithium Niobate (LN)

Step no.	Description	Material	Tool	Date
1	Sputtering	AlSiCu	CVC	-
Recipe				
AKAlSiCu		Time	Thickness	
		820 s	300 nm	
Notes	Sputter etch step (100 s) before deposition			

Step no.	Description	Tool	Date		
2	Etching AlSiCu (chlorine RIE)	Versaline	-		
Recipe					
Al slow LC w Ar		ICP [W]	Bias [W]	Pressure [mTorr]	Time
		425	25	5	35 s
Cl₂ [sccm]					
20		BCl₃ [sccm]		Post-etch	Post time
		10		Argon flow	3 min
		Ar [sccm]		O₂ [sccm]	
		10		0	
Notes	Wafer dipped into hot water (80° C) right after vent to prevent Al corrosion				

Step no.	Description	Tool	Date			
3	Ion milling LN etch	Millatron	-			
Current [μA]						
80		Voltage [V]		Angle	Time	Monitoring
		500		22.5	4 h	End point
Notes	2 μm LN thick film					

APPENDIX B: FREQUENCY PULLING

In this subchapter, the analytical derivation for the pulled anti-resonances (ω_p' and ω_{ps}') is reported in detail (Eq. B.1 – B.20). The pulled operating frequencies (ω_{RF}' and ω_{RF}'') of the main and spurious mode follow a similar approach. The reference circuits are reported in Fig. B1.

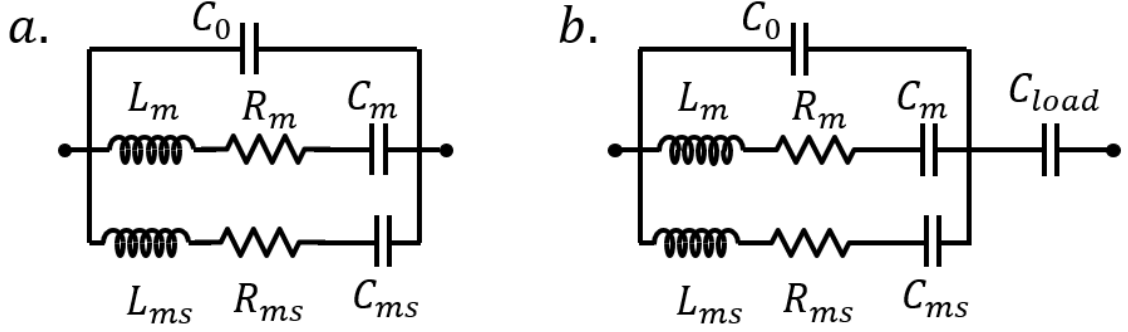


Figure B.1: (a) Multi-BVD model of a 1-port LVR. R_m , L_m , and C_m represent the motional parameters of the spurious modes; and (b) multi-BVD model interfaced in series with a capacitive load.

$$Y = j\omega C_0 + \frac{1}{R_m + j\omega L_m + \frac{1}{j\omega C_m}} + \frac{1}{R_{ms} + j\omega L_{ms} + \frac{1}{j\omega C_{ms}}} \quad (\text{B.1})$$

$$Y = \frac{j\omega C_0 \left(1 - \frac{\omega^2}{\omega_s^2}\right) \left(1 - \frac{\omega^2}{\omega_{ss}^2}\right) + j\omega C_m \left(1 - \frac{\omega^2}{\omega_{ss}^2}\right) + j\omega C_{ms} \left(1 - \frac{\omega^2}{\omega_{ss}^2}\right)}{\left(1 - \frac{\omega^2}{\omega_s^2}\right) \left(1 - \frac{\omega^2}{\omega_{ss}^2}\right)} \quad (\text{B.2})$$

$$\omega_s = \sqrt{\frac{1}{L_m C_m}} \quad (\text{B.3})$$

$$\omega_{ss} = \sqrt{\frac{1}{L_{ms} C_{ms}}} \quad (\text{B.4})$$

$$j\omega C_0 \left(1 - \frac{\omega^2}{\omega_s^2}\right) \left(1 - \frac{\omega^2}{\omega_{ss}^2}\right) + j\omega C_m \left(1 - \frac{\omega^2}{\omega_{ss}^2}\right) + j\omega C_{ms} \left(1 - \frac{\omega^2}{\omega_{ss}^2}\right) = 0 \quad (\text{B.5})$$

$$\begin{aligned} -\omega^2 \left[\frac{1}{\omega_s^2} \left(1 + \frac{C_{ms}}{C_0}\right) + \frac{1}{\omega_{ss}^2} \left(1 + \frac{C_m}{C_0}\right) \right] \\ = -\frac{\omega^2}{\omega_s^2 \omega_{ss}^2} \left[\omega_s^2 \left(\frac{C_0 + C_m}{C_0}\right) + \omega_{ss}^2 \left(\frac{C_0 + C_{ms}}{C_0}\right) \right] \end{aligned} \quad (\text{B.6})$$

$$\omega_s^2 \left(\frac{C_0 + C_m}{C_0}\right) = \omega_p^2 \quad (\text{B.7})$$

$$\omega_{ss}^2 \left(\frac{C_0 + C_m}{C_0} \right) = \omega_{ps}^2 \quad (\text{B.8})$$

$$\omega^4 - \omega^2(\omega_p^2 + \omega_{ps}^2) + \omega_{ss}^2 \omega_p^2 + \omega_s^2 \omega_{ps}^2 - \omega_s^2 \omega_{ss}^2 = 0 \quad (\text{B.9})$$

$$A\omega^4 - B\omega^2 + C = 0 \quad (\text{B.10})$$

$$x = \omega^2 \quad (\text{B.11})$$

$$Ax^2 + Bx + C = 0 \quad (\text{B.12})$$

$$A = 1 \quad (\text{B.13})$$

$$B = -(\omega_p^2 + \omega_{ps}^2) \quad (\text{B.14})$$

$$C = \omega_{ss}^2 \omega_p^2 + \omega_s^2 \omega_{ps}^2 - \omega_s^2 \omega_{ss}^2 \quad (\text{B.15})$$

$$x_{1,2} = -\frac{B}{2} \pm \sqrt{B^2 - 4AC} \quad (\text{B.16})$$

$$\omega'_p = \sqrt{\omega_{pc}^2 + \frac{1}{2} \sqrt{(\omega_p^2 + \omega_{ps}^2) - 4(\omega_{ss}^2 \omega_p^2 + \omega_s^2 \omega_{ps}^2 - \omega_s^2 \omega_{ss}^2)}} \quad (\text{B.17})$$

$$\omega'_{ps} = \sqrt{\omega_{pc}^2 - \frac{1}{2} \sqrt{(\omega_p^2 + \omega_{ps}^2) - 4(\omega_{ss}^2 \omega_p^2 + \omega_s^2 \omega_{ps}^2 - \omega_s^2 \omega_{ss}^2)}} \quad (\text{B.18})$$

$$\omega_{pc} = \sqrt{\frac{\omega_p^2 + \omega_{ps}^2}{2}} \quad (\text{B.19})$$

$$\delta_p^2 = \frac{1}{2} \sqrt{(\omega_p^2 + \omega_{ps}^2) - 4(\omega_{ss}^2 \omega_p^2 + \omega_s^2 \omega_{ps}^2 - \omega_s^2 \omega_{ss}^2)} \quad (\text{B.20})$$

APPENDIX C: STRESS GRADIENT EXTRACTION

As first step, the deflected beam profile must be extracted over the entire length with a measurement instrument, such as an optical 3D scanner. The second step is removing the part of the measured profile not belonging to the beam (Fig. C.1) via software. In this case, the data were imported from a .csv file.

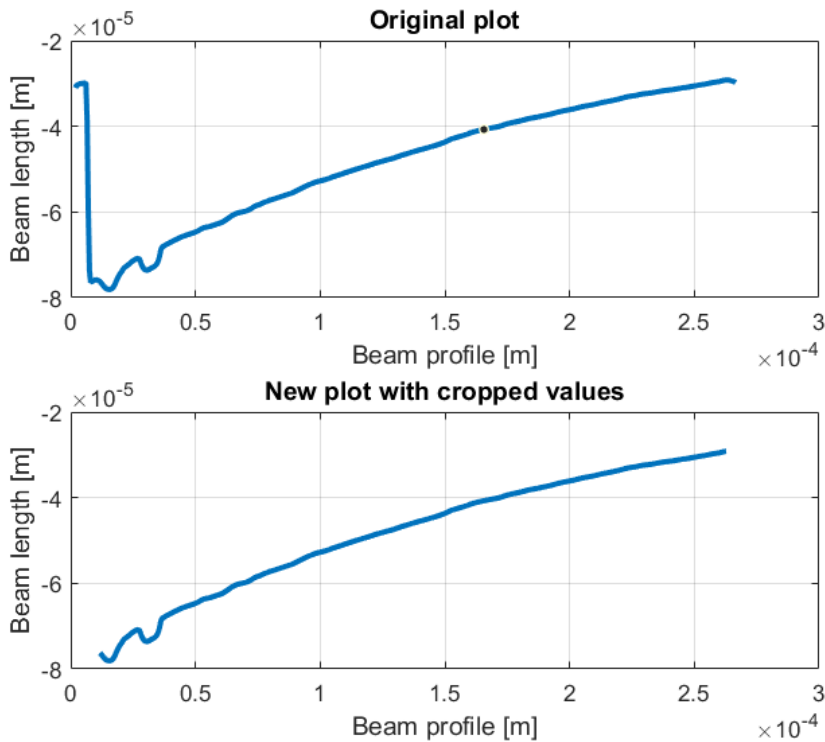


Figure C.1: Measured beam deflection and cropped beam.

The remaining curve must be fit to a 2nd order equation (MATLAB[®] function: *polyfit*) in the form reported by Eq. C.1. The deflection of a cantilever beam due to stress gradient can be calculated according to Eq. C.2, and the stress gradient easily calculated (Eq. C.3 – C.5), where σ_1 is the stress, H the beam thickness, E the Young's modulus, and ν the Poisson's ratio. Fig. C.2 reports the comparison between the measurement profile and the quadratic fitting used to extract the stress gradient (Eq. C.5). The MATLAB[®] code used for the stress gradient calculation is reported in Table C.1.

$$y = ax^2 + bx + c \quad (C.1)$$

$$y = \frac{\sigma_1}{H} \frac{1-\nu}{E} \left(\frac{x^2}{2} \right) \quad (\text{C.2})$$

$$a = \frac{\sigma_1(1-\nu)}{HE} \quad (\text{C.3})$$

$$\sigma_1 = \frac{aHE}{(1-\nu)} \quad (\text{C.4})$$

$$\frac{d\sigma_1}{dy} = \frac{2\sigma_1}{H} \quad (\text{C.5})$$

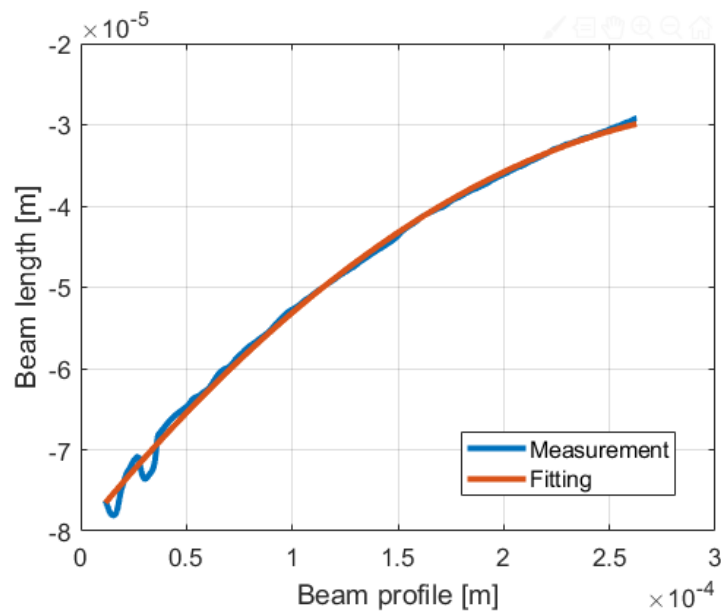


Figure C.2: Measured beam deflection and quadratic fitting.

Table C.1: MATLAB® code for stress gradient extraction.

```

%Load file
[filename1, pathname] = uigetfile('.csv', 'Select the CSV file');
filename = strcat(pathname, filename1);
data = xlsread(filename);

x = data(:,1);           %x dimension, in meters
y = data(:,2);           %y dimension, in meters

dx = x(2) - x(1);
dy = y(2) - y(1);

figure(2)
subplot(2,1,1)
plot(x, y, 'LineWidth', 3);
title('Original plot');
xlabel('Beam profile [m]');
ylabel('Beam length [m]');

```

```

set(gcf, 'color', 'white')
grid on
set(gca, 'FontSize', 13)

uiwait(msgbox('Select start x-value for cropping', 'modal'));
[x_user, ~] = ginput(1); % Let the user select an x-value from
which to crop.
x_tmp = x(x > x_user);
xStart = find(x == x_tmp(1));

uiwait(msgbox('Select end x-value for cropping', 'modal'));
[x_user, ~] = ginput(1); % Let the user select an x-value from
which to crop.
x_tmp = x(x < x_user);
xEnd = find(x == x_tmp(end));

xBeam = x(xStart:xEnd);
yBeam = y(xStart:xEnd);

subplot(2, 1, 2);
plot(xBeam, yBeam, 'LineWidth', 3)
title('New plot with cropped values');
xlabel('Beam profile [m]')
ylabel('Beam length [m]')
grid on
set(gca, 'FontSize', 13)

%Fitting the beam profile

fitCoeff = polyfit(xBeam, yBeam, 2);

yCalc = @(x) fitCoeff(1)*x.^2 + fitCoeff(2)*x + fitCoeff(3);

figure(3)
plot(xBeam, yBeam, 'LineWidth', 3)
hold on
plot(xBeam, yCalc(xBeam), 'LineWidth', 3)
xlabel('Beam profile [m]')
ylabel('Beam length [m]')
set(gcf, 'color', 'white')
grid on
set(gca, 'FontSize', 13)
legend('Measurement', 'Fitting')

%Stress gradient extraction

E = 173e9; %Young's modulus
nu = 0.25; %Poisson's ratio
t = 2.5e-6; %Film thickness

sigma1 = fitCoeff(1)*t*E/(1-nu);

dsigma1 = 2*sigma1/(t*1e6)*1e-6; % [MPa/um]

```

APPENDIX D: MATRIX ROTATIONS

A generic 2-D rotation of a vector V is reported in Fig. D.1. Assuming $|V| = 1$ and applying a rotation θ it is possible to calculate the rotation matrix (a) by following the steps reported by Eq. D.6 – D.7.

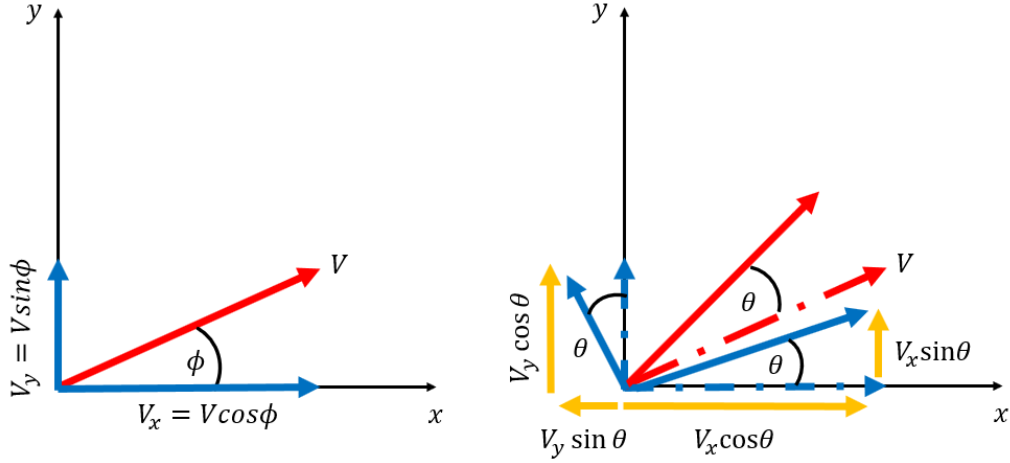


Figure D.1: Generic rotation of a vector V .

$$V_x = \cos \phi = \bar{x} \quad (\text{D.1})$$

$$V_y = \sin \phi = \bar{y} \quad (\text{D.2})$$

$$V = \begin{bmatrix} V_x \\ V_y \end{bmatrix} = \begin{bmatrix} \bar{x} \\ \bar{y} \end{bmatrix} \quad (\text{D.3})$$

$$\bar{x}' = \bar{x} \cos \theta - \bar{y} \sin \theta \quad (\text{D.4})$$

$$\bar{y}' = \bar{x} \sin \theta + \bar{y} \cos \theta \quad (\text{D.5})$$

$$V' = \begin{bmatrix} \bar{x}' \\ \bar{y}' \end{bmatrix} = \begin{bmatrix} \cos \theta & -\sin \theta \\ \sin \theta & \cos \theta \end{bmatrix} \begin{bmatrix} \bar{x} \\ \bar{y} \end{bmatrix} = a_x V \quad (\text{D.6})$$

$$a = \begin{bmatrix} \cos \theta & -\sin \theta \\ \sin \theta & \cos \theta \end{bmatrix} \quad (\text{D.7})$$

2-D rotation can be easily expanded to a 3-D space by following the convention reported in Fig. D.2. The rotation matrices (a_x , a_y , and a_z) around the three axes (x , y , and z) are captured by

Eq. D.8 – D.10. Rotations of vectors around x (YZ plane) and z (XY plane) are positive if counterclockwise, rotations around y (XZ plane) are positive if clockwise.

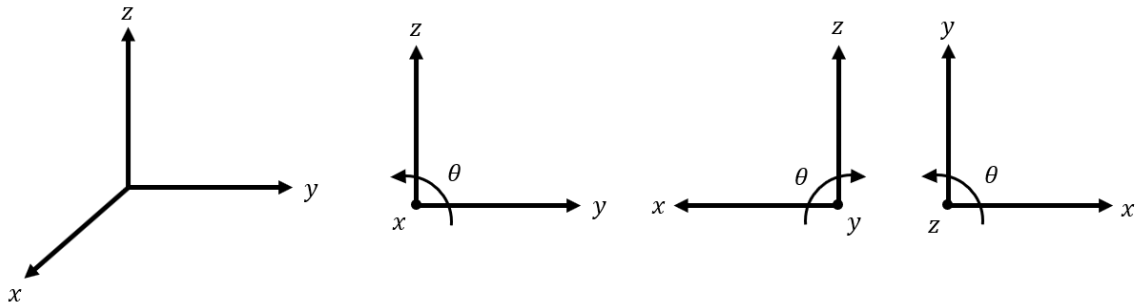


Figure D.2: Convention for rotation around x, y and z axes.

$$a_x = \begin{bmatrix} 1 & 0 & 0 \\ 0 & \cos\theta & -\sin\theta \\ 0 & \sin\theta & \cos\theta \end{bmatrix} \quad (\text{D.8})$$

$$a_y = \begin{bmatrix} \cos\theta & 0 & \sin\theta \\ 0 & 1 & 0 \\ -\sin\theta & 0 & \cos\theta \end{bmatrix} \quad (\text{D.9})$$

$$a_z = \begin{bmatrix} \cos\theta & -\sin\theta & 0 \\ \sin\theta & \cos\theta & 0 \\ 0 & 0 & 1 \end{bmatrix} \quad (\text{D.10})$$

Two different references system can be adopted: vector or frame (Fig. D.3). If the rotation is applied to the frame, the rotation matrices can be expressed according to Eq. D.11 – D.13, since $\cos(-\theta) = \cos(\theta)$ and $\sin(-\theta) = -\sin(\theta)$.

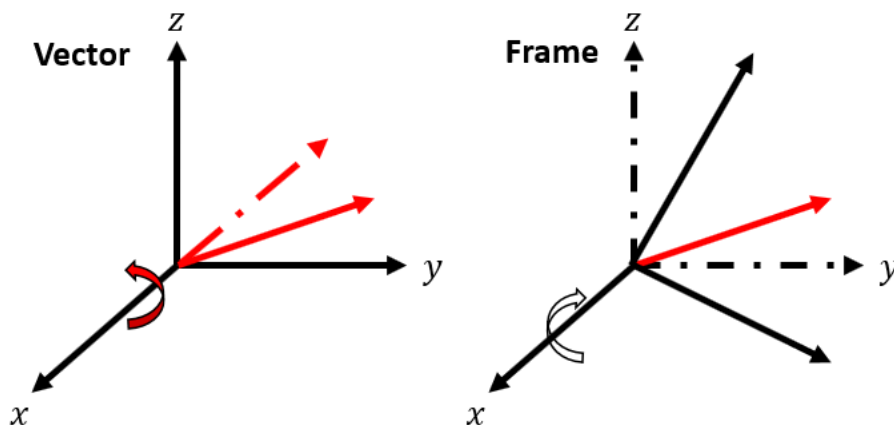


Figure D.3: Convention for rotation around vector (red) or frame (white).

$$a_x = \begin{bmatrix} 1 & 0 & 0 \\ 0 & \cos\theta & \sin\theta \\ 0 & -\sin\theta & \cos\theta \end{bmatrix} \quad (D.11)$$

$$a_y = \begin{bmatrix} \cos\theta & 0 & -\sin\theta \\ 0 & 1 & 0 \\ \sin\theta & 0 & \cos\theta \end{bmatrix} \quad (D.12)$$

$$a_z = \begin{bmatrix} \cos\theta & \sin\theta & 0 \\ -\sin\theta & \cos\theta & 0 \\ 0 & 0 & 1 \end{bmatrix} \quad (D.13)$$

For non square-matrices, such as the piezoelectric coupling matrices (d , e , g , or h depending on the equation form), the Bond method can be used to perform rotation and investigate the piezoelectric property of different crystal along specific orientations. The constitutive equations for piezoelectric material include matrices with three different dimensions (Eq. D.14 – Eq. D.15). To rotate matrices such as c and e it is necessary to introduce a matrix M , defined according to [89] and expressed as in Eq. D.17.

$$c = [\text{Stiffness}]_{6 \times 6} \quad (D.14)$$

$$e = [\text{Piezoelectric coupling coeff.}]_{3 \times 6} \quad (D.15)$$

$$\varepsilon = [\text{Dielectric constants}]_{3 \times 3} \quad (D.16)$$

$$M = \begin{bmatrix} a_{xx}^2 & a_{xy}^2 & a_{xz}^2 & & & & 2a_{xy}a_{xz} & 2a_{xz}a_{xx} & 2a_{xx}a_{xy} \\ a_{yx}^2 & a_{yy}^2 & a_{yz}^2 & & & & 2a_{yy}a_{yz} & 2a_{yz}a_{yx} & 2a_{yx}a_{yy} \\ a_{zx}^2 & a_{zy}^2 & a_{zz}^2 & & & & 2a_{zy}a_{zz} & 2a_{zz}a_{zx} & 2a_{zx}a_{zy} \\ a_{yx}a_{zx} & a_{yy}a_{zy} & a_{yz}a_{zz} & a_{yy}a_{zz} + a_{yz}a_{zy} & a_{xy}a_{zz} + a_{yz}a_{zx} & a_{yy}a_{zx} + a_{yx}a_{zy} & & & \\ a_{zx}a_{xx} & a_{zy}a_{xy} & a_{zz}a_{xz} & a_{xy}a_{zz} + a_{xz}a_{zy} & a_{xz}a_{zx} + a_{xx}a_{zz} & a_{xx}a_{zy} + a_{xy}a_{zx} & & & \\ a_{xx}a_{yx} & a_{xy}a_{yy} & a_{xz}a_{yz} & a_{xy}a_{yz} + a_{xz}a_{yy} & a_{xz}a_{yx} + a_{xx}a_{yz} & a_{xx}a_{yy} + a_{xy}a_{yx} & & & \end{bmatrix} \quad (D.17)$$

Matrices can be rotated according to Eq. D.18 – D.20. In case of concatenated rotations, a and M assume the form captured by Eq. D.21 – D.22.

$$c' = McM^T \quad (D.18)$$

$$e' = aeM^T \quad (D.19)$$

$$\varepsilon' = a\varepsilon a^T \quad (D.20)$$

$$a = \prod_{k=n}^0 a_k = a_n a_{n-1} \dots a_2 a_1 \quad (\text{D.21})$$

$$M = \prod_{k=n}^0 M_k = M_n M_{n-1} \dots M_2 M_1 \quad (\text{D.22})$$

An example is the calculation of the k_t^2 of Y-cut starting from Z-cut Lithium Niobate. As first step, it is necessary to rotate -90° around the x axis (frame convention) using matrices a_x and M_x to obtain Y-cut (Fig. D.4). As second optional step consist in rotating the wafer by -90° around y , using a_z and M_z to re-align the coordinate system (Fig. D.5). Ultimately, it is possible to sweep around y using a_z and M_z to calculate the parameters of interest (*i.e.*, k_t^2), as reported in Section X.

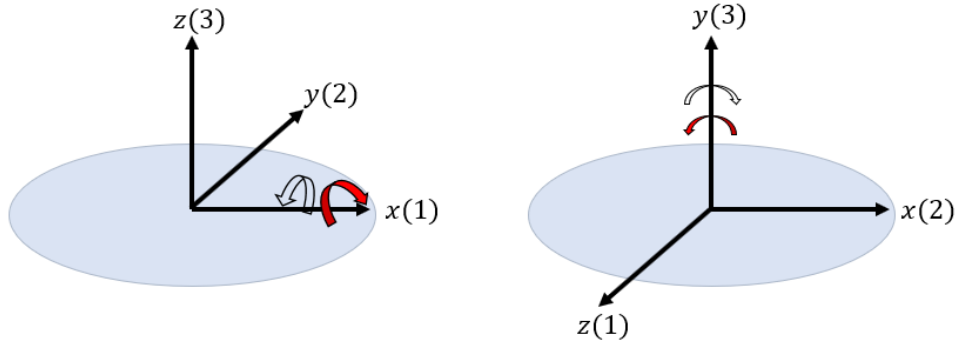


Figure D.4: Rotation to calculate Y-cut properties from Z-cut matrices.

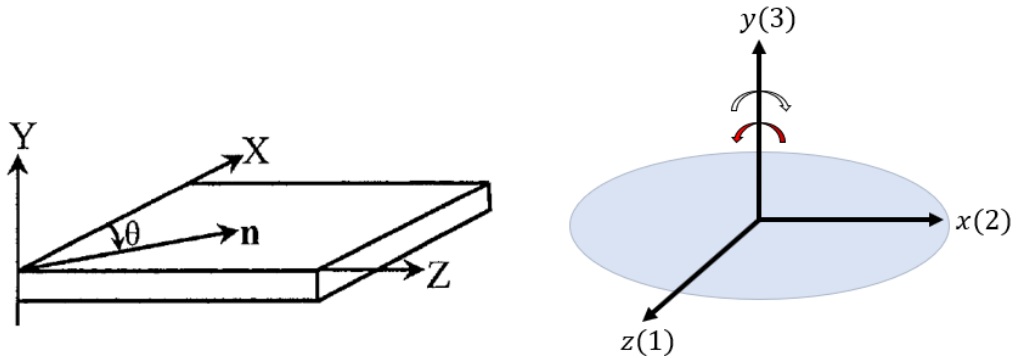


Figure D.5: Reference system reported in [62] for Y-cut LN compared to the one of the present dissertation.

Another example is the calculation of the k_t^2 of X-cut starting from Z-cut Lithium Niobate. In this case it is necessary to rotate by -90° (wafer convention) around y using matrices a_y and M_y to obtain X-cut. Then, a rotation of 90° must be performed around x using a_z and M_z to re-align the coordinate system. Ultimately, it is possible to investigate the parameter of interest by performing

a sweep around x (matrices a_z and M_z), as reported in Sections 3.2.3 and 3.2.4. Tables D.1 and D.2 reports the MATLAB® code used for the investigation of Y-cut and X-cut material properties.

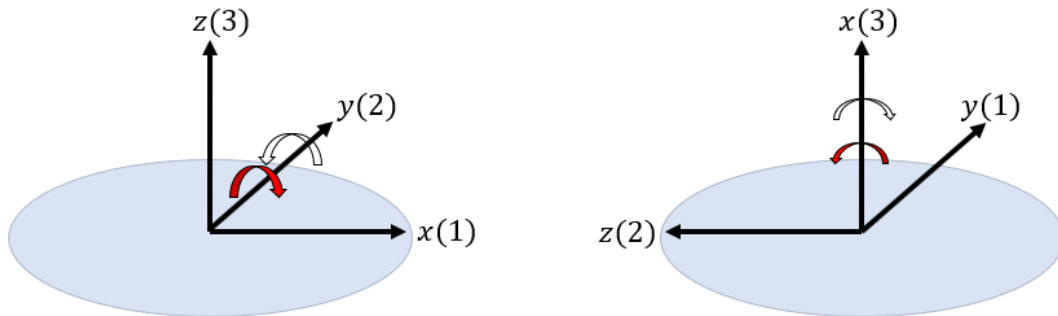


Figure D.6: Rotation to calculate X-cut properties from Z-cut matrices.

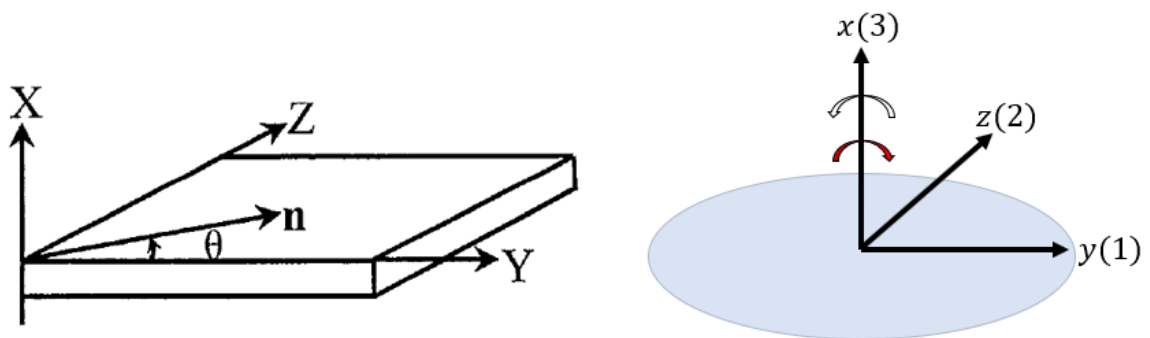


Figure D.7: Reference system reported in [62] for X-cut LN compared to the one of the present dissertation.

Table D.1: MATLAB® code for matrix rotation (Y-cut LN).

```
load("LiNbO3_Z.mat")
density = 4700;

thetaX = -90;

a1 = rotx(thetaX);
M1 = genM(a1);

thetaZ1 = 0;

a2 = rotz(thetaZ1);
M2 = genM(a2);

thetaZ2 = 1:1:180;

for i = 1:length(thetaZ2)

    a3 = rotz(thetaZ2(i));
    M3 = genM(a3);

    a = a3*a2*a1;
    M = M3*M2*M1;
```

```

eps0 = LiNbO3_Z.eps0;
c = LiNbO3_Z.c;
e = LiNbO3_Z.e;
eps = LiNbO3_Z.eps;

c = M*c*M';
e = a*e*M';
eps = a*eps*a';
%d = -(c\e)';

kt2_11(i) = (e(1,1)^2/(c(1,1)*eps(1,1)*eps0));
kt2_31(i) = (e(3,1)^2/(c(1,1)*eps(3,3)*eps0));
phv_11(i) = sqrt(c(1,1)/density);
epsR_11(i) = eps(1,1);
epsR_33(i) = eps(3,3);
kt2_16(i) = (e(1,6)^2)/(c(6,6)*eps(1,1)*eps0);

```

end

function M = genM(a)

```

axx = a(1,1);
axy = a(1,2);
axz = a(1,3);
ayx = a(2,1);
ayy = a(2,2);
ayz = a(2,3);
azx = a(3,1);
azy = a(3,2);
azz = a(3,3);

M1 = [axx^2 axy^2 axz^2
      ayx^2 ayy^2 ayz^2
      azx^2 azy^2 azz^2];

M2 = 2*[axy*axz axx*axz axx*axy;
      ayy*ayz ayx*ayz ayy*ayx;
      azy*azz azx*azz azz*azy];

M3 = [ayz*azx ayy*azy ayz*azz
      axx*azx axy*azy axz*azz
      axx*ayx axy*ayy axz*ayz];

M4 = [ayy*azz+ayz*azy ayx*azz+ayz*azx ayx*azy+ayy*azx;
      axy*azz+axz*azy axx*azz+axz*azx axx*azy+axy*azx;
      axy*ayz+axz*ayy axx*ayz+axz*ayx axx*ayy+axy*ayx];

M = [M1, M2;
      M3, M4];

```

end

Table D.2: MATLAB® code for matrix rotation (X-cut LN).

```
load("LiNbO3_Z.mat")
density = 4700;

thetaY = -90;

a1 = roty(thetaY);
M1 = genM(a1);

thetaZ1 = 90;

a2 = rotz(thetaZ1);
M2 = genM(a2);

thetaZ2 = 1:1:180;

for i = 1:length(thetaZ2)

    a3 = rotz(thetaZ2(i));
    M3 = genM(a3);

    a = a3*a2*a1;
    M = M3*M2*M1;

    eps0 = LiNbO3_Z.eps0;
    c = LiNbO3_Z.c;
    e = LiNbO3_Z.e;
    eps = LiNbO3_Z.eps;

    c = M*c*M';
    e = a*e*M';
    eps = a*eps*a';
    %d = -(c\e)';

    kt2_11(i) = (e(1,1)^2/(c(1,1)*eps(1,1)*eps0));
    phv_11(i) = sqrt(c(1,1)/density);
    epsR_11(i) = eps(1,1);
    kt2_16(i) = (e(1,6)^2)/(c(6,6)*eps(1,1)*eps0);

end
```

APPENDIX E: OVERETCH MODELING

A simple model to characterize the overetch due to the ion milling is reported in Fig. E.1. The typical angle between the Argon (Ar) ion beam and the rotating wafer surface in the ion milling available at the CMU Nanofab is 22.5° , while the measured etch rate perpendicular to the surface (a_{\perp}) is around 20 nm/min (cfr. Appendix A). Assuming a duty factor (δ_c) of 25%, given by the fact that the stage is rotating at a constant speed, it is possible to estimate the parallel etch rate according to Eq. E.1.

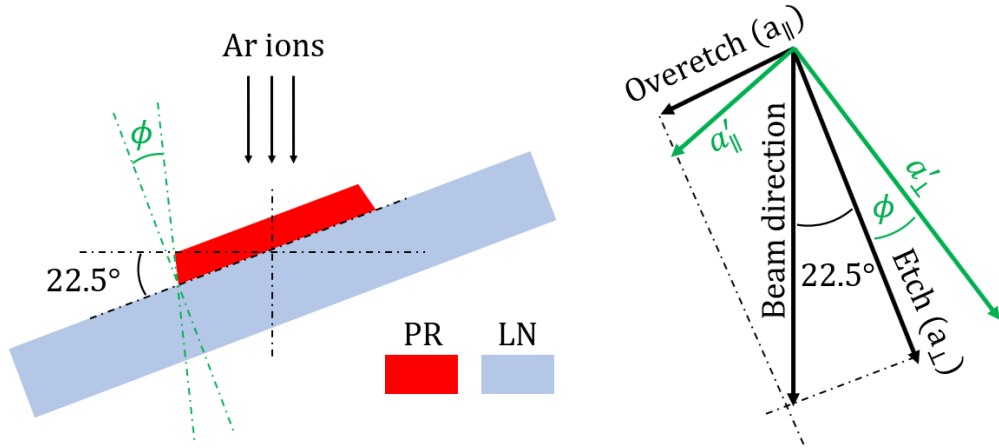


Figure E.1: Geometrical model for the overetch calculation.

$$a_{\parallel} = a_{\perp} \tan(22.5^\circ) \delta_c = 2 \frac{nm}{min} \quad (E.1)$$

This model does not consider the sidewall sloping of the photoresist (ϕ), which can be usually estimated between 10° and 20° according to the type of PR, exposure dose, development methods and baking procedure. In this case, the extra angle must be included in the calculation, as captured by Eq. E.2.

$$a'_{\parallel} = a_{\perp} \tan(22.5^\circ + \phi) \delta_c = 4 \frac{nm}{min} \quad (E.2)$$

Assuming an etching time of 2 hours, required to remove 2 μm of lithium niobate at 20 nm/min, plus few hundreds nm of Si to allow for an easier XeF_2 release, provides for a total overetch of roughly 0.5 μm . This value is in agreement with the value measured on previously fabricated 50 MHz and 400 MHz devices and must be added to each edge of the resonator plate.

BIBLIOGRAPHY AND REFERENCES

- [1] R. H. Olsson, R. B. Bogoslovov, and C. Gordon, “Event driven persistent sensing: Overcoming the energy and lifetime limitations in unattended wireless sensors”, *2016 IEEE Sensors*, 2016, pp. 1–3.
- [2] P. Bassirian, J. Moody, and S. M. Bowers, “Event-driven wakeup receivers: Applications and design challenges”, *2017 IEEE 60th International Midwest Symposium on Circuits and Systems (MWSCAS)*, 2017, pp. 1324–1327.
- [3] “NZERO DARPA BAA 15-14.” 2015.
- [4] David D. Wentzloff, “Low Power Radio Survey.” [Online]. Available: www.eecs.umich.edu/wics/low_power_radio_survey.html.
- [5] A. Kochhar *et al.*, “Resonant Microelectromechanical Receiver”, *J. Microelectromechanical Syst.*, pp. 1–17, 2019.
- [6] P. Bassirian *et al.*, “Nanowatt-Level Wakeup Receiver Front Ends Using MEMS Resonators for Impedance Transformation”, *IEEE Trans. Microw. Theory Tech.*, vol. 67, no. 4, pp. 1615–1627, Apr. 2019.
- [7] P.-H. P. Wang *et al.*, “A 6.1-nW Wake-Up Receiver Achieving –80.5-dBm Sensitivity Via a Passive Pseudo-Balun Envelope Detector”, *IEEE Solid-State Circuits Lett.*, vol. 1, no. 5, pp. 134–137, May 2018.
- [8] M. E. Galanko, A. Kochhar, G. Piazza, T. Mukherjee, and G. K. Fedder, “CMOS-MEMS resonant demodulator for near-zero-power RF wake-up receiver,” in *2017 19th International Conference on Solid-State Sensors, Actuators and Microsystems (TRANSDUCERS)*, 2017, pp. 86–89.
- [9] H. Jiang *et al.*, “24.5 A 4.5nW wake-up radio with –69dBm sensitivity”, in *2017 IEEE International Solid-State Circuits Conference (ISSCC)*, 2017, pp. 416–417.

- [10] J. Moody *et al.*, “A -76dBm 7.4nW wakeup radio with automatic offset compensation”, in *2018 IEEE International Solid - State Circuits Conference - (ISSCC)*, 2018, pp. 452–454.
- [11] C. Cassella *et al.*, “ 750 MHz ZERO-POWER MEMS-BASED WAKE-UP RECEIVER WITH -60 dBm SENSITIVITY”, *2018 Solid-State, Actuators, and Microsystems Workshop Technical Digest*, 2018, pp. 362–363.
- [12] A. Mahmoud *et al.*, “Acousto-optic gyroscope”, *2018 IEEE Micro Electro Mechanical Systems (MEMS)*, 2018, pp. 241–244.
- [13] L. Colombo, A. Kochhar, G. Vidal-Alvarez, and G. Piazza, “X-Cut Lithium Niobate Laterally Vibrating MEMS Resonator With Figure of Merit of 1560”, *J. Microelectromechanical Syst.*, vol. 27, no. 4, pp. 602–604, Aug. 2018.
- [14] L. Colombo, A. Kochhar, G. Vidal-Alvarez, Z. Schaffer, P. Simeoni, and G. Piazza, “Comparison between different MEMS Laterally Vibrating Resonator Technologies for Passive Voltage Amplification in an RF Front-End System”, *2018 IEEE MTT-S International Microwave Workshop Series on Advanced Materials and Processes for RF and THz Applications (IMWS-AMP)*, 2018, pp. 1–3.
- [15] R. Lu, T. Manzanque, Y. Yang, and S. Gong, “Exploiting parallelism in resonators for large voltage gain in low power wake up radio front ends”, *2018 IEEE Micro Electro Mechanical Systems (MEMS)*, 2018, pp. 747–750.
- [16] J. Moody *et al.*, “Interference Robust Detector-First Near-Zero Power Wake-Up Receiver”, *IEEE J. Solid-State Circuits*, vol. 54, no. 8, pp. 2149–2162, Aug. 2019.
- [17] V. Mangal and P. R. Kinget, “ 28.1 A 0.42nW 434MHz -79.1dBm Wake-Up Receiver with a Time-Domain Integrator”, *2019 IEEE International Solid- State Circuits Conference - (ISSCC)*, 2019, pp. 438–440.
- [18] L. Colombo *et al.*, “Ultra-low-power and high sensitivity resonant micromechanical receiver”, *2017 IEEE SENSORS*, 2017, pp. 1–3.

- [19] N. Khalid, J. Singh, H. P. Le, J. Devlin, and Z. Sauli, “A very high Q-factor inductor using MEMS technology”, *2009 Asia Pacific Conference on Postgraduate Research in Microelectronics & Electronics (PrimeAsia)*, 2009, pp. 77–80.
- [20] P.-H. P. Wang *et al.*, “A Near-Zero-Power Wake-Up Receiver Achieving -69 -dBm Sensitivity”, *IEEE J. Solid-State Circuits*, vol. 53, no. 6, pp. 1640–1652, Jun. 2018.
- [21] B. Epstein and R. H. Olsson, “IoT Networks: Frequency Control Considerations”, *2018 IEEE International Frequency Control Symposium (IFCS)*, 2018, pp. 1–5.
- [22] H. Bhugra and G. Piazza, Eds., *Piezoelectric MEMS Resonators*, Springer International Publishing, 2017.
- [23] R. Lu, M.-H. Li, Y. Yang, T. Manzaneque, and S. Gong, “Accurate Extraction of Large Electromechanical Coupling in Piezoelectric MEMS Resonators”, *J. Microelectromechanical Syst.*, vol. 28, no. 2, pp. 209–218, Apr. 2019.
- [24] D. A. Feld, R. Parker, R. Ruby, P. Bradley, and S. Dong, “After 60 years: A new formula for computing quality factor is warranted”, *2008 IEEE Ultrasonics Symposium*, 2008, pp. 431–436.
- [25] Y. Yu *et al.*, “Magnetic-free radio frequency circulator based on spatiotemporal commutation of MEMS resonators”, *2018 IEEE Micro Electro Mechanical Systems (MEMS)*, 2018, pp. 154–157.
- [26] “IEEE Standard on Piezoelectricity Standards Committee of the IEEE Ultrasonics, Ferroelectrics, and Frequency Control Society IEEE Standards Board American National Standards Institute”, 1987.
- [27] M. E. Galanko, Y. C. Lin, T. Mukherjee, and G. K. Fedder, “A SINGLE-CRYSTAL SILICON RESONATOR FOR AM DEMODULATION WITH ADDED SECOND-HARMONIC MODULATION”, *2018 Solid-State, Actuators, and Microsystems Workshop Technical Digest*, 2018, pp. 346–349.

- [28] C. T-C Nguyen, "Transceiver Front-End Architectures Using Vibrating Micromechanical Signal Processors"
- [29] Fang Chen, J. Brotz, U. Arslan, ChiuDg-Cheng Lo, T. Mukherjee, and G. K. Fedder, "CMOS-MEMS resonant RF mixer-filters", *18th IEEE International Conference on Micro Electro Mechanical Systems, 2005. MEMS 2005.*, pp. 24–27.
- [30] M. Koskenvuori and I. Tittonen, "GHz-range FSK-reception with microelectromechanical resonators", *Sensors Actuators A Phys.*, vol. 142, no. 1, pp. 346–351, Mar. 2008.
- [31] F. V. Pop, A. S. Kochhar, G. Vidal-Alvarez, and G. Piazza, "Investigation of Electromechanical Coupling and Quality Factor of X-Cut Lithium Niobate Laterally Vibrating Resonators Operating Around 400 MHz", *J. Microelectromechanical Syst.*, vol. 27, no. 3, pp. 407–413, Jun. 2018.
- [32] R. Ruby, "Positioning FBAR technology in the frequency and timing domain", in *2011 Joint Conference of the IEEE International Frequency Control and the European Frequency and Time Forum (FCS) Proceedings*, 2011, pp. 1–10.
- [33] T. Takai *et al.*, "High-Performance SAW Resonator on New Multilayered Substrate Using LiTaO₃ Crystal", *IEEE Trans. Ultrason. Ferroelectr. Freq. Control*, vol. 64, no. 9, pp. 1382–1389, Sep. 2017.
- [34] A. Kochhar, G. Vidal-Alvarez, L. Colombo, and G. Piazza, "Top electrode shaping for harnessing high coupling in thickness shear mode resonators in Y-cut lithium niobate thin films", *2018 IEEE Micro Electro Mechanical Systems (MEMS)*, 2018, pp. 71–74.
- [35] L. Colombo, A. Kochhar, C. Xu, G. Piazza, S. Mishin, and Y. Oshmyansky, "Investigation of 20% scandium-doped aluminum nitride films for MEMS laterally vibrating resonators", in *2017 IEEE International Ultrasonics Symposium (IUS)*, 2017, pp. 1–4.
- [36] A. Lozzi, E. Ting-Ta Yen, P. Murali, and L. G. Villanueva, "Al_{0.83}Sc_{0.17}N Contour-Mode Resonators With Electromechanical Coupling in Excess of 4.5%", *IEEE Trans. Ultrason. Ferroelectr. Freq. Control*, vol. 66, no. 1, pp. 146–153, Jan. 2019.

- [37] M. Kadota and S. Tanaka, “Improved quality factor of Hetero Acoustic Layer (HAL) SAW resonator combining LiTaO₃ thin plate and quartz substrate”, in *2017 IEEE International Ultrasonics Symposium (IUS)*, 2017, pp. 1–1.
- [38] S. S. Bedair, J. S. Pulskamp, R. Rudy, R. Polcawich, R. Cable, and L. Griffin, “Boosting MEMS Piezoelectric Transformer Figures of Merit via Architecture Optimization”, *IEEE Electron Device Lett.*, vol. 39, no. 3, pp. 428–431, Mar. 2018.
- [39] L. C. Popa and D. Weinstein, “2DEG electrodes for piezoelectric transduction of AlGa_N/Ga_N MEMS resonators”, in *2013 Joint European Frequency and Time Forum & International Frequency Control Symposium (EFTF/IFC)*, 2013, pp. 922–925.
- [40] C. Cassella and G. Piazza, “Thick aluminum nitride contour-mode resonators mitigate thermoelastic damping”, *2016 IEEE International Frequency Control Symposium (IFCS)*, 2016, pp. 1–2.
- [41] A. Kochhar, L. Colombo, G. Vidal-Alvarez, and G. Piazza, “Integration of bottom electrode in Y-cut lithium niobate thin films for high electromechanical coupling and high capacitance per unit area MEMS resonators”, *2017 IEEE 30th International Conference on Micro Electro Mechanical Systems (MEMS)*, 2017, pp. 962–965.
- [42] E. Calayir, “Heterogeneous Integration of AlN MEMS Contour-Mode Resonators and CMOS Circuits”, PhD thesis, Oct. 2017.
- [43] C. Cassella, J. Segovia-Fernandez, G. Piazza, M. Cremonesi, and A. Frangi, “Reduction of anchor losses by etched slots in aluminum nitride contour mode resonators”, *2013 Joint European Frequency and Time Forum & International Frequency Control Symposium (EFTF/IFC)*, 2013, pp. 926–929.
- [44] J. Segovia-Fernandez, M. Cremonesi, C. Cassella, A. Frangi, and G. Piazza, “Anchor Losses in AlN Contour Mode Resonators”, *J. Microelectromechanical Syst.*, vol. 24, no. 2, pp. 265–275, Apr. 2015.
- [45] C. Cassella, N. Singh, B. W. Soon, and G. Piazza, “Quality Factor Dependence on the

- Inactive Regions in AlN Contour-Mode Resonators,” *J. Microelectromechanical Syst.*, vol. 24, no. 5, pp. 1575–1582, Oct. 2015.
- [46] J. Zou, C.-M. Lin, A. Gao, and A. P. Pisano, “The Multi-Mode Resonance in AlN Lamb Wave Resonators”, *J. Microelectromechanical Syst.*, vol. 27, no. 6, pp. 973–984, Dec. 2018.
- [47] A. A. Nassr, W. H. Ahmed, and W. W. El-Dakhakhni, “Coplanar capacitance sensors for detecting water intrusion in composite structures”, *Meas. Sci. Technol.*, vol. 19, no. 7, p. 075702, Jul. 2008.
- [48] M. Abramowitz and I. A. Stegun, *Handbook of mathematical functions, with formulas, graphs, and mathematical tables.*, Dover Publications, 1965.
- [49] R. Ruby, “A decade of FBAR success and what is needed for another successful decade”, *2011 Symposium on Piezoelectricity, Acoustic Waves and Device Applications (SPAWDA)*, 2011, pp. 365–369.
- [50] G. Piazza, P. J. Stephanou, and A. P. Pisano, “Piezoelectric Aluminum Nitride Vibrating Contour-Mode MEMS Resonators”, *J. Microelectromechanical Syst.*, vol. 15, no. 6, pp. 1406–1418, Dec. 2006.
- [51] C. Cassella and G. Piazza, “AlN Two-Dimensional-Mode Resonators for Ultra-High Frequency Applications”, *IEEE Electron Device Lett.*, vol. 36, no. 11, pp. 1192–1194, Nov. 2015.
- [52] C. Cassella, Y. Hui, Z. Qian, G. Hummel, and M. Rinaldi, “Aluminum Nitride Cross-Sectional Lamé Mode Resonators”, *J. Microelectromechanical Syst.*, vol. 25, no. 2, pp. 275–285, Apr. 2016.
- [53] Z. A. Schaffer, L. Colombo, A. S. Kochhar, G. Piazza, S. Mishin, and Y. Oshmyansky, “Experimental investigation of damping factors in 20% scandium-doped aluminum nitride laterally vibrating resonators”, *2018 IEEE Micro Electro Mechanical Systems (MEMS)*, 2018, pp. 787–790.

- [54] F. Tasnádi *et al.*, “Origin of the Anomalous Piezoelectric Response in Wurtzite $\text{Sc}_x\text{Al}_{1-x}\text{N}$ Alloys”, *Phys. Rev. Lett.*, vol. 104, no. 13, p. 137601, Apr. 2010.
- [55] M. Akiyama, T. Kamohara, K. Kano, A. Teshigahara, Y. Takeuchi, and N. Kawahara, “Enhancement of Piezoelectric Response in Scandium Aluminum Nitride Alloy Thin Films Prepared by Dual Reactive Cosputtering”, *Adv. Mater.*, vol. 21, no. 5, pp. 593–596, Feb. 2009.
- [56] H. Liu, F. Zeng, G. Tang, and F. Pan, “Enhancement of piezoelectric response of diluted Ta doped AlN”, *Appl. Surf. Sci.*, vol. 270, pp. 225–230, Apr. 2013.
- [57] A. Konno *et al.*, “ScAlN Lamb wave resonator in GHz range released by XeF_2 etching”, *2013 IEEE International Ultrasonics Symposium (IUS)*, 2013, pp. 1378–1381.
- [58] S. Mishin and Y. Oshmyansky, “Manufacturability of highly doped Aluminum Nitride films”
- [59] M. Kadota and T. Ogami, “High frequency lamb wave resonator using LiNbO_3 crystal thin plate and application to tunable filter”, *2010 IEEE International Ultrasonics Symposium*, 2010, pp. 962–965.
- [60] S. Gong and G. Piazza, “Figure-of-Merit Enhancement for Laterally Vibrating Lithium Niobate MEMS Resonators”, *IEEE Trans. Electron Devices*, vol. 60, no. 11, pp. 3888–3894, Nov. 2013.
- [61] M. Kadota, T. Ogami, K. Yamamoto, H. Tochishita, and Y. Negoro, “High-frequency lamb wave device composed of MEMS structure using LiNbO_3 thin film and air gap”, *IEEE Trans. Ultrason. Ferroelectr. Freq. Control*, vol. 57, no. 11, pp. 2564–2571, Nov. 2010.
- [62] I. E. Kuznetsova, B. D. Zaitsev, S. G. Joshi, and I. A. Borodina, “Investigation of acoustic waves in thin plates of lithium niobate and lithium tantalate”, *IEEE Trans. Ultrason. Ferroelectr. Freq. Control*, vol. 48, no. 1, pp. 322–328, Jan. 2001.
- [63] S. Gong, L. Shi, and G. Piazza, “High electromechanical coupling MEMS resonators at 530

- MHz using ion sliced X-cut LiNbO₃ thin film”, *2012 IEEE/MTT-S International Microwave Symposium Digest*, 2012, pp. 1–3.
- [64] R. Lu, T. Manzanque, Y. Yang, A. Kourani, and S. Gong, “Lithium niobate lateral overtone resonators for low power frequency-hopping applications”, *2018 IEEE Micro Electro Mechanical Systems (MEMS)*, 2018, pp. 751–754.
- [65] L. Shi and G. Piazza, “Active reflectors for high performance lithium niobate on silicon dioxide resonators”, *2015 28th IEEE International Conference on Micro Electro Mechanical Systems (MEMS)*, 2015, pp. 992–995.
- [66] F. V. Pop, A. S. Kochhar, G. Vidal-Alvarez, and G. Piazza, “Laterally vibrating lithium niobate MEMS resonators with 30% electromechanical coupling coefficient”, *2017 IEEE 30th International Conference on Micro Electro Mechanical Systems (MEMS)*, 2017, pp. 966–969.
- [67] L. Shi and G. Piazza, “Lithium Niobate on Silicon Dioxide Suspended Membranes: A Technology Platform for Engineering the Temperature Coefficient of Frequency of High Electromechanical Coupling Resonators,” *J. Microelectromechanical Syst.*, vol. 23, no. 6, pp. 1318–1329, Dec. 2014.
- [68] A. Kochhar, G. Vidal-Alvarez, L. Colombo, and G. Piazza, “High coupling two-port lithium niobate MEMS resonators using capacitive ground concept”, *2017 IEEE International Ultrasonics Symposium (IUS)*, 2017, pp. 1–4.
- [69] S. Gevorgian, A. K. Tagantsev, and A. K. Vorobiev, *Tuneable film bulk acoustic wave resonators*, Springer, 2013.
- [70] T. Takai *et al.*, “Incredible high performance SAW resonator on novel multi-layered substrate”, *2016 IEEE International Ultrasonics Symposium (IUS)*, 2016, pp. 1–4.
- [71] S. Galliou, M. Goryachev, P. Abbe, X. Vacheret, M. E. Tobar, and R. Bourquin, “Quality Factor Measurements of Various Types of Quartz Crystal Resonators Operating Near 4 K”, *IEEE Trans. Ultrason. Ferroelectr. Freq. Control*, vol. 63, no. 7, pp. 975–980, Jul. 2016.

- [72] L. Shi, “Lithium Niobate-based High-Electromechanical-Coupling RF-MicroElectroMechanical Resonators for Wideband Filtering”, PhD thesis, Feb. 2016.
- [73] C. Zuniga, “Piezoelectric resonant nanochannels”, PhD thesis, Jan. 2012.
- [74] J. Segovia-Fernandez and G. Piazza, “Analytical and Numerical Methods to Model Anchor Losses in 65-MHz AlN Contour Mode Resonators”, *J. Microelectromechanical Syst.*, vol. 25, no. 3, pp. 459–468, Jun. 2016.
- [75] J. Charmet, R. Daly, P. Thiruvankatanathan, and A. A. Seshia, “The effect of mass loading on spurious modes in micro-resonators”, *Appl. Phys. Lett.*, vol. 107, no. 4, p. 043502, Jul. 2015.
- [76] R. S. Weis and T. K. Gaylord, “Lithium niobate: Summary of physical properties and crystal structure”, *Appl. Phys. A Solids Surfaces*, vol. 37, no. 4, pp. 191–203, Aug. 1985.
- [77] V. Kaajakari, *Practical MEMS*, Small Gear Pub, 2009.
- [78] S. Gong and G. Piazza, “Laterally vibrating lithium niobate MEMS resonators with high electromechanical coupling and Quality factor”, in *2012 IEEE International Ultrasonics Symposium*, 2012, pp. 1051–1054.
- [79] L. Colombo, A. Kochhar, G. Vidal-Alvarez, and G. Piazza, “Investigations on the Quality Factor of Lithium Niobate Laterally Vibrating Resonators with Figure of Merit Greater than 1,500”, in *2018 IEEE International Ultrasonics Symposium (IUS)*, 2018, pp. 1–4.
- [80] Y. Yang, R. Lu, T. Manzanque, and S. Gong, “1.7 GHz Y-Cut Lithium Niobate MEMS Resonators with FoM of 336 and fQ of 9.15×10^{12} ”, in *2018 IEEE/MTT-S International Microwave Symposium - IMS*, 2018, pp. 563–566.
- [81] J. Segovia-Fernandez and G. Piazza, “Thermoelastic Damping in the Electrodes Determines Q of AlN Contour Mode Resonators”, *J. Microelectromechanical Syst.*, vol. 26, no. 3, pp. 550–558, Jun. 2017.
- [82] R. Wang, S. A. Bhave, and K. Bhattacharjee, “High $kt^2 \times Q$, multi-frequency lithium niobate

- resonators”, *2013 IEEE 26th International Conference on Micro Electro Mechanical Systems (MEMS)*, 2013, pp. 165–168.
- [83] B. Drafts, “Acoustic wave technology sensors”, *IEEE Trans. Microw. Theory Tech.*, vol. 49, no. 4, pp. 795–802, Apr. 2001.
- [84] R. H. Olsson, K. E. Wojciechowski, and D. W. Branch, “Origins and mitigation of spurious modes in aluminum nitride microresonators”, *2010 IEEE International Ultrasonics Symposium*, 2010, pp. 1272–1276.
- [85] J. Segovia-Fernandez, N.-K. Kuo, and G. Piazza, “Impact of metal electrodes on the figure of merit ($kt^2 \cdot Q$) and spurious modes of contour mode AlN resonators”, *2012 IEEE International Ultrasonics Symposium*, 2012, pp. 299–302.
- [86] M. Giovannini, S. Yazici, N.-K. Kuo, and G. Piazza, “Apodization technique for spurious mode suppression in AlN contour-mode resonators”, *Sensors Actuators A Phys.*, vol. 206, pp. 42–50, Feb. 2014.
- [87] C. Xu, E. Calayir, G. Piazza, M. Li, and S. Zhao, “Fast and accurate prediction of spurious modes in aluminum nitride MEMS resonators using artificial neural network algorithm”, *2017 IEEE International Ultrasonics Symposium (IUS)*, 2017, pp. 1–4.
- [88] Y.-H. Song and S. Gong, “Spurious mode suppression in SH0 Lithium Niobate laterally vibrating MEMS resonators”, *2015 IEEE International Electron Devices Meeting (IEDM)*, 2015, pp. 18.5.1-18.5.4.
- [89] B. A. Auld, *Acoustic fields and waves in solids*, Wiley, 1973.